NASA Contractor Report 4698
R95–95707

Unsteady Aerodynamic Models for Turbomachinery Aeroelastic and Aeroacoustic Applications

Joseph M. Verdon, Mark Barnett, and Timothy C. Ayer

CONTRACT NAS3–25425
NOVEMBER 1995

National Aeronautics and
Space Administration

NASA Contractor Report 4698
R95–957907

Unsteady Aerodynamic Models for Turbomachinery Aeroelastic and Aeroacoustic Applications

Joseph M. Verdon, Mark Barnett, and Timothy C. Ayer
United Technologies Research Center
East Hartford, Connecticut

Prepared for
Lewis Research Center
under Contract NAS3–25425

National Aeronautics and
Space Administration
Office of Management
Scientific and Technical
Information Program
1995

Report R95–957907

Unsteady Aerodynamic Models for Turbomachinery Aeroelastic and Aeroacoustic Applications

Joseph M. Verdon
Mark Barnett
and
Timothy C. Ayer

Final Report, Tasks I through V,
prepared under Contract NAS3–25425

for

NASA Lewis Research Center

September 1995

Page intentionally left blank

Unsteady Aerodynamic Models for Turbomachinery Aeroelastic and Aeroacoustic Applications

Contents

List of Figures

Figure 4.13. Surface Mach-number distributions for inviscid (——) and viscous, at $Re = 10^5$ (- - - - -) and $Re = 10^6$ (- - -), flows through the 10th Standard Cascade operating at $M_{-\infty} = 0.70$, $\Omega_{-\infty} = 55$ deg.

Figure 4.14. Trailing-edge streamlines for 10th Standard Cascade operating at $M_{-\infty} = 0.70$, $\Omega_{-\infty} = 55$ deg, and $Re = 10^5$.

Figure 4.15. Effect of steady viscous displacement on pressure-displacement function response for subsonic flow ($M_{-\infty} = 0.7$, $\Omega_{-\infty} = 55$ deg) through the 10th Standard Cascade undergoing torsional blade vibrations about midchord at $\omega = 1$: (a) in-phase ($\sigma = 0$ deg) blade motion; (b) out-of-phase ($\sigma = 180$ deg) blade motion.

Figure 4.16. Effect of steady viscous displacement on pressure-displacement function response for subsonic flow ($M_{-\infty} = 0.7$, $\Omega_{-\infty} = 55$ deg) through the 10th Standard Cascade undergoing bending blade vibrations at $\omega = 1$: (a) in-phase ($\sigma = 0$ deg) blade motion; (b) out-of-phase ($\sigma = 180$ deg) blade motion.

Figure 4.17. Effect of steady viscous displacement on work per cycle responses for subsonic flow ($M_{-\infty} = 0.7$, $\Omega_{-\infty} = 55$ deg) through the 10th Standard Cascade undergoing prescribed blade vibrations at unit frequency ($\omega = 1$): (a) torsional vibrations about midchord (b) bending vibrations.

Figure 5.1. Unsteady pressure distributions along a blade and its wake for an unstaggered flat-plate cascade ($\Omega = \Theta = 0$ deg, $M_{-\infty} = 0.5$ and $G = 1$) subjected to a unit-amplitude, $|p_{I,-\infty}| = 1$, pressure excitation from upstream with $\kappa_{\eta,-\infty} = \sigma G^{-1} = 0$.

Figure 5.2. Unsteady pressure distributions along a blade and its wake for an unstaggered flat-plate cascade (with $\Omega = \Theta = 0$ deg, $M_{-\infty} = 0.5$ and $G = 1$) subjected to a unit-amplitude, $|p_{I,+\infty}| = 1$, pressure excitation from downstream with $\kappa_{\eta,+\infty} = \sigma G^{-1} = 0$.

Figure 5.3. Temporal mean and Fourier magnitudes of the displacement thickness, $\tilde{\bar{\delta}}$, wall shear stress, $\tilde{\bar{\tau}}_w$, and wake centerline velocity, $\tilde{V}_{\mathcal{L}}$, for turbulent flow through an unstaggered flat-plate cascade ($\Omega = \Theta = 0$ deg, $G = 1$, $M = 0.5$ and $\mathrm{Re} = 10^6$) subjected to an incident pressure disturbance from upstream with $p_{I,-\infty} = (0.5, 0)$, $\omega = 5$ and $\sigma = 0$ deg.

Figure 5.4. Temporal mean and Fourier magnitudes of the displacement thickness, $\tilde{\bar{\delta}}$, wall shear stress, $\tilde{\bar{\tau}}_w$, and wake centerline velocity, $\tilde{l}_{\mathcal{L}}$, for turbulent for turbulent flow through an unstaggered flat-plate cascade ($\Omega = \Theta = 0$ deg, $G = 1$, $M = 0.5$ and $\mathrm{Re} = 10^6$) subjected to an incident pressure disturbance from downstream with $p_{I,+\infty} = (0.5, 0)$, $\omega = 5$ and $\sigma = 0$ deg.

Figure 5.5. Fourier amplitudes of $\tilde{\bar{\delta}}$, $\tilde{\bar{\tau}}_w$ and $\tilde{V}_{\mathcal{L}}$ for an unstaggered flat-plate cascade ($\Omega = \Theta = 0$ deg, $G = 1$, $M = 0.5$ and $\mathrm{Re} = 10^6$) subjected to pressure excitations from upstream with $p_{I,-\infty} = (0.5, 0)$ and $\sigma = 0$ deg.

Figure 5.6. Relative phase angles of first-harmonic displacement thickness, wall shear stress, and wake centerline velocity for an unstaggered flat-plate cascade ($\Omega = \Theta = 0$ deg, $G = 1$, $M = 0.5$ and $\mathrm{Re} = 10^6$) subjected to pressure excitations from upstream with $p_{I,-\infty} = (0.5, 0)$ and $\sigma = 0$ deg.

Figure 5.7. Fourier amplitudes of $\tilde{\bar{\delta}}$, $\tilde{\bar{\tau}}_w$ and $\tilde{V}_{\mathcal{L}}$ for an unstaggered flat-plate cascade ($\Omega = \Theta = 0$ deg, $G = 1$, $M = 0.5$ and $\mathrm{Re} = 10^6$) subjected to pressure excitations from downstream with $p_{I,+\infty} = (0.5, 0)$ and $\sigma = 0$ deg.

Figure 5.8. Relative phase angles of first-harmonic displacement thickness, wall shear stress, and wake centerline velocity for an unstaggered flat-plate cascade ($\Omega = \Theta = 0$ deg, $G = 1$, $M = 0.5$ and $\mathrm{Re} = 10^6$) subjected to pressure excitations from downstream with $p_{I,+\infty} = (0.5, 0)$ and $\sigma = 0$ deg.

Figure 5.9. Fourier amplitudes of $\tilde{\bar{\delta}}$, $\tilde{\bar{\tau}}_w$ and $\tilde{V}_{\mathcal{L}}$ vs amplitude, $|p_{I,-\infty}|$, for an acoustic excitation from upstream, with $\omega = 5$ and $\sigma = 0$ deg, interacting with an unstaggered flat-plate cascade ($\Omega = \Theta = 0$ deg, $G = 1$, $M = 0.5$ and $\mathrm{Re} = 10^6$).

Figure 5.10. Fourier amplitudes of $\tilde{\bar{\delta}}$, $\tilde{\bar{\tau}}_w$ and $\tilde{V}_{\mathcal{L}}$ vs amplitude, $|p_{I,+\infty}|$, for an acoustic excitation from downstream with, $\omega = 5$ and $\sigma = 0$ deg, interacting with an unstaggered flat-plate cascade ($\Omega = \Theta = 0$ deg, $G = 1$, $M = 0.5$ and $\mathrm{Re} = 10^6$).

Figure 5.11. Contours of the in-phase component (real part) of the unsteady pressure for the turbine cascade subjected to an acoustic excitation from upstream with $p_{I,-\infty} = (0.35, 0)$, $\omega = 1$ and $\sigma = 0$.

Figure 5.12. Temporal mean values and upper and lower bounds of the inviscid surface (viscous-layer edge) velocity for the turbine cascade subjected to an upstream pressure excitation with $p_{I,-\infty} = (0.35, 0)$, $\omega = 1$ and $\sigma = 0$.

Figure 5.13. Velocity profiles in the neighborhood of a mean stagnation point location for the turbine cascade subjected to an upstream acoustic excitation with $p_{I,-\infty} = (0.35, 0)$, $\omega = 1$ and $\sigma = 0$: (a) $t = \pi/2$; (b) $t = \pi$; (c) $t = 3\pi/2$; (d) $t = 2\pi$.

Figure 5.14. Velocity profiles in the neighborhood of an instantaneous stagnation point location for the turbine cascade subjected to an upstream acoustic excitation with $p_{I,-\infty} = (0.35, 0)$, $\omega = 1$ and $\sigma = 0$: (a) through (d) as in Fig. 5.13.

Figure 5.15. Temporal mean values and upper and lower bounds for the displacement thickness and surface shear stress along a turbine blade surface for an unsteady flow excited by an upstream pressure excitation with $p_{I,-\infty} = (0.35, 0)$, $\omega = 1$ and $\sigma = 0$.

Figure 5.16. Temporal mean values and upper and lower bounds for the displacement thickness and minimum wake streamwise velocity along a turbine wake for an unsteady flow excited by an upstream pressure excitation with $p_{I,-\infty} = (0.35, 0)$, $\omega = 1$ and $\sigma = 0$.

Figure 5.17. Streamwise velocity profiles in the wake of a turbine for an unsteady flow excited by an acoustic excitation from upstream with $p_{I,-\infty} = (0.35, 0)$, $\omega = 1$ and $\sigma = 0$.

Unsteady Aerodynamic Models for Turbomachinery Aeroelastic and Aeroacoustic Applications

Summary

Theoretical analyses and computer codes have been developed for predicting compressible unsteady inviscid and viscous flows through blade rows of axial-flow turbomachines. Such analyses are needed to determine the impact of unsteady flow phenomena on the structural durability and noise generation characteristics of the blading. The emphasis here has been placed on developing analyses based on asymptotic representations of unsteady flow phenomena. Thus, high Reynolds number flows driven by small amplitude unsteady excitations in which viscous effects are concentrated within thin layers have been considered. The resulting analyses should apply in many practical situations and lead to a better understanding of the relevant flow physics. In addition, they will be efficient computationally, and therefore, appropriate for use in aeroelastic and aeroacoustic design studies. Finally, the asymptotic analyses will be useful for calibrating and validating the time-accurate, nonlinear, Euler/Navier-Stokes analyses that are currently being developed for predicting unsteady flows through turbomachinery blade rows.

Under the present research program, the effort has been focused on formulating inviscid/viscid interaction and linearized inviscid unsteady flow models, and on providing inviscid and viscid prediction capabilities for subsonic steady and unsteady cascade flows. In this report we describe the linearized, inviscid, unsteady aerodynamic, analysis, LINFLO, the steady, strong, inviscid/viscid interaction analysis, SFLOW-IVI, and the unsteady viscous layer analysis, UNSVIS, that have been developed under this program. The LINFLO analysis can be applied to efficiently predict the unsteady aerodynamic response of a two-dimensional blade row to prescribed structural, (i.e., blade) motions and external aerodynamic (acoustic, vortical and entropic) disturbances. The SFLOW-IVI analysis can be applied to predict steady cascade flows, at high Reynolds numbers, in which regions of strong inviscid/viscid interaction, including viscous layer separation, occur. The UNSVIS analysis can be applied to predict nonlinear unsteady flows in thin boundary layers and wakes. The capabilities of the three analyses are demonstrated via applications to unsteady flows through compressor and turbine cascades. The numerical results pertain to unsteady flows excited by prescribed vortical disturbances at inlet, acoustic disturbances at inlet and exit and blade bending and torsional vibrations. Recommendations are also given for the future research needed for extending and improving the foregoing asymptotic analyses, and to meet the goal of providing an efficient inviscid/viscid interaction capability for subsonic and transonic unsteady cascade flows.

1. Introduction

The unsteady aerodynamic analyses intended for use in predicting the aeroelastic and aeroacoustic responses of turbomachinery blading must be applicable over wide ranges of blade-row geometries, mean operating conditions, and modes and frequencies of unsteady excitation. In particular, these analyses must be capable of predicting unsteady pressure responses of blade rows to a variety of unsteady excitations. The latter include structural (blade) motions, variations in total temperature and total pressure (entropy and vorticity waves) at inlet and variations in static pressure (acoustic waves) at inlet and exit. Finally, because of the large number of controlling parameters involved, there is a stringent requirement for computational efficiency, if an analysis is to be used successfully in the blade design process. To satisfy this latter requirement a number of restrictive assumptions must be introduced into the development of appropriate unsteady aerodynamic models. The analyses described in this report have been developed to provide reliable and efficient theoretical prediction capabilities for inviscid and viscid, steady and small-disturbance unsteady, flows, at high Reynolds number, through two-dimensional cascades.

1.1 Background

The theoretical analyses that have been developed to predict the aeroelastic and aeroacoustic behavior of turbomachinery blading, i.e., the onset of blade flutter, the amplitudes of forced blade vibration and the sound pressure levels that exist upstream and downstream of the blade row have, for the most part, been based on the following geometric and aerodynamic assumptions. The blades of an isolated, two-dimensional cascade are usually considered with the aerodynamic effects associated with neighboring structures being represented via prescribed nonuniform flow conditions at inlet and exit. The unsteady excitations are assumed to be periodic in time and in the blade-to-blade direction. The flow Reynolds number is taken to be sufficiently high so that viscous effects have a negligible impact on the unsteady pressure field. Finally, the unsteady excitations are assumed to be sufficiently small so that a linearized treatment of the unsteady inviscid flow is justified.

Until fairly recently, the inviscid unsteady aerodynamic analyses that have been available for turbomachinery aeroelastic and aeroacoustic design applications have been based on classical linearized theory (see [Whi87] for a review). Here the steady and harmonic unsteady departures of the flow variables from their uniform free-stream values are regarded as small and of the same order of magnitude, leading to uncoupled, linear, constant coefficient, boundary value problems for the steady and the complex amplitudes of the unsteady disturbances. Thus, unsteady solutions based on the classical linearization apply essentially to cascades of unloaded flat-plate blades. Very efficient semi-analytic solution procedures have been developed for two-dimensional attached subsonic and supersonic flows and applied with some success in turbomachinery aeroelastic and aeroacoustic design calculations. It should also be mentioned that extensive efforts (as reviewed by Namba [Nam87]) have been made to develop three-dimensional unsteady aerodynamic analyses, based on the classical linearization.

Because of the limitations in physical modeling associated with the classical linearization, more general two-dimensional inviscid linearizations have been developed. These include the

effects of important design features such as real blade geometry, mean blade loading, and operation at transonic Mach numbers. Here, unsteady disturbances are regarded as small-amplitude harmonic fluctuations relative to a fully nonuniform, isentropic and irrotational, mean or steady background flow. The steady flow is determined as a solution of a nonlinear inviscid equation set, and the unsteady flow is governed by linear equations with variable coefficients that depend on the underlying steady flow. This type of analytical model is described in [Ver92, Ver93] and is often referred to as a linearized potential model; however, the potential-flow restriction applies only to the steady background flow. It has received considerable attention in recent years, and solution algorithms for the nonlinear steady and the linearized unsteady problem have reached the stage where they are being applied in turbomachinery aeroelastic and aeroacoustic design studies (e.g., see [Smi90, SS90, MM94]). In particular, one such analysis, the linearized inviscid flow analysis, LINFLO, has been extended under the present contract for cascade gust response predictions. In previous work, this analysis has been developed and applied to predict unsteady subsonic and transonic flows excited by blade vibrations or acoustic disturbances [VC84, Ver89a, UV91, KV93b] and, under the present contract, to predict unsteady subsonic flows excited by entropic and vortical gusts [VH90, HV91, VBHA91].

The unsteady flows of practical interest usually occur at high, but finite Reynolds number, so that viscous-layer displacements can have an impact on the unsteady pressure response. Provided that large-scale flow separations from the blade surfaces do not occur, the overall flow field can be divided conceptually into "inner" viscous or dissipative regions, consisting of thin boundary layers and wakes, and an "outer" inviscid region. Solutions to the complete flow problem can then be determined by an iterative procedure involving successive solutions to the inviscid and viscid equations. If the inviscid/viscid interaction is "weak", then at each step of the iteration process, the inviscid and viscid solutions can be determined sequentially with the pressure being determined by the inviscid flow. However, in most flows, strong inviscid/viscid interactions occur due, for example, to boundary-layer separations, shock/boundary-layer interactions and trailing-edge/near-wake interactions. For such flows the pressure must be determined by solving the inviscid and viscous layer equations simultaneously at each iteration level.

The construction of a high Reynolds number viscous cascade solver involves first, the development of component flow solvers, and second, the implementation of these component solvers into an overall computational procedure to provide an analysis for the complete flow field. Solution methods for steady, subsonic and transonic, inviscid flows through cascades and for steady boundary-layer and wake flows have been developed to a relatively mature state. Methods for coupling such solutions have also been developed and applied to predict steady cascade flows, with strong inviscid/viscid interactions (e.g., see [HSS79, JH83, CH80, BV89, BHE91, BVA93a, BVA93b]), with the work in [BVA93a, BVA93b] being performed as part of the present effort. Similar approaches are needed for unsteady flows. Under the present Contract, nonlinear steady and linearized unsteady inviscid analyses have been coupled to the unsteady viscous-layer analysis of [PVK91], but only to predict unsteady cascade flows with weak inviscid/viscid interactions [VBHA91, BV93]. To date, there has been very little effort to couple unsteady inviscid and viscous-layer analyses to provide a strong inviscid/viscid interaction analysis for unsteady cascade flows. As steps toward this goal, the steady inviscid/viscid interaction analysis for cascades, SFLOW–IVI, that can provide the foundation for an un-

steady procedure to be developed later, and the unsteady viscous-layer analysis (UNSVIS) have been developed under the present research program.

1.2 Scope of the Present Effort

The objectives of the research program conducted under Contract NAS3–25425 are to provide efficient theoretical analyses for predicting compressible unsteady flows through two-dimensional blade rows. Such analyses are needed to understand the impact of unsteady aerodynamic phenomena on the aeroelastic and aeroacoustic performances of turbomachinery blading. For this purpose, we have developed a detailed inviscid/viscid interaction formulation for unsteady cascade flows, which is described in § 2 of this report. We have also developed or extended several analyses that will form the components of an unsteady, inviscid/viscid interaction, solution procedure. The latter include the linearized inviscid unsteady aerodynamic analysis, LINFLO, the steady inviscid/viscid interaction analysis, SFLOW–IVI, and the unsteady viscous layer analysis, UNSVIS. The steady full potential analysis, SFLOW [HV93, HV94], which is also considered to be a component of the overall prediction scheme, has been developed at NASA Lewis under a separate, but related, research program. The present work has been directed primarily towards subsonic aeroelastic applications, however, for the most part, this work will apply, more generally, for predicting the aeroelastic and aeroacoustic responses of turbomachinery blading operating at subsonic and transonic Mach numbers.

In the first phase of this program [VH90, HV91] the linearized inviscid analysis (LINFLO) was extended to predict the responses of a cascade to entropic and vortical excitations. A velocity decomposition introduced by Goldstein [Gol78, Gol79], and later modified by Atassi and Grzedzinski [AG89], is employed to split the linearized unsteady velocity into rotational and irrotational components. This decomposition leads to a very convenient description of the linearized unsteady perturbation — one in which closed form solutions can be determined for the entropy and vorticity or rotational velocity fluctuations in terms of the drift and stream functions of the underlying steady flow. Numerical field methods are required only to determine the unsteady potential and from this, the unsteady pressure. The potential is governed by an inhomogeneous wave equation in which the source term depends upon the rotational velocity field. The potential fluctuations are determined numerically on an H-type mesh in which the streamlines of the steady background flow are used as mesh lines. Numerical solutions are reported in [VH90, HV91, VBHA91] for several configurations including flat-plate cascades, a compressor exit guide vane, a high-speed compressor cascade, and a turbine cascade. The LINFLO analysis is described in § 3 of this report, with particular emphasis on its capabilities for predicting unsteady flows excited by vortical gusts.

An efficient steady analysis for predicting strong inviscid/viscid interaction phenomena; such as, viscous-layer separation, shock/boundary-layer interaction and trailing-edge/near-wake interaction, in turbomachinery blade passages is needed as part of a comprehensive analytical blade design prediction system. Such an analysis, called SFLOW–IVI, has been reported in [BVA93a, BVA93b] and is described in § 4. Here, the flow in the outer or inviscid region is governed by the full-potential equation and that in the inner viscous region, by Prandtl's viscous-layer equations. The non-hierarchical nature of strong interactions is taken into account in the semi-inverse iteration procedure used to couple the two solutions.

The steady, full-potential analysis, SFLOW, [HV93, HV94] is employed in this procedure to determine inviscid solutions. SFLOW was constructed, for use with the LINFLO analysis, to provide comprehensive and compatible, steady and unsteady, inviscid, flow prediction capabilities for cascades.

In the IVI procedure, which is referred to as SFLOW–IVI, viscous effects are incorporated by adjusting the blade and wake surface boundary conditions in SFLOW to account for the effects of viscous displacement. Inviscid solutions are determined using an implicit, least-squares, finite-difference approximation, viscous-layer solutions using an inverse, finite-difference, space-marching method which is applied along the blade surfaces and wake streamlines. The inviscid and viscid solutions are coupled using a semi-inverse, global iteration procedure, which permits the prediction of boundary-layer separation and other strong-interaction phenomena, and allows nonlinear changes to the inviscid flow, due to viscous effects, to be evaluated. Results are presented for three cascades, with a range of inlet flow conditions considered for one of them, including conditions leading to large-scale flow separation. Comparisons with Navier-Stokes solutions and experimental data are also given.

Finally the UNSVIS analysis of [PVK91] was extended so that unsteady viscous effects in the vicinity of leading-edge stagnation points and in blade wakes could be predicted [VBHA91, BV93]. The nonlinear unsteady flow in a viscous layer is described by Prandtl's equations. As in the SFLOW–IVI analysis, algebraic models are used to account for the effects of transition and turbulence. The viscous-layer equations are solved in terms of Levy-Lees type variables using a finite-difference technique in which solutions are advanced in time and in the streamwise direction. Numerical solutions are determined by marching implicitly, first in time and then in the streamwise direction, over several periods of unsteady excitation, from an initial steady solution, and from an approximate time-dependent, upstream flow solution. This analysis, rather than one in which the results of separate nonlinear steady and linearized unsteady viscous-layer analyses are superposed, allows an assessment to be made of the relative importance of nonlinear unsteady effects in viscous regions.

Under the present effort, a similarity analysis was developed to predict unsteady viscous compressible flow in the vicinity of a moving leading-edge stagnation point and incorporated into the UNSVIS code. The stagnation region analysis provides the "initial" upstream flow information needed to advance or march a viscous-layer calculation downstream along the blade surfaces and into the wake. In addition, the wake analysis, used previously in UNSVIS, was extended so that the changes or jumps in the inviscid velocity that occur across vortex-sheet unsteady wakes could be properly accommodated. The linearized inviscid analysis, LINFLO, and the nonlinear viscous-layer analysis, UNSVIS, were also coupled to provide a weak viscid/inviscid interaction solution capability for unsteady cascade flows. The UNSVIS analysis is described in § 5, where it is also applied to study the viscous-layer responses of an unstaggered flat-plate cascade to pressure or acoustic excitations originating upstream and downstream of the blade row. Finally, the coupled LINFLO/UNSVIS analysis is applied to a turbine cascade subjected to a pressure excitation from upstream to demonstrate the current weak inviscid/viscid interaction solution capability on a realistic cascade configuration.

The component analyses, described in this report, are important in their own right. They can be applied to improve our understanding of the complex steady and unsteady flow processes that occur in turbomachine cascades, and to provide useful aeroelastic and aeroacoustic design information. Hopefully, along with the general inviscid/viscid interaction and inviscid

small-disturbance formulations, presented in § 2, they will contribute to the future development of a comprehensive inviscid/viscid interaction analysis for unsteady cascade flows. Such an analysis will provide useful aeroelastic and aeroacoutic response information for a wide range of blade-row geometries and operating conditions. It will also be of help in calibrating the time-accurate, nonlinear, Euler and Navier-Stokes analyses that are currently being developed for predicting turbomachinery unsteady flow fields.

2. Physical Problem and Mathematical Models

2.1 Unsteady Flow through a Two-Dimensional Cascade

We consider time-dependent flow, at high Reynolds number (Re) and with negligible body forces, of a perfect gas with constant specific heats and constant Prandtl number (Pr) through a two-dimensional cascade, such as the one shown in Figure 2.1. The unsteady fluctuations in the flow arise from one or more of the following sources: blade motions, upstream total temperature and total pressure disturbances, and upstream and/or downstream static pressure disturbances that carry energy toward the blade row. These excitations are assumed to be of small amplitude, periodic in time, and periodic in the blade-to-blade or cascade "circumferential" direction. Also, blade shape and orientation relative to the inlet freestream direction, the inlet to exit mean static pressure ratio and the amplitudes, modes, frequencies and wave numbers of the unsteady excitations are such that viscous effects are confined within thin layers, that lie along the blade surfaces and extend downstream from the blade trailing edges. We should note that the aerodynamic models to be developed below, apply to subsonic flows and to transonic flows containing normal shocks; however, the applications presented throughout this report are restricted to subsonic flows.

In the following discussion all physical variables are dimensionless. Vector quantities are in boldface type, and a tilde over a dependent variable indicates time dependence. Lengths have been scaled with respect to blade chord (L^*), time with respect to the ratio of blade chord to upstream freestream flow speed ($V^*_{-\infty}$), density with respect to the upstream freestream density ($\bar{\rho}^*_{-\infty}$), velocity with respect to the upstream freestream flow speed, and stress with respect to the product of the upstream freestream density and the square of the upstream freestream speed ($\bar{\rho}^*_{-\infty} {V^*_{-\infty}}^2$). Here the superscript $*$ denotes a dimensional quantity and the subscript $-\infty$ refers to the prescribed freestream conditions far upstream. The scalings for the remaining variables can be determined from the equations that follow, which have the same forms as their dimensional counterparts.

We will analyze the unsteady flow in a blade-row fixed coordinate frame in terms of the Cartesian (x, y) or (ξ, η) coordinates and the time t. Here, for example, ξ and η measure distances in the cascade axial and circumferential directions, respectively. To describe flows in which the fluid domain varies with time it is useful to consider two sets of independent variables, say $(\mathbf{x}, t)$ and $(\bar{\mathbf{x}}, t)$. The position vector $\mathbf{x}(\bar{\mathbf{x}}, t) = \bar{\mathbf{x}} + \boldsymbol{\mathcal{R}}(\bar{\mathbf{x}}, t)$ describes the instantaneous location of a moving point, say $\mathcal{P}$, $\bar{\mathbf{x}}$ refers to the reference or steady-state position of $\mathcal{P}$, and $\boldsymbol{\mathcal{R}}(\bar{\mathbf{x}}, t)$ is the displacement of $\mathcal{P}$ from its reference position. The displacement field, $\boldsymbol{\mathcal{R}}$, is usually prescribed so that the solution domain moves with solid boundaries and is stationary far from the blade row. If we set $\boldsymbol{\mathcal{R}} \equiv 0$, then the position vector $\mathbf{x}$, like $\bar{\mathbf{x}}$, describes a stationary point in the blade-row fixed reference frame.

The mean or steady-state positions of the blade chord lines coincide with the line segments $\bar{\eta} = \bar{\xi} \tan\Theta + mG, 0 \le \bar{\xi} \le \cos\Theta$, $m = 0, \pm 1, \pm 2, \ldots$, where m is a blade number index, Θ is the cascade stagger angle, and $\mathbf{G}$ is the cascade gap vector which is directed along the $\bar{\eta}$-axis with magnitude equal to the blade spacing. The blade motions are prescribed as functions of $\bar{\mathbf{x}}$ and t, i.e.,

$$\boldsymbol{\mathcal{R}}_{\mathrm{B}_m}(\bar{\mathbf{x}} + m\mathbf{G}, t) = \mathrm{Re}\{\mathbf{R}_{\mathrm{B}}(\bar{\mathbf{x}}) \exp[i(\omega t + m\sigma)]\}, \quad \text{for} \quad \bar{\mathbf{x}} \in \mathrm{B} \quad (\text{or} \quad \mathbf{x} \in \mathcal{B}) \,. \tag{2.1}$$

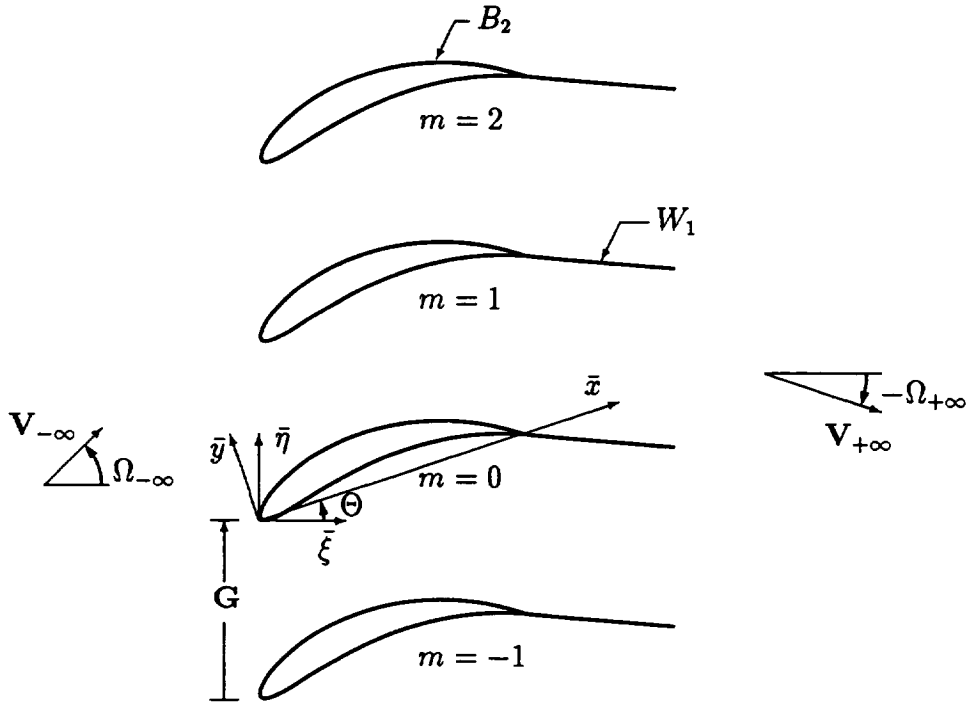

Figure 2.1: Two-dimensional compressor cascade.

Here $\mathcal{R}_{\mathrm{B}_m}$ is the displacement of a point on a moving blade surface ($\mathcal{B}_m$) relative to its mean or steady-state position (B_m); $\mathbf{R}_{\mathrm{B}}$ is the complex amplitude of the blade displacement; σ is the phase angle between the motions of adjacent blades; Re{ } denotes the real part of { }; and B denotes the reference ($m = 0$) blade surface. In the present report we will use the notations $\mathcal{R}_{\mathrm{B}_m}$ or $\mathcal{R}$, $\bar{\mathrm{x}} \in \mathrm{B}_m$, to indicate the displacement of a point on the mth blade surface. Similar notations, i.e., $\mathcal{R}_{W_m}$ or $\mathcal{R}$, $\bar{\mathrm{x}} \in W_m$, and $\mathcal{R}_{Sh_{m,n}}$ or $\mathcal{R}$, $\bar{\mathrm{x}} \in Sh_{m,n}$, will be used to represent inviscid wake and shock displacements.

For aeroelastic and aeroacoustic applications we are usually interested in a restricted class of unsteady flows; those in which the unsteady fluctuations can be regarded as perturbations of a background flow that is steady in the blade-row frame of reference. Thus, we consider situations in which the background flows far upstream (say $\bar{\xi} < \bar{\xi}_-$) and far downstream ($\bar{\xi} > \bar{\xi}_+$) from the blade-row consist of at most a small steady perturbation from a uniform flow. In this case any arbitrary unsteady aerodynamic excitation of small amplitude can be represented approximately as the sum of independent entropic, vortical, and acoustic disturbances that travel towards the blade row, as indicated in Figure 2.2.

The entropic, $\tilde{s}_{-\infty}(\bar{\mathrm{x}}, t)$, vortical, $\tilde{\zeta}_{-\infty}(\bar{\mathrm{x}}, t)$, and acoustic, $\tilde{p}_{I,\mp\infty}(\bar{\mathrm{x}}, t)$, excitations, where the subscripts $-\infty$ and $+\infty$ refer to the far upstream and far downstream flow regions, respectively, are also prescribed functions of $\bar{\mathrm{x}}$ and t. However, these functions must be solutions of the fluid-dynamic field equations that describe disturbances that travel towards

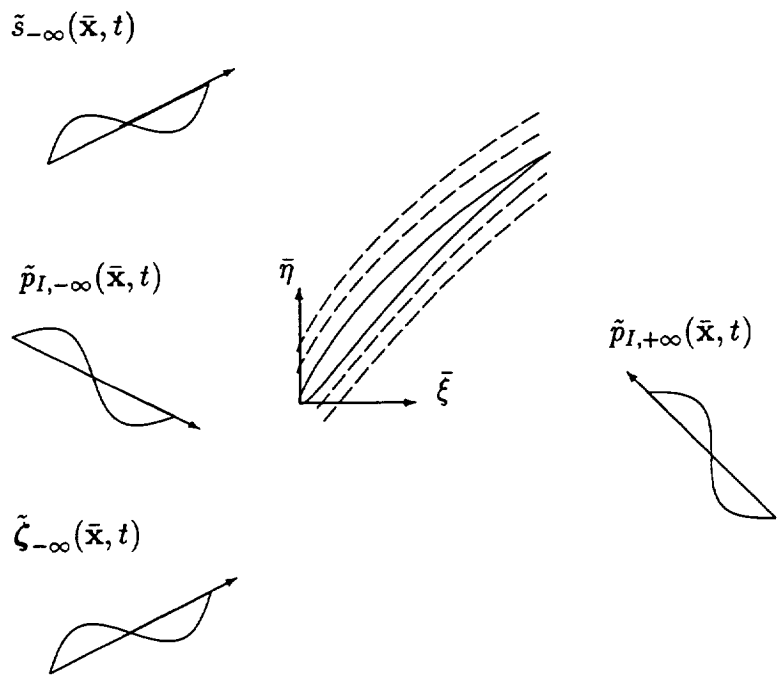

Figure 2.2: Unsteady excitations: blade motion, incident vortical and entropic disturbances from upstream, and incident acoustic disturbances from upstream and downstream.

the blade row. Since the unsteady aerodynamic excitations are periodic in $\bar{\eta}$ and t, it is often useful to represent them via Fourier series. In this case the complex amplitudes, temporal frequencies and circumferential wave numbers of the various excitations are the prescribed quantities. In the present study, the external aerodynamic excitations are small-amplitude, harmonic perturbations of a uniform freestream flow, and therefore must be of the form

$$\tilde{s}(\bar{\mathbf{x}},t) = \tilde{s}_{-\infty}(\bar{\mathbf{x}} - \mathbf{V}_{-\infty}t) = \mathrm{Re}\{s_{-\infty}\exp[i(\boldsymbol{\kappa}_{-\infty}\cdot\bar{\mathbf{x}} + \omega t)]\}\ldots\ , \quad \bar{\xi} < \bar{\xi}_-\ , \tag{2.2}$$

$$\tilde{\boldsymbol{\zeta}}(\bar{\mathbf{x}},t) = \tilde{\boldsymbol{\zeta}}_{-\infty}(\bar{\mathbf{x}} - \mathbf{V}_{-\infty}t) = \mathrm{Re}\{\boldsymbol{\zeta}_{-\infty}\exp[i(\boldsymbol{\kappa}_{-\infty}\cdot\bar{\mathbf{x}} + \omega t)]\}\ldots\ , \quad \bar{\xi} < \bar{\xi}_-\ , \tag{2.3}$$

and

$$\tilde{p}_I(\bar{\mathbf{x}},t) = \tilde{p}_{I,\mp\infty}(\bar{\mathbf{x}},t) = \mathrm{Re}\{p_{I,\mp\infty}\exp[-\beta_{\mp\infty}\bar{\xi} + i(\boldsymbol{\kappa}_{\mp\infty}\cdot\bar{\mathbf{x}} + \omega t)]\}\ldots\ , \quad \bar{\xi} \lesseqgtr \bar{\xi}_\mp\ . \tag{2.4}$$

Here $s_{-\infty}$, $\boldsymbol{\zeta}_{-\infty}$ and $p_{I,\mp\infty}$ are the complex amplitudes of the entropic, vortical and acoustic excitations, ω is the temporal frequency, $\boldsymbol{\kappa}_{\mp\infty}$ is the wave number, with $\kappa_{\eta,\mp\infty} = \sigma G^{-1}$, and the $\beta_{\mp\infty}$ are attenuation constants. It follows from the governing equations that the temporal frequency and wave number of an entropic or vortical excitation are related by $\omega = -\boldsymbol{\kappa}_{-\infty}\cdot\mathbf{V}_{-\infty}$, where $\mathbf{V}_{-\infty}$ is the uniform relative inlet velocity, but more complicated relationships exist between ω and $\boldsymbol{\kappa}_{\mp\infty}$ for pressure excitations [Ver89b].

2.2 Reynolds-Averaged Navier-Stokes Equations

The field equations that govern the fluid motion follow from the mass, momentum and energy conservation laws. After taking ensemble averages of the resulting equations, the so-called Reynolds-averaged Navier-Stokes equations for the (statistical) mean values of the flow variables can be determined. The conservation law forms of these equations are usually preferred in modern numerical simulations of steady and unsteady flows. However, for the present purpose of developing computationally efficient aerodynamic models, we will consider the conservative form of the mass equation and convective forms of the momentum and energy equations, i.e.,

$$\left.\frac{\partial \tilde{\bar{\rho}}}{\partial t}\right|_{\mathbf{x}} + \nabla_{\mathbf{x}} \cdot (\tilde{\bar{\rho}}\tilde{\mathbf{V}}) = 0 \tag{2.5}$$

$$\tilde{\bar{\rho}}\frac{D\tilde{\mathbf{V}}}{Dt} + \nabla_{\mathbf{x}}\tilde{P} = \nabla_{\mathbf{x}} \cdot (\tilde{\boldsymbol{\Pi}} - \tilde{\bar{\rho}}\overline{\tilde{\mathbf{v}}' \otimes \tilde{\mathbf{v}}'}) \tag{2.6}$$

and

$$\bar{\rho}\frac{D\tilde{H}_T}{Dt} - \left.\frac{\partial \tilde{P}}{\partial t}\right|_{\mathbf{x}} = \nabla_{\mathbf{x}} \cdot (\tilde{\boldsymbol{\Pi}} \cdot \mathbf{V} - \tilde{\mathbf{Q}} - \tilde{\bar{\rho}}\overline{\tilde{h}_T'\tilde{\mathbf{v}}'}) \tag{2.7}$$

Here, $D/Dt = \partial/\partial t|_{\mathbf{x}} + \tilde{\mathbf{V}} \cdot \nabla_{\mathbf{x}}$ is the material or convective derivative operator; $\tilde{\bar{\rho}}, \tilde{\mathbf{V}}$, $\tilde{P}$ and $\tilde{H}_T$ are the ensemble or Reynold's-averaged values of the time-dependent fluid density, velocity, pressure, and specific total enthalpy, respectively; $\tilde{\boldsymbol{\Pi}}$ is the viscous stress tensor; $\tilde{\mathbf{Q}}$ is the heat flux vector; $\overline{\tilde{\mathbf{v}}' \otimes \tilde{\mathbf{v}}'}$ and $\overline{\tilde{h}_T'\tilde{\mathbf{v}}'}$ are statistical correlations that account for the effects of random turbulent fluctuations on the ensemble-averaged flow; and $\otimes$ denotes the tensor or dyadic product of two vectors. To obtain a closure of the mean flow equations, the turbulent correlations can be related to gradients in the ensemble-averaged variables via algebraic eddy viscosity models. Note that, as is the usual practice in aerodynamic calculations, we have only included selected turbulent correlations in equations (2.6) and (2.7). For example, we could have also included density-velocity correlations in the mass, momentum and energy equations. We are assuming, therefore, that the correlations omitted have a negligible impact on the deterministic mean flows under consideration.

For a Newtonian fluid with zero coefficient of bulk viscosity, we can write

$$\tilde{\boldsymbol{\Pi}} = -\tilde{\bar{\mu}}(Re)^{-1}[(2\nabla_{\mathbf{x}} \cdot \tilde{\mathbf{V}}/3)\mathbf{I} - \nabla_{\mathbf{x}} \otimes \tilde{\mathbf{V}} - (\nabla_{\mathbf{x}} \otimes \tilde{\mathbf{V}}_C] \; . \tag{2.8}$$

Here, $\tilde{\bar{\mu}}$ is the coefficient of shear viscosity, $Re = \bar{\rho}^*_{-\infty}V^*_{-\infty}L^*/\bar{\mu}^*_{-\infty}$ is the flow Reynolds number, $\mathbf{I}$ is the unit tensor, and the subscript C denotes the conjugate dyadic. Assuming Fourier's Law for the conduction of heat, the heat flux $\tilde{\mathbf{Q}}$ is related to the gradient of the temperature $\tilde{T}$ by

$$\tilde{\mathbf{Q}} = -\tilde{\bar{k}}Pr^{-1}Re^{-1}\nabla_{\mathbf{x}}\tilde{T} \; , \tag{2.9}$$

where $\tilde{\bar{k}}$ is the coefficient of thermal conductivity, $Pr = \bar{\mu}^*C^*_P/\bar{k}^*$ is the flow Prandtl number and C^*_P is the dimensional value of the specific heat at constant pressure. The coefficients $\tilde{\bar{\mu}}$ and $\tilde{\bar{k}}$ in the foregoing equations are usually assumed to be known functions of the temperature. For example, the following empirical laws relating the molecular viscosity and the thermal

conductivity to the temperature,

$$\tilde{\bar{\mu}} = \tilde{\bar{k}} = \left(\frac{\tilde{T}}{T_{-\infty}}\right)^{3/2} \frac{T_{-\infty} + T_C}{\tilde{T} + T_C} , \tag{2.10}$$

are often used in Navier-Stokes calculations. Equation (2.10) is a form of Sutherland's equation. Here $T_{-\infty} = C_P^* T_{-\infty}^* / (V_{-\infty}^*)^2$ is the non-dimensional reference temperature, and T_C is a constant, which for air has a dimensional value, T_C^*, of 110°K [Sch60].

The pressure, $\tilde{P}$, and temperature, $\tilde{T}$, can be expressed in terms of the dependent variables $\tilde{\bar{\rho}}$, $\tilde{\mathbf{V}}$ and $\tilde{H}_T$. In particular, for a thermally and calorically perfect gas

$$\tilde{P} = \gamma^{-1}(\gamma - 1)\tilde{\bar{\rho}}(\tilde{H}_T - \tilde{V}^2/2) = \gamma^{-1}(\gamma - 1)\tilde{\bar{\rho}}\tilde{H} \tag{2.11}$$

and

$$\tilde{T} = (\tilde{H}_T - \tilde{V}^2/2) = \tilde{H} , \tag{2.12}$$

where γ is the specific heat ratio (constant pressure to constant volume) and $\tilde{H}$ is the specific enthalpy of the fluid. Although enthalpy and temperature are different fluid dynamic properties, the relationship $\tilde{H} = \tilde{T}$ applies here because of the scalings used to non-dimensionalize the various flow variables.

We will also find it useful to introduce the fundamental thermodynamic identity

$$\tilde{T} d\tilde{S} = d\tilde{H} - \tilde{\bar{\rho}}^{-1} d\tilde{P}, \tag{2.13}$$

where $\tilde{S}$ is the specific entropy of the fluid. It then follows from (2.11) through (2.13) that

$$\tilde{P}\tilde{\bar{\rho}}^{-\gamma} e^{-\gamma\tilde{S}} = (\tilde{P}\tilde{\bar{\rho}}^{-\gamma} e^{-\gamma\tilde{S}})_{\text{Ref}} , \tag{2.14}$$

where the subscript Ref refers to a reference thermodynamic state, which is usually taken to be the free-stream state far upstream of the blade row, i.e., at $\bar{\xi} = \bar{\xi}_{-\infty}$. We can make use of (2.13) and the equation of motion (2.6) to re-write the energy equation (2.7) in the form

$$\tilde{\bar{\rho}}\tilde{T}\frac{D\tilde{S}}{Dt} = \tilde{\Upsilon} - \boldsymbol{\nabla}_{\mathbf{x}} \cdot (\tilde{\mathbf{Q}} + \tilde{\bar{\rho}}\overline{\tilde{h}_T'\tilde{\mathbf{v}}'}) + (\mathbf{V} \cdot \boldsymbol{\nabla}_{\mathbf{x}})(\tilde{\bar{\rho}}\overline{\tilde{\mathbf{v}}' \otimes \tilde{\mathbf{v}}'}) , \tag{2.15}$$

where $\tilde{\Upsilon} = \tilde{\boldsymbol{\Pi}} : \boldsymbol{\nabla}_{\mathbf{x}} \otimes \tilde{\mathbf{V}}$ is the viscous dissipation and the symbol : indicates the scalar product of two tensors.

Boundary Conditions

For application to turbomachinery unsteady flows the foregoing field equations must be supplemented by conditions at the vibrating blade surfaces and conditions at the inflow and outflow boundaries. Since transient unsteady aerodynamic behaviors are usually not considered, a precise knowledge of the initial state of the fluid is not required. The no-slip condition, i.e.,

$$\tilde{\mathbf{V}} = \dot{\boldsymbol{\mathcal{R}}} \quad \text{for} \quad \mathbf{x} \in \mathcal{B}_m \quad (\text{or } \bar{\mathbf{x}} \in \mathrm{B}_m) , \tag{2.16}$$

where $\mathcal{R}_{B_m}$ is prescribed, applies at blade surfaces. In addition, either the heat flux $\tilde{\mathbf{Q}} \cdot \mathbf{n}$ or the temperature $\tilde{T}$ must be prescribed at such surfaces, i.e.,

$$\tilde{\mathbf{Q}} \cdot \mathbf{n} = \tilde{Q}_w(\mathbf{x}, t) \quad \text{or} \quad \tilde{T} = \tilde{T}_w(\mathbf{x}, t), \quad \mathbf{x} \in \mathcal{B}_m \quad (\text{or } \bar{\mathbf{x}} \in \mathrm{B}_m) \tag{2.17}$$

We also require conditions on the flow far upstream and far downstream from the blade row, i.e., at the inflow and outflow boundaries of the computational domain. Typically the circumferentially- and temporally-averaged values of the total pressure, total temperature and the inlet flow angle are specified at the inflow boundary. At the outflow boundary, the "circumferentially" and temporally averaged pressure is specified. In addition, total pressure and total temperature fluctuations at inlet and pressure fluctuations at inlet and exit, that carry energy towards the blade row, must be specified. Total pressure and total temperature fluctuations at exit and unsteady pressure disturbances at inlet and exit, that carry energy away from the blade row, are determined as part of the unsteady solution.

2.3 Inviscid/Viscid Interaction Model

The Reynolds-averaged Navier-Stokes equations must be considered if viscous effects are expected to be important throughout the fluid domain. However, for most flows of practical interest the Reynolds number (Re) is usually sufficiently high so that such effects are concentrated in relatively thin layers across which the flow properties vary rapidly. Provided that large scale flow separations do not occur, these layers generally lie adjacent to the blade surfaces (boundary layers) and extend downstream from the blade trailing edges (wakes). Thus, if we assume that the Reynolds number is high and the flow remains essentially "attached" to the blade surfaces, we can apply an inviscid/viscid interaction (IVI) analysis to determine the unsteady flow field. The terminology "inviscid/viscid interaction" refers to all flow situations in which viscous layers have a significant influence on the pressure field. Weak interactions are defined as those in which viscous effects on the pressure are small, or more specifically, on the order of the viscous-layer displacement thickness, $\tilde{\delta} \sim \mathcal{O}(Re^{-1/2})$. If viscous effects on the pressure disturbance are larger than this, i.e., $> \mathcal{O}(\tilde{\delta})$, the interaction is classified as strong [Mel80].

In an IVI analysis separate sets of approximate equations, i.e., reduced forms of the Navier-Stokes equations, are constructed, using the method of matched asymptotic expansions, to describe the flows in "outer" inviscid and "inner" viscous-layer regions. This approach offers the potential for providing efficient predictions of the effects of viscous layer displacement and curvature on the unsteady aerodynamic behaviors of blade rows. The governing equations can be derived with respect to moving, shear-layer surfaces $\mathcal{S}_m$, each of which is contained entirely within a viscous layer. These surfaces are usually taken to coincide with the suction and pressure surfaces of the blades and lie entirely within the viscous wake, e.g., see Figure 2.3. The curvatures of the reference shear layer surfaces are assumed to be $\mathcal{O}(1)$ or less, and here we will assume that their motions, which depend on the blade motions, are also of $\mathcal{O}(1)$ or less. Ultimately, we will assume that the motions of the blades and their wakes, and hence, those of the reference shear-layer surfaces are of small amplitude. The inviscid and viscous layer equations must be solved simultaneously, subject to appropriate matching conditions along the blades and wakes, to determine the flows in the inviscid and viscous-layer regions.

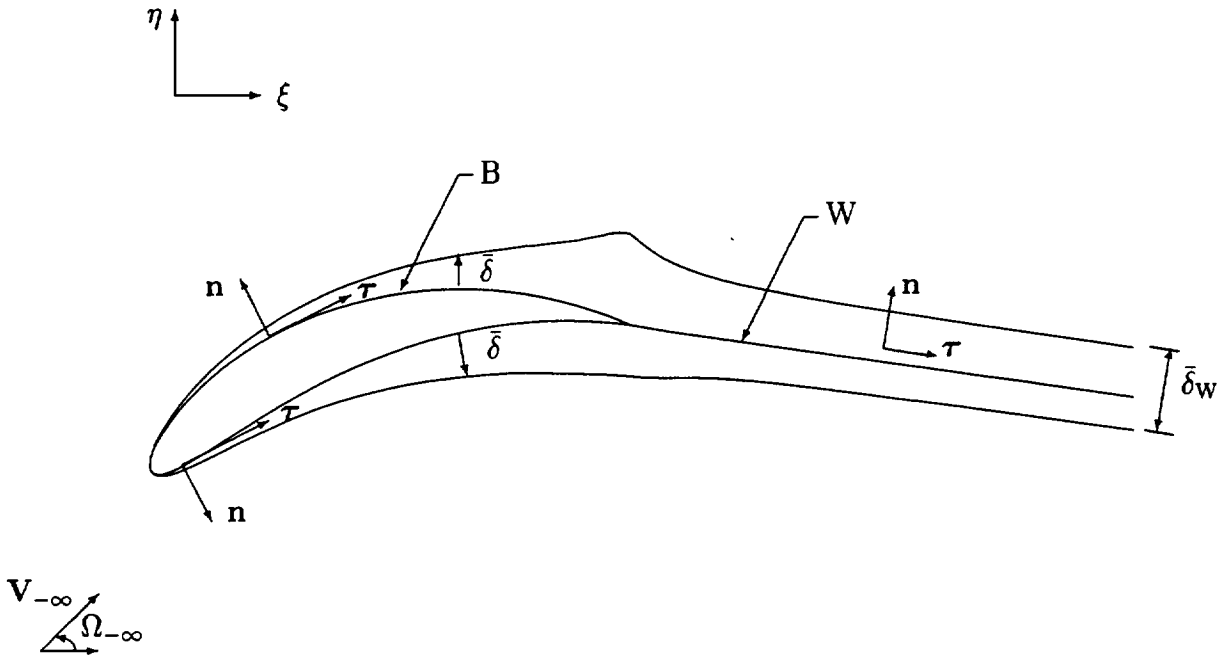

Figure 2.3: Two-dimensional steady flow, at high Reynolds number, over a blade surface.

In the limit as $Re \to \infty$, viscous effects become negligible, and it is sufficient to consider only the outer or inviscid flow.

To arrive at the governing equations for the flows in the inner and outer regions the dependent fluid variables are expanded in power series in the small parameter, $\tilde{\bar{\delta}}$. For example, the series expansions for the pressure have the form

$$\tilde{P} = \tilde{P}_0^{\mathcal{I}} + \tilde{\bar{\delta}}\tilde{P}_1^{\mathcal{I}} + \tilde{\bar{\delta}}\tilde{P}_2^{\mathcal{I}} + \ldots \quad \text{and} \quad \tilde{P} = \tilde{P}_0^{\mathcal{O}} + \tilde{\bar{\delta}}\tilde{P}_1^{\mathcal{O}} + \tilde{\bar{\delta}}\tilde{P}_2^{\mathcal{O}} + \ldots \tag{2.18}$$

where the superscripts $\mathcal{I}$ and $\mathcal{O}$ refer to the inner and outer regions respectively. The lead terms in the inner-region expansions for the components of the fluid velocity, $\tilde{\mathbf{V}}$, tangential and normal to the shear layer surface $\mathcal{S}$, i.e., in the $\boldsymbol{\tau}-$ and $\mathbf{n}-$ directions, are assumed to be of $\mathcal{O}(1)$ and of $\mathcal{O}(\tilde{\bar{\delta}})$, respectively. The lead terms in the remaining inner region and in all outer region series expansions for the deterministic unsteady flow variables are assumed to be of $\mathcal{O}(1)$. The turbulent correlations $\overline{\tilde{\mathbf{v}}' \otimes \tilde{\mathbf{v}}'}$ and $\overline{\tilde{h}_T' \tilde{\mathbf{v}}'}$ are assumed to be $\mathcal{O}(\tilde{\bar{\delta}})$ in viscous regions and of higher order, i.e., $\mathcal{O}(\tilde{\bar{\delta}}^2)$ or higher, in the inviscid region.

Scalings for the independent variables are also introduced. The thickness of the viscous layers is assumed to be $\mathcal{O}(\tilde{\bar{\delta}})$, hence, in the inner region, distances, n, normal to the shear

layer surfaces are of $\mathcal{O}(\tilde{\bar{\delta}})$ and partial derivatives in the normal direction are of order $\tilde{\bar{\delta}}^{-1}$, i.e.,

$$\mathbf{n} \cdot \boldsymbol{\nabla}_{\mathbf{x}} \approx \frac{\partial}{\partial n} \approx \mathcal{O}(\tilde{\bar{\delta}}^{-1}) \,. \tag{2.19}$$

Partial derivatives along the surface, $\boldsymbol{\tau} \cdot \boldsymbol{\nabla}_{\mathbf{x}}$, and local time derivatives, $\partial/\partial t|_{\mathbf{x}}$, are assumed to be of $\mathcal{O}(1)$ in both the inner and outer regions. In the outer region, normal derivatives, $\mathbf{n} \cdot \boldsymbol{\nabla}_{\mathbf{x}}$, are also assumed to be of $\mathcal{O}(1)$.

Approximate field equations that describe the flows in the inner and outer regions are determined by simply substituting the series expansions for the dependent variables and the scalings for the independent variables into the Reynolds-averaged Navier-Stokes equations and equating terms of like power in $\tilde{\bar{\delta}}$. When expressed in terms of the original variables, $\tilde{P}$, $\tilde{\mathbf{V}}$, etc., the zeroth-order inviscid flow is governed by the Euler equations, i.e., equations (2.5), (2.6) and (2.7) or (2.15) with right-hand-sides set equal to zero; the zeroth-order viscous flows, by Prandtl's viscous-layer equations, which will be given below. The inviscid flow in the outer region is determined as a solution of the Euler equations subject to flow tangency conditions at the blade surfaces and jump conditions at shocks and at blade wakes. The blade and wake conditions contain terms that account for the effects of viscous-layer displacement and curvature, which become negligible as $Re \to \infty$. The viscous flows in the inner regions are determined as solutions to Prandtl's equations subject to edge conditions that depend on the behaviors of the inviscid flow variables along the blade and wake surfaces. The specific forms of the inviscid and viscid blade and wake conditions follow from an asymptotic matching of the outer inviscid and the inner viscous-layer solutions, e.g., see [Mel80].

Inviscid Region

The field equations that govern continuous, inviscid, fluid motion are determined from the Reynolds averaged Navier-Stokes equations, (2.5), (2.6) and, in this case, (2.15), and are given by

$$\left.\frac{\partial \tilde{\bar{\rho}}}{\partial t}\right|_{\mathbf{x}} + \boldsymbol{\nabla}_{\mathbf{x}} \cdot (\tilde{\mathbf{V}} \tilde{\bar{\rho}}) = 0 \tag{2.20}$$

$$\tilde{\bar{\rho}} \frac{D\tilde{\mathbf{V}}}{Dt} + \boldsymbol{\nabla}_{\mathbf{x}} \tilde{P} = 0 \tag{2.21}$$

$$\frac{D\tilde{S}}{Dt} = 0 \tag{2.22}$$

For turbomachinery applications, we require solutions of these equations subject to boundary conditions at moving blade surfaces, jump conditions at moving wake and shock surfaces, and appropriate conditions far from the blade row.

The inviscid solution for the normal component of the fluid velocity at a moving blade surface must match the viscous solution for this velocity at the outer edge of the viscous layer. This is equivalent to the condition that the inviscid flow must be tangential to the blade and wake displacement surfaces. After carrying out the asymptotic matching process and neglecting terms of second and higher order in $\tilde{\bar{\delta}}$, we find that the normal component of the inviscid fluid velocity must satisfy the condition

$$(\tilde{\mathbf{V}} - \dot{\boldsymbol{\mathcal{R}}}) \cdot \mathbf{n} = \tilde{\bar{\rho}}_e^{-1} [\partial(\tilde{\bar{\rho}}_e \tilde{\bar{\delta}})/\partial t|_{\mathbf{x}} + \partial(\tilde{\bar{\rho}}_e \tilde{V}_{\tau,e} \tilde{\bar{\delta}})/\partial \tau] + (\dot{\boldsymbol{\mathcal{R}}} \cdot \boldsymbol{\nabla}_{\mathbf{x}}) \tilde{\bar{\delta}} \,, \quad \mathbf{x} \in \mathcal{B}_m \tag{2.23}$$

at the mth ($m = 0, \pm 1, \pm 2, \ldots$) moving blade surface. In equation (2.23), $\tilde{\bar{\rho}}_e$ and $\tilde{V}_{\tau,e}$ are the inviscid values of the fluid density and streamwise velocity at the moving blade surface, $\mathcal{B}_m$, or the viscous density and streamwise velocity at the edge (e) of the viscous layer, τ is the distance measured along this surface downstream from the leading-edge, and $\mathbf{n}$ is a unit vector normal to $\mathcal{B}_m$ and pointing into the fluid.

Two types of terms arise from the wake matching conditions, one due to the displacement thickness effect and the other, to the wake curvature effect. The first leads to the requirement that the inviscid solution for the normal component of the fluid velocity must be discontinuous across a wake with jump given by

$$[\![\tilde{\mathbf{V}}]\!] \cdot \mathbf{n} = \langle \tilde{\bar{\rho}}_e^{-1} [\partial(\tilde{\bar{\rho}}_e \tilde{\bar{\delta}})/\partial t\big|_{\mathbf{x}} + \partial(\tilde{\bar{\rho}}_e \tilde{V}_{\tau,e} \tilde{\bar{\delta}})/\partial \tau] \rangle + (\dot{\mathcal{R}} \cdot \nabla_{\mathbf{x}}) \langle \tilde{\bar{\delta}} \rangle \ , \quad \mathbf{x} \in \mathcal{W}_m \ . \tag{2.24}$$

Here $[\![\ ]\!]$ and $\langle\ \ \rangle$ denote the difference (upper minus lower) and the sum (upper plus lower), respectively, across a wake, and $\mathbf{n}$ is an "upward" pointing, unit vector, normal to the moving reference wake surface, $\mathcal{W}$. Note that $\langle \tilde{\bar{\delta}} \rangle = \tilde{\bar{\delta}}_W$ is the displacement thickness of the complete wake. The wake curvature effect gives rise to a pressure difference across the wake. The requirement that the outer inviscid flow match this pressure difference leads to the condition

$$[\![\tilde{P}]\!] = \langle \tilde{\bar{\rho}}_e \tilde{V}_{\tau,e} (\tilde{\bar{\delta}} + \tilde{\bar{\theta}}) \left[\tilde{\bar{\kappa}} (\tilde{V}_{\tau,e} - \dot{\mathcal{R}}_\tau) - \mathbf{n} \cdot \partial \dot{\mathcal{R}} / \partial \bar{\tau} \right] \rangle \ , \quad \mathbf{x} \in \mathcal{W}_m \tag{2.25}$$

where $\langle \tilde{\bar{\theta}} \rangle = \tilde{\bar{\theta}}_W$ is the momentum thickness of the complete wake and $\tilde{\bar{\kappa}} = \boldsymbol{\tau} \cdot \partial \mathbf{n} / \partial \tau |_{\mathcal{W}}$ is the curvature of the reference wake surface, which is taken as positive when the curvature is concave upwards. Since there is some ambiguity in establishing the shape and location of a viscous wake the right-hand-side of (2.25) is usually ignored in inviscid/viscid interaction calculations. Consequently, the pressure jump across the wake is usually set equal to zero.

In deriving the surface conditions (2.23)–(2.25), we have assumed that the viscous layer is thin, i.e., $\tilde{\bar{\delta}} << 1$, and therefore, that the effects of terms of second and higher order in the viscous displacement thickness are negligible. In the inviscid limit $\mathrm{Re} \to \infty$, the thicknesses of the viscous layers, and hence, the right-hand-sides of (2.23)–(2.25) become zero.

Jump conditions must also be imposed at inviscid shock discontinuities. Such conditions are obtained from the integral conservation laws by considering a control volume that contains a segment of a shock surface, and taking limits, first, as the lateral extent of this volume, normal to the surface segment, approaches zero, and, then, as the area of the segment approaches zero. The resulting jump conditions for conserving mass momentum and energy at a shock are given by

$$[\![\tilde{M}_f]\!] = 0 \ , \quad \tilde{M}_f [\![\tilde{\mathbf{V}}]\!] + [\![\tilde{P}]\!] \mathbf{n} = 0 \ , \quad \text{and} \quad \tilde{M}_f [\![\tilde{E}_T]\!] + [\![\tilde{P}\tilde{\mathbf{V}}]\!] \cdot \mathbf{n} = 0 \ , \quad \mathbf{x} \in \mathcal{S}h_{m,n} \tag{2.26}$$

respectively. Here $[\![\ ]\!]$ denotes the jump in a flow quantity as experienced by an observer in moving across the shock $\mathcal{S}h_{m,n}$ in the $\mathbf{n}$ direction,

$$\tilde{M}_f = \tilde{\bar{\rho}} (\tilde{\mathbf{V}} - \dot{\mathcal{R}}) \cdot \mathbf{n} \ , \quad \mathbf{x} \in \mathcal{S}h_{m,n} \tag{2.27}$$

is the fluid mass flux through the shock, $\tilde{E}_T = \tilde{H}_T - \tilde{P}/\tilde{\bar{\rho}}$ is the total specific internal energy of the fluid and the subscripts m, n refer to the nth shock associated with the mth blade.

In the inviscid limit, the conditions (2.26) also apply across the vortex-sheet "viscous" layers. In this case, since $[\![V_\tau]\!] \neq 0$, and the inviscid jump conditions (2.26) indicate that, for vortex sheets, $\tilde{M}_f = 0$, $[\![\tilde{P}]\!] = 0$, and $[\![\tilde{\mathbf{V}}]\!] \cdot \mathbf{n} = 0$. At shocks, $\mathcal{S}h_{m,n}$, the mass flux is generally nonzero (i.e., $\tilde{M}_f \neq 0$). Hence, it follows from (2.26) that the component of fluid velocity tangent to a shock surface, $\tilde{\mathbf{V}} \cdot \boldsymbol{\tau}$, must be continuous across the shock. The remaining jump conditions, along with the thermodynamic equations of state, are then required to determine the shock velocity, $\mathcal{R}_{\mathcal{S}h_{m,n}}$, and the changes in the normal component of the fluid velocity and the thermodynamic properties of the fluid as it passes through the shock.

The far-field conditions used in the inviscid approximation are the same as those indicated in § 2.2 for Navier-Stokes simulations. In particular, averaged values of the inlet total pressure, total temperature and flow angle and the exit static pressure are specified along with the entropic and vortical fluctuations at inlet and the static pressure disturbances at inlet and exit that carry energy towards the blade row. In addition, disturbances generated within the solution domain must be allowed to pass through the inflow and outflow boundaries without reflection.

Viscous Layers

The flows in the viscous layers are governed by Prandtl's equations and are subject to no-slip and prescribed heat-flux or wall temperature conditions, cf. (2.16) and (2.17), at the moving blade surfaces. In addition, the streamwise velocity and the thermodynamic properties of the fluid at the edges of the viscous layers are determined by the values of the corresponding inviscid quantities at the blade surfaces and along the reference wake (shear-layer) surfaces. We describe the flow in these layers in terms of curvilinear coordinates τ and n which measure distance along and normal to, respectively, a moving, reference, shear-layer surface $\mathcal{S}$. The unit vectors $\boldsymbol{\tau}(\bar{\tau}, t)$ and $\mathbf{n}(\bar{\tau}, t)$, where $\bar{\tau}$ measures distance along the mean position of the shear layer surface, are tangent and normal to $\mathcal{S}$.

The field equations that govern the lead terms, $\tilde{V}^{\mathcal{I}}_{\mathcal{S},0}$, $\tilde{\mathbf{V}}^{\mathcal{I}}_1 \cdot \mathbf{n}$, $P^{\mathcal{I}}_0$, etc., in the inner-region series expansions, are determined in a manner similar to that used for the inviscid region. In particular, the series expansions for the inner-region dependent variables and the scalings for the independent variables are substituted into the Reynolds-averaged Navier-Stokes equations, (2.5), (2.6) and (2.7), and only terms of $\mathcal{O}(1)$ are retained. Then, in terms of the original variables, the zeroth-order equations for the two-dimensional flows in the thin boundary layers that lie along the upper and lower surfaces of each blade and in the thin wake that extends downstream from the blade trailing edge have the form

$$\left.\frac{\partial \tilde{\bar{\rho}}}{\partial t}\right|_{\mathbf{x}} + \frac{\partial}{\partial \tau}(\tilde{\bar{\rho}} \tilde{V}_\tau) + \frac{\partial}{\partial n}(\tilde{\bar{\rho}} \tilde{V}_n) = 0 \,, \tag{2.28}$$

$$\tilde{\bar{\rho}} \frac{D\tilde{V}_\tau}{Dt} + \frac{\partial \tilde{P}}{\partial \tau} - (\mathrm{Re})^{-1} \frac{\partial}{\partial n}\left(\tilde{\bar{\mu}} \frac{\partial \tilde{V}_\tau}{\partial n}\right) + \frac{\partial}{\partial n}(\tilde{\bar{\rho}} \overline{v'_\tau v'_n}) = 0 \,, \tag{2.29}$$

and

$$\tilde{\bar{\rho}} \frac{D\tilde{H}_T}{Dt} - \left.\frac{\partial \tilde{P}}{\partial t}\right|_{\mathbf{x}} - (\mathrm{Re})^{-1} \frac{\partial}{\partial n}\left[\left(\tilde{\bar{\mu}} - (Pr)^{-1} \tilde{\bar{k}}\right) \tilde{V}_\tau \frac{\partial \tilde{V}_\tau}{\partial n} + (Pr)^{-1} \tilde{\bar{k}} \frac{\partial \tilde{H}_T}{\partial n}\right] + \frac{\partial}{\partial n}(\tilde{\bar{\rho}} \overline{h'_T v'_n}) = 0 \,. \tag{2.30}$$

Here

$$D/Dt = \left.\frac{\partial}{\partial t}\right|_{\mathbf{x}} + (1+\kappa n)^{-1}\tilde{V}_\tau \frac{\partial}{\partial \tau} + \tilde{V}_n \frac{\partial}{\partial n} \approx \left.\frac{\partial}{\partial t}\right|_{\mathbf{x}} + \tilde{V}_\tau \frac{\partial}{\partial \tau} + \tilde{V}_n \frac{\partial}{\partial n} \ , \tag{2.31}$$

$\tilde{H}_T = \tilde{H} + \tilde{V}^2/2 \approx \tilde{H} + \tilde{V}_\tau^2/2$, and $\tilde{V}_\tau$ and $\tilde{V}_n$ are the fluid velocity components in the positive τ- and n-directions, respectively. The viscous layer equations (2.28)–(2.30) are based upon the approximations $\tilde{\bar{\delta}} << 1$, $\tilde{\mathbf{V}} \cdot \mathbf{n} \sim \mathcal{O}(\tilde{\bar{\delta}})$ and $\partial/\partial n \sim \mathcal{O}(\tilde{\bar{\delta}}^{-1})$, where $\tilde{\bar{\delta}}$ is the viscous-layer displacement thickness. These equations are written relative to a fixed reference frame, but the tangential and normal coordinates are measured relative to moving blade and wake surfaces.

The turbulent correlations $\overline{v'_\tau v'_n}$ and $\overline{\tilde{h}'_T v'_n}$, appearing in equations (2.29) and (2.30), are related to gradients of the mean-flow variables, using Prandtl's mixing-length hypothesis; i.e., we set

$$\tilde{\bar{\rho}}\overline{v'_\tau v'_n} = -\tilde{\bar{\epsilon}}(Re)^{-1}\frac{\partial \tilde{V}_\tau}{\partial n} \quad \text{and} \quad \tilde{\bar{\rho}}\overline{\tilde{h}'_T v'_n} = -(Re)^{-1}\left[\tilde{\bar{\epsilon}}_H \frac{\partial \tilde{H}_T}{\partial n} + (\tilde{\bar{\epsilon}} - \tilde{\bar{\epsilon}}_{\tilde{H}})\tilde{V}_\tau \frac{\partial \tilde{V}_\tau}{\partial n}\right] . \tag{2.32}$$

Here $\tilde{\bar{\epsilon}}$ and $\tilde{\bar{\epsilon}}_{\tilde{H}}$ are the eddy viscosity and eddy diffusivity, respectively, and play roles similar to their molecular counterparts. The eddy diffusivity is related to the eddy viscosity, i.e., $\tilde{\bar{\epsilon}}_H = (Pr_T)^{-1}\epsilon$, through the introduction of the turbulent Prandtl number, Pr_T, which has a value near one for the flows of interest in turbomachinery applications. Values for $\tilde{\bar{\epsilon}}$ are provided via the use of an algebraic turbulence model; e.g., see [CS74] or [BL78].

It follows from the momentum equation (2.6) and the viscous layer approximations, that the component of the pressure gradient normal to the shear layer surface is given by

$$\mathbf{n} \cdot \boldsymbol{\nabla}_{\mathbf{x}} \tilde{P} = \frac{\partial \tilde{P}}{\partial n} = -\tilde{\bar{\rho}}\mathbf{n} \cdot \frac{D\tilde{\mathbf{V}}}{Dt} + \ldots \approx \tilde{\bar{\rho}}\tilde{\bar{\kappa}}\tilde{V}_\tau^2 + \ldots \ . \tag{2.33}$$

Since the right-hand-side of (2.33) is of $\mathcal{O}(1)$ and the thickness of the viscous layer is $\mathcal{O}(\tilde{\bar{\delta}})$, the change in pressure across this layer must be of $\mathcal{O}(\tilde{\bar{\delta}})$. Hence, in the zeroth-order approximation, the pressure in the viscous layer can be set equal to the inviscid pressure at the shear layer surface. Therefore, as a consequence of the high Re assumption, the pressure in thin viscous layers is a function only of τ and t. Also, the pressure within and the flow properties at the edge of each viscous layer are equal to the inviscid values of these variables at the reference shear layer surface.

The behaviors of the remaining flow variables in the viscous layer are determined by solving the mass (2.28), momentum (2.29), and energy (2.30) equations subject to appropriate surface and edge conditions. Also, since the system of viscous-layer field equations is parabolic in time (t) and in the streamwise ($\tau-$) direction, the density, $\tilde{\bar{\rho}}$, surface velocity, $\tilde{V}_\tau$, and total enthalpy, $\tilde{H}_T$, must be known for all time at some upstream location, and these variables, along with the normal velocity, must be known throughout the solution domain at some initial time.

A no-slip condition and either a prescribed temperature or heat flux condition must be imposed at the solid blade surfaces, i.e.,

$$\tilde{\mathbf{V}} = \dot{\boldsymbol{\mathcal{R}}} \ , \quad \mathbf{x} \in \mathcal{B}_m \quad \text{or} \quad n = 0 \ , \tau \leq \tau_{TE} \ ,$$

and

$$\tilde{H}_T = \tilde{H}_{T,w}(\tau, t) \quad \text{or} \quad \frac{\partial \tilde{H}_T}{\partial n} - \tilde{V}_\tau \frac{\partial \tilde{V}_\tau}{\partial n} = -\tilde{\bar{k}}^{-1}(Re \cdot Pr)^{-1}\tilde{Q}_w \quad \text{for} \quad \mathbf{x} \in \mathcal{B}_m \ , \tag{2.34}$$

and a condition on the normal component of the fluid velocity, i.e.,

$$(\tilde{\mathbf{V}} - \dot{\mathcal{R}}) \cdot \mathbf{n} = 0 \quad \text{for} \quad \mathbf{x} \in \mathcal{W}_m \quad \text{or} \quad n = 0 \ , \quad \tau > \tau_{\text{TE}} \tag{2.35}$$

must be enforced at the reference wake surfaces. At the edge(s) of the viscous layer we require that

$$\tilde{V}_\tau \to \tilde{V}_{\tau,e}(\tau, t) \quad \text{and} \quad \tilde{H}_T \to \tilde{H}_{T,e}(\tau, t) \quad \text{for} \quad n \to \infty \ , \tag{2.36}$$

where the limit $n \to \infty$ refers to the edges of the upper and lower surface boundary layers and the upper and lower edges of a wake. Here the subscripts w and e denote the values of the fluid properties at a solid wall and at the edge of the viscous layer, respectively, and the subscript TE refers to a blade trailing-edge. The fluid velocity, $\tilde{V}_{\tau,e}$, and total enthalpy, $\tilde{H}_{T,e}$, at the edges of the viscous layers are determined by the inviscid solution along the blade and reference wake surfaces. Note that the exact locations of the reference wake surfaces are unknown *a priori*; however, to within lowest order, the wake boundary conditions can be referenced to any arbitrary surface emanating from a blade trailing edge and lying within the actual viscous wake [Vel80].

The displacement, $\tilde{\bar{\delta}}$, and momentum, $\tilde{\bar{\theta}}$, thicknesses of a viscous layer are needed to determine the effects of viscous displacement and wake curvature, cf. (2.23)–(2.25), on the outer inviscid flow. For the two-dimensional unsteady flows, considered herein, these parameters are defined by

$$\tilde{\bar{\delta}}(\tau, t) = \int_0^\infty \left(1 - \frac{\tilde{\bar{\rho}}(\tilde{V}_\tau - \dot{\mathcal{R}}_\tau)}{\tilde{\bar{\rho}}_e(\tilde{V}_{\tau,e} - \dot{\mathcal{R}}_\tau)} \right) dn \tag{2.37}$$

and

$$\tilde{\bar{\theta}}(\tau, t) = \int_0^\infty \frac{\tilde{\bar{\rho}}(\tilde{V}_\tau - \dot{\mathcal{R}}_\tau)}{\tilde{\bar{\rho}}_e(\tilde{V}_{\tau,e} - \dot{\mathcal{R}}_\tau)} \left(1 - \frac{\tilde{V}_\tau - \dot{\mathcal{R}}_\tau}{\tilde{V}_{\tau,e} - \dot{\mathcal{R}}_\tau} \right) dn \ , \tag{2.38}$$

where the integrations are carried out along lines normal to a moving blade or wake surface.

2.4 Linearized Inviscid Unsteady Aerodynamic Model

Even with the simplifications resulting from the assumption of a high Reynolds number, attached flow, the unsteady aerodynamic problem still involves prohibitive computing times and computational resources. Because of this, the traditional approach has been to assume that the unsteady excitations are of small-amplitude, harmonic in time, and exhibit a phase-lagged blade-to-blade periodicity, cf. (2.1)–(2.4). These assumptions lead to time-independent, linear equations for the inviscid unsteady perturbation, that can be solved over a single, extended, blade-passage region, for the complex amplitudes of the first-order unsteady flow variables. Because they are governed by linear equations, the first-order unsteady motions that arise from various Fourier modes of unsteady excitation are not coupled. Therefore, solutions for arbitrary excitations can then be obtained by a superposition of solutions for fundamental harmonic excitations. These features can lead to useful and efficient theoretical predictions of the unsteady aerodynamic response information needed in turbomachinery aeroelastic and aeroacoustic design studies.

Thus, we regard the unsteady flow in the inviscid region as a small perturbation of a non-linear mean or steady background flow. Since the unsteady excitations are of small amplitude

[i.e., of $\mathcal{O}(\epsilon) << 1$], the unsteady part of the inviscid flow can be approximated as a first-order (in ϵ) perturbation of an underlying nonlinear background flow, that is steady in the blade-row frame of reference. In this case, the first-order unsteady fluid motions are governed by linear equations with variable coefficients that depend upon the steady background flow. Also, since the unsteady excitations are harmonic in time and the equations that govern the first-order flow properties are linear, these properties will have a harmonic time-dependence. We will take advantage of this feature by introducing complex representations for the first-order flow variables; thereby removing explicit physical time dependence from the linear unsteady problem.

To determine the inviscid small-disturbance equations we first expand the dependent flow variables into asymptotic series of the form

$$\tilde{\mathbf{V}}[\mathbf{x}(\bar{\mathbf{x}},t),t] = \mathbf{V}(\bar{\mathbf{x}}) + \tilde{\mathbf{v}}[\mathbf{x}(\bar{\mathbf{x}},t),t] + \ldots = \mathbf{V}(\bar{\mathbf{x}}) + Re[\mathbf{v}(\bar{\mathbf{x}})\exp(i\omega t)] + \ldots \ . \tag{2.39}$$

Here $\mathbf{V}(\bar{\mathbf{x}}) \sim \mathcal{O}(1)$ and $\tilde{\mathbf{v}}[\mathbf{x}(\bar{\mathbf{x}},t),t] \sim \mathcal{O}(\epsilon)$ are the velocities in the steady background flow at $\bar{\mathbf{x}}$ and the first-order unsteady flow at $\mathbf{x} = \bar{\mathbf{x}} + Re\{\mathbf{R}(\bar{\mathbf{x}})\exp(i\omega t)\}$, respectively, $\mathbf{v}$ is the complex amplitude of the linearized unsteady velocity, ω is the temporal frequency of the unsteady motion, $|\mathbf{R}| \sim \mathcal{O}(\epsilon)$, and the dots refer to higher order terms.

The asymptotic expansion (2.39), with a field-point displacement field $\mathcal{R}(\bar{\mathbf{x}},t)$ that satisfies the condition $\mathcal{R}(\bar{\mathbf{x}},t) = \mathcal{R}_{B_m}(\bar{\mathbf{x}},t)$ for $\bar{\mathbf{x}} \in B_n$, has been employed in recent linearized Euler analyses [HC93a, HC93b, KK93, MV94]. It leads to a rather complicated set of unsteady field equations, but allows blade-surface boundary conditions to be imposed directly at the blade surfaces. However, since the blade motions are of small amplitude, we can set $\mathbf{x} \equiv \bar{\mathbf{x}}$, in (2.39), i.e., $\mathcal{R} \equiv 0$, which then becomes identical to the asymptotic expansion used in earlier linearized analyses [Whi87, Ver92, Ver93]. The latter expansion will be applied herein. It leads to a more convenient set of linearized unsteady field equations and precludes the need to prescribe a displacement field $\mathcal{R}(\bar{\mathbf{x}},t)$ over the solution domain. However, Taylor series expansions, e.g.,

$$\tilde{\mathbf{V}}_{\mathcal{S}} = \left[\tilde{\mathbf{V}} + (\mathcal{R}\cdot\nabla)\tilde{\mathbf{V}} + \ldots\right]_{\mathrm{S}} \tag{2.40}$$

must be applied to refer surface information from moving blade, wake and shock surfaces ($\mathcal{S}$) to the mean positions (S) of such surfaces. Thus, in the present linearization the spatial coordinates $\mathbf{x}$ and $\bar{\mathbf{x}}$, refer to the same fixed location in the cascade frame of reference.

The field equations that govern the zeroth-order steady and the first-order unsteady flows are obtained by substituting the asymptotic expansions for the flow variables [e.g., (2.39)] into the governing nonlinear field equations; equating terms of like power in ϵ; and neglecting terms of second and higher order in ϵ. Conditions on the unsteady perturbation at the mean blade, wake and shock surfaces are obtained by substituting the asymptotic (2.39) and Taylor (2.40) series expansions, and the relations between the unit tangent and normal vectors at corresponding points on the instantaneous ($\mathcal{S}$) and mean surface (S) positions, i.e.,

$$\boldsymbol{\tau}_{\mathcal{S}_m} = \boldsymbol{\tau}_{\mathrm{S}_m} + \left(\mathbf{n}_{\mathrm{S}_m}\cdot\frac{\partial\mathcal{R}_{\mathcal{S}_m}}{\partial\tau}\right)\mathbf{n}_{\mathrm{S}_m} + \ldots \quad \text{and} \quad \mathbf{n}_{\mathcal{S}_m} = \mathbf{n}_{\mathrm{S}_m} - \left(\mathbf{n}_{\mathrm{S}_m}\cdot\frac{\partial\mathcal{R}_{\mathcal{S}_m}}{\partial\tau}\right)\boldsymbol{\tau}_{\mathrm{S}_m} + \cdots \ , \tag{2.41}$$

into the full time-dependent surface conditions, subtracting out the corresponding zeroth-order conditions and neglecting terms of higher than first order in ϵ. These procedures lead to

nonlinear and linear variable-coefficient equations, respectively, for the zeroth- and first-order flows. The variable coefficients that appear in the linearized unsteady equations depend upon the steady background flow.

Note also, that as a consequence of the assumptions regarding cascade geometry, the inlet and exit mean-flow conditions, and the temporal and circumferential behaviors of the unsteady excitations, the steady background flow will be periodic from blade-to-blade and the first-order unsteady flow will exhibit a phase-lagged, blade-to-blade periodicity. Thus, for example, we can write

$$\mathbf{V}(\bar{\mathbf{x}} + m\mathbf{G}) = \mathbf{V}(\bar{\mathbf{x}}) \quad \text{and} \quad \mathbf{v}(\bar{\mathbf{x}} + m\mathbf{G}) = \mathbf{v}(\bar{\mathbf{x}}) \exp(im\sigma) \; . \tag{2.42}$$

Such conditions allow numerical resolutions of the steady and linearized unsteady flows to be limited to a single extended blade-passage region.

Steady Background Flow

The field equations for the steady background flow are [cf. (2.20), (2.21) and (2.22)] are

$$\nabla_{\bar{\mathbf{x}}} \cdot (\bar{\rho}\mathbf{V}) = 0 \; , \tag{2.43}$$

$$\bar{\rho}(\mathbf{V} \cdot \nabla_{\bar{\mathbf{x}}})\mathbf{V} + \nabla_{\bar{\mathbf{x}}} P = 0 \; , \tag{2.44}$$

and

$$\mathbf{V} \cdot \nabla_{\bar{\mathbf{x}}} S = 0 \; . \tag{2.45}$$

Here $\bar{\rho}$, $\mathbf{V}$, P and S are the density, velocity, pressure and entropy, respectively, in the steady background flow. The steady pressure can be determined in terms of the dependent variables $\bar{\rho}$ and S, using the steady form of (2.14), i.e.,

$$P = \left[P\bar{\rho}^{-\gamma} \exp(-\gamma S)\right]_{\text{Ref}} \bar{\rho}^{\gamma} \exp(\gamma S) \tag{2.46}$$

Surface conditions for the steady background flow follow from (2.23) through (2.25) and are imposed at the reference or mean positions of the blade, wake and shock surfaces. Mean blade positions are prescribed, but the mean wake and shock locations must be determined as part of the steady flow solution.

The conditions

$$\mathbf{V} \cdot \bar{\mathbf{n}} = \bar{\rho}_e^{-1} \partial(\bar{\rho}_e V_{\bar{\tau},e} \bar{\delta})/\partial\bar{\tau} \; , \quad \text{for } \bar{\mathbf{x}} \in B_m \; , \tag{2.47}$$

apply at the mean blade surfaces. In addition, the zeroth-order normal velocity and pressure must satisfy the conditions

$$[\![\mathbf{V}]\!] \cdot \bar{\mathbf{n}} = \langle \bar{\rho}_e^{-1} \partial(\bar{\rho}_e V_{\bar{\tau},e} \bar{\delta})/\partial\bar{\tau} \rangle \quad \text{and} \quad [\![P]\!] = \bar{\kappa} \langle \bar{\rho}_e V_{\bar{\tau},e}^2 (\bar{\delta} + \bar{\theta}) \rangle \; , \quad \text{for } \bar{\mathbf{x}} \in W_m \; , \tag{2.48}$$

along blade wakes. Note that in the limit $Re \to \infty$, $\bar{\delta} \to 0$ and $\bar{\theta} \to 0$; therefore, the fluid normal velocity approaches zero at blade surfaces and the normal velocity and pressure become continuous across blade wakes.

Finally, the requirements of mass, momentum and energy conservation provide the following conditions on the mean flow variables at the mean shock locations, $\bar{\mathbf{x}} \in \text{Sh}_{m,n}$:

$$[\![M_f]\!] = 0 \; , \quad M_f [\![\mathbf{V}]\!] + [\![P]\!] \bar{\mathbf{n}} = 0 \; , \quad \text{and} \quad M_f [\![E_T]\!] + [\![P\mathbf{V}]\!] \cdot \bar{\mathbf{n}} = M_f [\![H_T]\!] = 0 \; , \tag{2.49}$$

where $M_f = \bar{\rho}\mathbf{V} \cdot \bar{\mathbf{n}}$. It follows from (2.49) that the tangential component of the fluid velocity, V_τ, must be continuous across shocks. In principle, the shock-jump conditions must be imposed in nonlinear inviscid calculations, but the usual practice is to capture shocks by solving conservative forms of the inviscid field equations across shocks using special differencing techniques.

Steady-state, non-reflecting, inflow and outflow, boundary conditions (e.g., see [Gil90]) must be imposed on the steady background flow far upstream and far downstream from the blade row. In particular, averaged values of the inlet total temperature, total pressure and flow angle and the exit static pressure are specified, and circumferential harmonics of the mean flow variables, caused by the interaction of the mean flow with the blade row, are determined as part of the mean-flow solution. In addition, blade-to-blade periodicity conditions, cf. (2.42), can be imposed to restrict the steady flow solution domain to a single extended blade passage region. Since the inlet and exit conditions are imposed at finite distances from the blade row, say at $\xi = \xi_-$ and $\xi = \xi_+$, respectively, the numerical solution domain is further restricted to a single extended blade passage region of finite axial extent.

Linearized Unsteady Flow

The differential equations that govern the first-order or linearized inviscid unsteady flow in continuous regions can be written as

$$i\omega\rho + \nabla_{\bar{\mathbf{x}}} \cdot (\rho\mathbf{V} + \bar{\rho}\mathbf{v}) = 0 \ , \tag{2.50}$$

$$\bar{\rho}\left[\frac{\bar{D}\mathbf{v}}{Dt} + (\mathbf{v} \cdot \nabla_{\bar{\mathbf{x}}})\mathbf{V}\right] + \rho(\mathbf{V} \cdot \nabla_{\bar{\mathbf{x}}})\mathbf{V} + \nabla_{\bar{\mathbf{x}}} p = 0 \tag{2.51}$$

and

$$\frac{\bar{D}s}{Dt} + (\mathbf{v} \cdot \nabla_{\bar{\mathbf{x}}})S = 0 \ . \tag{2.52}$$

Here ρ, $\mathbf{v}$, p and s are the complex amplitudes of the time-dependent first-order density, velocity, pressure and entropy, respectively, and $\bar{D}/Dt = i\omega + \mathbf{V} \cdot \nabla$ is a convective derivative operator based on the mean flow velocity. To complete this system we require an additional equation that relates the first-order density, pressure and entropy. This is obtained by expanding the thermodynamic relation (2.14) and using (2.46) to obtain

$$\rho = \bar{\rho}[\gamma^{-1}p/P - s] = A^{-2}p - \bar{\rho}s = 0 \ , \tag{2.53}$$

where A is the speed of sound propagation in the steady background flow.

The thermodynamic relation (2.53) can be used to eliminate the density ρ from the linearized momentum (2.51) and continuity (2.50) equations, thereby expressing these equations in useful alternative forms. After performing the necessary algebra, we find that the linearized momentum and continuity equations can be written as

$$\frac{\bar{D}}{Dt}(\mathbf{v} - s\mathbf{V}/2) + [(\mathbf{v} - s\mathbf{V}/2) \cdot \nabla_{\bar{\mathbf{x}}}]\mathbf{V} + \nabla_{\bar{\mathbf{x}}}(p/\bar{\rho}) = \mathbf{V}(\mathbf{v} \cdot \nabla_{\bar{\mathbf{x}}}S)/2 + \bar{\rho}^{-1}p\nabla_{\bar{\mathbf{x}}}S \ , \tag{2.54}$$

and

$$\frac{\bar{D}}{Dt}[p/(\bar{\rho}A^2) - s] + \bar{\rho}^{-1}\nabla_{\bar{\mathbf{x}}} \cdot (\bar{\rho}\mathbf{v}) = 0 \ , \tag{2.55}$$

respectively. The linearized unsteady flow can then be determined by solving the system of convection equations (2.52), (2.54) and (2.55), subject to appropriate surface and far-field conditions, for the complex amplitudes, s, $\mathbf{v}$ and p, of the first-order unsteady entropy, velocity and pressure. Note that, if the mean flow is isentropic, the right-hand side of (2.54) is zero.

Conditions on the inviscid unsteady perturbation at the reference or mean positions of the blade, wake and shock surfaces are obtained by substituting the asymptotic (e.g., (2.39)) and Taylor (e.g., (2.40)) series expansions and the surface vector relations (2.41) into the full time-dependent surface conditions (2.23)–(2.26), subtracting out the corresponding zeroth-order conditions (2.47)–(2.49), and neglecting terms of higher than first order in ϵ. We have also made use of the steady field equations (2.43)–(2.45) and jump conditions (2.49) to write the first-order surface conditions in more convenient forms. We find that the linearized unsteady flow tangency condition can be expressed as

$$\begin{aligned}[\mathbf{v} - i\omega\mathbf{R} - V_{\bar\tau}\partial\mathbf{R}/\partial\bar\tau + (\mathbf{R}\cdot\boldsymbol{\nabla}_{\bar{\mathbf{x}}})\mathbf{V}]\cdot\bar{\mathbf{n}} &= -(\bar\rho^{-1}\rho + \bar{\boldsymbol{\tau}}\cdot\partial\mathbf{R}/\partial\bar\tau)\,\mathbf{V}\cdot\bar{\mathbf{n}} + i\omega\bar\rho^{-1}(\rho\bar\delta + \bar\rho\delta) \\ &+\bar\rho^{-1}\bar{\boldsymbol{\tau}}\cdot\boldsymbol{\nabla}_{\bar{\mathbf{x}}}\left[(\bar\rho\mathbf{v}\bar\delta + \rho\mathbf{V}\bar\delta + \bar\rho\mathbf{V}\delta + \bar\delta\mathbf{R}\cdot\boldsymbol{\nabla}_{\bar{\mathbf{x}}}(\bar\rho\mathbf{V}))\cdot\bar{\boldsymbol{\tau}}\right]\ ,\quad \bar{\mathbf{x}}\text{ on } B_m\ ,\end{aligned} \tag{2.56}$$

where $\tilde{\bar\delta}(\mathbf{x},t) = \bar\delta(\bar{\mathbf{x}}) + Re\{\delta(\bar{\mathbf{x}})\exp(i\omega t)\} + \ldots$ and $\bar\delta$ and $\delta \sim \mathcal{O}(|\mathbf{R}|\bar\delta)$ are the steady and the complex amplitude of the first-harmonic components of the viscous displacement thickness, respectively, and $\mathbf{R}(\bar{\mathbf{x}})$, $\bar{\mathbf{x}} \in B_m$, is the complex amplitude of the unsteady blade displacement. As a convenience, we have omitted the subscript e on the densities and velocities appearing in the surface conditions (2.56) and those given below. But, it is to be understood that the values of these inviscid fluid properties at a blade or wake surface are equal to their viscous values at the edges of the corresponding viscous layers.

The linearized conditions on the jumps in the normal velocity and the pressure across wakes follow from (2.24) and (2.25), and the corresponding zeroth-order conditions, and have the form

$$\begin{aligned}[\![\mathbf{v}]\!]\cdot\bar{\mathbf{n}} \ &- \ [\,[\![V_{\bar\tau}]\!]\partial\mathbf{R}/\partial\bar\tau + (\mathbf{R}\cdot\boldsymbol{\nabla}_{\bar{\mathbf{x}}})[\![\mathbf{V}]\!]\,]\cdot\bar{\mathbf{n}} = [\![\mathbf{v}]\!]\cdot\bar{\mathbf{n}} + R_{\bar\tau}\partial[\![V_{\bar n}]\!]/\partial\bar\tau \\ &- \ \partial(R_{\bar n}[\![V_{\bar\tau}]\!])/\partial\bar\tau - R_{\bar n}[\![(\mathbf{V}\cdot\boldsymbol{\nabla})\ln\bar\rho]\!] - \bar\kappa R_{\bar n}[\![V_{\bar n}]\!] \\ &= \ [\![(\rho\bar\rho^{-1} + \bar{\boldsymbol{\tau}}\cdot\partial\boldsymbol{\mathcal{R}}/\partial\bar\tau)\,\mathbf{V}]\!]\cdot\bar{\mathbf{n}} + \langle i\omega\bar\rho^{-1}(\rho\bar\delta + \bar\rho\delta)\rangle \\ &+ \ \langle\bar\rho^{-1}\frac{\partial}{\partial\bar\tau}[(\bar\rho\mathbf{v}\bar\delta + \rho\mathbf{V}\bar\delta + \bar\rho\mathbf{V}\delta + \bar\delta\mathbf{R}\cdot\boldsymbol{\nabla}_{\bar{\mathbf{x}}}(\bar\rho\mathbf{V}))\cdot\bar{\boldsymbol{\tau}}]\rangle\ ,\quad \bar{\mathbf{x}}\text{ on } W_m\ .\end{aligned} \tag{2.57}$$

and

$$\begin{aligned}[\![p]\!] \ &+ \ (\mathbf{R}\cdot\boldsymbol{\nabla}_{\bar{\mathbf{x}}})[\![P]\!] = [\![p]\!] + R_{\bar\tau}\partial[\![P]\!]/\partial\bar\tau - R_{\bar n}[\![\bar\rho(\mathbf{V}\cdot\boldsymbol{\nabla}_{\bar{\mathbf{x}}})\mathbf{V}]\!]\cdot\mathbf{n} \\ &= \ \bar\kappa\langle\bar\rho V_{\bar\tau}^2(\delta+\theta)\rangle + \bar\kappa\langle V_{\bar\tau}[(\rho + \mathbf{R}\cdot\boldsymbol{\nabla}_{\bar{\mathbf{x}}}\bar\rho)V_{\bar\tau} + 2\bar\rho(v_{\bar\tau} + (\mathbf{R}\cdot\boldsymbol{\nabla}_{\bar{\mathbf{x}}})V_{\bar\tau})](\bar\delta+\bar\theta)\rangle \\ &+ \ \langle\bar\rho V_{\bar\tau}(\bar\delta+\bar\theta)\,(\kappa V_{\bar\tau} - i\omega\partial R_{\bar n}/\partial\bar\tau)\rangle\ ,\quad \bar{\mathbf{x}}\text{ on } W_m\ ,\end{aligned} \tag{2.58}$$

where $\bar\kappa = \bar{\boldsymbol{\tau}}\cdot\partial\bar{\mathbf{n}}/\partial\bar\tau$ and κ are the steady and the complex amplitude of the first-order unsteady wake curvatures.

As do the steady, the first-order unsteady blade and wake conditions also simplify considerably in the inviscid limit $Re \to \infty$. In particular, the right-hand-sides of (2.56)–(2.58) become zero. Also, for $Re \to \infty$ the left-hand-sides of the first-order wake conditions can be simplified by making use of the inviscid forms of steady wake-jump conditions and the field equations (2.43) and (2.44). After performing the necessary algebra, we find that

$$[\![\mathbf{v}]\!] \cdot \bar{\mathbf{n}} = \partial(R_{\bar{n}}[\![V_{\bar{\tau}}]\!])/\partial\bar{\tau} + R_{\bar{n}}[\![V_{\bar{\tau}}\partial(\ln\bar{\rho})/\partial\bar{\tau}]\!], \quad \bar{\mathbf{x}} \in W_m \ , \tag{2.59}$$

and

$$[\![p]\!] = -\bar{\kappa}R_{\bar{n}}[\![\bar{\rho}V_{\bar{\tau}}^2]\!], \quad \bar{\mathbf{x}} \in W_m \ . \tag{2.60}$$

Equations (2.57) and (2.58) provide two independent relations for determining the jump in the linearized unsteady normal velocity and pressure across each wake. However, since the wake normal displacement, $\mathbf{R} \cdot \bar{\mathbf{n}}$, $\bar{\mathbf{x}} \in W_m$, is unknown *a priori*, these relations are not sufficient to determine $[\![p]\!]$ and $[\![\mathbf{v}]\!] \cdot \mathbf{n}$, unless the steady tangential velocity, $\mathbf{V} \cdot \bar{\boldsymbol{\tau}}$, and density, $\bar{\rho}$, are continuous across wakes.

The linearized equations that ensure that mass, momentum and energy are conserved across shock discontinuities are

$$[\![m_f]\!] = [\![m_{fc}]\!] = [\![\bar{\rho}\mathbf{v} + \rho\mathbf{V} - i\omega\bar{\rho}\mathbf{R}]\!] \cdot \bar{\mathbf{n}} - \partial(R_{\bar{n}}[\![\bar{\rho}]\!]V_{\bar{\tau}})/\partial\bar{\tau} = 0, \quad \bar{\mathbf{x}} \text{ on } \mathrm{Sh}_{m,n} \ , \tag{2.61}$$

$$\begin{aligned} &M_f[\![\mathbf{v} + [\partial(R_{\bar{n}}V_{\bar{n}})/\partial\bar{\tau} + R_{\bar{n}}\bar{\zeta}]\bar{\boldsymbol{\tau}}]\!] + m_{fc}[\![V_{\bar{n}}]\!]\bar{\mathbf{n}} + [\![p]\!]\bar{\mathbf{n}} \\ &-\bar{\kappa}R_{\bar{n}}[\![\bar{\rho}(V_{\bar{n}}^2 - V_{\bar{\tau}}^2)]\!]\bar{\mathbf{n}} - R_{\bar{n}}V_{\bar{\tau}}[\![\bar{\rho}\partial V_{\bar{n}}/\partial\bar{\tau}]\!]\bar{\mathbf{n}} = 0 \ , \quad \mathbf{x} \text{ on } \mathrm{Sh}_{m,n} \end{aligned} \tag{2.62}$$

and

$$M_f[\![e_T + p/\bar{\rho}]\!] + m_{fc}[\![E_T]\!] + [\![P\mathbf{v}]\!] \cdot \bar{\mathbf{n}} - \partial(R_{\bar{n}}V_{\bar{\tau}}[\![P]\!])/\partial\bar{\tau} - R_{\bar{n}}V_{\bar{\tau}}[\![\bar{\rho}\partial E_T/\partial\bar{\tau}]\!] = 0, \quad \mathbf{x} \text{ on } \mathrm{Sh}_{m,n} \ , \tag{2.63}$$

where $\bar{\boldsymbol{\zeta}} = \boldsymbol{\nabla}_{\bar{\mathbf{x}}} \times \mathbf{V}$ and $e_T = e + \mathbf{V} \cdot \mathbf{v}$. Equations (2.61), (2.62) and (2.63), with the first-order mass fluxes, m_{fc} and m_f defined by

$$\begin{aligned} m_{fc} &= (\bar{\rho}\mathbf{v} + \rho\mathbf{V} - i\omega\bar{\rho}\mathbf{R}) \cdot \bar{\mathbf{n}} - \partial(\bar{\rho}R_{\bar{n}}V_{\bar{\tau}})/\partial\bar{\tau} \ , \\ \text{and} \qquad m_f &= m_{fc} - \bar{\kappa}\bar{\rho}R_{\bar{n}}V_{\bar{n}} + R_{\bar{\tau}}\partial(\bar{\rho}V_{\bar{n}})/\partial\bar{\tau} \end{aligned} \tag{2.64}$$

respectively, are the relations needed for determining the jumps in the first-order fluid properties across moving shocks and the normal component of the shock displacement $\mathbf{R} \cdot \bar{\mathbf{n}}$, $\bar{\mathbf{x}} \in Sh_{m,n}$. These conditions along with the zeroth-order conditions (2.49) must be enforced to ensure that mass, momentum and energy are conserved to within first-order across moving shocks. Again, however, there is one more unknown associated with the unsteady shock-jump conditions, than there are independent equations. Therefore, these conditions are not sufficient for determining the relevant unsteady shock information.

The first-order density and specific total internal energy can be eliminated from the first-order shock jump conditions by applying the thermodynamic relations (2.53) and

$$e = \bar{\rho}^{-1}[\gamma^{-1}p + (\gamma-1)^{-1}Ps] = (\gamma\bar{\rho})^{-1}p + \gamma^{-1}(\gamma-1)^{-1}A^2s \tag{2.65}$$

to (2.61)–(2.64). By so doing, we would retain the convention, adopted in the derivation of the field equations, of regarding pressure, entropy and velocity as the dependent variables of the linearized unsteady flow problem. However, since the jump conditions, derived above, are not sufficient for fitting wakes and shocks into an unsteady solution, based on the linearized Euler equations, additional information will be required.

The foregoing equations provide linearized surface conditions, in which viscous displacement and wake curvature effects are taken into account. Such conditions are needed to account for viscous effects in a linearized inviscid analysis of the unsteady perturbation of a nonlinear steady background flow. The flow tangency condition (2.56) applies at the mean blade positions, and also on the upper and lower sides of the mean wakes; the jump conditions on normal velocity and pressure (2.57) and (2.58) also apply at mean wake positions; and the mass, momentum and energy conservation conditions (2.61), (2.62) and (2.63), respectively, apply at the mean shock positions. Unfortunately, these surface conditions are quite complicated and, to date, they have not been fully incorporated into a linearized unsteady aerodynamic analysis. Indeed, as presently posed, the wake and shock conditions are not sufficient to determine the jumps in the flow variables across a wake or shock surface and the surface normal displacement. Inviscid forms of the flow tangency condition (2.56) have been used successfully in linearized Euler calculations in which wake and shock effects are captured [HC93a, KK93, MV94], but there have not been any attempts to include the viscous terms on the right-hand-side of (2.56) in such calculations.

In addition to the foregoing surface conditions, phase-lagged periodicity [cf. (2.42)] and far-field conditions must be imposed on the linearized unsteady flow. The latter must allow for the prescription of incoming entropy, vorticity and pressure disturbances at the inflow boundary and incoming pressure disturbances at the outflow boundary of the computational domain. In addition, unsteady disturbances coming from within the solution domain must pass through the computational inflow and outflow boundaries without distortion or reflection.

It should be noted that to be precise, we have presented the foregoing steady and linearized unsteady equations in terms of the independent variable $\bar{\mathbf{x}}$, the mean-surface coordinates $\bar{\tau}$ and $\bar{n}$, and the mean-surface, unit vectors $\bar{\boldsymbol{\tau}}$ and $\bar{\mathbf{n}}$. However, since the displacement field $\mathcal{R} \equiv 0$ and, as a result, the surface coordinates and unit vectors in the resulting steady and linearized unsteady equations always apply to the mean surface locations, we could have omitted the overbars in presenting the governing equations. To simplify the nomenclature, we will adopt the latter strategy in describing the LINFLO and SFLOW-IVI analyses in § 3 and § 4, respectively.

2.5 Discussion

We have presented an inviscid/viscid interaction model for two-dimensional unsteady flows, occurring at high Reynolds numbers, in which the unsteadiness is driven by excitations of small amplitude. Although we have not yet developed solution procedures for the complete model, we have developed and evaluated solution procedures for several of the components needed for a complete inviscid/viscid interaction analysis of unsteady cascade flows. In particular, we have developed efficient flow solvers for linearized inviscid unsteady flows, for steady flows with strong inviscid/viscid interactions, and for unsteady flows with weak inviscid/viscid interactions. In constructing these analyses we have restricted our consideration to flows in which

any shocks that might occur are of weak to moderate strength and in which the free-stream flow conditions far upstream of blade rows are uniform. In such cases, the steady background flows in the inviscid regions can be regarded as isentropic and irrotational. For potential mean flows, the inviscid wake-and shock-jump conditions become well-posed, in that, there are a sufficient number of conditions to determine the flow properties at wakes and shocks. In addition, the potential mean flow assumption leads to two-dimensional, steady and unsteady, aerodynamic analyses that are very efficient computationally.

In the following sections of this report we will describe the component unsteady aerodynamic analyses mentioned above. In particular, in § 3 we will describe the linearized inviscid analysis LINFLO, which applies to flows in which the unsteadiness can be regarded as a small perturbation of an isentropic and irrotational mean or steady background flow. The SFLOW–IVI analysis for steady flows with strong inviscid/viscid interactions will be described in § 4. Finally, the unsteady viscous layer analysis UNSVIS, which can be used in conjunction with LINFLO to predict unsteady flows with weak inviscid/viscid interactions, will be presented in § 5.

To demonstrate these analyses, we will apply them to three of the cascades studied in previous investigations [VH90, VBHA91, BVA93a] — a compressor exit guide vane (EGV), a high speed compressor (HSC) cascade, known as the Tenth Standard Cascade Configuration [FS83, FV93], and a turbine cascade, known as the Fourth Standard Cascade Configuration [FS83]. The blades of the EGV and HSC cascades are constructed by superposing the thickness distribution of a modified NACA four-digit series airfoil on a circular-arc camber line. The thickness distribution is given by

$$T(\bar{x}) = H_T[2.969\bar{x}^{1/2} - 1.26\bar{x} - 3.516\bar{x}^2 + 2.843\bar{x}^3 - 1.036\bar{x}^4], \qquad 0 \le \bar{x} \le 1 \ . \tag{2.66}$$

where H_T is the nominal blade thickness. The coefficient of the $\bar{x}^4$ term in (2.66) differs from that used in the standard NACA airfoil definition (i.e., -1.015) so that the example blades close in wedge-shaped trailing edges. The camber distribution is given by

$$C(\bar{x}) = H_C - R + [R^2 - (\bar{x} - 0.5)^2]^{1/2} \ , \qquad 0 \le \bar{x} \le 1 \ , \tag{2.67}$$

where H_C (> 0) is the height at midchord and $R = (2H_C)^{-1}(H_C^2 + 0.25)$ is the radius of the circular-arc camber line. Thus, the surface coordinates for the reference blade are given by

$$[X, Y]_{B,\pm} = [\bar{x} \mp 0.5T(\bar{x}) \sin\theta, \ C(\bar{x}) \pm 0.5T(\bar{x}) \cos\theta] \ , \quad 0 \le \bar{x} \le 1 \ , \tag{2.68}$$

where $\theta = \tan^{-1}(dC/d\bar{x})$.

The blades of the compressor exit guide vane (EGV) are constructed by setting $H_T = 0.12$ and $H_C = 0.13$. This cascade has a stagger angle Θ of 15 deg, a blade spacing G of 0.6 and operates at an inlet Mach number and inlet flow angle of 0.3 and 40 deg, respectively. The blades of the high speed compressor cascade are constructed by setting $H_T = 0.06$ and $H_C = 0.05$. This cascade operates at a high-subsonic inlet condition, i.e., $M_{-\infty} = 0.7$ and $\Omega_{-\infty} = 55$ deg, and has a blade spacing and a stagger angle of unity and 45 deg, respectively.

As a representative turbine configuration we have selected the Fourth Standard Configuration, but for the present study we have modified the blade profiles, defined in [FS83], so that our example blades close in sharp, wedge-shaped, trailing edges. The turbine cascade

operates at an inlet Mach number of 0.19 and an inlet flow angle of 45 deg. The blade spacing G is 0.76, and the stagger angle Θ is 56.6 deg. In addition to the foregoing "real" blade cascades, we will also consider unsteady flows through flat-plate cascades. Here, the blade mean positions are aligned with the mean inlet flow direction, i.e., $\Theta = \Omega_{-\infty}$; therefore, the local steady Mach number, $M = M_{-\infty}$, and flow angle, $\Omega = \Omega_{-\infty}$, are constants throughout the flat-plate flow fields.

3. The Linearized Inviscid Analysis: LINFLO

In this Section, we will describe the linearized inviscid unsteady aerodynamic analysis, called LINFLO, in which unsteady disturbances are regarded as small perturbations of a potential steady background flow. The latter assumption leads to very efficient unsteady aerodynamic response predictions for realistic cascades and mean-flow operating conditions. The LINFLO analysis applies to unsteady flows excited by prescribed blade vibrations and/or external entropic, vortical and acoustic excitations. However, in the following discussion we will emphasize the application of LINFLO to unsteady flows excited by vortical gusts, as this was the major capability developed under contract NAS3–25425.

For more details on the development and application of LINFLO to subsonic, transonic and supersonic unsteady flows excited by prescribed blade motions (the flutter problem) we refer the reader to [VC84, Ver89a, UV91, MVF94]. Applications of LINFLO to unsteady flows excited by prescribed acoustic disturbances and to controlling the noise produced by wake/blade row interactions can be found in [KV93b] and [KV93a, KV94], respectively. Finally the LINFLO analysis has been applied recently to help validate modern, time-accurate, Euler and Navier-Stokes analyses of unsteady cascade flows. These applications are described in [AV94] for unsteady subsonic and transonic flows excited by blade vibrations, and in [DV94] for subsonic flows excited by vortical and acoustic disturbances.

3.1 Unsteady Perturbations of a Potential Mean Flow

We consider inviscid unsteady flows through two-dimensional cascades in which the unsteadiness is caused by excitations of small-amplitude. We assume that the steady background flow far upstream of the blade row is at most a small, isentropic and irrotational, perturbation of a uniform freestream, and any shocks that occur are at most of weak to moderate strength. Because of these assumptions, the steady background flows will be isentropic (with $S = 0$) and irrotational; i.e., $\nabla \times \mathbf{V} = 0$. Thus, we can set $\mathbf{V} = \nabla\Phi$ and $(\mathbf{V} \cdot \nabla)\mathbf{V} = \nabla(\nabla\Phi)^2/2$, where Φ is the steady velocity potential. We also assume that the steady flow far downstream is a small perturbation from a uniform stream. In this case, analytical representations for the entropic, vortical and acoustic excitations at inlet and the acoustic excitations at exit can be provided, cf. (2.2)–(2.4). Also, closed form solutions can be determined to describe the unsteady entropic and vortical perturbations throughout the flow field. Therefore, numerical field methods are required only for determining the first-order unsteady pressure fluctuations.

Note that in the present development $\mathcal{R} \equiv 0$ throughout the field; therefore, the spatial coordinates $\mathbf{x}$ and $\bar{\mathbf{x}}$ are identical, both referring to a fixed point in the blade-row frame of reference. Thus, as a convenience, in this and the following chapter, we will simply use ∇ to indicate the gradient operator with respect to $\mathbf{x}$ or $\bar{\mathbf{x}}$, $\mathcal{R}$ to denote a surface (blade, wake, or shock) motion and $\boldsymbol{\tau}$ and $\mathbf{n}$ to denote unit tangent and normal vectors, respectively, at a mean surface location.

The overall procedure for determining linearized unsteady solutions is first to determine the steady flow for a given cascade configuration, characterized by G, Θ, the blade shape and the inlet and exit flow conditions; and then, to determine the unsteady flow through this cascade for an unsteady excitation at a prescribed amplitude, frequency, ω, and circumferential wave number, $\kappa_\eta = \sigma/G$, or interblade phase angle, σ. Because of the assumptions used in

developing the linearized unsteady aerodynamic model the solution domains for the nonlinear steady and the linearized unsteady problems can be restricted to a single extended blade-passage region of finite extent in the axial flow direction.

The Steady Background Flow

For a potential steady background flow the mass conservation equation (2.43) reduces to

$$\boldsymbol{\nabla} \cdot (\bar{\rho} \boldsymbol{\nabla} \Phi) = 0 \tag{3.1}$$

and the momentum equation (2.44) can be integrated and combined with the thermodynamic relations for a perfect gas to yield the following (Bernoulli) relations for the mean flow variables

$$\begin{aligned} (M_{-\infty} V/M)^2 = (M_{-\infty} A)^2 = \bar{\rho}^{\,\gamma-1} = (\gamma M_{-\infty}^2 P)^{(\gamma-1)/\gamma} = (\gamma-1) M_{-\infty}^2 T \\ = 1 - \frac{\gamma-1}{2} M_{-\infty}^2 [(\boldsymbol{\nabla}\Phi)^2 - 1] = \frac{2+(\gamma-1)M_{-\infty}^2}{2+(\gamma-1)M^2} \ . \end{aligned} \tag{3.2}$$

Here M and A are the local Mach number and speed of sound propagation, respectively, in the mean or steady background flow and γ is the specific heat ratio of the fluid.

Surface conditions for the inviscid zeroth-order or steady background flow apply at the mean positions, B_m, W_m and $\mathrm{Sh}_{m,n}$, of the blade, wake and shock surfaces. Since, by assumption, the flow remains attached to the blade surfaces, a flow tangency condition, cf. (2.48), which for inviscid flow has the form

$$\boldsymbol{\nabla}\Phi \cdot \mathbf{n} = 0 \ , \quad \text{for} \quad \mathbf{x} \in B_m \ , \tag{3.3}$$

applies at such surfaces. In addition, the steady normal velocity component and pressure must be continuous across the blade wakes (W_m), i.e.,

$$[\![\mathbf{V}]\!] \cdot \mathbf{n} = 0 \quad \text{and} \quad [\![P]\!] = 0 \ , \quad \text{for} \quad \mathbf{x} \in W_m \ , \tag{3.4}$$

respectively. Since entropy and vorticity changes across shocks ($\mathrm{Sh}_{m,n}$) are regarded as negligible, the mass, momentum and energy conservation laws cannot all be enforced at such surfaces. The usual practice is to require only that mass and tangential momentum be conserved, i.e.,

$$[\![\bar{\rho}\mathbf{V}]\!] \cdot \mathbf{n} = 0 \ , \quad \text{and} \quad [\![\tilde{\mathbf{V}}]\!] \cdot \boldsymbol{\tau} = 0 \ , \quad \text{for} \quad \mathbf{x} \in Sh_{m,n} \ , \tag{3.5}$$

respectively.

Numerical procedures for determining two-dimensional, steady, potential flows through cascades have been developed extensively, e.g., see [WN85, Cas83, HV93, HV94], particularly for flows with subsonic relative inlet and exit Mach numbers (i.e., $M_{\mp\infty} < 1$). In such calculations far-field boundary conditions are imposed at axial stations placed at finite distances upstream and downstream (i.e., at $\xi = \xi_{\mp}$) from the blade row, where linearized solutions describing the behavior of the steady potential can be matched to a nonlinear near-field solution. In addition, a Kutta condition is usually imposed at blade trailing edges in lieu of prescribing an exit freestream flow property. Finally, the usual practice is to solve the conservative form of the mass-balance equation (3.1) throughout the entire fluid domain. Thus, the shock- and wake-jump conditions are not imposed explicitly. Instead, shock phenomena

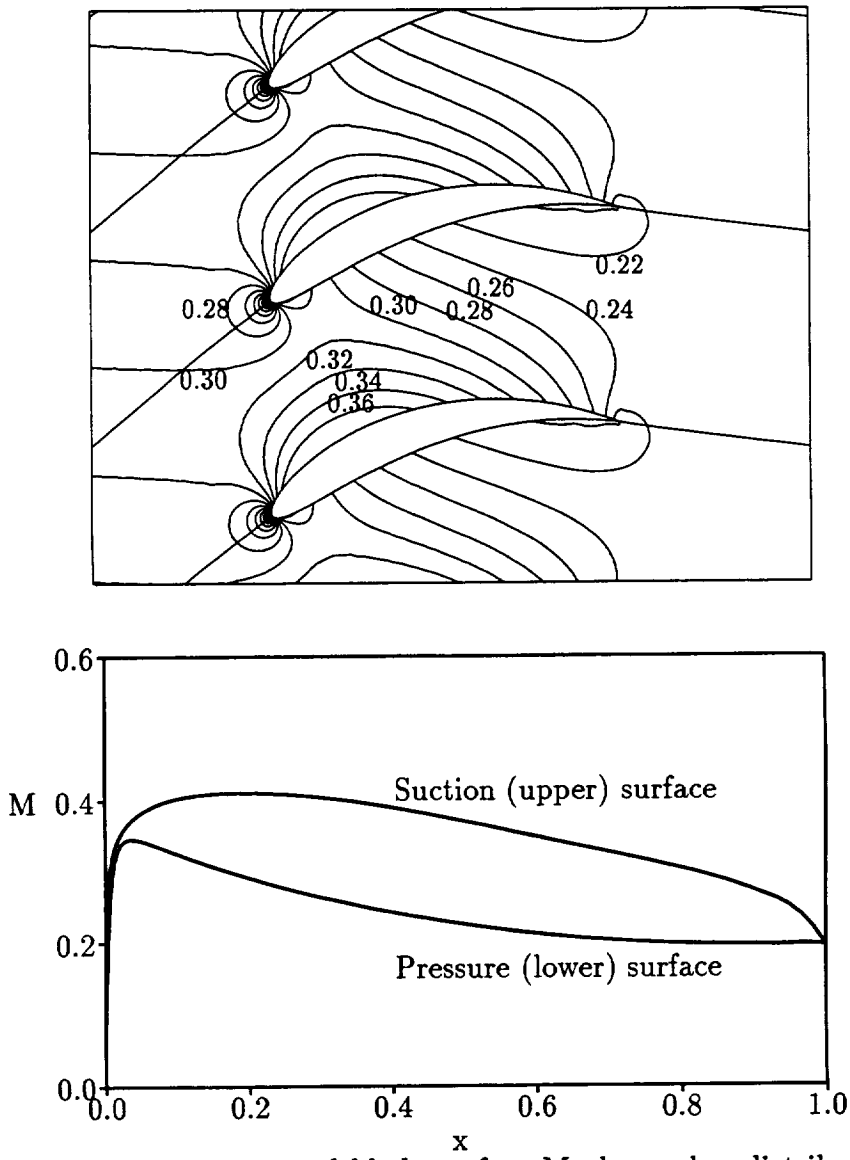

Figure 3.1: Mach number contours and blade surface Mach number distributions for steady flow at $M_{-\infty} = 0.3$ and $\Omega_{-\infty} = 40$ deg through the EGV cascade.

are captured through the use of special differencing techniques. Wake conditions are satisfied implicitly, because, in a potential flow, the fluid properties are continuous and differentiable across wakes. If needed, mean shock and wake (i.e., the downstream stagnation streamlines) locations can be determined *a posteriori* from the resulting steady flow solutions.

Steady flows through the EGV and turbine cascades, that will be used here to demonstrate the vortical gust prediction capabilities of the LINFLO analysis, are illustrated in Figures 3.1 and 3.2, respectively. These solutions have been determined using the methods of [Cas83]. In each case a Kutta condition has been applied at blade trailing edges; therefore, only inlet uniform flow information, e.g., $M_{-\infty}$ and $\Omega_{-\infty}$, have been specified for the steady calculations. The predicted steady Mach number field and Mach number distribution along a blade surface for the steady flow at $M_{-\infty} = 0.3$ and $\Omega_{-\infty} = 40$ deg through the EGV are shown in Figure 3.1.

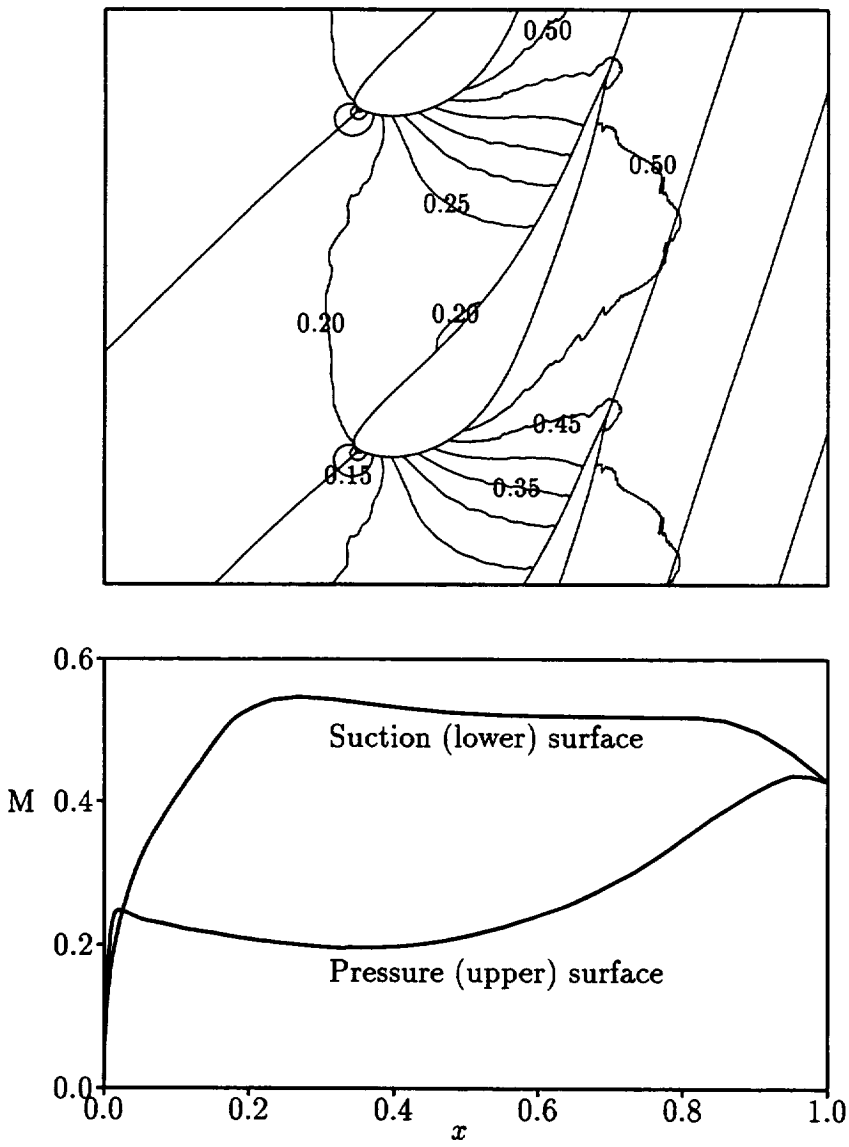

Figure 3.2: Mach number contours and blade surface Mach number distributions for steady flow at $M_{-\infty} = 0.19$ and $\Omega_{-\infty} = 45$ deg through the turbine cascade.

The calculated exit Mach number and exit flow angle for this flow are 0.226 and -7.4 deg, respectively, and the mean lift force, F_y, acting on each blade is 0.360. The predicted steady Mach number contours and blade-surface Mach number distributions for the steady flow at $M_{-\infty} = 0.19$ and $\Omega_{-\infty} = 45$ deg through the turbine are shown in Figure 3.2. For the turbine cascade, the calculated exit Mach number and flow angle are 0.49 and 72.0 deg, respectively, and the mean lift acting on each blade is -2.11.

The Linearized Unsteady Equations

The field equations that govern the first-order unsteady perturbation of an isentropic and irrotational steady flow can be expressed as a system of coupled differential equations for the complex amplitudes of the first-order entropy ($\tilde{s}$), velocity ($\tilde{\mathbf{v}}$) and pressure ($\tilde{p}$), respectively (see [Gol78, Ver87]). In general, we require a solution to this system subject to prescribed flow conditions far upstream and far downstream from the blade row, flow tangency conditions at moving blade surfaces, and, since the inviscid field equations apply only in continuous regions of the flow, jump conditions at moving shocks and blade wakes.

As indicated by Goldstein [Gol78, Gol79] the system of field equations that governs the linearized unsteady flow can be cast into a very convenient form by decomposing the unsteady velocity into rotational ($\mathbf{v}_R$) and irrotational ($\boldsymbol{\nabla}\phi$) parts. The rotational velocity, $\mathbf{v}_R$, is taken to be divergence-free far upstream of the blade row, i.e., $\boldsymbol{\nabla} \cdot \mathbf{v}_R \equiv 0$ for $\xi < \xi_-$, and the unsteady pressure depends only upon the potential ϕ through the relation $p = -\bar{\rho}\bar{D}\phi/Dt$, where $\bar{D}/Dt = i\omega + \boldsymbol{\nabla}\Phi \cdot \boldsymbol{\nabla}$ is a convective derivative operator based on the mean flow velocity. The unsteady vorticity is given by $\boldsymbol{\zeta} = \boldsymbol{\nabla} \times \mathbf{v}_R$. For realistic blade profiles $\mathbf{v}_R \cdot \mathbf{n}$ and hence, $\boldsymbol{\nabla}\phi \cdot \mathbf{n}$, will be singular along the mean blade and wake surfaces. Therefore, Atassi and Grzedzinski [AG89] introduced a modified form of the Goldstein decomposition, by setting

$$\mathbf{v} = \mathbf{v}_* + \boldsymbol{\nabla}\phi = \mathbf{v}_R + \boldsymbol{\nabla}\phi_* + \boldsymbol{\nabla}\phi \,, \tag{3.6}$$

to facilitate the numerical resolution of the velocity potential, ϕ. Here, ϕ_* is a convected or pressure-less potential (i.e., $\bar{D}\phi_*/Dt = 0$) which satisfies the condition $\boldsymbol{\nabla}\phi_* \cdot \mathbf{n} = -\mathbf{v}_R \cdot \mathbf{n}$ at blade and wake mean positions.

The system of field equations that governs the linearized unsteady flow variables, s, $\mathbf{v}_R$ and ϕ is determined by substituting $S = 0$, $\mathbf{V} = \boldsymbol{\nabla}\Phi$ and the velocity decomposition, Eq. (3.6), into the linearized Euler equations (2.52), (2.54) and (2.55) to obtain

$$\frac{\bar{D}s}{Dt} = 0 \tag{3.7}$$

$$\frac{\bar{D}}{Dt}(\mathbf{v}_R - s\boldsymbol{\nabla}\Phi/2) + [(\mathbf{v}_R - s\boldsymbol{\nabla}\Phi/2) \cdot \boldsymbol{\nabla}]\boldsymbol{\nabla}\Phi = 0 \tag{3.8}$$

and

$$\frac{\bar{D}}{Dt}(A^{-2}\frac{\bar{D}\phi}{Dt}) - \bar{\rho}^{-1}\boldsymbol{\nabla} \cdot (\bar{\rho}\boldsymbol{\nabla}\phi) = \bar{\rho}^{-1}\boldsymbol{\nabla} \cdot [\bar{\rho}(\mathbf{v}_R + \boldsymbol{\nabla}\phi_*)] = \bar{\rho}^{-1}\boldsymbol{\nabla} \cdot (\bar{\rho}\mathbf{v}_*) \,. \tag{3.9}$$

These equations are coupled only sequentially; hence, they can be solved in order to determine the complex amplitudes, s, v_R and ϕ, of the unsteady entropy, rotational velocity and velocity potential, respectively. Moreover, closed form solutions [Gol78, HV91] can be determined for the entropy and rotational velocity fluctuations in terms of the prescribed entropy and rotational velocity fluctuations at inlet. The velocity potential, ϕ, is governed by convected wave equation with source term $\bar{\rho}^{-1}\boldsymbol{\nabla} \cdot (\bar{\rho}\mathbf{v}_*)$ and depends, therefore, upon the rotational velocity, the convected potential, the conditions imposed at wake and shock surfaces, and far upstream and far downstream of the blade row. Phase-lagged periodicity conditions [cf. (2.42)], e.g.,

$$\phi(\mathbf{x} + m\mathbf{G}) = \phi(\mathbf{x})\exp(im\sigma) \tag{3.10}$$

are also imposed on the entropy, rotational velocity and velocity potential to reduce the computational domain to a single, extended, blade-passage region.

Surface Conditions

As a consequence of the small unsteady-disturbance approximation, conditions on the linearized unsteady perturbation at moving blade, shock and wake surfaces can be transferred to the mean positions of these surfaces (see [Ver87]), with the mean wake, i.e., the downstream stagnation streamlines, and shock locations being determined from the nonlinear steady solution. Thus, the (inviscid) flow tangency condition, cf. (2.56), can be written as

$$\mathbf{v}\cdot\mathbf{n} = \boldsymbol{\nabla}\phi\cdot\mathbf{n} = [i\omega\mathbf{R} + (\boldsymbol{\nabla}\Phi\cdot\boldsymbol{\tau})(\boldsymbol{\tau}\cdot\boldsymbol{\nabla})\mathbf{R} - (\mathbf{R}\cdot\boldsymbol{\nabla})\boldsymbol{\nabla}\Phi]\cdot\mathbf{n}, \quad \mathbf{x}\in B_m \tag{3.11}$$

where the complex amplitude of the blade displacement, $\mathbf{R}(\mathbf{x})$, $\mathbf{x}\in \mathrm{B}_m$, is a prescribed quantity. In addition, since the irrotational steady velocity and pressure are continuous and have continuous derivatives across the mean-flow downstream stagnation streamlines, the wake conditions, (2.57) and (2.58), reduce to

$$[\![\mathbf{v}\cdot\mathbf{n}]\!] = [\![\boldsymbol{\nabla}\phi]\!]\cdot\mathbf{n} = 0 \quad \text{and} \quad [\![p]\!] = [\![\bar{D}\phi/Dt]\!] = 0\ , \quad \mathbf{x}\in W_m\ . \tag{3.12}$$

Finally, if we neglect changes in entropy and rotational velocity across shocks, the conservation laws for mass and tangential momentum yield the following linearized shock-jump condition for a shock that terminates in the fluid

$$\begin{aligned}[\![\bar{\rho}(\boldsymbol{\nabla}\phi + \mathbf{v}_R - A^{-2}\frac{\bar{D}\phi}{Dt}\boldsymbol{\nabla}\Phi)]\!]\cdot\mathbf{n} = -[\![\bar{\rho}]\!][i\omega + (\boldsymbol{\nabla}\Phi\cdot\boldsymbol{\tau})\boldsymbol{\tau}\cdot\boldsymbol{\nabla}][([\![\boldsymbol{\nabla}\Phi]\!]\cdot\mathbf{n})^{-1}[\![\phi]\!]\,] \\ - (\boldsymbol{\nabla}\Phi\cdot\mathbf{n})^{-1}[\![\phi]\!]\,\boldsymbol{\tau}\cdot\boldsymbol{\nabla}([\![\bar{\rho}]\!]\boldsymbol{\nabla}\Phi\cdot\boldsymbol{\tau})\ , \quad \mathbf{x}\in \mathrm{Sh}_{m,n}\ .\end{aligned} \tag{3.13}$$

Equation (3.13) provides a relation for determining the jump in the unsteady potential, $[\![\phi]\!]$, at the mean position of a shock. The shock displacement normal to the mean shock locus is then given by $\mathbf{R}\cdot\mathbf{n} = -([\![\boldsymbol{\nabla}\Phi]\!]\cdot\mathbf{n})^{-1}[\![\phi]\!]$. Because the mean flow is potential, the mean flow variables are continuous across blade wakes, and we have assumed that s and $\mathbf{v}_R$ are continuous across shocks, the foregoing wake- and shock-jump conditions provide sufficient information for determining the jumps in the unsteady potential, and hence, the remaining unsteady flow variables, across wake and shock surfaces.

Far-Field Behavior

We have assumed that the mean or steady flow is at most a small (i.e., of $\mathcal{O}(\epsilon)$) perturbation from a uniform stream both far upstream ($\xi < \xi_-$) and far downstream ($\xi > \xi_+$) from the blade row. Therefore, in these regions, the first-order (in ϵ) unsteady field equations can be reduced to constant coefficient equations for which analytical solutions can be determined (see [Ver89b]).

For example, it follows after replacing $\boldsymbol{\nabla}\Phi$ by $\mathbf{V}_{-\infty}$ in (3.7) and (3.8), that far upstream of the blade row, the complex amplitudes of the entropy and rotational velocity fluctuations have the form (see also (2.2) and (2.3))

$$s(\mathbf{x}) = s_{-\infty}\exp(i\boldsymbol{\kappa}_{-\infty}\cdot\mathbf{x}), \quad \xi < \xi_-\ , \tag{3.14}$$

and

$$\mathbf{v}_R(\mathbf{x}) = \mathbf{v}_{R,-\infty} \exp(i\boldsymbol{\kappa}_{-\infty} \cdot \mathbf{x}), \quad \xi < \xi_- \ . \tag{3.15}$$

Here, $s_{-\infty}$ and $\mathbf{v}_{R,-\infty}$ are the complex amplitudes (at $\mathbf{x} = 0$) and $\boldsymbol{\kappa}_{-\infty}$ is the wave number of the entropic and rotational velocity disturbances. The wave number vector has a component $\kappa_{\eta,-\infty} = \boldsymbol{\kappa}_{-\infty} \cdot \mathbf{e}_\eta = \sigma G^{-1}$ in the cascade "circumferential" or η-direction and a component $\kappa_T = \boldsymbol{\kappa}_{-\infty} \cdot \mathbf{e}_T = -\omega V_{-\infty}^{-1} = -\omega$ in the inlet freestream direction. Therefore, we can write

$$\begin{aligned} \boldsymbol{\kappa}_{-\infty} &= -(\omega \sec \Omega_{-\infty} + \sigma G^{-1} \tan \Omega_{-\infty})\mathbf{e}_\xi + \sigma G^{-1} \mathbf{e}_\eta \\ &= -\omega \mathbf{e}_T + (\omega \tan \Omega_{-\infty} + \sigma G^{-1} \sec \Omega_{-\infty})\mathbf{e}_N \ , \end{aligned} \tag{3.16}$$

where, $\mathbf{e}_\xi$ and $\mathbf{e}_\eta$ are unit vectors pointing in the axial ($\xi-$) and circumferential ($\eta-$) directions, respectively, and $\mathbf{e}_T$ and $\mathbf{e}_N$ are unit vectors pointing in the inlet freestream and normal to the inlet freestream directions, such that $\mathbf{e}_z = \mathbf{e}_T \times \mathbf{e}_N$ points out from the page.

The complex amplitudes, $s_{-\infty}$ and $\mathbf{v}_{R,-\infty} \cdot \mathbf{e}_N$, of the entropy and the rotational velocity component normal to the freestream direction are prescribed quantities. The component of the gust velocity in the inlet freestream direction, $\mathbf{v}_{R,-\infty} \cdot \mathbf{e}_T$, is determined by the divergence-free or orthogonality condition, $i\boldsymbol{\kappa}_{-\infty} \cdot \mathbf{v}_{R,-\infty} \equiv 0$. The complex amplitude of the vorticity far upstream of the blade row is given by

$$\boldsymbol{\zeta}_{-\infty} = (\nabla \times \mathbf{v}_R)_{-\infty} = i\boldsymbol{\kappa}_{-\infty} \times \mathbf{v}_{R,-\infty} = i\kappa_{-\infty}^2 \mathbf{v}_{R,-\infty} \cdot \mathbf{e}_N / \kappa_{T,-\infty} \ , \tag{3.17}$$

and, since the vectors $\boldsymbol{\kappa}_{-\infty}$ and $\mathbf{v}_{R,-\infty}$ are orthogonal, we can write

$$\mathbf{v}_{R,-\infty} = i(\boldsymbol{\kappa}_{-\infty} \times \boldsymbol{\zeta}_{-\infty})/|\boldsymbol{\kappa}_{-\infty}|^2 \ . \tag{3.18}$$

The entropy and vorticity, or rotational velocity at inlet are essentially prescribed functions; at exit, these quantities are determined as part of the unsteady solution

The velocity potential fluctuations in the far upstream and far downstream regions depend upon the prescribed acoustic excitation as well as the acoustic response of the cascade. To describe these fluctuations, we can set

$$\phi(\mathbf{x}) = \phi_E(\mathbf{x}) + \phi_R(\mathbf{x}) \quad \text{for } \xi \lessgtr \xi_\mp \ , \tag{3.19}$$

where the potential component ϕ_E accounts for acoustic excitations, i.e., pressure disturbances that either attenuate as they approach the blade row or propagate and carry energy towards the blade row. In particular, it follows from (3.9) with $\nabla\Phi = \mathbf{V}_{\mp\infty}$ that for an acoustic excitation at temporal frequency ω, ϕ_E has the form (see [Ver89b])

$$\phi_E(\mathbf{x}) = \phi_{I,\mp\infty} \exp[\beta_{\mp\infty}\xi + i\boldsymbol{\kappa}_{\mp\infty} \cdot \mathbf{x}], \quad \xi \lessgtr \xi_\mp \ , \tag{3.20}$$

where

$$\phi_{I,\mp\infty} = \bar{\rho}_{\mp\infty}^{-1} \{\beta_{\mp\infty} V_{\mp\infty} \cos \Omega_{\mp\infty} - i[\omega + (\boldsymbol{\kappa}_{\mp\infty} \cdot \mathbf{V}_{\mp\infty})]\}^{-1} p_{I,\mp\infty} \ , \tag{3.21}$$

the complex amplitudes $p_{I,\mp\infty}$ are prescribed, $\kappa_{\eta,\mp\infty} = \sigma/G$, and $\beta_{\mp\infty}$ and $\kappa_{\xi,\mp\infty}$ depend upon the inlet/exit freestream conditions, and the temporal frequency (ω) and interblade phase angle (σ) of the acoustic excitation. The potential component ϕ_R is associated with the

acoustic and vortical response of the blade row and therefore, must be determined as part of the unsteady solution.

Usually only acoustic excitations that are of propagating type are considered. For subsonic inlet and exit conditions ($M_{\mp\infty} < 1$) the velocity potential corresponding to a propagating acoustic excitation at temporal frequency $\omega > 0$ has the form (3.20) with $\beta_{\mp\infty} = 0$, and

$$\kappa_{\eta,\mp\infty}^{(-)} \leq \kappa_{\eta,\mp\infty} = \sigma G^{-1} \leq \kappa_{\eta,\mp\infty}^{(+)} , \tag{3.22}$$

where the $\kappa_{\eta,\mp\infty}^{(\mp)}$ are the circumferential wave numbers at which cut-off or acoustic resonance occurs. These wave numbers are given by

$$\kappa_{\eta,\mp\infty}^{(\mp)} = \omega V_{\mp\infty}^{-1} M_{\mp\infty}(1 - M_{\mp\infty}^2)^{-1}(M_{\mp\infty}\sin\Omega_{\mp\infty} \pm \sqrt{1 - M_{\mp\infty}^2\cos^2\Omega_{\mp\infty}}) . \tag{3.23}$$

It follows from (3.9), that the axial wave number of the propagating acoustic excitation is

$$\kappa_{\xi,\mp\infty} = \mp|d_{\mp\infty}| - M_{\mp\infty}^2\delta_{\mp\infty}\cos\Omega_{\mp\infty} , \tag{3.24}$$

where

$$|d_{\mp\infty}| = |(1 - M_{\mp\infty}\cos^2\Omega_{\mp\infty})^{-1}\kappa_\eta^2 - M_{\mp\infty}^2\delta_{\mp\infty}^2|^{1/2} , \tag{3.25}$$

and

$$\delta_{\mp\infty} = (\omega V_{\mp\infty}^{-1} + \kappa_\eta \sin\Omega_{\mp\infty})/(1 - M_{\mp\infty}^2\cos^2\Omega_{\mp\infty}) . \tag{3.26}$$

Analytic solutions to (3.9), with $\nabla\Phi = \mathbf{V}_{\mp\infty}$, for the far-field potential component ϕ_R which satisfy the requirements that acoustic response disturbances either attenuate with increasing axial distance from the blade row or propagate carrying energy away from or parallel to the blade row, and that vorticity must be convected downstream are given in [Ver89b]. These solutions contain arbitrary constants that are determined by matching the far-field analytic solutions for the velocity potential to a near field numerical solution.

3.2 Linearized Unsteady Solutions

At this point we have presented the linearized equations that govern a general inviscid unsteady perturbation of a potential steady background flow, and we have indicated the quantities, i.e., ω, σ, $\mathbf{R}_B$, $s_{-\infty}$, $\mathbf{v}_{R,-\infty}\cdot\mathbf{e}_N$ and $p_{I,\mp\infty}$ that must be prescribed to determine the unsteady perturbation. We proceed to describe the procedures currently used in the LINFLO analysis to determine the unsteady entropy, rotational velocity and velocity potential. Once the unsteady potential is determined, it is a simple matter to determine response information needed for aeroelastic and aeroacoustic design applications, i.e., the unsteady pressures acting on the blades and in the far upstream and downstream regions of the flow.

Entropy and Rotational Velocity

Closed form solutions for the linearized entropy and rotational velocity fluctuations can be determined in terms of independent variables that describe the steady background flow [Gol78, HV91]. For this purpose we introduce the Lagrangian coordinate vector

$$\mathbf{X} = \Delta\mathbf{e}_T + \Psi\mathbf{e}_N . \tag{3.27}$$

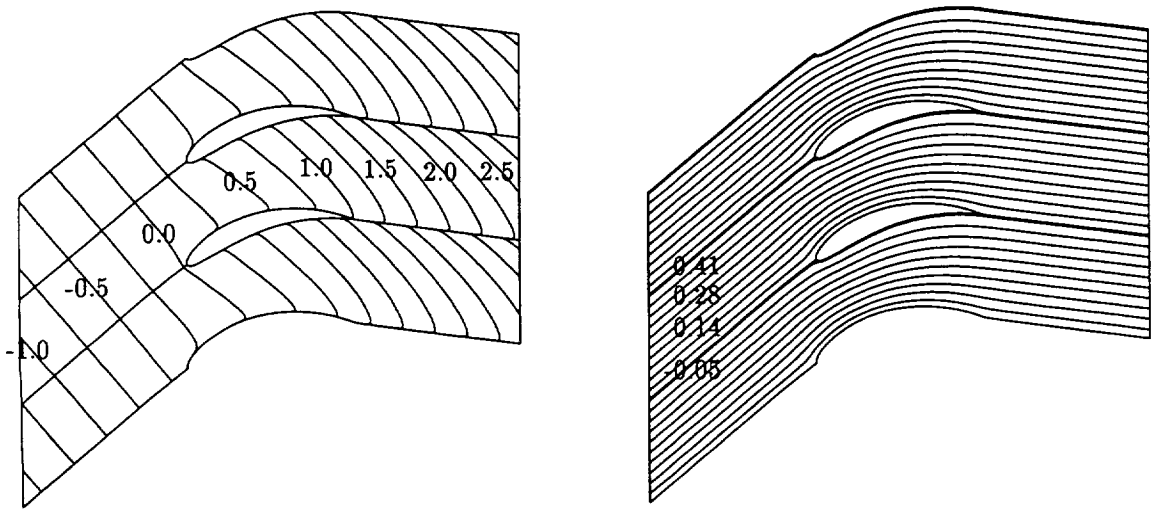

Figure 3.3: Drift and stream function contours for steady flow at $M_{-\infty} = 0.3$ and $\Omega_{-\infty} = 40$ deg through the EGV cascade.

Here,

$$\Delta(\mathbf{x}) = \mathbf{x}_- \cdot \mathbf{e}_T + \int_{\mathbf{x}_- + [\Psi(\mathbf{x}) - \Psi(\mathbf{x}_-)]\mathbf{e}_N}^{\mathbf{x}} V^{-1} d\tau_\Psi \quad \text{and} \quad \Psi(\mathbf{x}) = \mathbf{x}_- \cdot \mathbf{e}_N + \int_{\mathbf{x}_-}^{\mathbf{x}} \bar{\rho}(\mathbf{e}_z \times \mathbf{V}) \cdot d\boldsymbol{\tau} \quad (3.28)$$

are the drift and stream functions, respectively, of the steady background flow. Also, $\mathbf{x}_-$ is the position vector to the point of intersection (ξ_-, η_-) of the reference blade stagnation streamline and the axial line $\xi = \xi_-$, $d\tau_\Psi$ is a differential element of arc length along a streamline, and $d\boldsymbol{\tau}$ is a differential vector tangent to the path of integration.

Drift and stream function contours for the EGV operating at $M_{-\infty} = 0.3$, $\Omega_{-\infty} = 40$ deg and for the turbine operating at $M_{-\infty} = 0.19$, $\Omega_{-\infty} = 45$ deg are shown in Figures 3.3 and 3.4, respectively. These results have been calculated from the steady solutions depicted in Figures 3.1 and 3.2. Far upstream of each blade row, the drift function contours are parallel to each other and perpendicular to the inlet freestream direction, but as the flow proceeds downstream, gradients in the steady velocity field produce distortions. For the EGV, these distortions are mild over most of the blade passage, but severe in the immediate vicinity of the blade and wake surfaces, where the drift function contours stretch downstream from the leading-edge stagnation point. In addition, to the severe distortions near the blades and wakes, the drift function contours for the turbine are highly stretched within a blade and wake passage, because of the high steady velocities at mid passage.

To determine the closed form solutions for the entropy and rotational velocity, we first note that $\bar{D}\mathbf{X}/Dt = (\mathbf{V} \cdot \boldsymbol{\nabla})\mathbf{X} = \mathbf{V}_{-\infty} = \mathbf{e}_T$ and $\mathbf{X} \to \mathbf{x}$ as $\xi \to -\infty$. The solution to the entropy transport equation (3.7), which satisfies the far upstream condition (3.14), is then given by

$$s(\mathbf{x}) = s_{-\infty} \exp(i\boldsymbol{\kappa}_{-\infty} \cdot \mathbf{X}) \ , \quad (3.29)$$

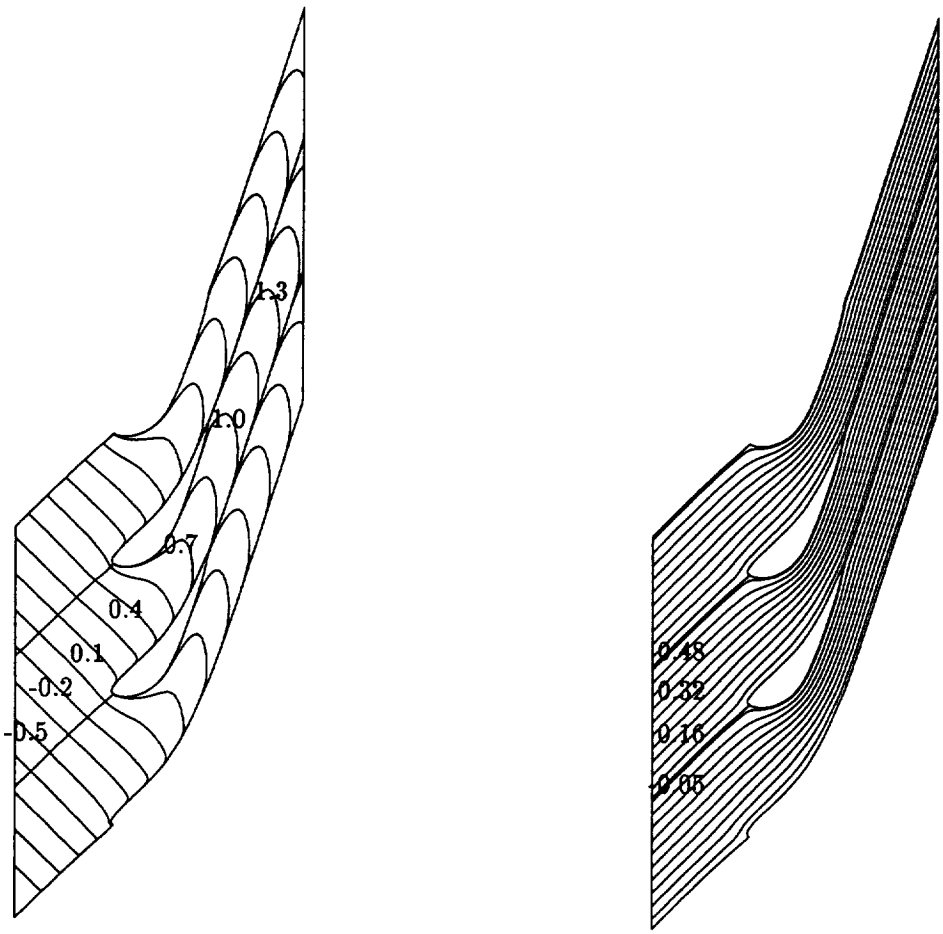

Figure 3.4: Drift and stream function contours for steady flow at $M_{-\infty} = 0.19$ and $\Omega_{-\infty} = 45$ deg through the turbine cascade.

and the solution to the rotational velocity transport equation (3.8), which satisfies the far upstream condition (3.15), is

$$\mathbf{v}_R(\mathbf{x}) = [\boldsymbol{\nabla}(\mathbf{X}\cdot\boldsymbol{\mathcal{A}}_{-\infty}) + s_{-\infty}\boldsymbol{\nabla}\Phi/2]\exp(i\boldsymbol{\kappa}_{-\infty}\cdot\mathbf{X}) \;, \tag{3.30}$$

where

$$\boldsymbol{\mathcal{A}}_{-\infty} = \mathbf{v}_{R,-\infty} - s_{-\infty}\mathbf{V}_{-\infty}/2 \;. \tag{3.31}$$

It follows from (3.30) that

$$\boldsymbol{\zeta} = \boldsymbol{\nabla}\times\mathbf{v}_R = \boldsymbol{\nabla}(i\boldsymbol{\kappa}_{-\infty}\cdot\mathbf{X})\times[\boldsymbol{\nabla}(\boldsymbol{\mathcal{A}}_{-\infty}\cdot\mathbf{X}) + s_{-\infty}\boldsymbol{\nabla}\Phi/2]\exp(i\boldsymbol{\kappa}_{-\infty}\cdot\mathbf{X}) \;, \tag{3.32}$$

and $\boldsymbol{\zeta} \rightarrow \boldsymbol{\zeta}_{-\infty}\exp(i\boldsymbol{\kappa}_{-\infty}\cdot\mathbf{x}) = i\boldsymbol{\kappa}_{-\infty}\times\mathbf{v}_{R,-\infty}\exp(i\boldsymbol{\kappa}_{-\infty}\cdot\mathbf{x})$ as $\mathbf{X}\rightarrow\mathbf{x}$.

If the steady background flow stagnates in the vicinity of a blade leading edge, as it will for realistic configurations, the drift function will have a logarithmic singularity at the mean blade and wake surfaces, i.e., $\Delta \rightarrow a_0 \ln n$ as $n \rightarrow 0$, where n is the normal distance from

the surface and a_0 is a real constant. As a result, the exponential function $\exp(i\boldsymbol{\kappa}_{-\infty}\cdot\mathbf{X})$ will be indeterminate, and the normal component of the rotational velocity will be singular, i.e., $\mathbf{v}_R\cdot\mathbf{n}\rightarrow a_1 n^{-1}\exp(i\boldsymbol{\kappa}_{-\infty}\cdot\mathbf{X})$, where a_1 is a complex constant, at such surfaces. We can remove this singular behavior from the blade and wake surface conditions that are used to determine the unsteady potential, ϕ, by prescribing a convected potential of the form [AG89]

$$\phi_* = \left[-i\omega^{-1}\boldsymbol{\mathcal{A}}_{-\infty}\cdot\mathbf{V}_{-\infty} + F(\Psi)\right]\exp(i\boldsymbol{\kappa}_{-\infty}\cdot\mathbf{X})\ , \tag{3.33}$$

where

$$F(\Psi) = \frac{\omega^{-1}(\boldsymbol{\kappa}_{-\infty}\times\boldsymbol{\mathcal{A}}_{-\infty})\cdot\mathbf{e}_z G\cos\Omega_{-\infty}}{2\pi(1-ia_0\omega)}\sin\left[\frac{2\pi[\Psi(\mathbf{x})-\Psi(\mathbf{x}_-)]}{G\cos\Omega_{-\infty}}\right] \tag{3.34}$$

is a complex function that depends upon, among other things, the behavior of the mean flow in the vicinity of a leading-edge stagnation point. This choice of ϕ_* ensures that $\mathbf{v}_*\cdot\mathbf{n} = (\mathbf{v}_R+\boldsymbol{\nabla}\phi_*)\cdot\mathbf{n} = 0$ at blade and wake mean positions.

After combining (3.30), (3.33) and (3.34), we find that the complex amplitude of the source-term velocity, $\mathbf{v}_* = \mathbf{v}_R + \boldsymbol{\nabla}\phi_*$, is given by

$$\mathbf{v}_* = \left[F\boldsymbol{\nabla}(i\boldsymbol{\kappa}_{-\infty}\cdot\mathbf{X}) + \left(\frac{dF}{d\Psi} - \omega^{-1}(\boldsymbol{\kappa}_{-\infty}\times\boldsymbol{\mathcal{A}}_{-\infty})\cdot\mathbf{e}_z\right)\boldsymbol{\nabla}\Psi + s_{-\infty}\boldsymbol{\nabla}\Phi/2\right]\exp(i\boldsymbol{\kappa}_{-\infty}\cdot\mathbf{X})\ . \tag{3.35}$$

It follows from (3.34) and (3.35) that $\mathbf{v}_*$ behaves like $s_{-\infty}\boldsymbol{\nabla}\Phi\exp(i\boldsymbol{\kappa}_{-\infty}\cdot\mathbf{X})/2$ in the immediate vicinity of the mean blade and wake surfaces, i.e., as $n\rightarrow 0$. Thus, $\mathbf{v}_*\cdot\mathbf{n} = 0$, but, if $s_{-\infty}\neq 0$, the tangential component of the source-term velocity will be indeterminate at such surfaces. It would be useful in future work to construct a convected potential, ϕ_*, that also removes this indeterminacy, thereby allowing more accurate numerical resolutions of unsteady flows excited by entropic disturbances.

The velocities $\mathbf{v}_R$ and $\mathbf{v}_*$ depend upon Δ and Ψ and the first partial derivative of these functions. Therefore, the complex amplitudes of the unsteady vorticity, $\boldsymbol{\zeta} = \boldsymbol{\nabla}\times\mathbf{v}_R = \boldsymbol{\nabla}\times\mathbf{v}_*$, and the source term, $\bar{\rho}^{-1}\boldsymbol{\nabla}\cdot(\bar{\rho}\mathbf{v}_*)$, in (3.9) depend also upon the second partial derivatives of Δ and Ψ. Thus, an accurate solution for the nonlinear steady background flow is a critical prerequisite for determining the unsteady effects associated with entropic and vortical excitations.

The complex amplitudes of the entropy, rotational velocity, vorticity, and source term velocity are readily determined once the values of the drift and stream functions and their spatial derivatives are specified over the single extended blade-passage solution domain. For this purpose it is convenient to use an H-grid in which one set of mesh lines are the streamlines of the steady background flow, for resolving unsteady flows excited by entropic and vortical gusts. An H- grid which covers the solution domain, i.e., one which is bounded by the upstream and downstream axial lines $\xi = \xi_{\mp}$ and two neighboring mean-flow stagnation streamlines, is appropriate. The locations of the latter are determined *a posteriori* from the solution for the *non*linear steady background flow. Once the boundaries of the H-grid are established, the locations of the interior grid points can be determined using an elliptic grid generation technique, as described in [VH90, HV91].

Because a streamline mesh is used, the drift function can be evaluated at each point in the computational domain by a straightforward numerical integration of (3.28). The procedure

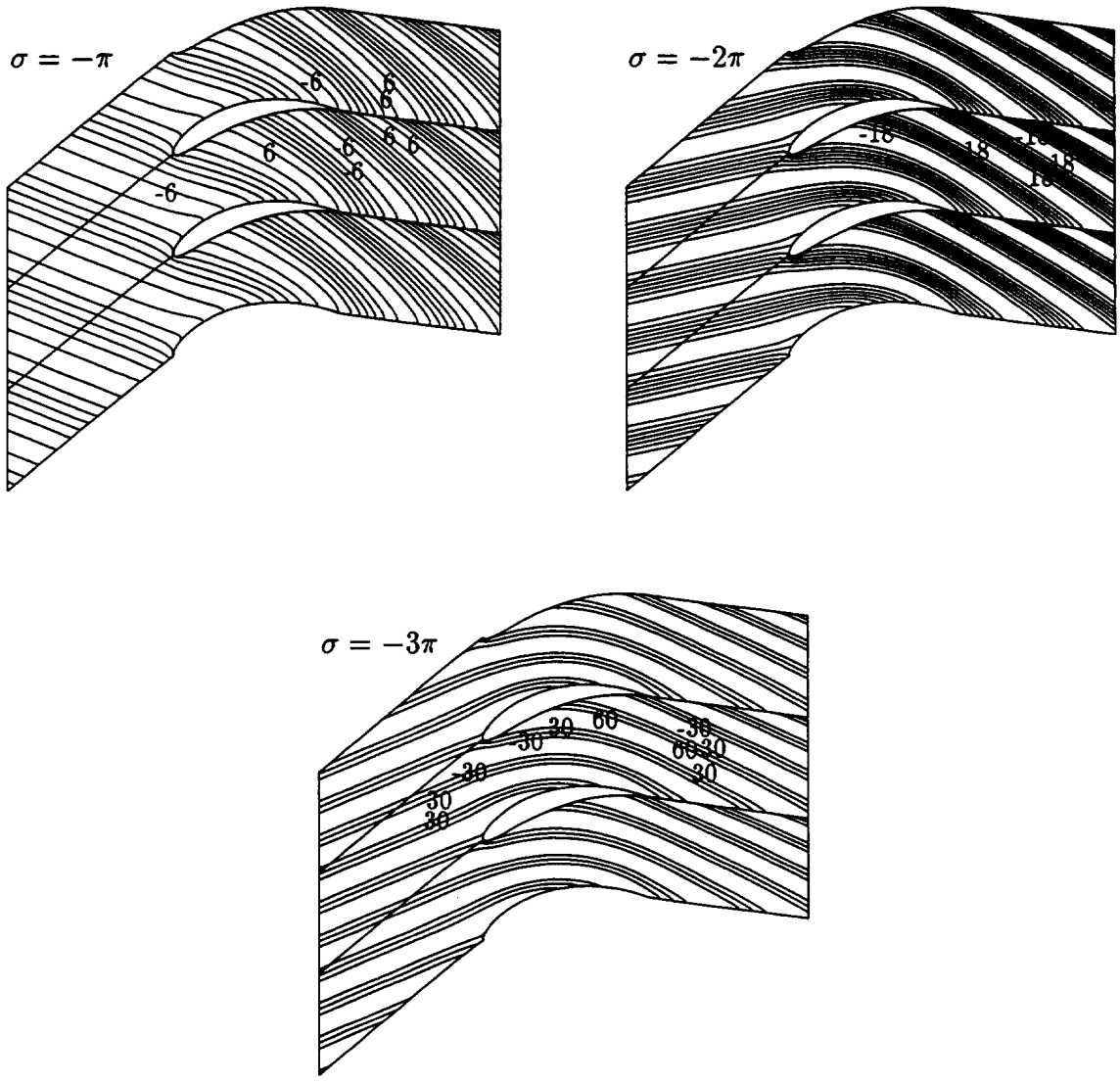

Figure 3.5: Contours of the in-phase component of the unsteady vorticity for the EGV cascade subjected to vortical gusts with $\mathbf{v}_{R,-\infty} \cdot \mathbf{e}_N = (1,0)$ and $\omega = 5$.

used in [VH90, HV91] is simply to specify the drift function along the far upstream boundary $\xi = \xi_-$, and then to evaluate this function along each streamline using a second-order accurate difference approximation. The derivatives of the drift and stream functions at a given grid point are determined using the finite difference operators developed by Caspar and Verdon [CV81]. Because the drift function is singular at blade and wake surfaces, one-sided difference approximations are used to evaluate the derivatives of this function at points on the mesh streamlines adjacent to these surfaces.

Calculated vorticity and source term fields for unsteady flows through the example EGV and turbine cascades excited by vortical gusts with $\mathbf{v}_{R,-\infty} \cdot \mathbf{e}_N = (1,0)$, $\omega = 5$, and $\sigma =$

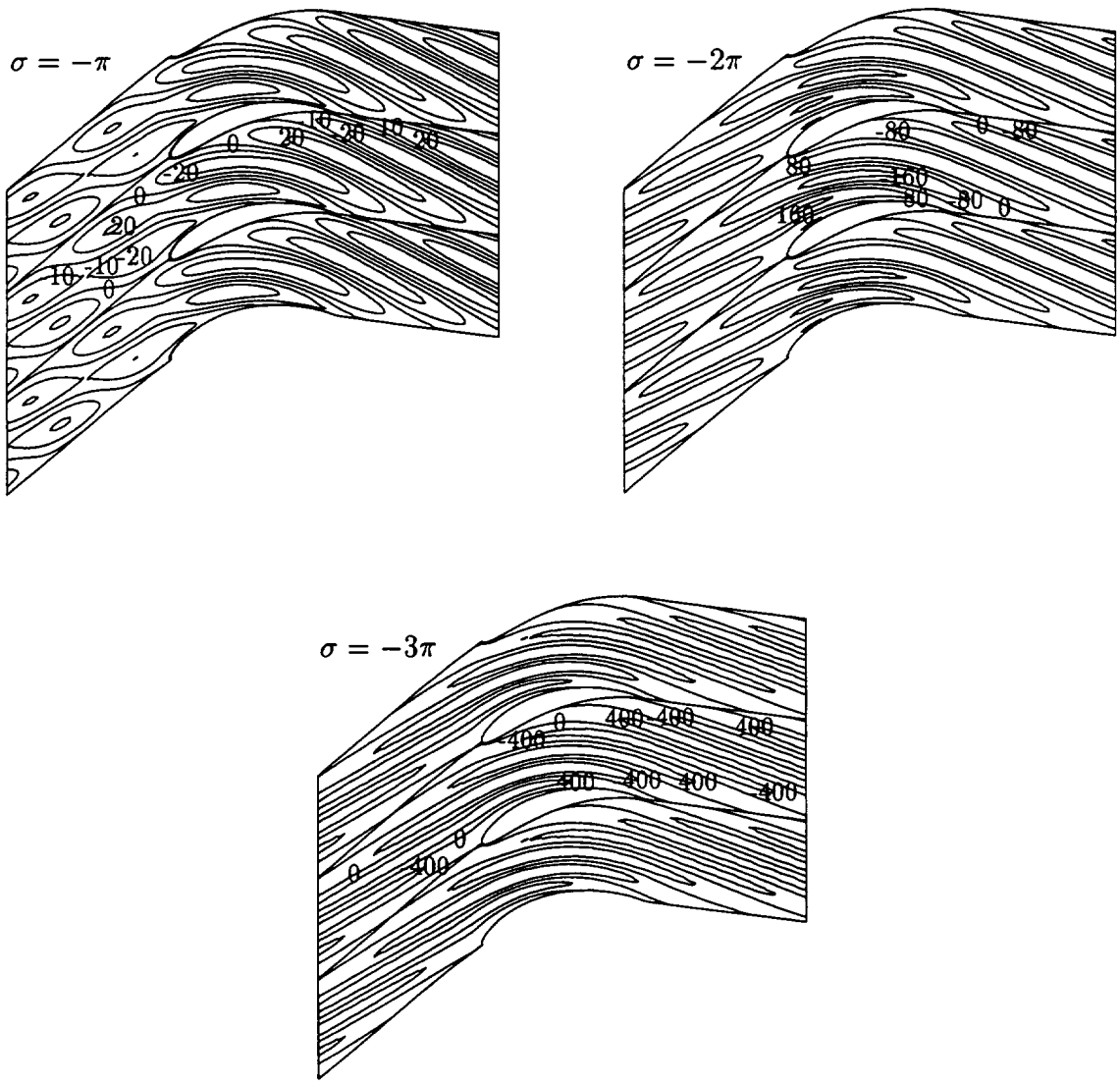

Figure 3.6: Contours of the in-phase component of the source term for the EGV cascade subjected to vortical gusts with $\mathbf{v}_{R,-\infty} \cdot \mathbf{e}_N = (1, 0)$ and $\omega = 5$.

$-\pi$, -2π and -3π are shown in Figures 3.5 through 3.8. These results were determined by performing the unsteady calculations on a (155 $\times$ 40) streamline H-mesh. Contours of the in-phase component or real part of the unsteady vorticity and source term are shown in Figures 3.5 and 3.6, respectively, for the EGV operating at $M_{-\infty} = 0.3$, $\Omega_{-\infty} = 40$ deg. The wave-number magnitudes, $|\boldsymbol{\kappa}_{-\infty}|$, associated with the gusts at $\sigma = -\pi$, -2π and -3π are 5.65, 10.71 and 17.08, respectively, and the arguments relative to the axial flow direction, $\alpha_{-\infty} = \tan^{-1}(\kappa_{\eta,-\infty}/\kappa_{\xi,-\infty})$, are -112.2 deg, -77.8 deg and -67.0 deg, respectively. The vortical gusts are distorted as they are convected by the nonuniform mean flow through the EGV. The vorticity contours in Figure 3.5 and the source term contours in Figure 3.6 indicate

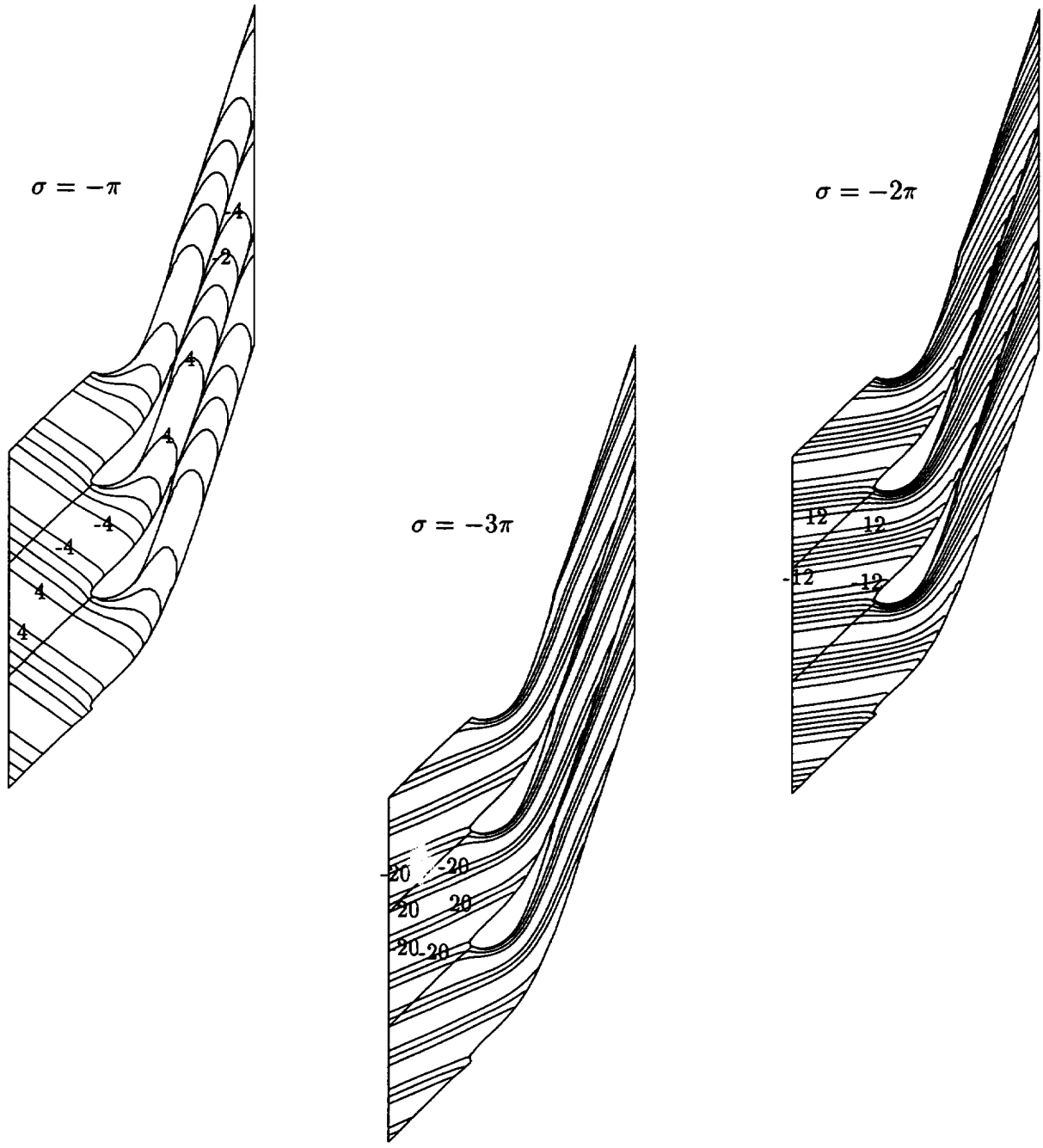

Figure 3.7: Contours of the in-phase component of the unsteady vorticity for the turbine cascade subjected to vortical gusts with $\mathbf{v}_{R,-\infty} \cdot \mathbf{e}_N = (1, 0)$ and $\omega = 5$.

that this distortion increases in severity, i.e., the vorticity and source-term contours are more severely stretched and re-oriented within the blade and wake passages with increasing values of $|\sigma|$. The results in Figure 3.6 reveal the rather strong variations in the source term that

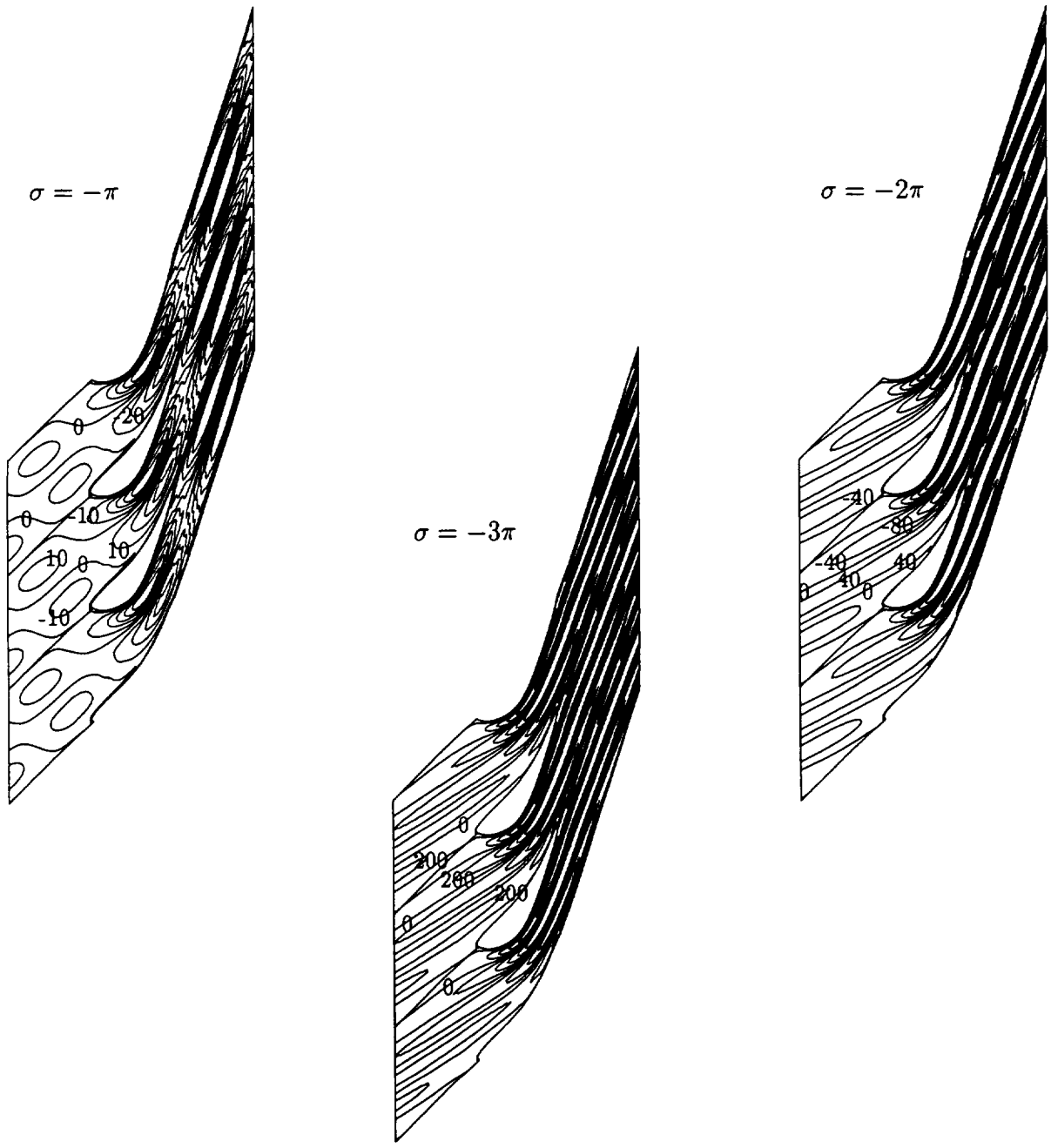

Figure 3.8: Contours of the in-phase component of the source term for the turbine cascade subjected to vortical gusts with $\mathbf{v}_{R,-\infty} \cdot \mathbf{e}_N = (1, 0)$ and $\omega = 5$.

occur over the extended blade passage solution domain, particularly for the gust at $\sigma = -3\pi$.

Similar results for the turbine cascade operating at $M_{-\infty} = 0.19$, $\Omega_{-\infty} = 45$ deg are shown in Figures 3.7 and 3.8 respectively. The wave number magnitudes, $|\boldsymbol{\kappa}_{-\infty}|$, and arguments with respect to the axial-flow direction, $\alpha_{-\infty}$, for the vortical excitations at $\sigma = -\pi$, -2π and -3π

are 5.07, 8.35 and 13.50 and −125.4 deg, −81.8 deg and −66.7 deg, respectively. As indicated in Figures 3.7 and 3.8, the vortical gusts are highly distorted as they are convected past the thick, highly cambered turbine blades. The unsteady vorticity and source term contours for the gusts at $\sigma = -2\pi$ and $\sigma = -3\pi$ are quite different from those for the gust at $\sigma = -\pi$. For $\sigma = -\pi$ the rectilinear vorticity contours far upstream of the blade row evolve into bowed shapes as the gust is carried through the blade row by the mean flow. The vorticity contours, within the passage and far downstream of the blade row, for the gusts at $\sigma = -2\pi$ and $\sigma = -3\pi$ are close to being straight lines. These lie at substantially different orientations than the contours upstream of the blade row. The source term contours in Figure 3.8 are severely distorted for the turbine blade row from mid-blade passage to the downstream boundary of the solution domain, particularly for the vortical gusts at $\sigma = -2\pi$ and $\sigma = -3\pi$. Also, the source terms associated with the gusts at $\sigma = -2\pi$ and $\sigma = -3\pi$ have very large gradients within the blade passage and downstream of the blade row. These features make it difficult to determine an accurate numerical resolution of the unsteady potential, for these turbine unsteady flows.

Velocity Potential

The unsteady potential (ϕ) is determined as a solution of the field equation (3.9) subject to conditions at the mean blade, wake and shock surfaces, and conditions in the far field. Flow tangency [cf. (3.11)] applies at the blade surfaces, the fluid pressure and normal velocity must be continuous [cf. (3.12)] across blade wakes, and mass and tangential momentum must be conserved [cf. (3.13)] across shocks. The velocity potential in the far field is given by (3.19); the potential due to an acoustic excitation at frequency ω and circumferential wave number $\kappa_{\eta,\mp\infty} = \sigma/G$, by (3.20).

A numerical resolution of the linear, variable-coefficient, boundary-value problem for ϕ is required over a single, extended, blade-passage region of finite axial extent. The field equation must be solved in continuous regions of the flow subject to the surface and far field conditions on the unsteady potential. In particular, the near-field numerical solution for the potential must be matched to far-field analytical solutions at finite distances ($\xi = \xi_{\mp}$) upstream and downstream from the blade row. Numerical methods for determining ϕ for isentropic and irrotational (i.e., $s \equiv \zeta \equiv 0$) unsteady, subsonic, transonic, and supersonic flows have been reported in [CV81, VC82, VC84, UV91, MVF94]. Such solutions apply to unsteady flows excited by prescribed blade motions and/or acoustic excitations at inlet and exit. Numerical solution procedures for unsteady flows excited by entropic and/or vortical gusts [VH90, HV91, VBHA91] have been developed and implemented only for subsonic flows. The development of such procedures for transonic and supersonic flows remains, therefore, as a subject for future research.

Because of the stringent and conflicting requirements placed on computational meshes for cascade flows, a composite-mesh (see Figure 3.9), which is constructed by overlaying a polar-type local mesh on an H-type cascade mesh, has been adopted for determining the unsteady potential. The H mesh is used to resolve unsteady phenomena over the entire solution domain; the local surface-fitted mesh, to resolve phenomena in the vicinities of rounded blade leading edges and/or normal shocks. The cascade mesh facilitates the imposition of the phase-lagged, periodicity conditions [cf. (3.10)] and the matching of the analytic and numerical unsteady

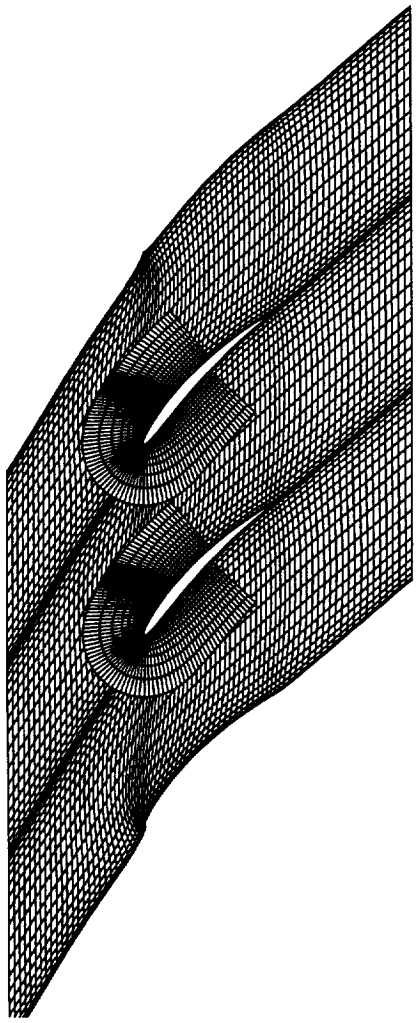

Figure 3.9: Extended blade-passage solution domain and composite mesh used in LINFLO unsteady transonic calculations.

solutions at the far upstream ($\xi = \xi_-$) and far downstream ($\xi = \xi_+$) boundaries of the numerical solution domain. Use of this mesh alone is often sufficient for resolving unsteady subsonic flows, and this has been the strategy applied for calculating the unsteady subsonic solutions for cascade/vortical gust interactions presented in this report. The local mesh allows an accurate modeling of the unsteady flow in the vicinities of blade leading edges and normal shocks. It is constructed so that two "radial" lines coincide with the predicted mean shock locus to provide upstream and downstream shock mesh lines for the accurate imposition of unsteady shock-jump conditions.

Since the cascade and local body-fitted meshes differ topologically, a zonal solution procedure for overlapping meshes has been adopted in [UV91] for determining the unsteady potential. In the region of intersection between the two meshes, i.e., the region covered by the local mesh, certain cascade mesh points are eliminated depending upon their location within the local mesh domain. The discrete equations are written separately for the cascade and local meshes and coupled implicitly through special interface conditions, resulting in a single composite system of finite-difference equations that describe the unsteady flow over the entire

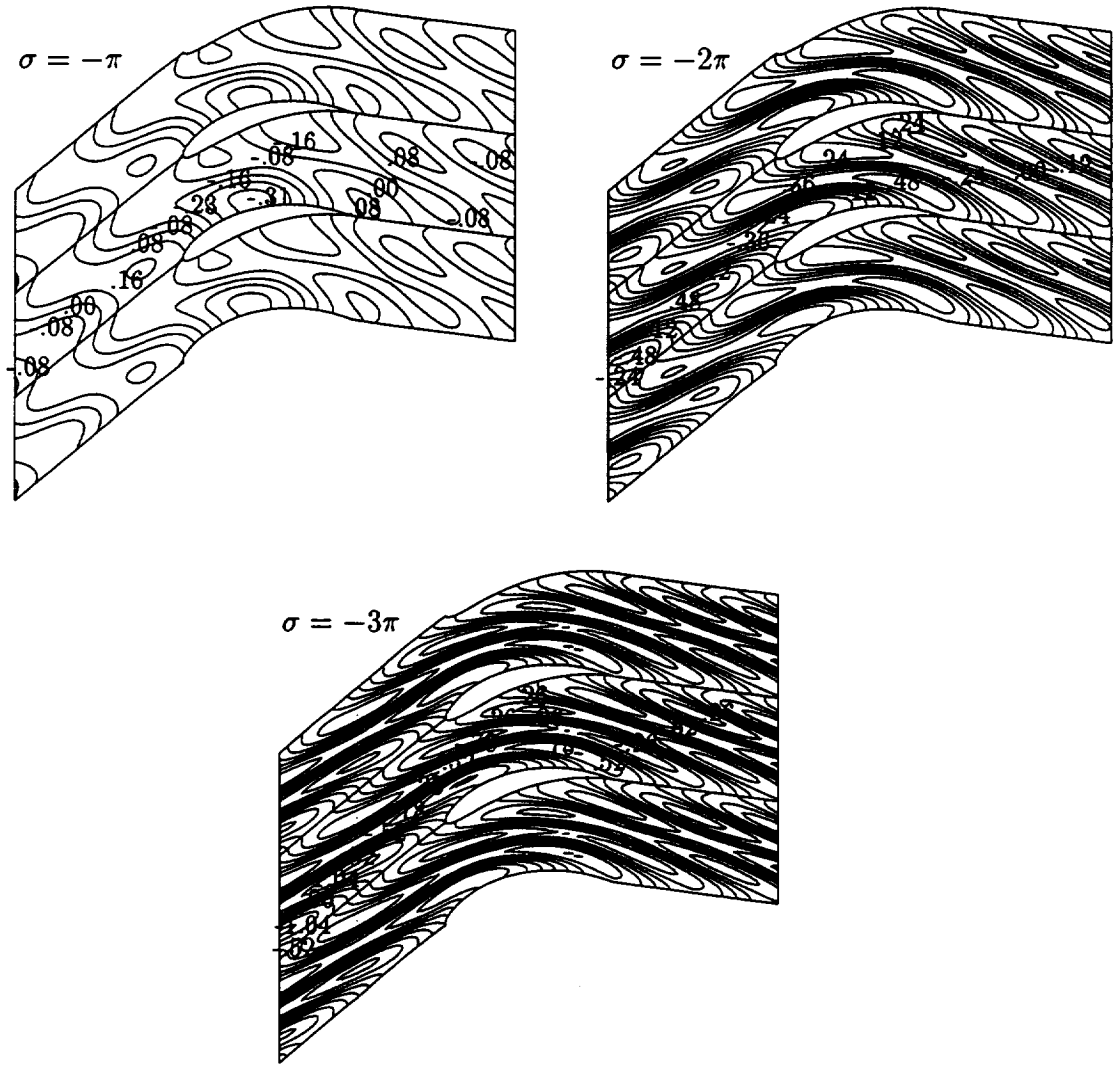

Figure 3.10: Contours of the in-phase component of the unsteady potential for the EGV cascade subjected to vortical gusts with $\mathbf{v}_{R,-\infty} \cdot \mathbf{e}_N = (1, 0)$ and $\omega = 5$.

solution domain.

The finite-difference model used to approximate the unsteady equations on the cascade and local meshes has been described in detail in [CV81]. Algebraic approximations to the various linear operators, which make up the unsteady boundary-value problem, are obtained using an implicit, least-squares, interpolation procedure that is applicable on arbitrary grids. This procedure employs a nine point "centered" difference star at subsonic field points, and a twelve point difference star at supersonic points. At a blade boundary point a nine point one-sided difference star is used on the cascade mesh, whereas nine- or six-point one-sided stars are used on the local mesh. Normal shocks are fitted in the local-mesh calculation by approximating the shock-jump condition (3.13) using one-sided difference expressions to

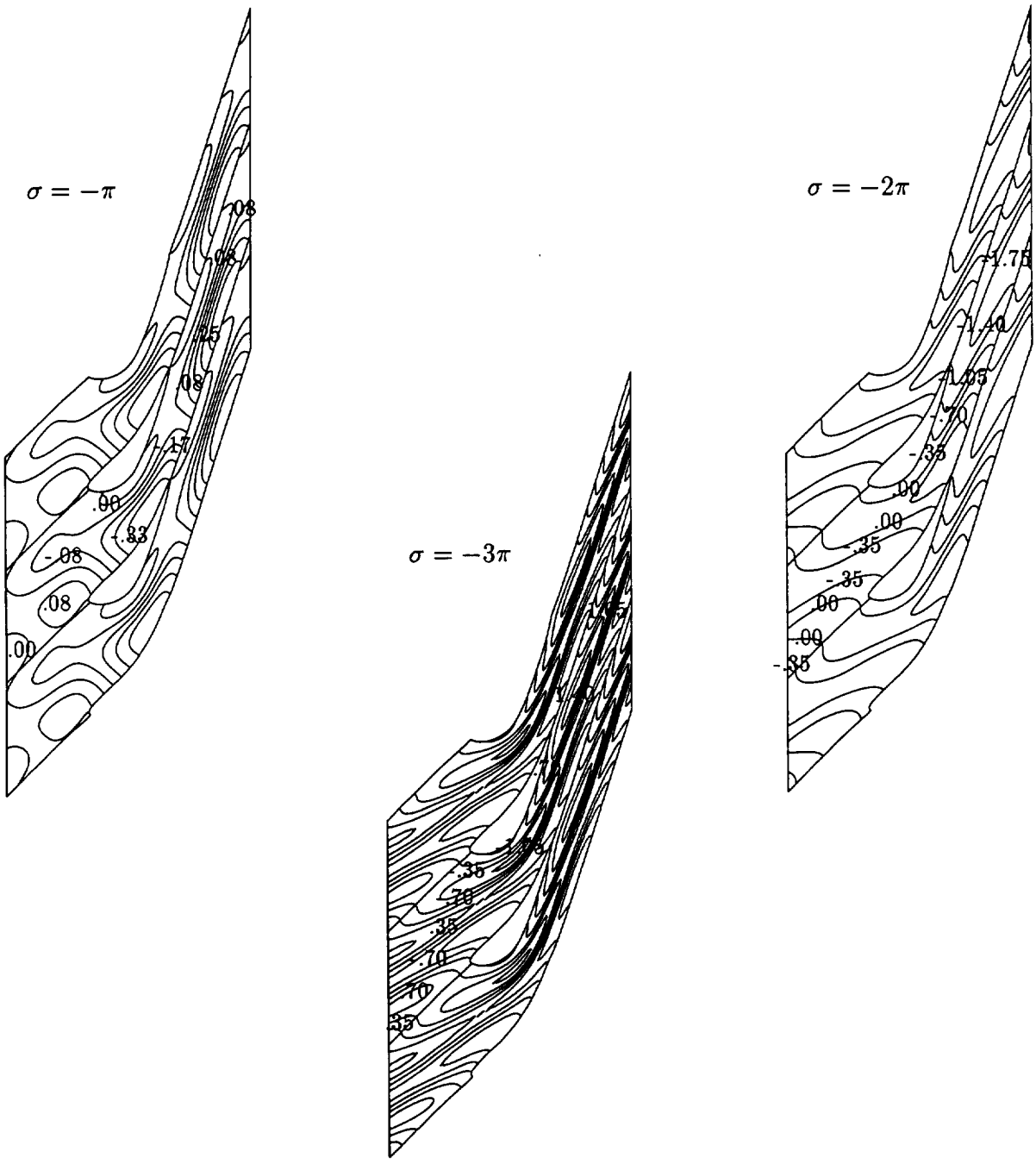

Figure 3.11: Contours of the in-phase component of the unsteady potential for the turbine cascade subjected to vortical gusts with $\mathbf{v}_{R,-\infty} \cdot \mathbf{e}_N = (1, 0)$ and $\omega = 5$.

evaluate the normal derivatives of the unsteady potential on the upstream (supersonic) and downstream (subsonic) sides of the shock. At those points along the shock mesh lines at which the steady flow is continuous (i.e., at points lying beyond the end of the shock), the condition $[\![\phi]\!] = 0$ is imposed.

The systems of linear algebraic equations that approximate the unsteady boundary-value problem on the cascade and local meshes are block-tridiagonal for subsonic flow and, because shocks are fitted, block-pentadiagonal for transonic flow. A subsonic solution on the H-mesh alone is determined using a direct block inversion scheme. Composite (cascade/local) mesh solutions are determined using a different scheme. Because of the cascade/local mesh coupling conditions, the composite system of discrete equations contains a sparse coefficient matrix of large bandwidth. Consequently, special storage and inversion techniques must be applied to achieve an efficient solution. Once the composite system of unsteady equations is cast into an appropriate format, it can be solved using Gaussian elimination [UV91].

The calculated unsteady potential (ϕ) fields associated with the interactions of vortical gusts with the example EGV and turbine configurations are depicted in Figures 3.10 and 3.11, respectively. In particular, contours of the in-phase components of the unsteady potential, $Re\{\phi\}$, are given for vortical gusts at $\mathbf{v}_{R,-\infty} \cdot \mathbf{e}_N = (1,0)$, $\omega = 5$, and $\sigma = -\pi$, -2π and -3π. Vorticity and source-term fields for the unsteady flows through the EGV are shown in Figures 3.5 and 3.6, respectively; those for the flows through the turbine, in Figures 3.7 and 3.8. The potential solutions depicted in Figures 3.10 and 3.11 were determined on 155×40 streamline meshes and show variations over a blade passage that are associated primarily with the source term on the right-hand-side of (3.9). Once the unsteady potential is determined, the complete, linearized, inviscid, unsteady flow problem is solved.

3.3 The Inviscid Response

At this point we have provided a linearized unsteady aerodynamic formulation that describes the general first-order fluid-dynamic perturbation of an isentropic and irrotational mean or steady background flow. We have also outlined the solution procedures used in the LINFLO analysis to determine the unsteady entropy, rotational velocity and velocity potential. Solutions to the linearized unsteady problem are required to determine the aerodynamic response information needed for aeroacoustic and aeroelastic applications, e.g., the unsteady pressure fields far upstream and far downstream of the blade row, and the unsteady pressures acting at the moving blade surfaces. We refer the reader to [Ver89a, Ver92] for detailed derivations of other local and global unsteady aerodynamic response parameters that are used in aeroelastic investigations.

Approximate solutions for the full, nonlinear, time-dependent flow properties are constructed by superposing the results for the steady and the linearized unsteady flow properties, e.g., we can write

$$\tilde{P}(\mathbf{x},t) = P(\mathbf{x}) + \tilde{p}(\mathbf{x},t) + \sum \tilde{P}_{Sh_{m,n}}(\mathbf{x},t) + \dots \ , \tag{3.36}$$

where $\tilde{p}(\mathbf{x}) = \mathrm{Re}\{p(\mathbf{x})\exp(i\omega t)\}$. The first two terms on the right-hand-side of Eq. (3.36) account for the steady and the first-harmonic contributions to the time-dependent fluid pressure acting at the point $\mathbf{x}$. The third term accounts for the anharmonic contribution to the time-dependent pressure caused by the motions of normal shocks, and is determined by analytically continuing the steady solution from the mean to the instantaneous shock locations [Wil79, Ver89a]. Thus, the first-order anharmonic response depends on the jumps, e.g. $[\![P]\!]_{Sh_{m,n}}$, in the steady values of the fluid properties at the mean shock locations and the

unsteady shock displacements normal to the mean shock loci, $\mathcal{R} \cdot \mathbf{n}$, $\mathbf{x} \in Sh_{m,n}$. The regions of anharmonicity are confined to thin strips that contain the mean shock loci.

The steady background flow is described by the velocity potential, Φ, which is determined in terms of a prescribed inlet Mach number ($M_{-\infty}$), flow angle ($\Omega_{-\infty}$), and cascade geometry. The steady velocity, $\mathbf{V} = \nabla\Phi$, is determined from this potential, as are the steady values of the thermodynamic properties of the fluid [cf. (3.2)]. The total enthalpy, $H_T = T + V^2/2$, in the steady background flow is constant and is given by

$$H_T = H_{T,-\infty} = (\gamma - 1)^{-1} M_{-\infty}^{-2} + \frac{1}{2} \tag{3.37}$$

The linearized unsteady flow is described by the time-dependent, first-order, dependent flow variables $\tilde{s}$, $\tilde{\mathbf{v}}_*$, $\tilde{\phi}$ and $\mathcal{R}_{\mathrm{Sh}} \cdot \mathbf{n}$, which are determined in terms of prescribed values of the frequency ω, interblade phase angle σ, and the complex amplitudes, $\mathbf{R}_{\mathrm{B}}$, $s_{-\infty}$, $\zeta_{-\infty}$ and $p_{I,\mp\infty}$, of the imposed unsteady excitation. The first-harmonic unsteady velocity is $\tilde{\mathbf{v}} = \tilde{\mathbf{v}}_* + \nabla\tilde{\phi}$, and the first-harmonic thermodynamic properties of the fluid can be determined in terms of the independent variables $\tilde{s}$ and $\tilde{\phi}$.

It follows from the equation of state for a perfect gas [cf. (2.11)] that

$$\tilde{p} = \gamma^{-1}(\gamma - 1)(\bar{\rho}\tilde{h} + \tilde{\rho}H) \ , \tag{3.38}$$

where $\tilde{h}$ is the linearized unsteady component of the fluid specific enthalpy. After combining (3.38) with the fundamental thermodynamic identity relating the first-order entropy, pressure and density [cf. (2.53)] and recalling that $\tilde{p} = -\bar{\rho}\bar{D}\tilde{\phi}/Dt = -\bar{\rho}(\partial/\partial t + \nabla\Phi \cdot \nabla)\tilde{\phi}$, we find that the first-harmonic flow properties are related by

$$\tilde{\rho}/\bar{\rho} + \tilde{s} = \gamma^{-1}\tilde{p}/P = (\gamma - 1)^{-1}(\tilde{h}/H - \tilde{s}) = -A^{-2}\bar{D}\tilde{\phi}/Dt \ . \tag{3.39}$$

In addition, the first-harmonic total enthalpy, $\tilde{h}_T$, is given by

$$\tilde{h}_T = T\tilde{s} - \bar{D}\tilde{\phi}/Dt + \nabla\Phi \cdot [\tilde{\mathbf{v}}_* + \nabla\tilde{\phi}] + \ \ldots \ . \tag{3.40}$$

The Inviscid Flow Along Moving Blade and Wake Surfaces

The values of the inviscid flow quantities along the moving blade and wake surfaces ($\mathcal{S}$) must be available to perform an analysis of the unsteady flows in the viscous boundary layers and wakes. These can be determined in terms of their values at the mean surface locations (S) and the blade and wake displacements via Taylor series expansions, e.g.,

$$\tilde{P}_{\mathcal{S}} = P_{\mathrm{S}} + \tilde{p}_{\mathrm{S}} + \mathcal{R} \cdot \nabla P|_{\mathrm{S}} + \sum \tilde{P}_{\mathcal{S}h_{m,n}} + \ \ldots \ , \tag{3.41}$$

where $\mathcal{R}$, $\mathbf{x} \in \mathrm{S}$ is the surface displacement vector. In addition, relations between the unit tangent and normal vectors at the instantaneous and mean surface positions, cf. (2.41), are needed to determine the velocity components at the moving surface from information available at the mean surface. Here, the subscript $\mathcal{S}$ refers to points $\mathbf{x}_{\mathcal{S}} = \mathbf{x}_{\mathrm{S}} + \mathcal{R}_{\mathrm{S}}$ on the moving surface, and the subscript S, to the corresponding points $\mathbf{x}_{\mathrm{S}}$ on the mean surface.

If we now restrict our consideration to continuous, i.e., shock-free steady background flows, the unsteady velocity at a moving blade or wake surface is given by

$$\tilde{\mathbf{V}}_{\mathcal{S}} = [\mathbf{V} + \tilde{\mathbf{v}} + (\mathcal{R} \cdot \nabla)\mathbf{V}]_{\mathrm{S}} + \ \ldots = [\nabla\Phi + \tilde{\mathbf{v}}_* + \nabla\tilde{\phi} + (\mathcal{R} \cdot \nabla)\nabla\Phi]_{\mathrm{S}} + \ \ldots \tag{3.42}$$

Expressions for the tangential and normal components of the fluid velocity at a moving blade and wake surface follow from (2.41), (3.42) and the conditions $\nabla\Phi \cdot \mathbf{n}_S = 0$ and $\tilde{\mathbf{v}}_* \cdot \mathbf{n}_S = 0$. We find that

$$\tilde{\mathbf{V}}_{\mathcal{S}} \cdot \boldsymbol{\tau}_{\mathcal{S}} = [\nabla\Phi + \tilde{\mathbf{v}}_* + \nabla\tilde{\phi} + (\boldsymbol{\mathcal{R}} \cdot \nabla)\nabla\Phi]_S \cdot \boldsymbol{\tau}_S + \ \ldots \tag{3.43}$$

and

$$\tilde{\mathbf{V}}_{\mathcal{S}} \cdot \mathbf{n}_{\mathcal{S}} = [\nabla\tilde{\phi} + (\boldsymbol{\mathcal{R}} \cdot \nabla)\nabla\Phi]_S \cdot \mathbf{n}_S + \ \ldots \ = \frac{\partial \boldsymbol{\mathcal{R}}}{\partial t} \cdot \mathbf{n}_S \ . \tag{3.44}$$

The thermodynamic properties at the moving blade and wake surfaces are determined using Taylor series expansions along with the thermodynamic property relations for the steady (3.2) and linearized unsteady (3.39) flows. After performing the necessary algebra, we find that for shock-free flows

$$\frac{\tilde{\rho}_{\mathcal{S}}}{\bar{\rho}_S} + \tilde{s}_S = \frac{\gamma^{-1}\tilde{p}_{\mathcal{S}}}{P_S} = (\gamma-1)^{-1}\left(\frac{\tilde{h}_{\mathcal{S}}}{H_S} - \tilde{s}_S\right) = -A_S^{-2}\left(\frac{\bar{D}\tilde{\phi}}{Dt} + \boldsymbol{\mathcal{R}} \cdot \nabla[(\nabla\Phi)^2/2]\right)_S + \ \ldots \ . \tag{3.45}$$

Finally, the total enthalpy of the fluid at a moving blade or wake is given by

$$H_{T,\mathcal{S}} = [H_T + \tilde{h}_T + \boldsymbol{\mathcal{R}} \cdot \nabla H_T]_S + \ \ldots \ . \tag{3.46}$$

Since the total enthalpy is constant in the steady background flow, i.e., $H_T = H_{T,-\infty}$, and $\nabla\Phi \cdot \tilde{\mathbf{v}}_* = \tilde{s}(\nabla\Phi \cdot \boldsymbol{\tau})^2/2$ at blade and wake mean positions, we can write

$$\begin{aligned} \tilde{H}_{T,\mathcal{S}} &= H_{T,-\infty} + [T\tilde{s} - [\bar{D}\tilde{\phi}/Dt] + \nabla\Phi \cdot (\nabla\tilde{\phi} + \tilde{\mathbf{v}}_*)]_S + \ \ldots \\ &= [H_{T,-\infty}(1+\tilde{s}) - \bar{D}\tilde{\phi}/Dt + \nabla\Phi \cdot \nabla\tilde{\phi}]_S + \ldots \ . \end{aligned} \tag{3.47}$$

Expressions for the anharmonic values of the time-dependent flow properties in the field and at moving blade and wake surfaces can be determined following the methods of [Wil79, Ver89a]. However, for the subsonic inviscid and viscous-layer flows that are of primary concern in the present effort, only the steady and first-harmonic values of the time-dependent inviscid flow properties are required.

3.4 Numerical Results: Cascade/Vortical Gust Interactions

Response predictions will be given below for two-dimensional, unsteady flows excited by prescribed vortical gusts. The intent is to demonstrate further the capabilities added to the linearized inviscid unsteady flow analysis, LINFLO, under Contract NAS3–25425. This analysis will be applied to predict the unsteady pressure responses of the EGV cascade, and a flat-plate counterpart to harmonic, in time and space, vortical excitations at inlet. The two cascades operate at a mean inlet Mach number ($M_{-\infty}$) and flow angle ($\Omega_{-\infty}$) of 0.3 and 40 deg, respectively, and have a blade spacing (G) of 0.6. The blades of the EGV cascade are staggered at $\Theta = 15$ deg; those of the flat-plate cascade are aligned with the mean inlet flow direction, therefore, $\Theta = \Omega_{-\infty} = 40$ deg. The predicted steady Mach number field and blade-surface Mach number distribution for the steady flow through the EGV are shown in Figure 3.1; the drift (Δ) and stream (Ψ) function contours, in Figure 3.3. As noted previously, the calculated exit Mach number, exit flow angle and mean lift force, F_y, acting on each EGV

blade are 0.226, −7.4 deg and 0.360, respectively. The steady background flow through the unloaded ($F_y = 0$) flat plate cascade is uniform with $M = 0.3$ and $\Omega = 40$ deg.

The unsteady flows are excited by vortical disturbances that are convected through the blade row by the steady background flow. A single harmonic component of such a disturbance is described by specifiying the temporal frequency, ω, interblade phase angle, σ, and either the complex amplitude, $\zeta_{-\infty}$, of the vortical excitation or, as is done here, the complex amplitude of the normal component of the rotational velocity, i.e., $\mathbf{v}_{R,-\infty} \cdot \mathbf{e}_N$, that is associated with this vortical excitation. For a pure vortical excitation, the rotational velocity and vorticity are given by (3.30) and (3.32), respectively, with $s_{-\infty} = 0$ and $\mathcal{A}_{-\infty} = \mathbf{v}_{R,-\infty}$. The wave number $\boldsymbol{\kappa}_{-\infty}$ of this excitation is given in terms of the frequency ω, interblade phase angle σ, blade spacing G and inlet flow angle, $\Omega_{-\infty}$, in equation (3.16). For the example flat-plate cascade and far upstream of the EGV cascade, $\mathbf{v}_R(\mathbf{x}) = \mathbf{v}_{R,-\infty} \exp(i\boldsymbol{\kappa}_{-\infty} \cdot \mathbf{x})$ and the complex amplitude of the gust vorticity is $\zeta_{-\infty} = i\kappa_{-\infty}^2 \mathbf{v}_{R,-\infty} \cdot \mathbf{e}_N / \kappa_{T,-\infty}$.

A vortical gust at a given frequency and interblade phase angle can be regarded as a harmonic component of a wake excitation from an upstream blade row. For example, consider an upstream row that has the circumferential blade (wake) spacing G_{EXC} and moves at circumferential velocity $V_{\mathrm{EXC}}\mathbf{e}_\eta$, where V_{EXC} is the wheel speed, relative to the reference row, in our case the EGV or corresponding flat-plate blade row. The circumferential wave number and temporal frequency of the first-harmonic component, i.e., the component at the blade passing frequency (BPF), of the wake excitation are $\kappa_{\eta,-\infty} = -2\pi/G_{\mathrm{EXC}} = \sigma/G$ and $\omega = 2\pi V_{\mathrm{EXC}}/G_{\mathrm{EXC}} = -\sigma V_{\mathrm{EXC}}/G$. Thus, a vortical gust at $\sigma = -\pi$ and $\omega = 5$ represents the first harmonic component of a wake excitation from an upstream blade row having twice the gap or one-half the number of blades ($N_{\mathrm{EXC}} = N_{\mathrm{REF}}/2$) as the reference row. The temporal frequency $\omega = 5$ corresponds to an upstream flow coefficient, i.e., ratio of mean flow axial speed to wheel speed, $V_{-\infty} \cos\Omega_{-\infty}/V_{\mathrm{EXC}}$, of 0.802. In this case the vortical gusts at $\sigma = -\pi n$, $\omega = 5n$, $n = 2, 3, \ldots$, i.e., at $n \times$ BPF, describe the higher harmonic content of the wake excitation. The strengths of the various harmonics are determined by their complex amplitudes, $\mathbf{v}_{R,n,-\infty} \cdot \mathbf{e}_N$. Alternatively, the gusts at $\sigma = -\pi n$, $\omega = 5n$, $n = 2, 3, \ldots$, can be thought of as the first-harmonics of wake excitations associated with upstream blade rows having blade spacings of $G_{\mathrm{EXC}} = 2G/n$ or blade counts of $N_{\mathrm{EXC}} = nN_{\mathrm{REF}}/2$.

In general, for the example EGV and flat-plate cascades operating at an upstream flow coefficient of 0.802, the interblade phase angle and temporal frequency of the mth harmonic of a wake excitation from upstream are

$$\sigma = \pi(2mG/G_{\mathrm{EXC}}) = -\pi n \quad \text{and} \quad \omega = \pi G^{-1} V_W (2mG/G_{\mathrm{EXC}}) = 5n \tag{3.48}$$

Thus, the coefficient $n = 2mG/G_{\mathrm{EXC}} = 2mN_{\mathrm{EXC}}/N_{\mathrm{REF}}$ varies inversely with blade spacing, or directly with the number of blades in the upstream row, and directly with m.

We will examine the response of the EGV and the corresponding flat-plate cascade to vortical gusts with $\mathbf{v}_{R,-\infty} \cdot \mathbf{e}_N = (1, 0)$, $\omega = 5n$ and $\sigma = -\pi n$. The wave-numbers, $\boldsymbol{\kappa}_{-\infty}$, associated with these gusts have magnitudes $|\boldsymbol{\kappa}_{-\infty}| = 5.65n$ and arguments relative to the axial flow direction, $\alpha = \tan^{-1}(\kappa_{\eta,-\infty}/\kappa_{\xi,-\infty})$, of −112.2 deg. The complex amplitudes of the vortical disturbances at inlet are $\zeta_{-\infty} = (0, 6.384n)$. It should be noted that, with the conventions adopted herein, ω and σ must be of opposite sign to model a realistic cascade/vortical gust interaction. We have chosen to set $\omega > 0$, and therefore, σ must be taken to be less than zero.

We will determine the linearized unsteady pressure responses caused by the interactions of vortical gusts at $\omega = 5n$, $\sigma = -n\pi$ $n = 1, 2$, and 3 with the EGV and flat-plate cascades. We will also examine the behaviors of the unsteady aerodynamic lift (f_y) and moment (m) acting on the reference ($m = 0$) blades of the EGV and flat-plate cascades for $0.1 \leq n \leq 5$. It is helpful in interpreting these results to recall that for subsonic flows an unsteady excitation that produces an acoustic response in which all pressure waves attenuate with increasing axial distance from the blade row is termed subresonant. A superresonant (m, n) excitation is one that produces an acoustic response in which m and n pressure waves persist far upstream and far downstream, respectively, and travel away from the blade row. Acoustic resonance occurs if at least one acoustic response wave persists far upstream or far downstream, but travels only circumferentially, i.e., along the blade row, relative to an observer moving at the mean flow velocity.

The linearized unsteady solutions reported below have been determined by performing LINFLO calculations on a global H-type mesh consisting of 40 mean-flow streamlines and 155 "axial" lines, and extending one axial chord upstream and downstream of the blade row. The mesh streamlines were packed near the blade and wake surfaces; the axial lines, near the blade edges. The global mesh analysis is very efficient; for example, a complete unsteady flow calculation on a 155×40 global mesh requires about 2 minutes of CPU time on an IBM 370 work station. Most of the information determined from such a calculation can be saved and re-used in subsequent unsteady flow calculations for different frequencies, interblade phase angles, and modes of excitation, which then require only about 30 seconds of CPU time for each unsteady case. It should be noted that LINFLO composite-mesh calculations typically require four (4) times the CPU time required for a global mesh calculation.

As part of the present study, response predictions, i.e., unsteady pressure difference distributions $[\Delta p(x) = p(\mathbf{x}_B^-) - p(\mathbf{x}_B^+)]$ and unsteady lifts and moments, have also been determined for the flat-plate cascades using the classical linearized analysis of Smith [Smi72]. Recall that in the LINFLO formulation the unsteady potential equation (3.9) contains the source term $\bar{\rho}^{-1}\nabla \cdot (\bar{\rho}\mathbf{v}_*)$, and the normal derivative of the potential, $\nabla\phi \cdot \mathbf{n}$, is zero at the mean blade surfaces. For flat-plate blades aligned with the inlet flow direction the source term reduces to $\nabla^2\phi_*$. In the classical linearization the potential equation is homogeneous, and the normal derivative of the potential cancels the normal component of the gust velocity at the mean blade surfaces. Thus, a comparison between the LINFLO and classical linear solutions is very meaningful, because it reveals the ability of the numerical approximations used in the former analysis, to accurately account for the strong source term variations that occur over the solution domain.

Results for the unsteady flows arising from the interactions of vortical gusts at $\mathbf{v}_{R,-\infty} \cdot \mathbf{e}_N = (1, 0)$, $\omega = 5n$, and $\sigma = \pi n$, with the EGV and flat-plate cascades are shown in Figures 3.12 through 3.18. Contours of the in-phase component or real part of the unsteady vorticity for $\omega = 5$ and $\sigma = -\pi$ and those for the in-phase components of the unsteady pressure responses to the vortical gusts at $n = 1, 2$ and 3 are shown in Figure 3.12 for the EGV and in Figure 3.13 for the flat-plate cascade. Surface pressure responses for the gusts at $n = 1, 2$ and 3 are shown in Figures 3.14–3.16, and the behaviors of the unsteady lift and moment versus n for $0.1 \leq n \leq 5$ are presented in Figures 3.17 and 3.18, respectively.

The contours of the real part of the unsteady vorticity for the interaction of a vortical gust at $\omega = 5$, $\sigma = -\pi$, i.e., at say, the blade passing frequency (BPF), of a wake excitation,

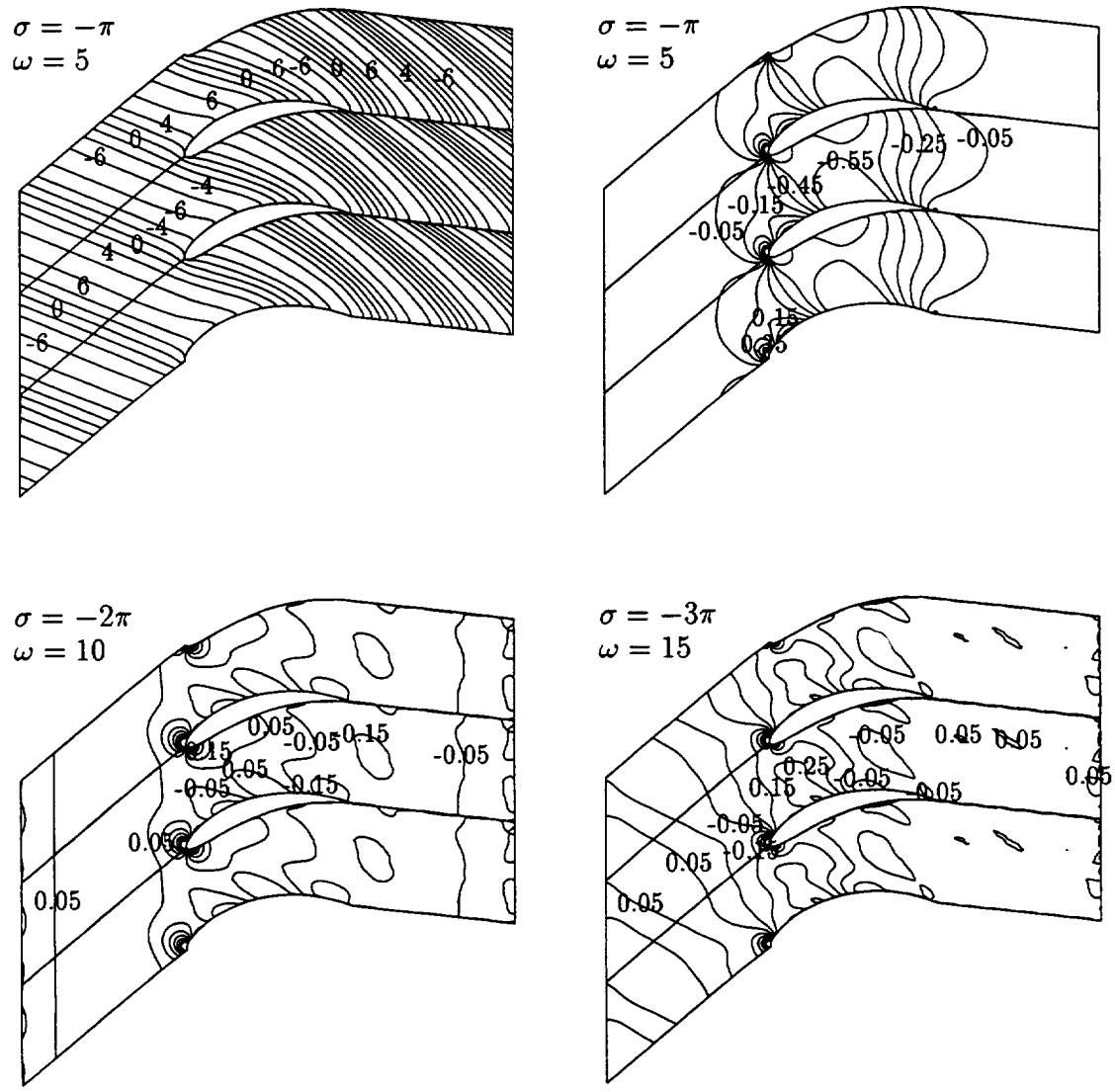

Figure 3.12: Contours of the in-phase components of the unsteady vorticity and the unsteady pressure responses for the EGV cascade subjected to vortical gusts with $\mathbf{v}_{R,-\infty} \cdot \mathbf{e}_N = (1, 0)$.

and the contours of the real parts of the unsteady pressure responses of the EGV to vortical excitations at BPF, twice BPF and three times BPF are shown in Figure 3.12. Although, the complex amplitudes $\zeta_{-\infty}$ and wave number magnitudes $|\kappa_{-\infty}|$ of the vortical gusts vary linearly with n, the vorticity contours associated with the excitations at 2BPF and 3BPF have very similar shapes to those shown in Figure 3.12 for the excitation at BPF. The vortical gusts are convected through the EGV blade row and distorted from the rectilinear pattern that exists far upstream by the nonuniform steady background flow.

The interactions of the vortical gusts with the EGV blading produce unsteady pressure or acoustic responses. The vortical gust at $\omega = 5$ and $\sigma = -\pi$ ($n = 1$) produces a subresonant acoustic response, i.e., all pressure response waves attenuate with increasing axial distance from the blade row. The vortical excitation at 2BPF ($n = 2$) produces a superresonant (1,1)

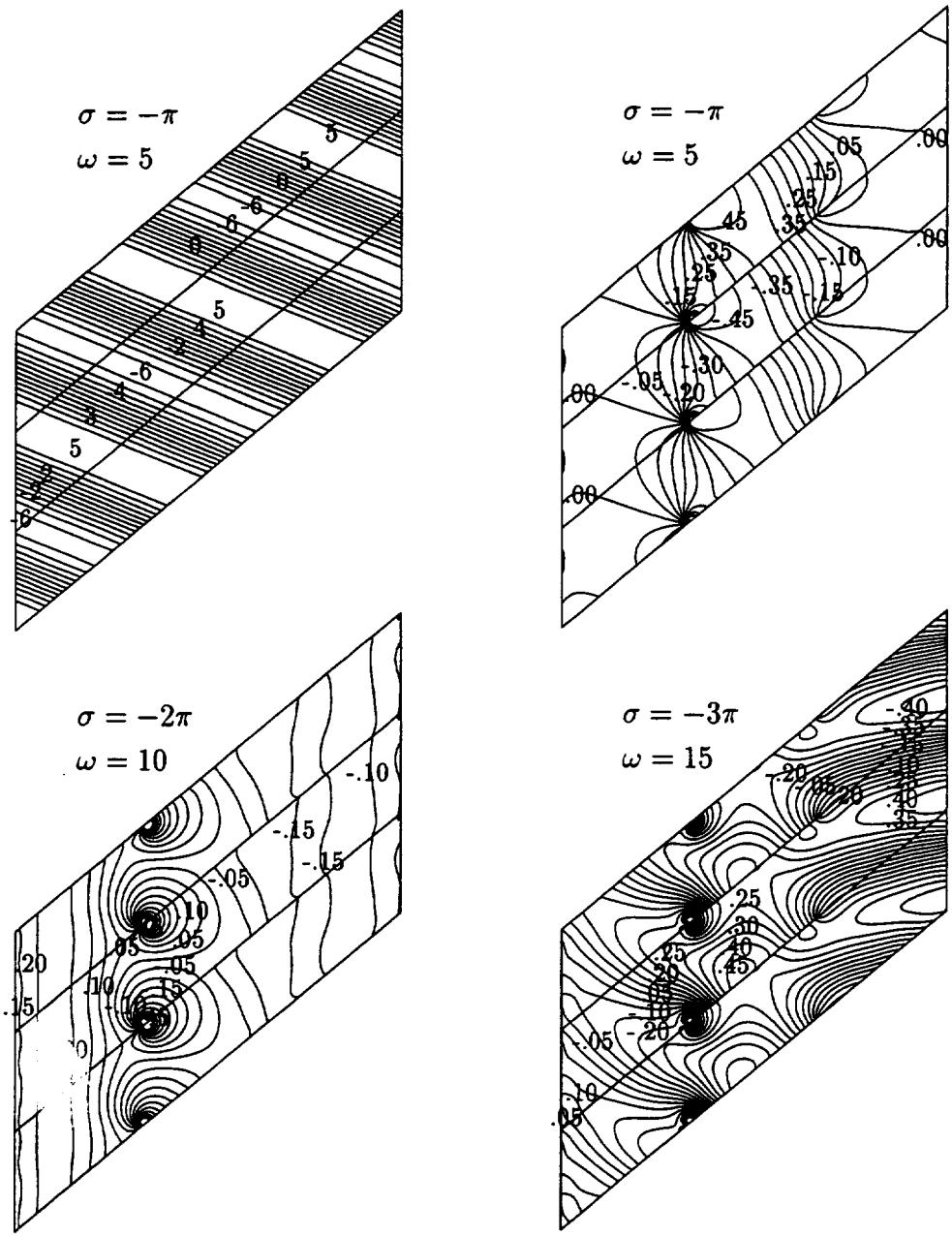

Figure 3.13: Contours of the in-phase components of the unsteady vorticity and the u eady pressure responses for the flat-plate cascade subjected to vortical gusts with $\mathbf{v}_{R,-\infty} \cdot \mathbf{e}_N = (1, 0)$.

response in which a pressure response disturbance, at $\omega = 10$ and $\sigma_1 = \sigma + 2\pi = \kappa_{\eta,1} G = 0$ propagates away from the blade row in both the far upstream and far downstream directions. The axial wave numbers, $\kappa_{\xi,1,\mp\infty}$, of these far upstream and far downstream pressure disturbances are 3.895 and -2.440, respectively, and their amplitudes, $|p_{1,\mp\infty}|$ are 0.119 and 0.120. The vortical excitation at 3BPF (n=3) produces a superresonant (1,0) response in which one.

acoustic response wave at $\omega = 15$, $\sigma_2 = \sigma + 4\pi = \kappa_{\eta,2}G = \pi$ propagates far upstream of the blade row and all other waves attenuate with increasing distance from the EGV blade row. The propagating wave has a wave number vector with magnitude $|\kappa_{2,-\infty}| = 6.325$ and argument, $\alpha_{2,-\infty} = 55.9$ deg relative to the axial flow or positive ξ-direction, and an amplitude $|p_{2,-\infty}| = 0.070$.

Note that spurious pressure behaviors, as indicated in Figure 3.12, are predicted at the upstream and downstream boundaries of the solution domain for the vortical gust at $n = 2$ and at the downstream boundary for the gust at $n = 3$. These behaviors can be attributed to the nonuniform spacings between the mesh streamlines in the global H-meshes used for the LINFLO calculations. The mesh streamlines must be packed near the blade and wake surfaces to resolve the vortical flows near these surfaces, but this packing leads to a loss in accuracy in matching the numerical near-field and analytical far-field solutions for the unsteady potential at the inlet and exit boundaries, and thus, in predicting the complex amplitudes of the far-field acoustic response waves.

The vortical excitation at $\omega = 5$ and $\sigma = -\pi$ and the unsteady pressure responses of the flat-plate blade row to vortical excitations at $\omega = 5n$ and $\sigma = -\pi n$ are shown in Figure 3.13 for $n = 1, 2$ and 3. Note that for flat-plate cascades having blades aligned with the mean flow direction, the vortical gusts are convected through the blade row, without distortion, by the uniform steady background flow. Thus the rectilinear vorticity pattern that exists far upstream of the blade row is maintained throughout the entire flow field. For the flat-plate cascade, the vortical gust at BPF (n=1) produces a subresonant pressure response. The gusts at 2BPF and 3BPF produce superresonant (1,1) responses. At 2BPF acoustic waves at $\omega = 10$ and $\sigma_1 = \sigma + 2\pi = \kappa_{\eta,1}G = 0$ propagate away from the blade row in the negative and positive axial directions. For the upstream propagating wave, $\kappa_{\xi,1,-\infty} = 3.895$ and $|p_{1,-\infty}| = 0.225$; for the downstream propagating wave, $\kappa_{\xi,1,+\infty} = -2.439$ and $|p_{1,+\infty}| = 0.167$. The gust at 3BPF produces upstream and downstream propagating acoustic response waves at $\omega = 15$, $\sigma_2 = \sigma + 4\pi = \kappa_{\eta,2}G = \pi$. For the upstream propagating wave $|\kappa_{2,-\infty}| = 6.325$, $\alpha_{2,-\infty} = 55.9$ deg and $|p_{2,-\infty}| = 0.122$, and for the relatively strong downstream propagating wave, $|\kappa_{2,+\infty}| = 5.308$, $\alpha_{2,+\infty} = 99.5$ deg and $|p_{2,+\infty}| = 0.424$.

The acoustic response behaviors of the EGV and the flat plate cascades to the excitation at $\omega = 15$, $\sigma = -3\pi$ differ in the far-downstream region. The reason for this is that different mean flow conditions prevail far downstream of the two blade rows, which, for the excitation at 3BPF, lead to very different far-downstream acoustic environments. Recall that the EGV operates at an exit Mach number and flow angle of 0.226 and -7.4 deg; the flat plate cascade, at $M_{+\infty} = M = 0.3$ and $\Omega_{+\infty} = \Omega = 40$ deg. A vortical excitation at $\omega = 15$ and $\sigma = -3\pi$, is superresonant (1,0) for the EGV cascade; therefore, a propagating acoustic wave persists far upstream, but all acoustic response waves attenuate with increasing distance downstream. This same excitation produces a superresonant (1,1) acoustic response for the flat-plate blade row, with a relatively strong propagating acoustic response wave in the far downstream field.

Surface pressure responses at the reference ($m = 0$) blades of the EGV and flat-plate cascades are depicted in Figures 3.14–3.16. These results indicate the effects of gust distortion, due to nonuniform mean flow phenomena, on local unsteady blade loading. The surface pressure distributions along the EGV and flat-plate blades for the vortical gusts at BPF (Figure 3.14) and 2BPF (Figures 3.15) show somewhat similar qualitative behaviors, but the EGV results show a more wave-like character and there are important quantitative differences

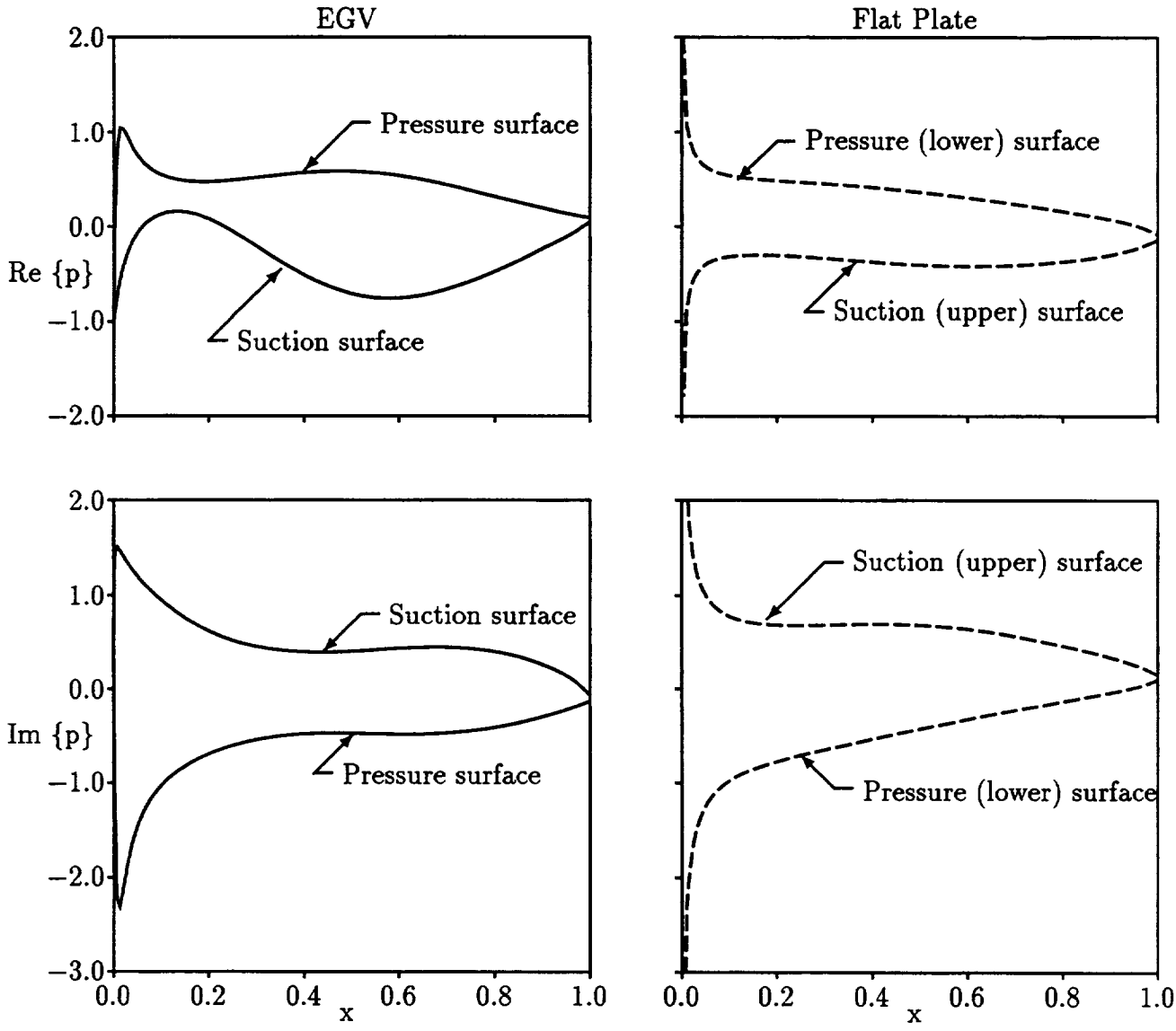

Figure 3.14: Unsteady surface pressure responses of the EGV and corresponding flat-plate cascades to a vortical gust with $\mathbf{v}_{R,-\infty} \cdot \mathbf{e}_N = (1, 0)$, $\omega = 5$ and $\sigma = -\pi$.

between the unsteady loads acting on the two cascades. In contrast, because of the different acoustic response environments that exist far downstream of the two blade rows, the surface pressure responses of the EGV and flat-plate blades to the vortical gust at 3BPF (Figure 3.16) bear little qualitative resemblance.

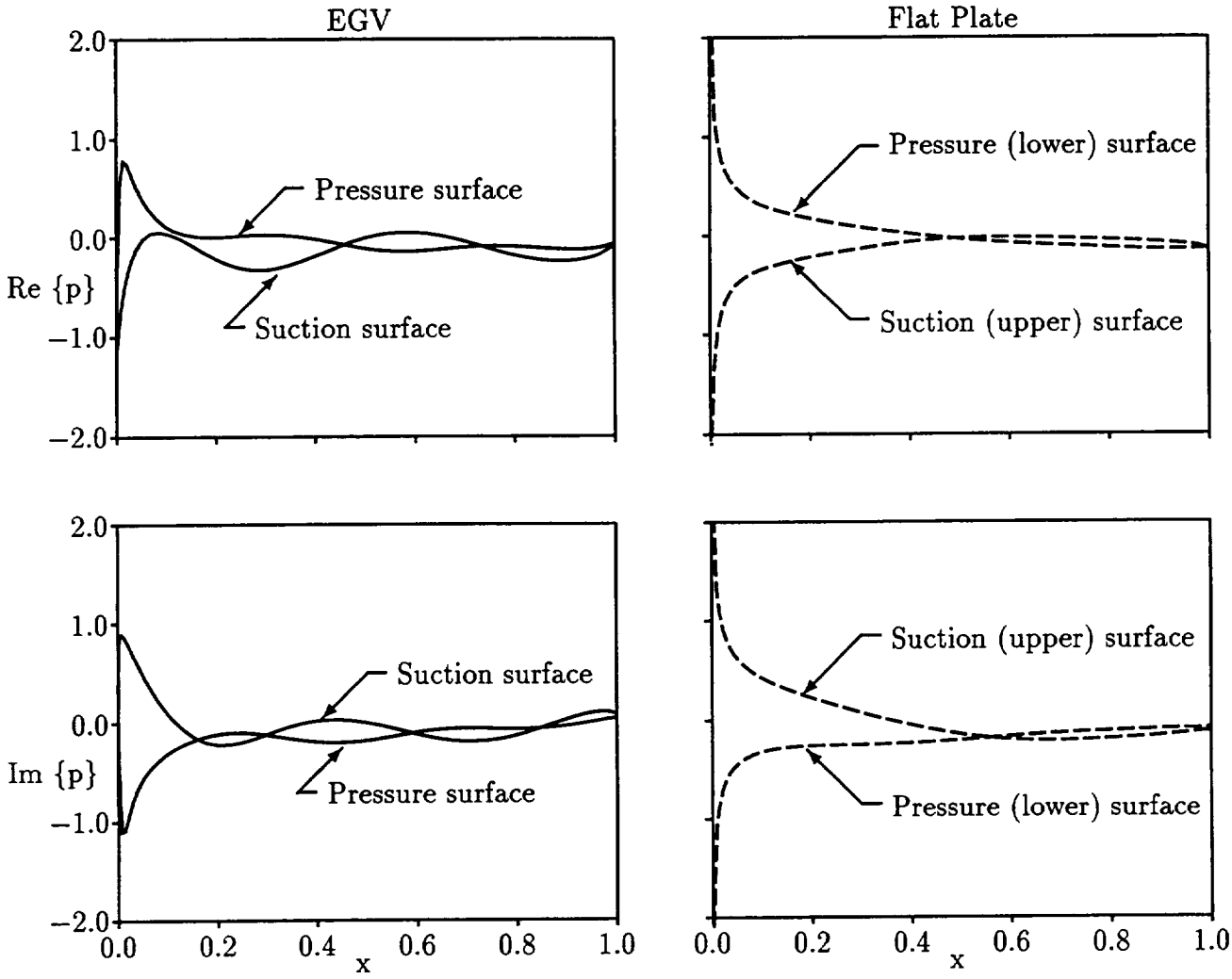

Figure 3.15: Unsteady surface pressure responses of the EGV and corresponding flat-plate cascades to a vortical gust with $\mathbf{v}_{R,-\infty} \cdot \mathbf{e}_N = (1,0)$, $\omega = 10$ and $\sigma = -2\pi$.

The complex amplitudes of the unsteady lift and moment acting on the reference EGV and flat blade blades for the unsteady flows considered in Figures 3.14 through 3.16 are listed below. The unsteady moment is taken about blade midchord.

Vortical Excitation $\mathbf{v}_{R,-\infty} \cdot \mathbf{e}_N = (1,0)$	EGV Cascade	Flat Plate Cascade
$\omega = 5,\ \sigma = -\pi$	$f_y = 0.827, -1.100$	$f_y = 0.732, -1.184$
	$m = -0.014, \quad 0.142$	$m = -0.074, \quad 0.197$
$\omega = 10,\ \sigma = -2\pi$	$f_y = 0.122, -0.141$	$f_y = 0.223, -0.268$
	$m = -0.036, \quad 0.053$	$m = -0.108, \quad 0.115$
$\omega = 15,\ \sigma = -3\pi$	$f_y = -0.010, \quad 0.059$	$f_y = -0.406, \quad 0.074$
	$m = \quad 0.013, \quad 0.020$	$m = -0.066, \quad 0.133$

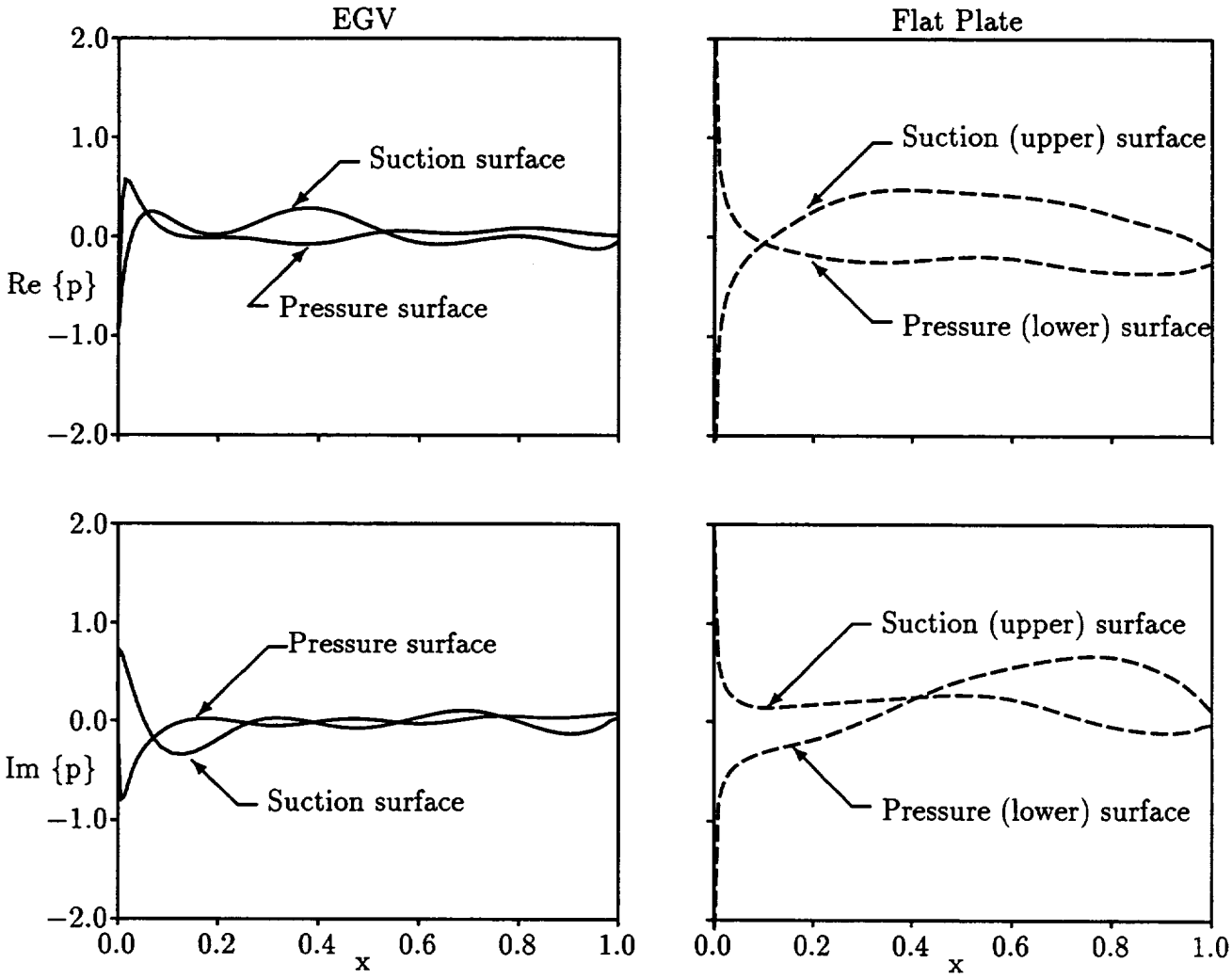

Figure 3.16: Unsteady surface pressure responses of the EGV and corresponding flat-plate cascades to a vortical gust with $\mathbf{v}_{R,-\infty} \cdot \mathbf{e}_N = (1,0)$, $\omega = 15$ and $\sigma = -3\pi$.

These results indicate large differences between the global unsteady airloads, due to vortical gusts, that act on the EGV and the flat plate blades.

We should note that the blade pressure-difference distributions and the aerodynamic lifts and moments predicted by the LINFLO and Smith (CLT) analyses for the flat-plate flows considered in Figures 3.14–3.16 are in excellent agreement. Indeed, the pressure-difference curves predicted by the two analyses are almost coincident for the gusts at $n = 1$ and $n = 2$, and show only slight differences for the gust at $n = 3$.

Predictions for the EGV and flat-plate lift and moment responses for vortical excitations at $\mathbf{v}_{R,-\infty} \cdot \mathbf{e}_N = (1,0)$, $\omega = 5n$ and $\sigma = -\pi n$ are given in Figures 3.17 and 3.18. Here we consider the behaviors of the unsteady aerodynamic lift (f_y) and moment (m) about midchord that act on the reference blades of the EGV and flat-plate cascades versus n, as n varies from 0.1 to 5. LINFLO predictions are given for the EGV and both LINFLO and classical linear theory predictions are given for the flat-plate cascade. The LINFLO and classical linear theory predictions for the lift and moment responses are in excellent agreement. The lift

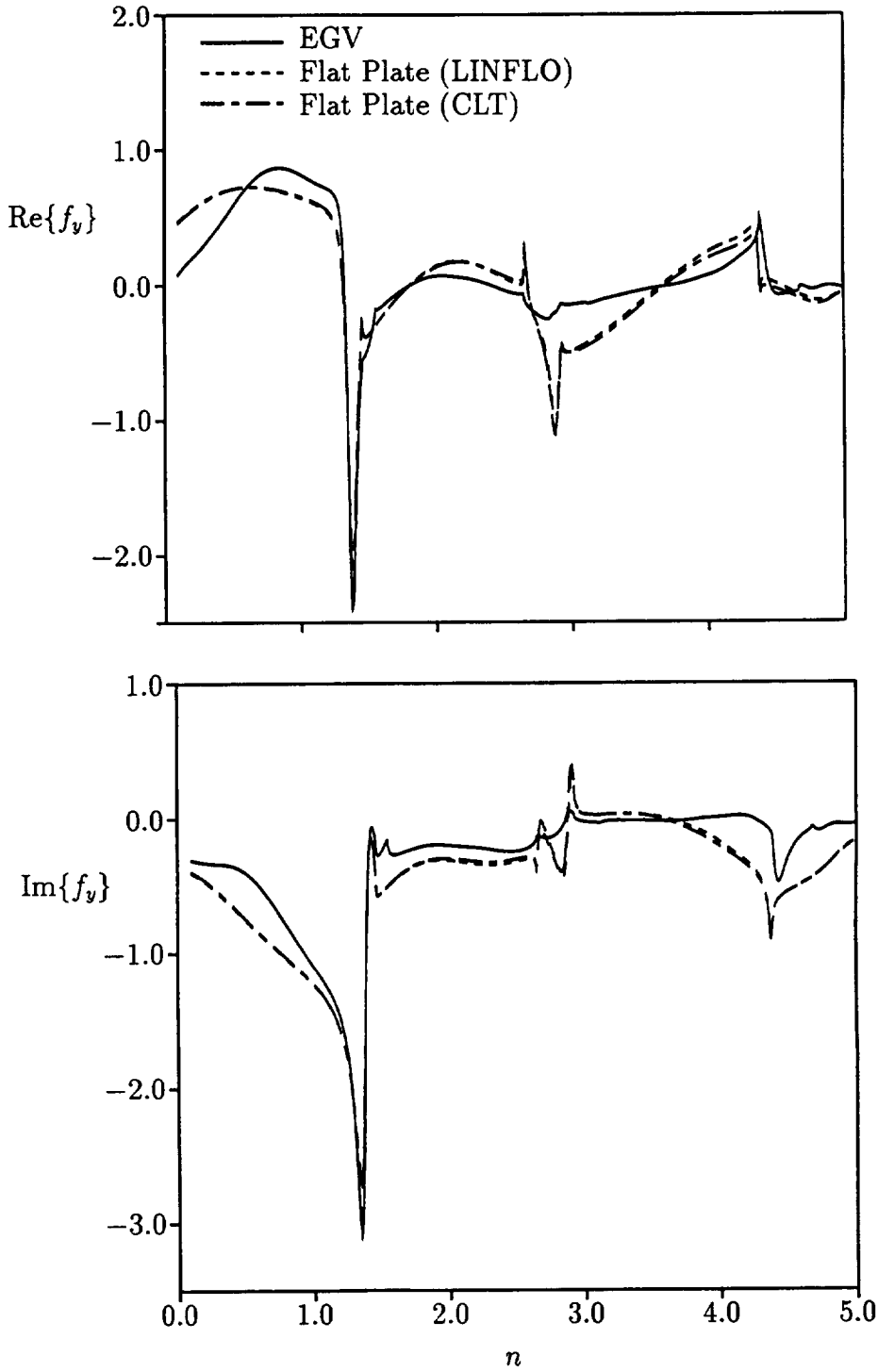

Figure 3.17: Unsteady lift versus n for the EGV and flat plate cascades subjected to vortical gusts at $\mathbf{v}_{R,-\infty} \cdot \mathbf{e}_n = (1, 0)$, $\omega = 5n$, $\sigma = -\pi n$.

forces (Figure 3.17) acting the EGV and flat-plate blades differ, but not substantially, over the entire range $0.1 < n < 5$; however, there are more significant differences between the moments (Figure 3.18) acting on the blades of the two cascades.

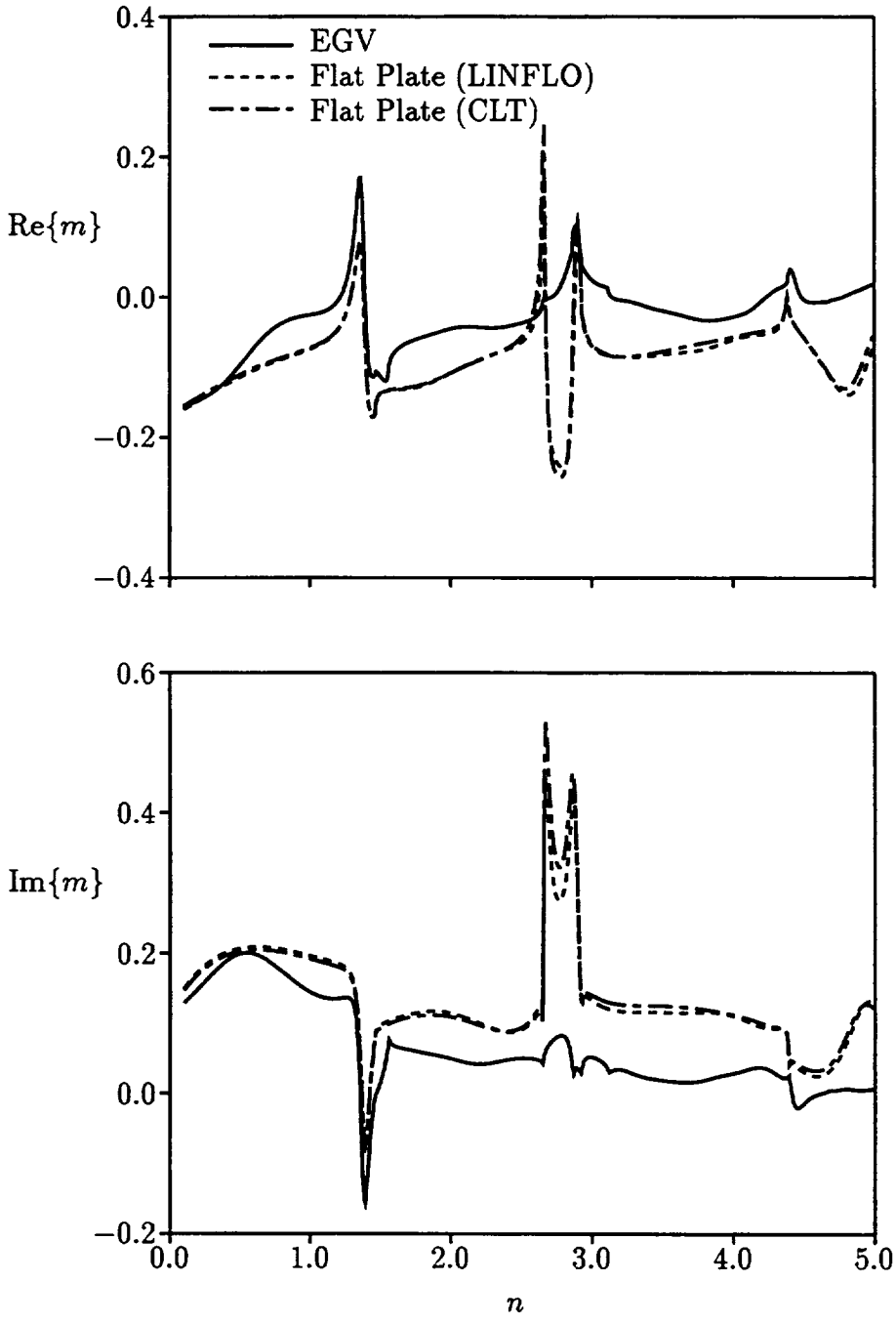

Figure 3.18: Unsteady moment about midchord versus n for the EGV and the corresponding flat plate cascades subjected to vortical excitations at $\mathbf{v}_{R,-\infty} \cdot \mathbf{e}_N$, $\omega = 5n$ and $\sigma = -\pi n$.

It is helpful for interpreting the lift and moment responses indicated in Figures 3.17 and 3.18, to describe the features of the far-field acoustic response for the two cascades. The vortical excitations at $n = 1.463$, 2.688, 2.926 and 4.389 produce an acoustic response disturbance at a cut-off or acoustic resonance condition far upstream of the EGV and both far

upstream and far downstream of the flat plate cascade. The excitation at $n = 2.688$ produces a resonant acoustic response disturbance that travel along the blade row in the positive η-direction; those at n =1.463, 2.926 and 4.389 produce resonant disturbances that travel down the blade row, i.e., in the negative η-direction. Vortical excitations at n =1.558, 2.865, 3.115 and 4.673 produce a cut-off or resonant acoustic reponse disturbance far downstream of the EGV. The resonant response disturbance at n =2.865 travels upward along the blade row; those at n =1.558, 3.115 and 4.673 travel downward. As is readily determined from the curves in Figures 3.17 and 3.18, the unsteady aerodynamic lift and moment undergo abrupt and often large changes in the vicinity of an acoustic resonance condition. Such a condition also represents a boundary for different types of unsteady response behaviors.

For example, the responses of the flat-plate cascade to the vortical excitations in the range $0.1 < n < 5.0$ are subresonant for $n < 1.463$ and $2.688 < n < 2.926$; superresonant (1,1) for $1.463 < n < 2.688$ and $2.926 < n < 4.389$; and superresonant (2,2) for $n > 4.389$. Because the inlet and exit free-stream conditions for the EGV differ, this blade row has a wider variety of far-field acoustic response behaviors than its flat plate counterpart. For example, the acoustic responses of the EGV are superresonant (0,1) for vortical excitations at $2.688 < n < 2.865$; subresonant for $2.865 < n < 2.926$; superresonant (1,0) for $2.926 < n < 3.115$ and superresonant (1,1) for $3.115 < n < 4.389$. The different types of far-field acoustic response behavior seem to have a strong impact on the unsteady blade loads. In particular, the flat plate cascade has large amplitude moment responses to vortical excitations in the range $2.688 < n < 2.926$ which produce subresonant acoustic responses. The moment responses of the EGV to vortical excitations in this range are much smaller in magnitude. The acoustic responses of the EGV are superresonant (0,1) for $2.688 < n < 2.865$ and subresonant for $2.865 < n < 2.926$.

Discussion

This completes our description of the LINFLO analysis and of the capabilities of this analysis, developed under Contract NAS3–25425, to describe cascade/vortical gust interactions. In subsequent sections of this report we will describe a steady inviscid/viscid interaction analysis and an unsteady viscous layer analysis that are being developed for use in conjunction with LINFLO to provide efficient prediction capabilities for unsteady viscous flows. We will also present LINFLO results for unsteady flows caused by prescribed blade motions and acoustic excitations.

The LINFLO analysis represents a powerful analytical capability for efficiently predicting the unsteady aerodynamic information needed in blade row aeroelastic and aeroacoustic response studies, in which many controlling parameters are involved. In recent studies [DV94, AV94] LINFLO has been applied to assist in calibrating modern, time-accurate, Euler/Navier-Stokes analyses. Very good agreement between LINFLO predictions and nonlinear Euler and Navier-Stokes predictions has been determined for unsteady subsonic flows excited by small-amplitude, vortical or acoustic disturbances [DV94] and for unsteady subsonic and transonic flows excited by prescribed blade vibrations [AV94]. Based upon the limited ranges of parametric studies that were conducted using the nonlinear analyses, it was also found that unsteady pressure responses are linear over surprisingly wide ranges of excitation amplitudes. Such results provide evidence on the usefulness of a linearized inviscid, unsteady, aerodynamic analysis for aeroelastic and aeroacoustic design studies.

4. The Steady Inviscid/Viscid Interaction Analysis: SFLOW–IVI

Efficient analyses for predicting the effects of strong inviscid/viscid interaction (IVI) phenomena, due, for example, to viscous-layer separations, shock/boundary-layer interactions and trailing-edge/near-wake interactions, on the aerodynamic, aeroelastic, and aeroacoustic performances of turbomachinery blading are needed as part of a comprehensive analytical design prediction system. The focus here will be on the development of an accurate and efficient IVI analysis for steady cascade flows, that can provide the foundation for an unsteady procedure to be developed later. The steady analysis is described below and is being developed as part of an overall research program, which has the goal of providing reliable and efficient theoretical prediction methods for steady and unsteady viscous flows, at high Reynolds numbers, through subsonic and transonic cascades.

The present steady analysis uses an inviscid/viscid interaction (IVI) approach, in which the flow in the outer inviscid region is assumed to be potential, and the flows in the inner or viscous-layer regions are governed by Prandtl's viscous-layer equations. The inviscid equations are solved using a Newton iteration procedure and an implicit, least-squares, finite-difference approximation, similar to that used in LINFLO. The viscous-layer equations are solved using a modified Levy-Lees transformation and an inverse, finite-difference, space-marching method, which is applied along the blade surfaces and the wake streamlines. Complete details on the inviscid and viscous solution procedures can be found in [HV93, HV94] and [BVA93a], respectively. The inviscid and viscid solutions are coupled via a semi-inverse global iteration procedure that permits the prediction of boundary-layer separation and other strong-interaction phenomena. Numerical results will be presented below for the three example cascades described in § 2.5 with a range of inlet flow conditions considered for one of them, including conditions leading to large-scale flow separations. Comparisons with Navier-Stokes solutions and experimental data will also be given.

4.1 General Concepts

For the flows of practical interest in either internal or external aerodynamics, the Reynolds number is usually sufficiently high so that the flow past an airfoil or blade can be divided into two regions: an "inner" dissipative region consisting of boundary layers and wakes, and an "outer" inviscid region. The principal interaction between the flows in the viscid and inviscid regions arises from the displacement thickness effect which leads to thickened semi-infinite equivalent bodies with corresponding changes in surface pressures.

If the interaction is "weak," then the complete flow problem can be solved sequentially. In this case the pressure distributions along the blades and wakes are first determined by a pure inviscid solution. These distributions are then imposed when solving the viscous-layer equations to determine viscous displacement thickness, $\bar{\delta}(\tau)$, distributions along the blades and wakes. The latter are then used to obtain a new inviscid solution, that accounts for viscous displacement effects. The resulting changes in the blade pressure distributions and in the downstream freestream flow properties (e.g., Mach number and flow angle) can then be calculated. It is sometimes possible to continue this sequential solution procedure until a converged solution for the entire flow is achieved.

Flows over airfoils or blades, however, involve both a weak overall interaction arising from standard displacement thickness and wake curvature effects, and local strong-displacement interactions caused, for example, by viscous-layer separations, shock/boundary-layer interactions, and trailing-edge/near-wake interactions. Viscous displacements in a strong-interaction region can cause substantial changes in the local inviscid pressure and, in some cases, in the overall pressure field. The concept of an inner viscous region and an outer inviscid region still applies, but the classical hierarchical structure of the flow breaks down. In particular, for flows with strong interactions the inviscid/viscid hierarchy changes from "direct", in which the pressure is determined by the inviscid flow, to "interactive" in which the pressure is determined by the mutual interaction between the flows in the inviscid and the viscous-layer regions. This change must be accommodated within an inviscid/viscid interaction solution procedure.

The construction of an IVI analysis involves, first, the development of component, i.e., inviscid and viscous-layer analyses, and, second, the implementation of these components into a strong-interaction iteration procedure to produce a solution for the complete flow field. Solution methods for steady subsonic and transonic inviscid flows through cascades (e.g., see [Cas83, HV94]) and for steady boundary-layer and wake flows (e.g., [VV85] and [BV87]) have been developed to a relatively mature state. Methods for coupling such solutions have also been developed and assessed through a number of model problem studies (e.g., see [Vel80, VV85, BV87]). Inviscid/viscid interaction procedures for predicting steady flows in cascades have also been developed [HSS79, JH83, CH80, BV89, BHE91] and applied over a wide range of inlet flow conditions, including conditions leading to stall [BHE91].

In the present approach we consider high Reynolds number ($Re = \bar{\rho}^*_{-\infty} V^*_{-\infty} L^* / \bar{\mu}^*_{-\infty}$) steady flow, with negligible body forces, of a perfect gas with constant specific heats and Prandtl number through a two-dimensional cascade (cf. Figures 2.1 and 2.3). In particular, we will restrict our consideration to adiabatic flows at unit Prandtl number, however, it is a relatively simple matter to extend the analysis to heat conducting flows at arbitrary Prandtl numbers. The flow in the outer inviscid region is assumed to be isentropic and irrotational and hence, governed by the full-potential equation; those in the inner viscous-layer regions, by Prandtl's viscous-layer equations. The non-hierarchical nature of strong interactions is taken into account by the procedure used to couple the inviscid and viscid solutions. In addition, an inverse viscous-layer calculation, in which the displacement thickness is specified instead of the pressure, is employed to permit viscous solutions to be continued through local strong-interaction regions, including regions of separated flow. In regions of the flow where the inviscid/viscid interactions are weak, the pressure, as determined from the inviscid solution, can be imposed, instead of the displacement thickness, to obtain a direct viscous-layer solution.

In the present approach, the steady, cascade, full-potential analysis (SFLOW) developed by Hoyniak and Verdon [HV93, HV94] is employed to determine the flow in the inviscid region. SFLOW has been constructed for use with the linearized inviscid unsteady flow analysis, LINFLO, to provide compatible and comprehensive steady and unsteady inviscid flow prediction capabilities for cascades. In the IVI calculation procedure (which is referred to as SFLOW–IVI), viscous effects are incorporated by modifying the blade and wake boundary conditions used in SFLOW to account for the effects of viscous displacement. The nonlinear inviscid analysis, coupled with the IVI iteration procedure, allows nonlinear changes to the inviscid base flow due to viscous effects to be evaluated. The ability to treat such nonlinear

perturbations is especially important in transonic flows in which shock positions and strengths are significantly altered by viscous displacements. Although the analysis described below is presently restricted to subsonic flows, it can be extended to treat transonic flows in the future.

4.2 Inviscid/Viscid Interaction Analysis

Inviscid Region

The flow in the inviscid region is determined as a solution of the field equations (3.1) and (3.2) subject to flow tangency conditions at the blade surfaces, jump conditions on the normal velocity and pressure across the blade wakes, and prescribed uniform flow conditions far upstream of the blade row. Blade-to-blade periodicity conditions [cf. (2.42)] are applied upstream and downstream of the blade row to limit the computational domain to a single, extended, blade-passage. Kutta conditions at the blade trailing edges and a global mass conservation condition that relates the flows at the inlet and exit boundaries and accounts for the blockage effects of the viscous layers are enforced in lieu of specifying the uniform flow far downstream of the blade row. For the flows considered here, the inlet and exit velocities are subsonic.

The field equation (3.1) can be written in the form

$$A^2\nabla^2\Phi - \nabla\Phi\cdot\nabla(\nabla\Phi)^2/2 = 0 \tag{4.1}$$

where the speed of sound propagation A is given in terms of the potential Φ in (3.2). The SFLOW inviscid analysis is based on this non-conservative form of the full potential equation.

The specific forms of the blade and wake conditions for the potential steady flow in the inviscid region can be determined by setting $\mathbf{V} = \nabla\Phi$ in (2.47) and (2.48). Thus, at each blade surface

$$\nabla\Phi\cdot\mathbf{n} = \bar{\rho}_e^{-1}d(\bar{\rho}_e V_{\tau,e}\bar{\delta})/d\tau \ , \quad \text{for} \quad \mathbf{x}\in \mathrm{B}_m \ , \tag{4.2}$$

where $\bar{\rho}_e$ and $V_{\tau,e} = \partial\Phi/\partial\tau|_e$ are the inviscid density and velocity at this surface, or the viscous density and streamwise velocity component at the edge of the viscous layer, and $\bar{\delta}$ is the boundary-layer displacement thickness (see Figure 2.3). The quantities τ and $\mathbf{n}$ denote the arc distance along the blade (positive in the downstream direction and zero at the leading-edge stagnation point) and the local unit normal vector directed outward from the surface, respectively. At the blade wakes the inviscid solution for the normal component of the fluid velocity and the pressure must be discontinuous with jumps given by

$$[\![\nabla\Phi]\!]\cdot\mathbf{n} = \langle\bar{\rho}_e^{-1}d(\bar{\rho}_e V_{\tau,e}\bar{\delta})/d\tau\rangle \quad \text{and} \quad [\![P]\!] = \bar{\kappa}\langle\bar{\rho}_e V_{\tau,e}^2(\bar{\delta}+\bar{\theta})\rangle \ , \quad \text{for} \quad \mathbf{x}\in W_m \ , \tag{4.3}$$

where $\mathbf{n}$ is the upward pointing unit normal vector to the reference wake streamline (i.e., W in Figure 2.3), $\langle\bar{\delta}\rangle = \bar{\delta}_W$ and $\langle\bar{\theta}\rangle = \bar{\theta}_W$ are the displacement and momentum thicknesses of the complete wake, and $\bar{\kappa}$ is the curvature of the wake which is taken as positive when the reference wake streamline is concave upwards.

As mentioned in § 2.3, a complication arises in that the location of the reference wake streamline is unknown *a priori*; however, to within lowest order, the wake conditions can be referenced to any arbitrary curve emanating from the trailing edge and lying within the actual viscous wake [Vel80]. Usually, wake curvature effects are regarded as negligible. In this case

the inviscid pressure, density and tangential velocity are continuous across blade wakes, and the wake conditions (4.3) reduce to

$$[\![\nabla\Phi]\!]\cdot\mathbf{n} = \bar{\rho}d(\bar{\rho}_e V_{\tau,e}\bar{\delta}_W)/d\tau \quad \text{and} \quad [\![P]\!] = 0,\ \mathbf{x}\in W_m\ . \tag{4.4}$$

For steady flows, the reference wake streamline is taken to be the aft stagnation streamline as determined by a pure inviscid solution. This is adequate except in extreme cases where the location of the stagnation streamline is significantly altered by viscous effects. In this case, it is possible to periodically update the location of the wake streamline during the calculation, although this has not been done in the present study.

The foregoing boundary-value problem is solved using a Newton iteration procedure. Thus, we set

$$\Phi_{n+1} = \Phi_n + \bar{\phi}_n, \quad n = 0,1,2,\ldots \tag{4.5}$$

where Φ_n is the estimate to the final solution at the nth iteration level and $\bar{\phi}_n$ is a correction to this estimate. The quantity $\bar{\phi}_n$ is determined at each step of the iteration process by solving linear equations that are derived by substituting (4.5) into (4.1)–(4.3) and neglecting terms that are of second and higher order in $\bar{\phi}_n$. For example, the linear field equation for the correction, $\bar{\phi}_n$, is

$$A_n^2\nabla^2\bar{\phi}_n - (\gamma-1)\nabla^2\Phi_n\frac{\bar{D}\bar{\phi}_n}{Dt} - \frac{\bar{D}^2\bar{\phi}_n}{Dt^2} - \nabla(\nabla\Phi)^2\cdot\nabla\bar{\phi}\ /2 = -A_n^2\nabla^2\Phi_n + \nabla\Phi_n\cdot\nabla(\nabla\Phi_n)^2/2\ , \tag{4.6}$$

where A_n, the nth estimate to the speed of sound propagation, is determined from (3.2) with Φ replaced by Φ_n and $\bar{D}/Dt = \nabla\Phi_n\cdot\nabla$. The right-hand side of (4.6) is known and the linear operator on the left-hand side is readily derived from the linear unsteady operator appearing on the left-hand side of (3.9). The various equations used to determine ϕ_n are approximated using the same implicit, least-squares, finite-difference approximations as those used in the LINFLO analysis. The resulting linear system of algebraic equations that approximate the linear boundary value problem for $\bar{\phi}_n$ is solved by direct matrix inversion, as in LINFLO, using lower-upper decomposition and Gaussian elimination. The Newton iterations are continued until $||\bar{\phi}_n|| < \hat{\epsilon}$, where $||\quad||$ denotes a prescribed norm and $\hat{\epsilon} << 1$ is a user specified tolerance level. This nonlinear steady analysis, called SFLOW, is described in detail in [HV93, HV94].

The present inviscid solutions were obtained on a "streamline" type H-mesh, rather than on the "sheared" H-mesh described in [VC84] and [HV93]. The SFLOW analysis was modified by Hoyniak to use the streamline H-mesh developed by Hall and Verdon [HV91]. Thus, prior to initiating an IVI calculation, a pure inviscid solution is first obtained on a sheared H-mesh. The resulting solution is then used to generate a streamline H-mesh, in which one set of mesh lines corresponds to the streamlines of the inviscid flow, and the second set consists of lines that are "nearly" orthogonal to the first set. The principal advantage of the streamline H-mesh over the sheared mesh is an improved resolution of the flow in the vicinities of blade leading edges.

An alternative to this procedure is available in SFLOW and was used for one of the cases described in this report, i.e., the turbine cascade. In the turbine case, a useful streamline H-mesh could not be determined from the solution on a sheared H-mesh, because the latter provided an inadequate resolution of the flows at blade leading-edges. To remedy this, the initial inviscid solution was obtained on a composite mesh constructed by overlaying a local,

surface-fitted, C-mesh on a global sheared H-mesh. A detailed description of this procedure, as applied to linearized unsteady flows, can be found in [UV91].

Viscous Layers

The flows in the inner or viscous regions are assumed to be governed by Prandtl's viscous-layer equations [cf. (2.28)–(2.32)]. For steady flows ($\partial\,/\partial t|_{\mathbf{x}} \equiv 0$ and $\tilde{P} = P$, $\tilde{\bar{\rho}} = \bar{\rho}$, etc.) the continuity and streamwise momentum equations have the form

$$\frac{\partial(\bar{\rho}V_\tau)}{\partial\tau} + \frac{\partial(\bar{\rho}V_n)}{\partial n} = 0 \tag{4.7}$$

and

$$\bar{\rho}\left[V_\tau\frac{\partial V_\tau}{\partial\tau} + V_n\frac{\partial V_n}{\partial n}\right] - \bar{\rho}_e V_{\tau,e}\frac{dV_{\tau,e}}{d\tau} = (Re)^{-1}\frac{\partial}{\partial n}\left(\bar{\mu}_{\text{eff}}\frac{\partial V_\tau}{\partial n}\right) . \tag{4.8}$$

We assume that the flow in the viscous layer is adiabatic and occurs at unit Prandtl number. In this case the energy equation, cf. (2.30), reduces to the requirement that the total enthalpy of the fluid, $H_T \approx T + V_\tau^2/2$, must be constant across the viscous layer.

In equation (4.8) the subscript e refers to fluid properties at the edge of the viscous layer, and the effective viscosity, $\bar{\mu}_{\text{eff}}$, is defined to be

$$\bar{\mu}_{\text{eff}} = \bar{\mu} + \bar{\epsilon} , \tag{4.9}$$

where $\bar{\mu}$ is the molecular viscosity, which is assumed to be a function of temperature alone, $\bar{\epsilon} \propto \gamma_{T_\tau}$ is the turbulent eddy viscosity, and $\bar{\gamma}_{T_\tau}$ is the streamwise intermittency factor. In the present study, the molecular viscosity, $\bar{\mu}$, is determined by Sutherland's equation (2.10); the eddy viscosity in blade boundary layers, using the Cebeci-Smith model [CS74], as modified in [BV87] to account for flow separation; and the eddy viscosity in wakes, using the model of Chang, et al. [CBCW86]. The specific turbulence model, used in the present study, is described in detail in § 5.1. For the present IVI calculations, instantaneous transition, i.e., $\bar{\gamma}_{T_\tau}$ changes abruptly from 0 to 1, is assumed to occur at specified locations along the blade surfaces.

The foregoing field equations govern the flow in the viscous layers along the upper and lower surfaces of the blades and in the blade wakes. They are solved subject to conditions at the edges of the viscous layers, on the blade surfaces, and along the reference wake streamlines, i.e.,

$$V_\tau \to V_{\tau,e} \quad \text{for } n \to \infty\ ,\ \tau \geq 0\ , \tag{4.10}$$

$$V_\tau = V_n = 0 \quad \text{for } n = 0,\ 0 \leq \tau \leq \tau_{TE}^{\pm} \tag{4.11}$$

and

$$V_n = 0 \quad \text{for } n = 0,\ \tau > \tau_{TE}^{\pm}\ , \tag{4.12}$$

respectively, where $\tau_{TE}^{\pm}$ are the trailing-edge values of the upper- (+) and lower-surface (−) arc-length coordinates measured from the leading-edge stagnation point. The condition expressed by (4.10) is also applied along a wake streamline for $n \to -\infty$. Equations (4.11) and (4.12) imply that the curve $n = 0$ corresponds to the blade surfaces and reference wake streamlines, respectively.

The displacement ($\bar{\delta}$) and momentum ($\bar{\theta}$) thicknesses of the viscous layers are needed to determine the effects of viscous displacement and wake curvature on the outer inviscid flow. For steady flows, these quantities are determined by [see also (2.37) and (2.38)]

$$\bar{\delta}(\tau) = \int_0^\infty \left(1 - \frac{\bar{\rho}V_\tau}{\bar{\rho}_e V_{\tau,e}}\right) dn \tag{4.13}$$

and

$$\bar{\theta}(\tau) = \int_0^\infty \frac{\bar{\rho}V_\tau}{\bar{\rho}_e V_{\tau,e}} \left(1 - \frac{V_\tau}{V_{\tau,e}}\right) dn \ , \tag{4.14}$$

where the zero lower bound on the integrals is replaced with $-\infty$ when determining the displacement and momentum thicknesses of a wake.

Levy-Lees Transformation

To facilitate the numerical resolution of the viscous-layer equations we introduce a modified version [BV87] of the Levy-Lees transformation [Blo70]. Thus, we define new independent variables

$$\xi = \int_0^s \bar{\rho}_e V_{\tau,e} \bar{\mu}_{\text{eff},e} d\tau \quad \text{and} \quad \eta = (Re/2\xi)^{1/2} V_{\tau,e} \int_0^n \bar{\rho} dn \ , \tag{4.15}$$

and new dependent variables

$$F = V_\tau / V_{\tau,e} \quad \text{and} \quad f = (Re/2\xi)^{1/2} \Psi \ . \tag{4.16}$$

Here ξ and η are scaled streamwise and normal spatial coordinates, F is the ratio of the local to the edge value of the streamwise velocity, and f is a scaled stream function for the flow in the viscous layer. The quantity $\mu_{\text{eff},e}(\tau)$ in (4.15) is the effective viscosity at the edge of the viscous layer. It is used in the definition of ξ to maintain a nearly constant value of η at the edge of a turbulent viscous layer [VWV82]. The variable Ψ in (4.16) is the stream function of the flow; therefore, $\partial\Psi/\partial n = \bar{\rho}V_\tau$ and $\partial\Psi/\partial\tau = -\bar{\rho}V_n$. The Levy-Lees transformation permits the leading-edge, stagnation-point, laminar, similarity solution to be easily recovered and leads to a reduced truncation error in the numerical approximation to the viscous-layer equations relative to that associated with an analysis based on the use of primitive flow variables.

After applying the transformation relations (4.15) and (4.16), we find that the continuity (4.7) and momentum (4.8) equations can be written as

$$F = \frac{\partial f}{\partial \eta} \tag{4.17}$$

and

$$\frac{\partial}{\partial \eta}\left(\ell \frac{\partial F}{\partial \eta}\right) - 2\xi F \frac{\partial F}{\partial \xi} + \left(f + 2\xi \frac{\partial f}{\partial \xi}\right) \frac{\partial F}{\partial \eta} + \beta(\bar{\theta} - F^2) = 0 \ . \tag{4.18}$$

Here $\ell = \bar{\rho}\bar{\mu}_{\text{eff}}/(\bar{\rho}_e \bar{\mu}_{\text{eff},e})$, $\bar{\theta} = \bar{\rho}_e/\bar{\rho}$, and β is a pressure gradient parameter, defined by

$$\beta = \frac{2\xi}{V_{\tau,e}} \frac{dV_{\tau,e}}{d\xi}. \tag{4.19}$$

Since the total enthalpy $H_T \approx T + V_\tau^2/2$ and the pressure are constant across the viscous layer, it follows from the Bernoulli relations (3.2) and the equation of state for a thermally perfect gas, cf. (2.11), that

$$\bar{\theta} = T/T_e = (\bar{\rho}/\bar{\rho}_e)^{-1} = 1 + \frac{\gamma - 1}{2} M_e^2 (1 - F^2) \,, \tag{4.20}$$

where T/T_e and $\bar{\rho}/\bar{\rho}_e$ are the ratios of the local to the edge values of the fluid temperature (or enthalpy) and density.

The following boundary conditions are applied. The stream function is constant along the blades and the reference wake streamlines (i.e., at $\eta = 0$). Therefore, without loss in generality, we can set

$$f = 0 \quad \text{at} \quad \eta = 0 \,. \tag{4.21}$$

The no-slip condition applies at a blade surface, i.e.,

$$F = 0 \quad \text{at} \quad \eta = 0 \quad \text{for} \quad \xi \leq \xi_{TE} \,, \tag{4.22}$$

where ξ_{TE} is the trailing-edge value of ξ. At the edges of the blade-surface boundary layers

$$F(\eta_e) = 1 \quad \text{for} \quad \xi < \xi_{TE} \,, \tag{4.23}$$

since $V_\tau \to V_{\tau,e}$ as $\eta \to \eta_e$. This condition forces the flow variables to approach their appropriate edge (inviscid) values as $\eta \to \eta_e$.

The edge conditions for a wake are more complicated because of the jumps in the inviscid flow variables, associated with wake curvature [cf. (4.3)]. We indicate the upper- and lower-edge values of η and the edge velocity, $V_{\tau,e}$, by the superscripts $+$ and $-$. If we use upper surface flow variables to define the Levy-Lees transformation for the wake calculation, e.g., if we set $F = V_\tau / V_{\tau,e}^+$, then

$$F(\eta_e^+) = 1 \quad \text{and} \quad F(\eta_e^-) = V_{\tau,e}^- / V_{\tau,e}^+ \quad \text{for} \quad \xi > \xi_{TE} \,. \tag{4.24}$$

If the curvature effect is negligible, i.e., if $[\![P]\!] \approx 0$ for $x \in W$, the wake-edge conditions become $F(\eta_e^\pm) = 1$.

Solution Procedure

The viscous-layer equations are parabolic in the ξ-direction and therefore require initial conditions. These are provided by determining a similarity solution which holds in the vicinity of a leading-edge stagnation point, i.e., near $\xi = 0$. Such a solution is obtained by solving the Levy Lees equations with $\beta = 1$. Solutions for the flows along a blade surface and its wake are then obtained using space-marching in the downstream direction. As discussed in § 4.1, a complete IVI calculation requires the ability to solve the viscous-layer equations in both the "direct" mode, in which the pressure gradient parameter β is specified and the displacement thickness $\bar{\delta}$ is determined, and in the "inverse" mode, in which $\bar{\delta}$ is specified and β is determined. In the present study the equations are solved in the direct mode over a forward part of the blade, that includes the leading edge stagnation point, and in the inverse mode downstream of an axial station, whose location is either specified in advance or

determined during the calculation to ensure that the inverse mode is initiated upstream of a strong interaction region. A wake is calculated entirely in the inverse mode. For a calculation in the inverse mode, the quantities β and $V_{\tau,e}$ are unknown. Thus, a supplemental equation relating these two variables is needed. This is obtained by discretizing (4.19), which defines β in terms of $V_{\tau,e}$.

In the direct viscous-layer calculation, the value of β is determined by the inviscid analysis and the displacement thickness is obtained from the viscous analysis. In the inverse procedure, the displacement thickness is specified, and the edge values of the flow variables, $V_{\tau,e}$, M_e, etc., are obtained as part of the viscous-layer solution. This is accomplished via the introduction of a "mass deficit parameter", $\overline{m} = \bar{\rho}_e V_{\tau,e} \bar{\delta}$. An expression relating the value of f at the edge of the viscous layer to $\overline{m}$ is derived by integrating equation (4.17) across the boundary layer and employing the definitions of $\bar{\delta}$, η and $\bar{\theta}$, cf. equations (4.13), (4.15) and (4.20). We find that

$$f(\eta_e) = \int_0^{\eta_e} \bar{\theta} d\eta - (Re/2\xi)^{1/2} \overline{m} \; . \tag{4.25}$$

Equation (4.25) is used at blade surfaces to impose the specified value of $\overline{m}$ through the corresponding value of f at the outer edge of the viscous layer, i.e., at $\eta = \eta_e$. The integral term in (4.25) is determined from the previous global IVI iteration, and is therefore specified or lagged in the current iteration.

An expression for the difference between the stream function values at the upper and lower edges of a wake is obtained by integrating (4.17) across the entire wake (i.e., from η_e^- to η_e^+), to obtain

$$f(\eta_e^+) - f(\eta_e^-) = \int_{\eta_e^-}^{\eta_e^+} \bar{\theta} d\eta - (Re)^{1/2} [\bar{m}^+/(2\xi^+)^{1/2} + \bar{m}^-/(2\xi^-)^{1/2}] \; . \tag{4.26}$$

Equation (4.26) is used to impose the mass deficit parameters, $\overline{m}^{\pm} = \bar{\rho}_e^{\pm} V_{\tau,e}^{\pm} \bar{\delta}^{\pm}$, in the wake. If wake curvature effects are regarded as negligible the last term in (4.26) can be replaced by $\overline{m}_W/(2\xi_W)^{1/2}$, where $\overline{m}_W = \bar{\rho} V_{\tau,e} \bar{\delta}_W/(2\xi_W)^{1/2}$ and ξ_W is the continuation of the upper surface ξ-variable into the wake. The integral term in (4.26) is determined from the previous iterative solution.

The discretized field equations, boundary conditions and auxiliary conditions, equations (4.17)–(4.26), are quasi-linearized and the resulting tridiagonal system of algebraic equations is solved at each streamwise (i.e., $\tau-$ or $\xi-$) station of the computational domain, using a fixed-point iteration to update the nonlinear terms. The inversion algorithm used in the wake is modified to account for the application of one boundary condition (4.21) at $\eta = 0$ and two others at the upper and lower edges of the viscous layer, as well as to account for the application of the jump condition (4.26) on the values of f at the upper and lower edges of the viscous wake. Finally, the so-called FLARE approximation, which prevents instabilities in the viscous-layer solution, due to flow reversal, is applied by turning off the convective terms in the momentum equation wherever $F < 0$. Further details on the viscous-layer numerical analysis can be found in [BVA93a].

Inviscid/Viscid Iteration Procedure

The present IVI approach determines the complete flow field by iteratively updating the mass deficit parameter, $\overline{m}(\tau)$, which affects both the inviscid and viscous solutions through

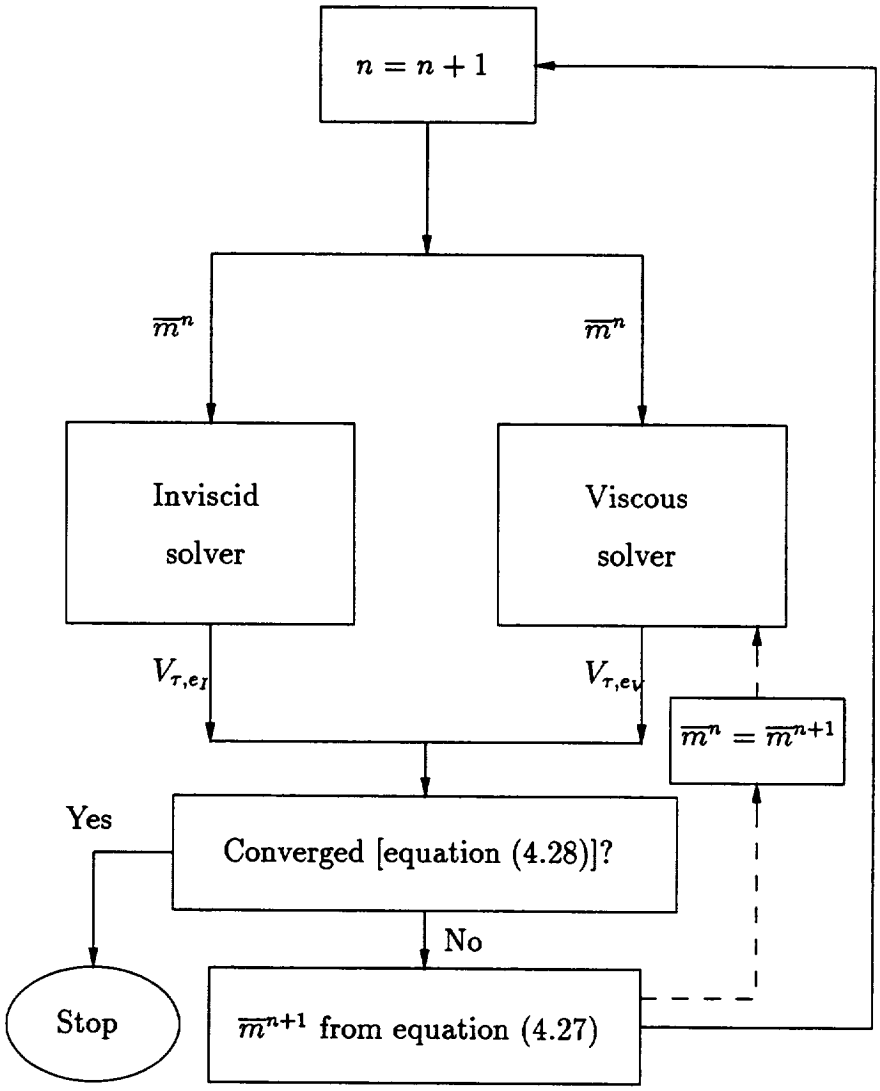

Figure 4.1: Semi-inverse inviscid/viscid iteration procedure.

their respective boundary conditions. For an arbitrary $\overline{m}$ distribution, two different surface and wake streamline velocity distributions generally result: one, $V_{\tau,e_I}(\tau)$, from the inviscid calculation and one, $V_{\tau,e_V}(\tau)$, from the viscous-layer calculation. The objective is to determine a converged inviscid/viscid interaction solution by finding the mass deficit parameter distribution that minimizes the differences between the V_{τ,e_I} and V_{τ,e_V} distributions.

In this investigation the "semi-inverse" iteration procedure of Carter [Car79], which is illustrated schematically in Figure 4.1, has been used to update $\overline{m}$ at every streamwise mesh station on the blade and wake surfaces. Thus, we set

$$\overline{m}^{n+1} = \overline{m}^n[1 + \hat{\omega}(V^n_{\tau,e_V}/V^n_{\tau,e_I} - 1)] \,, \tag{4.27}$$

where the superscript n is the global iteration count and $\hat{\omega}$ is a relaxation parameter. The

solution is considered to be converged when

$$\max_i |V_{\tau,e_{V_i}} - V_{\tau,e_{I_i}}| / V_{\tau,e_{I_i}} < \hat{\epsilon} \ , \ i = 1, \ldots, IE \ , \tag{4.28}$$

where the value of $\hat{\epsilon}$ is specified by the user and IE is the number of streamwise mesh stations. Equation (4.28) is applied on both blade surfaces and along the wake. The viscous-layer solution is obtained at the locations corresponding to the intersections of the inviscid mesh lines with the blades and the reference wake streamlines. This avoids the need for interpolation between different inviscid and viscid streamwise mesh.

During the global iterations, the independent variable ξ is updated using equation (4.15), where the current values of the variable appearing in the integrand are applied. Because a major objective of this study has been to develop an efficient analysis, various techniques for accelerating convergence were examined. We found that one of the most effective approaches for reducing the CPU time needed to obtain a converged IVI solution is to use the largest value of the relaxation parameter, $\hat{\omega}$, for which the iterative procedure remains stable. It was also observed that the inviscid velocity distribution, V_{τ,e_I}, changes relatively little between the initial purely inviscid solution and the final IVI solution. This is in contrast to the significantly larger changes observed in the viscous velocity distribution, V_{τ,e_V}. This observation prompted the introduction of a sub-iteration loop in which the viscous equations are solved repeatedly during each global iteration. Thus, equation (4.27) is applied N_V times during a single global iteration, with V_{τ,e_I} being frozen at its most recent value and V_{τ,e_V} being re-calculated during each sub-iteration by solving the viscous-layer equations using the latest $\overline{m}$ distribution. The value of N_V is a user-specified input, and the standard iteration procedure is recovered if $N_V = 1$. This strategy is only effective in reducing the total CPU time if the number of global iterations needed to obtain a converged IVI solution, N_G, can be reduced enough to more than balance the increased computational effort needed for the additional viscous calculations performed at each global iteration level. Of the three cascades examined in § 4.3, the sub-iteration procedure was of benefit only for the turbine. The dashed lines in Figure 4.1 correspond to the viscous subiteration technique described above.

4.3 Numerical Examples: Steady Flows with Strong Inviscid/Viscid Interactions

The foregoing inviscid/viscid interaction analysis has been applied to the cascade configurations described in § 2.5; in particular, the compressor exit guide vane (EGV), the high-speed compressor (HSC) cascade known as the Tenth Standard Cascade, and the turbine cascade, which is a modified version of the Fourth Standard Configuration. Surface pressure coefficient, $C_P = (P - P_{-\infty})/2$, or Mach number, M, displacement thickness, $\bar{\delta}$, and surface shear stress, $\bar{\tau}_w = Re^{-1}\bar{\mu}\partial V_\tau/\partial n|_{n=0}$, distributions will be presented, as functions of chordwise distance x, for the three cascades. IVI solutions for the compressor cascades will be evaluated via comparisons with Navier-Stokes solutions; the solution for the turbine against experimental measurements. In addition, predicted values of the total pressure loss, the exit flow angle, and separation point location will be presented for the EGV operating over a wide range of inlet flow conditions. These predictions were obtained using the mixing analysis of Stewart [Ste55]. Finally, the performance of the SFLOW–IVI analysis, i.e., its efficiency and convergence properties, will be discussed.

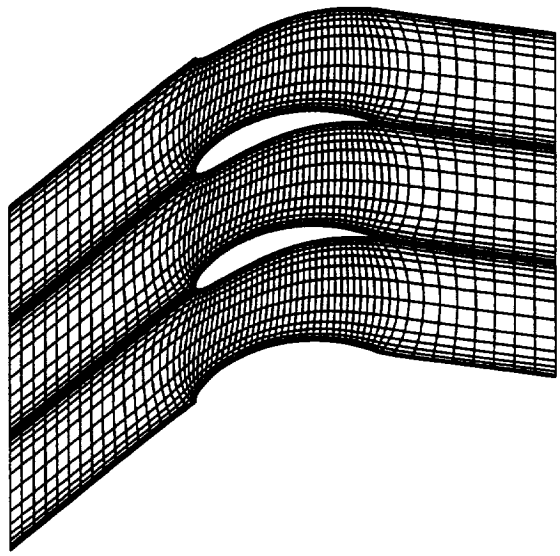

Figure 4.2: The EGV cascade and streamline H-mesh.

In the calculations described below, the SFLOW–IVI analysis was applied using the norm (4.28) and a convergence tolerance, $\hat{\epsilon}$, of 0.001. The inviscid H-meshes used for the two compressor cascades consisted of 90 axial and 31 circumferential lines, with 24 axial lines upstream of the blade leading edges, 41 lines intersecting the blade surfaces and 25 lines aft of the trailing edges. The meshes used for the viscous-layer analyses employed a total of 81 and 25 streamwise grid lines along the blade and wake, respectively, with 71 normal grid lines across a surface boundary layer and 141 normal grid lines across the wake. The inviscid mesh used for the turbine cascade had 150 axial and 31 circumferential lines, with 39 points upstream of the leading edge, 51 points along each blade surface and 60 points along the wake. A total of 101 surface and 25 wake stations were used in the turbine viscous-layer analysis. The normal mesh had the same dimensions as those used for the compressor cascades. For the cases considered in this study, the wake curvature effect was assumed to be negligible; thus, $[\![P]\!]_W$ was set equal to zero, [cf. (4.4)].

Compressor Exit Guide Vane (EGV)

The EGV cascade consists of highly cambered, modified NACA 0012 airfoils. It has a stagger angle, Θ, of 15 deg, a gap-chord ratio, G, of 0.6 and operates at a prescribed inlet Mach number, $M_{-\infty}$, and inlet flow angle, $\Omega_{-\infty}$, of 0.3 and 40 deg, respectively. Calculations were performed for a purely inviscid flow, and for viscous flows at Reynolds numbers of 10^5 and 10^6. Instantaneous transition from laminar to turbulent flow was assumed to occur at one percent of the arc distance measured along the blade surfaces from the leading-edge stagnation point to the trailing edge on both the suction and pressure surfaces of the blades. A streamline H-mesh is depicted in Figure 4.2, where three adjacent EGV blade passages are shown. For the purpose of illustration, the mesh shown in this figure has approximately one-half the number of axial and circumferential grid lines as were used for the actual calculations.

Results of the inviscid and IVI calculations are shown in Figure 4.3. The blade and wake, pressure coefficient and displacement thickness distributions are shown in Figures 4.3a and 4.3b, respectively; the blade-surface shear-stress distributions, in Figure 4.3c. The expected approach of the viscous solutions to the inviscid solution as Re is increased is evident in the pressure coefficient predictions. The rate of growth of the suction-surface displacement thickness increases dramatically with increasing chordwise distance, x, as the viscous-layer separation point is approached. As shown in Figure 4.3c, suction-surface separation bubbles ($\bar{\tau}_w < 0$) exist and span approximately 14 percent of chord for $Re = 10^6$ and about 24 percent of chord for $Re = 10^5$. The decrease in the extent of the separation bubble as Re is increased is consistent with the behavior expected for turbulent flows. Note that the suction-surface pressure distributions in Figure 4.4a flatten after the flow separates from the blade, but adverse pressure gradients still persist within the separation regions, because the suction surface pressures rise to meet those on the pressure surface as the trailing edge is approached.

The blade-surface pressure coefficient, displacement thickness and shear-stress distributions, as predicted by the SFLOW–IVI analysis for $Re = 10^6$, are compared in Figure 4.4 with results obtained using the Navier-Stokes analysis of Dorney, et al. [DDE92]. This Navier-Stokes analysis uses the Baldwin-Lomax turbulence model [BL78], which is very similar to the Cebeci-Smith model used in SFLOW–IVI. Good agreement between the results of the two analyses, particularly for the shear-stress distributions, has been obtained over most of the blade surface. However, the agreement, particularly that between the displacement thickness distributions, deteriorates in the vicinity of the trailing edge. This is due to the use of an O-mesh around the blades in the Navier-Stokes analysis, which is not well-suited for predicting flows over thin or wedge-shaped trailing edge geometries. In such cases the lines of the O-mesh become severely skewed in the vicinity of the trailing edge, introducing inaccuracies into the numerical solution. Also, the displacement thickness [cf. (4.13)] should be evaluated by integrating along lines that are normal to the body surface. However, near the trailing edge the skewed "radial" lines of the O-mesh deviate significantly from lines normal to the body surface, producing questionable results for $\bar{\delta}$ in the vicinity of a blade trailing edge. Both the Navier-Stokes and the IVI analyses predict separation ($\bar{\tau}_w < 0$) near the trailing edge, and give almost identical predictions for the location of the separation point ($\bar{\tau}_w = 0$); as indicated in Figure 4.4c.

To test the robustness of the SFLOW–IVI analysis, additional calculations were carried out for viscous flows at $Re = 10^6$. The inlet Mach number was held at $M_{-\infty} = 0.3$, but a wide

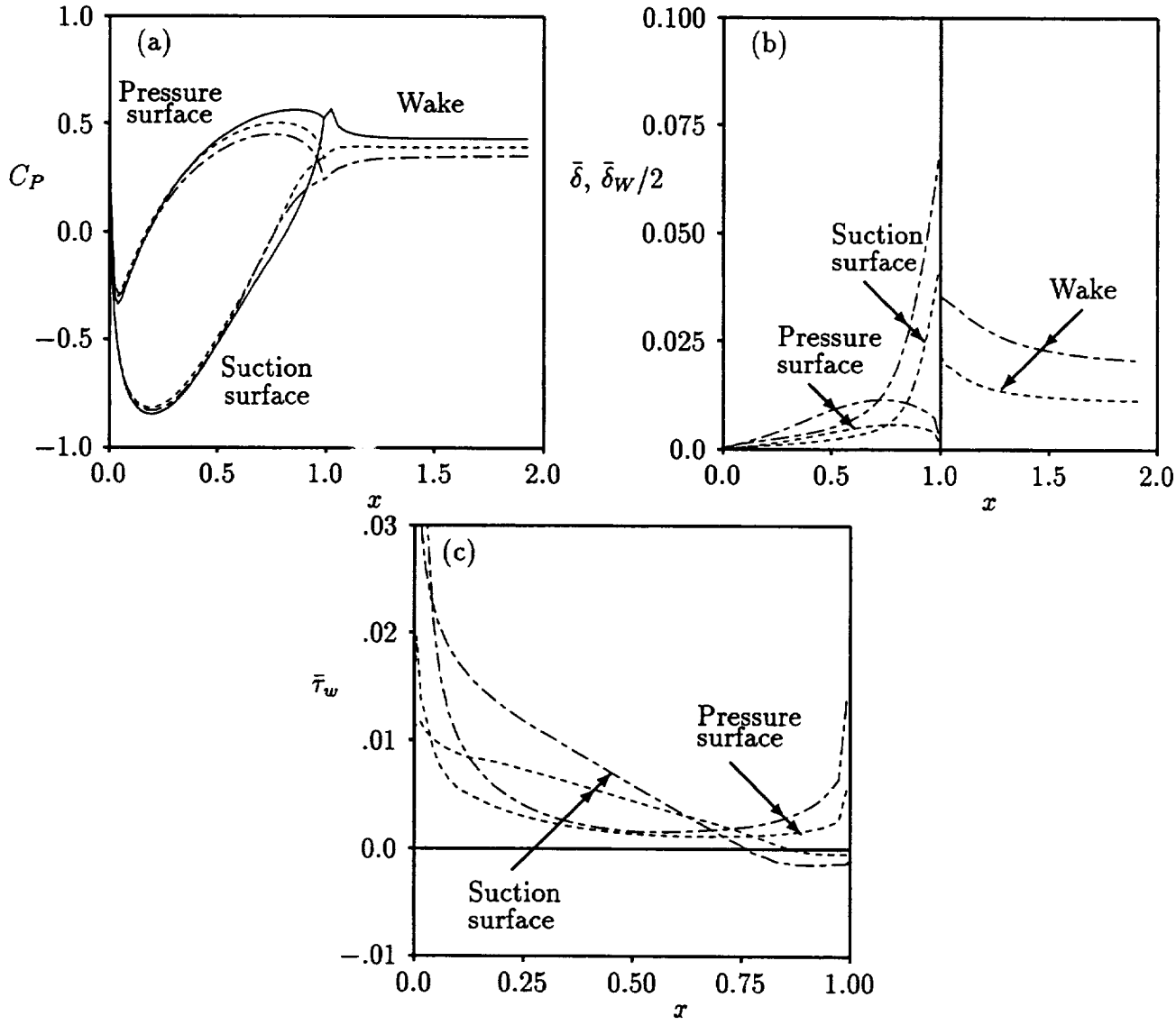

Figure 4.3: Inviscid (———) and IVI, at $Re = 10^5$ (— - — - —) and $Re = 10^6$ (- - - - -), solutions for the EGV cascade: (a) pressure coefficient; (b) displacement thickness; (c) surface shear stress.

range of inlet flow angles, i.e., 36 deg $\leq \Omega_{-\infty} \leq$ 54 deg was considered. The transition point locations were held fixed at $\tau/\tau_{TE} = 0.01$ for all values of $\Omega_{-\infty}$. This location is the same as that reported earlier for the baseline ($\Omega_{-\infty} = 40$ deg) calculation. The results are shown in Figure 4.5. Here, the predicted total pressure loss parameter, $\overline{\omega} = (P_{T_{-\infty}} - P_{T_{+\infty}})/(P_{T_{-\infty}} - P_{-\infty})$, where P_T is the total pressure, exit flow angle, $\Omega_{+\infty}$, and suction-surface separation point location, x_{sep}, are plotted as functions of inlet flow angle $\Omega_{-\infty}$. At $\Omega_{-\infty} = 54$ deg, the viscous flow is approaching stall, with the separation region spanning approximately 35 percent of chord. Above 54 deg the IVI calculations did not converge due to a numerical instability. This is consistent with the known stability properties of the semi-inverse IVI iteration procedure when applied to flows with large-scale separations [Wig81].

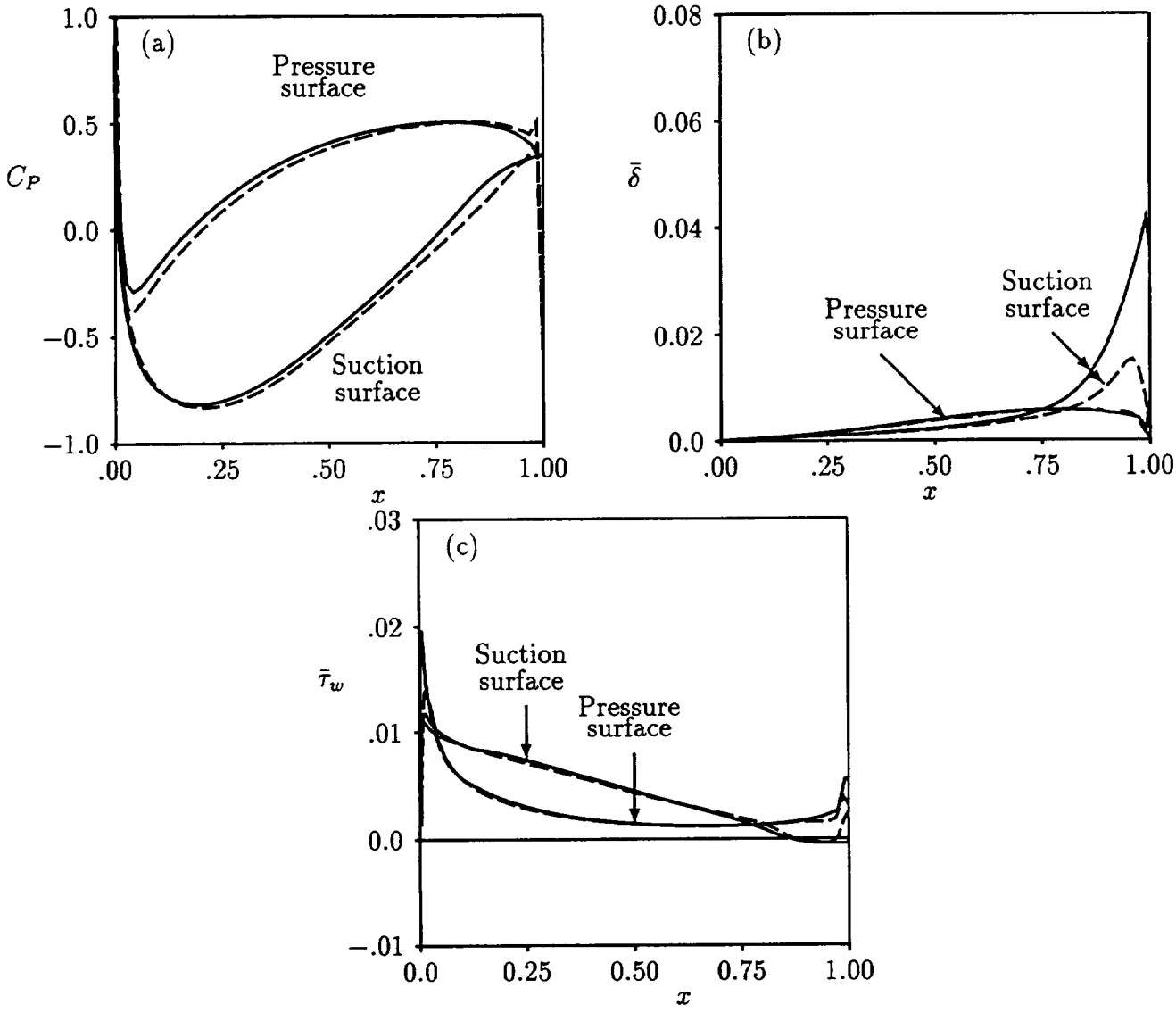

Figure 4.4: Comparison of IVI (———) and Navier-Stokes (- - - - -) solutions for the EGV cascade at $Re = 10^6$: (a) pressure coefficient; (b) displacement thickness; (c) surface shear stress.

The total pressure loss parameter and the exit flow angle are plotted versus $\Omega_{-\infty}$ in Figures 4.5a and 4.5b, respectively. There is a range of inlet flow angles over which the loss remains relatively low, but $\overline{\omega}$ increases rapidly as the inlet flow angle is increased above 50 deg. The latter behavior corresponds to a significant increase in the extent of the separation region with increasing $\Omega_{-\infty}$ for $\Omega_{-\infty} > 50$ deg, as can be seen from the results for x_{sep} shown in Figure 4.5c. A striking similarity exists between the variations in $-\Omega_{+\infty}$ and x_{sep} with $\Omega_{-\infty}$, as is apparent from the results shown in Figure 4.5. The streamwise growth of the separation bubble, with increasing $\Omega_{-\infty}$, is accompanied by an increase in the suction-surface displacement thickness in the vicinity of the trailing edge. This produces a thickened displacement body

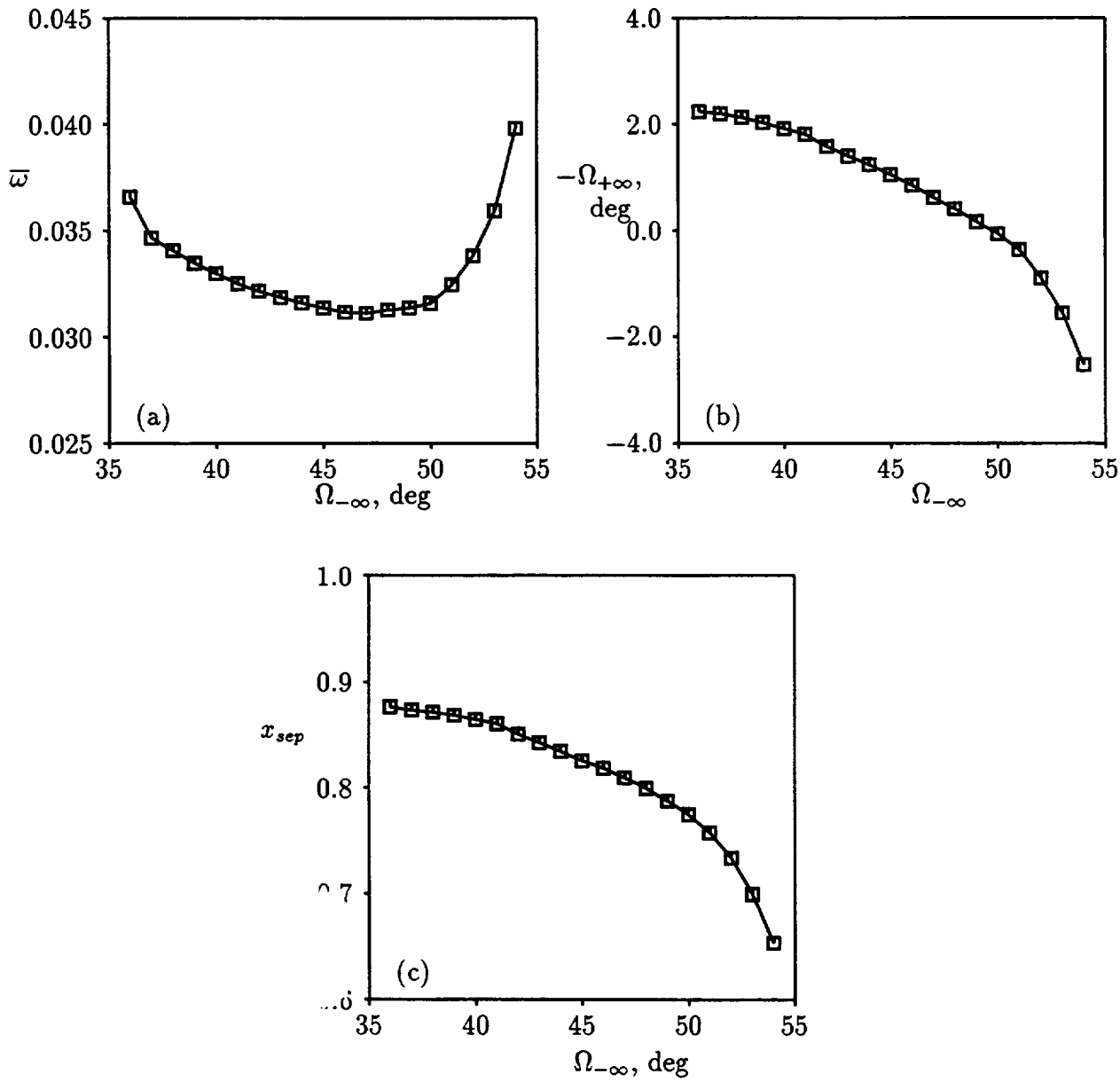

Figure 4.5: SFLOW–IVI predictions for the EGV cascade operating over a range of inlet flow angles: (a) loss parameter; (b) exit flow angle; (c) separation point location.

(i.e., the profile made up of the viscous displacement thickness superimposed on the actual blade), thereby reducing the effective camber of the blade, and hence, the blade loading. As a direct consequence, there is a reduction in the turning of the flow, i.e., an increase in $\Omega_{+\infty}$.

The predicted streamline patterns indicating the size of the trailing-edge separation bubble for $\Omega_{-\infty} = 36$, 45 and 54 deg are shown in Figure 4.6. For $36 \leq \Omega_{-\infty} \leq 45$ deg, the separation bubble grows slowly, whereas a much more rapid growth occurs between 45 and 54 deg [see Figure 4.5c]. The "decambering" effect produced by the growth of the separation bubble is also indicated by the results in Figure 4.6. The kinks that appear in the streamlines near

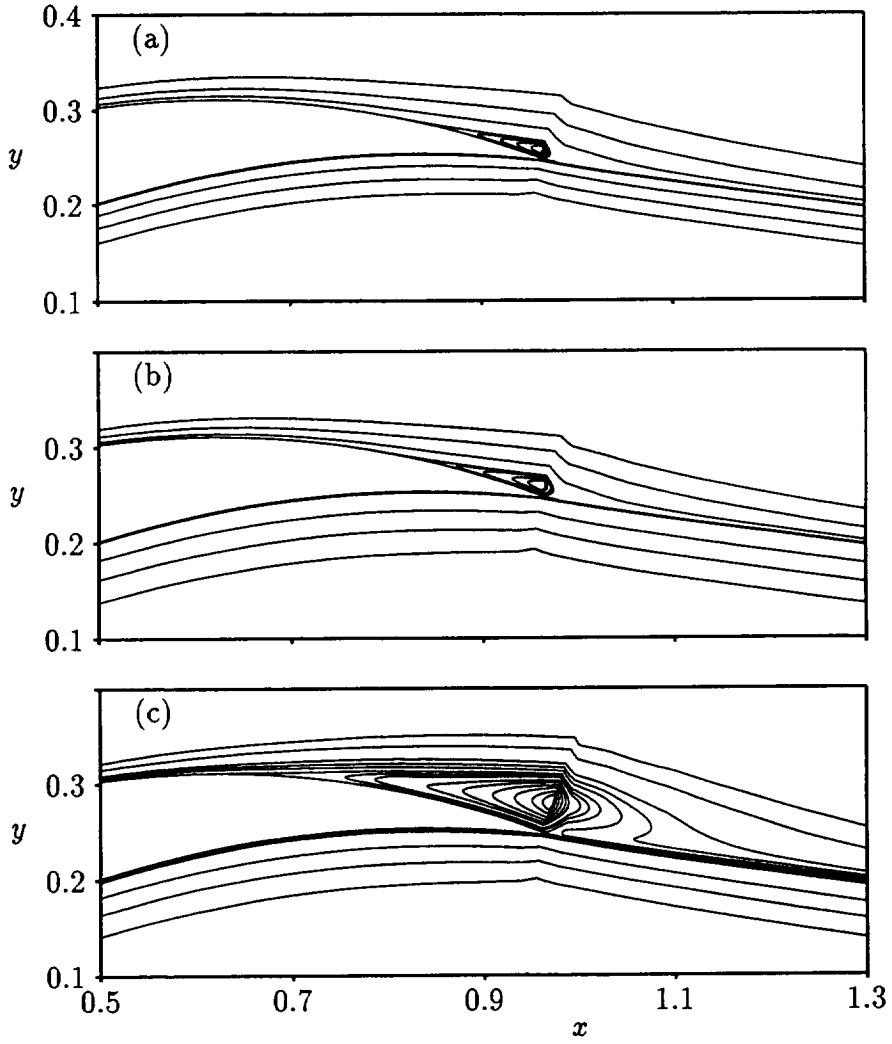

Figure 4.6: Trailing-edge streamline patterns for the EGV cascade: (a) $\Omega_{-\infty} = 36$ deg; (b) $\Omega_{-\infty} = 45$ deg; (c) $\Omega_{-\infty} = 54$ deg.

the trailing edge require some explanation. Since the blade trailing edge is wedge shaped, the surface coordinate line formed by the blade surface and reference wake streamline has a geometric singularity of "kink" at the trailing edge. This singularity influences the solution throughout the trailing-edge region as shown by the streamline plots in Figure 4.6. Because this singular behavior is highly localized, its effect on the solution for the overall flow field appears to be negligible.

High-Speed Compressor Cascade (HSC)

The HSC cascade or Tenth Standard Configuration, consists of modified NACA 5506 airfoils. It has a blade spacing of unity and a stagger angle of 45 deg. We consider a high-subsonic inlet operating condition, i.e., $M_{-\infty} = 0.7$ and $\Omega_{-\infty} = 55$ deg, and viscous flows at Reynolds numbers of 10^5 and 10^6. Instantaneous transition is assumed to occur at ten and at

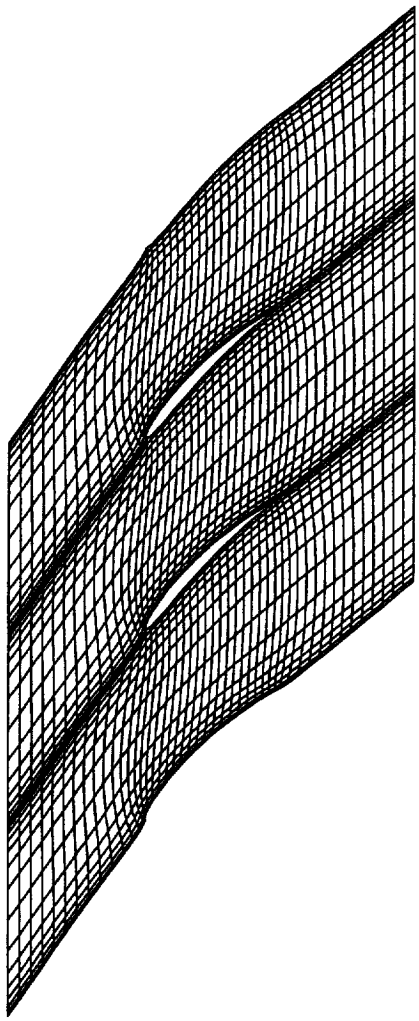

Figure 4.7: Streamline H-mesh for the HSC cascade.

one percent of the surface arc length for the flows at $Re = 10^5$ and 10^6, respectively, on both the suction and pressure surfaces of each blade. The IVI analysis for the flow at $Re = 10^5$ was found to be sensitive to the specified transition location. In particular, the iterative solutions would not converge, if transition was specified to occur at one percent of arc length, whereas if transition was assumed to occur further downstream, the iterations converged. The cascade along with a streamline H-mesh, which has, for the sake of clarity, a lower grid point density than that used for the actual calculations, are shown in Figure 4.7. The results of the inviscid and viscous calculations are presented in Figures 4.8 and 4.9.

The predicted pressure and displacement thickness distributions along the blade surfaces and the wake are shown in Figures 4.8a and 4.8b, respectively, for pure inviscid flow and for the viscous flows at $Re = 10^5$ and $Re = 10^6$. The behavior of both of these quantities is similar to that observed for the EGV. The surface shear-stress distributions, shown in Figure 4.8c,

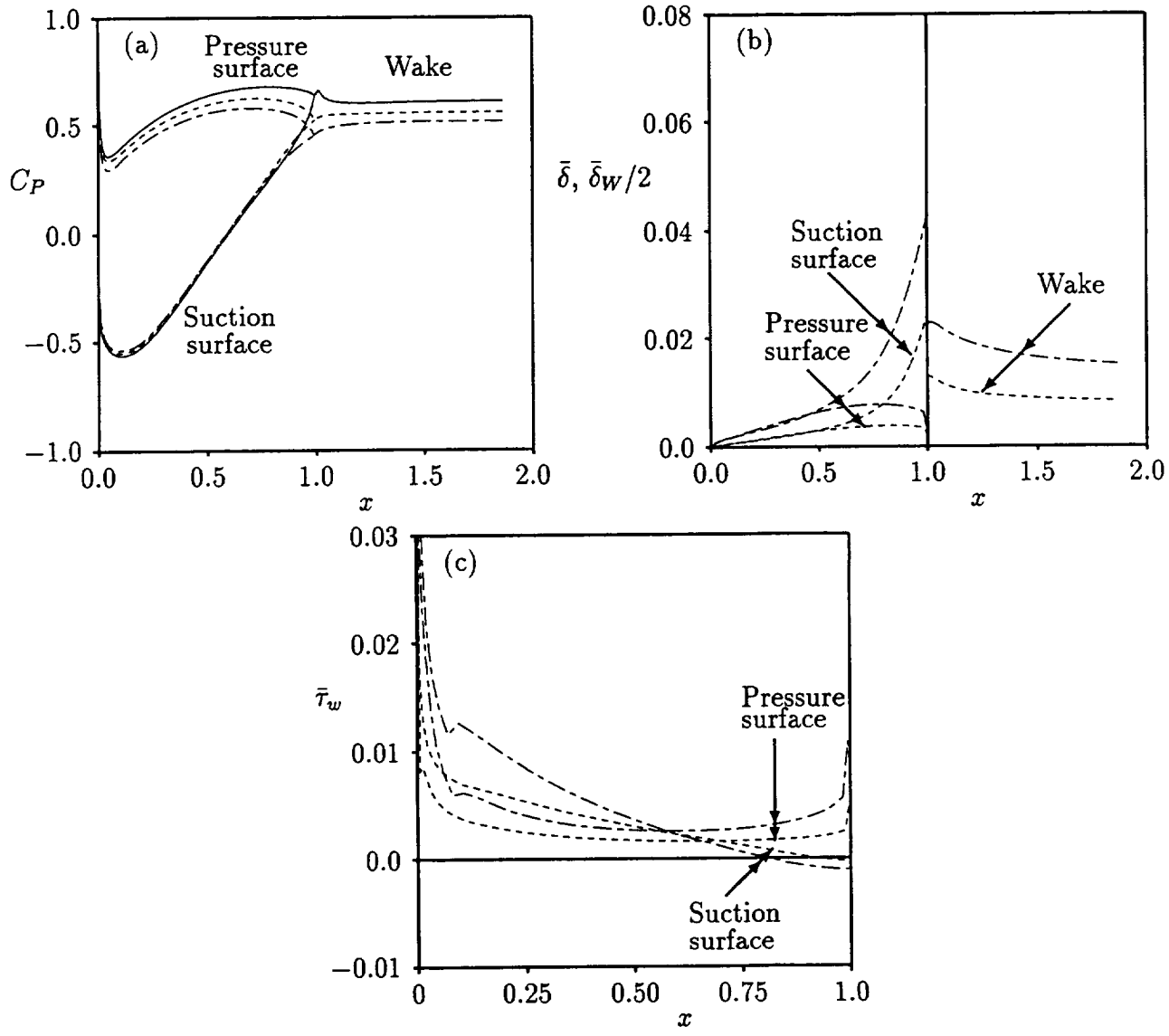

Figure 4.8: Inviscid (———) and IVI, at $Re = 10^5$ (— - — - —) and $Re = 10^6$ (- - - - -), solutions for the 10th Standard Cascade: (a) pressure coefficient; (b) displacement thickness; (c) surface shear stress.

indicate that the streamwise extents of the suction-surface separation bubbles are smaller than those predicted for the EGV cascade, decreasing from approximately 20 percent to about 8 percent of chord as the Reynolds number is increased from 10^5 to 10^6. The kinks in the shear-stress distributions for the $Re = 10^5$ case are associated with the instantaneous transition that occurs at $\tau/\tau_{TE} = 0.1$ on both the suction and pressure surfaces of each blade.

The surface pressure coefficient, displacement thickness and shear-stress distributions determined for the flow at $Re = 10^6$ using SFLOW–IVI are compared with those obtained using the Navier-Stokes analysis of [DDE92] in Figure 4.9. The agreement is excellent except in the immediate vicinity of the trailing edge. Again, the differences between the two solutions are

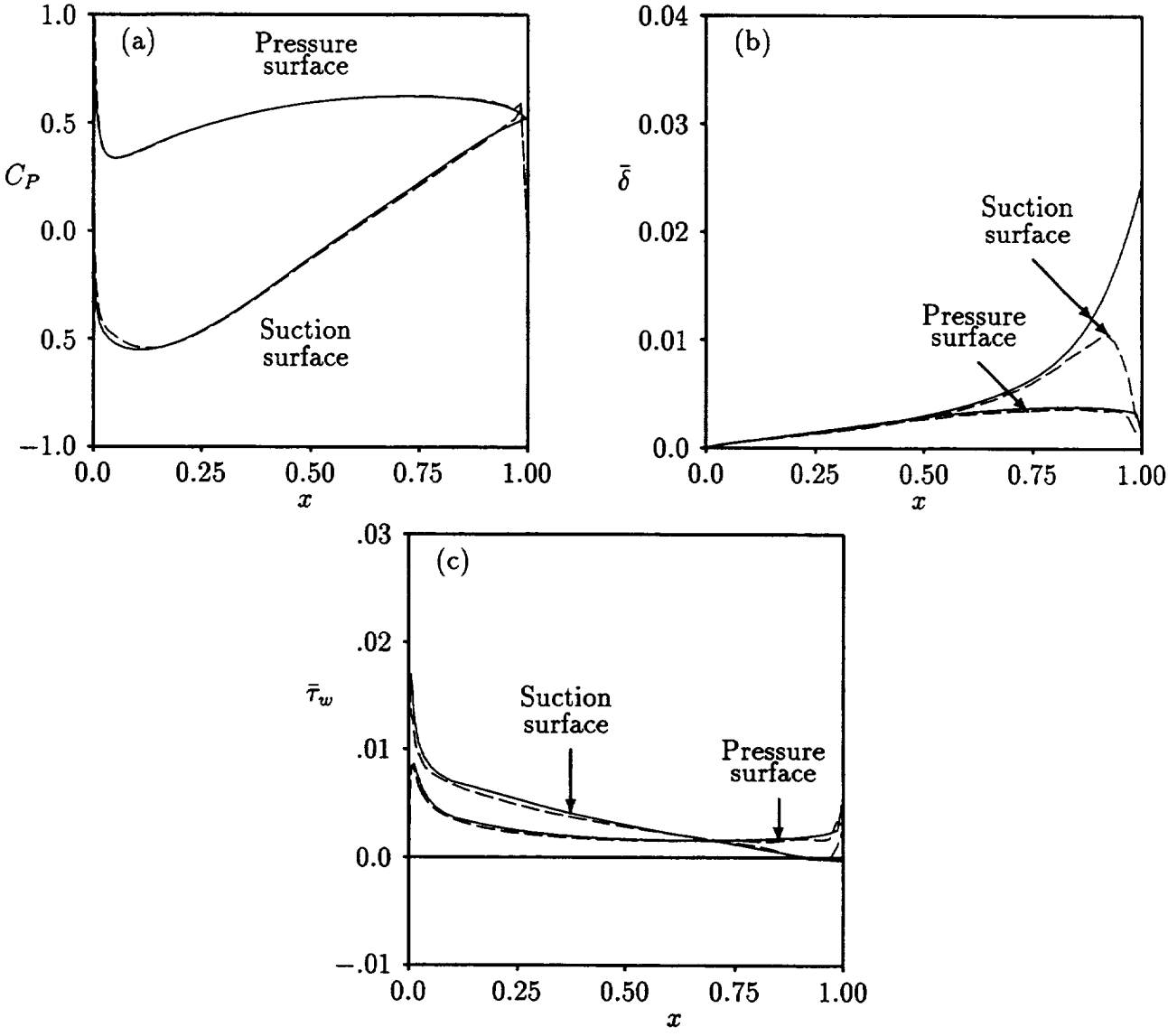

Figure 4.9: Comparison of IVI (———) and Navier-Stokes (- - - - -) solutions for the 10th Standard Cascade at $Re = 10^6$: (a) pressure coefficient; (b) displacement thickness; (c) surface shear stress.

attributed to the use of different meshes (H- and O-) around the blade. The two analyses give almost identical predictions for the location of the separation point.

Turbine Cascade

The turbine cascade is a modified version of the Fourth Standard Configuration described in the study of Fransson and Suter [FS83]. The blade geometry is shown in Figure 4.10 and was obtained by modifying the original blunt trailing-edge geometry to produce a wedge-shaped trailing edge, while retaining the original chord length, as discussed in [HV93]. As for the compressor solutions discussed above, the mesh shown in the figure has fewer grid lines than

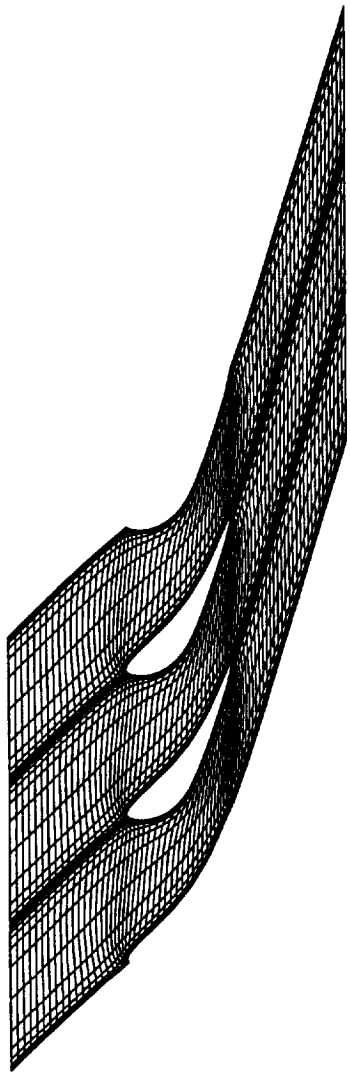

Figure 4.10: The turbine cascade and streamline H-mesh.

were used in the actual calculation. The streamline mesh employed for the turbine calculation was obtained from an inviscid solution calculated on a composite mesh (see, e.g., Figure 3.9). The composite mesh solution capability [UV91] is available in both the SFLOW and LINFLO analyses.

The blade spacing and stagger angle for the turbine cascade are 0.76 and 56.6 deg, respectively, and the inlet Mach number $M_{-\infty}$ and flow angle $\Omega_{-\infty}$ are 0.205 and 45 deg. The value of $M_{-\infty}$ has been adjusted from the experimentally measured value of 0.190 to improve

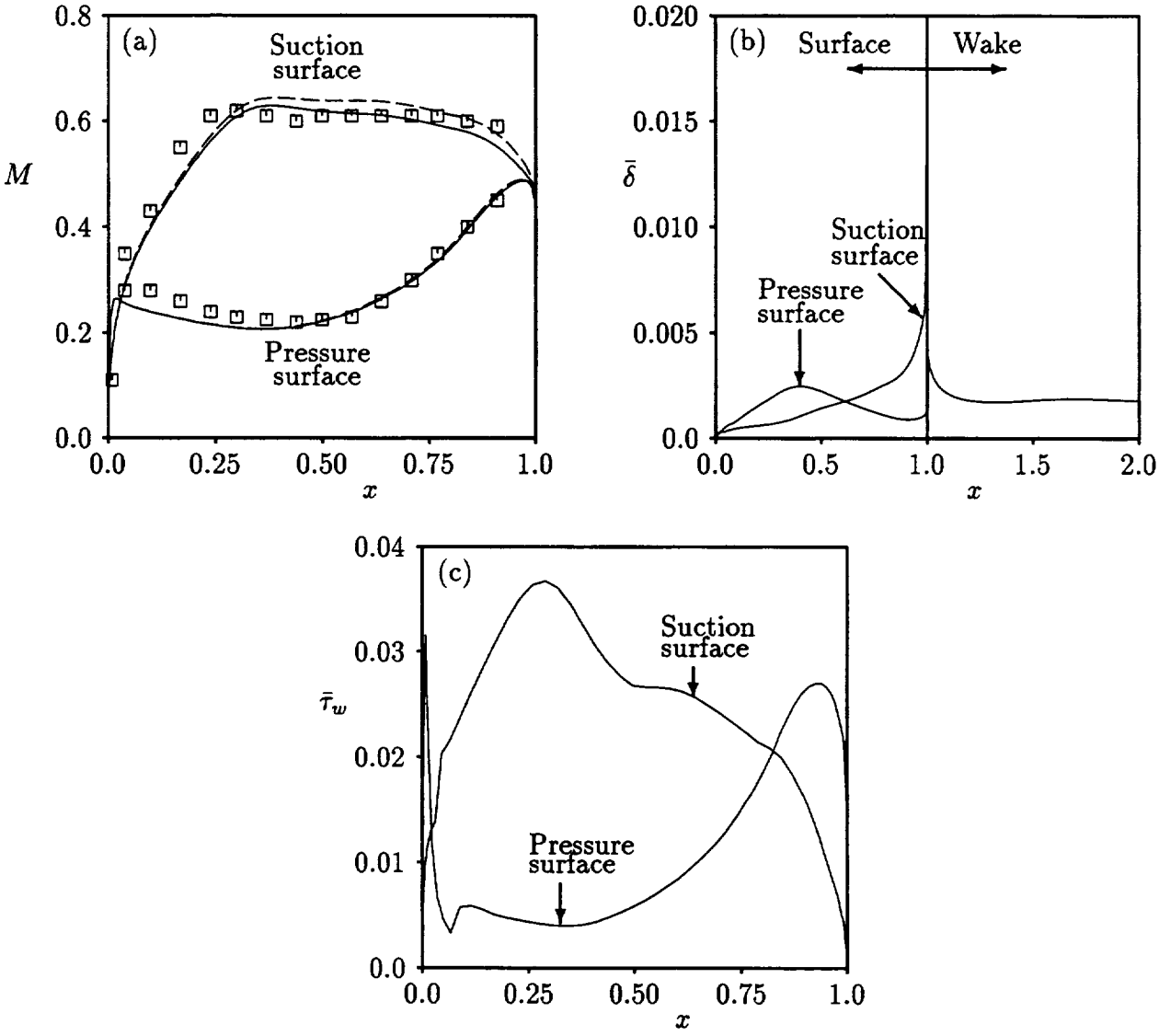

Figure 4.11: Results for turbine cascade: (a) comparison of predicted and measured Mach number distributions: (———) IVI; (– – – –) inviscid; symbols: experiment; (b) predicted displacement thickness distribution; (c) predicted surface shear-stress distribution.

the agreement with the measured pressure distribution. The calculation was carried out at a Reynolds number of 5×10^5 with instantaneous transition occurring at 10 percent of the surface arc length downstream from the leading-edge stagnation point along both the suction and pressure surfaces of the blades. A converged solution could not be obtained for the turbine if the location of transition was specified to be too close to the leading edge. This is consistent with the behavior observed for the HSC cascade for the flow at $Re = 10^5$.

The IVI solution was obtained in 12 global inviscid/viscid iterations. The viscous subiteration procedure described in § 4.2 was very effective for this case, reducing the CPU time needed to converge the calculation from 1371 seconds without subiteration (requiring 115

global iterations) to 224 seconds (in 12 global iterations), using four viscous subiterations (i.e., $N_V = 4$) during each global IVI iteration.

The computed and measured blade surface Mach number distributions are shown in Figure 4.11a. Viscous effects produce a nearly uniform decrease in the suction surface Mach number distribution aft of $x \approx 0.4$, whereas the pressure surface Mach number distribution is almost unaffected. The agreement between the IVI solution and the experimental data is reasonable; the disagreement in the trailing-edge region can be attributed to the geometric modification mentioned above. It is difficult to draw definitive conclusions regarding the comparison between the predictions and the data because the solution for this case is particularly sensitive to the inviscid mesh used. The predicted displacement thickess and surface skin-friction coefficient distributions are shown in Figures 4.11b and 4.11c, respectively. No separation was predicted for the flow conditions considered, however, the suction-surface viscous-layer is close to separation at the trailing edge.

Timing Study and Convergence Behavior

Because the development of an efficient analysis has been a major objective of this analytical investigation, a timing study was conducted for the three cascade configurations examined herein. This study provides both a measure of the computational effort currently required to obtain solutions using SFLOW–IVI, and benchmarks against which future efforts to improve efficiency can be compared. The results are summarized in Table 1. In addition to the CPU time t_C, the relaxation factor $\hat{\omega}$, and the number of global iterations N_G required to converge solutions using a tolerance level $\hat{\epsilon}$ of 0.001 are given in Table 1. The execution times were determined using a nearly optimal value of $\hat{\omega}$, as determined by a trial and error procedure.

The calculations were carried out on an HP-Apollo 720 workstation where SFLOW–IVI has been compiled using an optimizing preprocessor. No attempt has been made to "tune" the code to take advantage of special features of the optimizer. The times given in Table 1 are CPU times for the portion of the calculation associated with the IVI iteration loop. Any overhead associated with the initialization of the data structure, the generation of the mesh and the calculation of the initial inviscid solution is not included. However, this overhead amounts to a small percentage of the overall CPU time required by the SFLOW–IVI analysis. Note that each of the solutions was obtained in less than five minutes. Recent calculations on an IBM RS/6000 3CT workstation indicate a factor of four (4) reduction in the computing times reported in Table 1.

It is difficult to make direct comparisons with Navier-Stokes CPU times since these can vary considerably, even by orders of magnitude, depending on numerous factors, including whether the code is a research or a design code, the number of grid points, the grid stretching, the convergence tolerance, and so on. An estimate based on a Navier-Stokes analysis that is currently used in design indicates that the present IVI analysis requires one to two orders of magnitude less CPU time to produce similar results.

The convergence behavior of two parameters of interest to compressor blade designers was examined to determine if a different measure of convergence than that given by equation (4.28) would be more appropriate for engineering applications. For the two compressor cascades, the total pressure loss parameter $\overline{\omega}$ and exit flow angle $\Omega_{+\infty}$ were monitored during the IVI iteration procedure. We have found that the values of $\overline{\omega}$ and $\Omega_{+\infty}$ could be considered

Table 1. Summary of SFLOW-IVI CPU times, t_C, for different cascade configurations.

Configuration	$\hat{\omega}$	N_G	t_C (secs)
EGV, $Re = 10^6$	1.20	24	197
EGV, $Re = 10^5$	0.85	38	277
HSC, $Re = 10^6$	1.20	27	203
HSC, $Re = 10^5$	0.80	40	296
Turbine	0.55	12	224

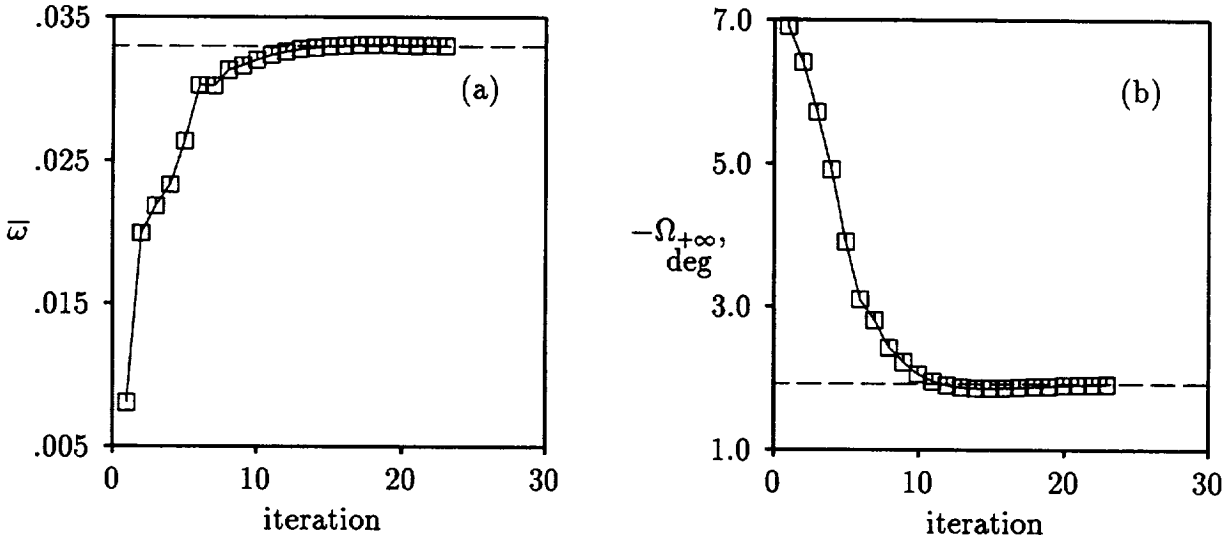

Figure 4.12: Convergence history for the EGV cascade at $Re = 10^6$ and $\Omega_{-\infty} = 40$ deg: (a) total pressure loss parameter; (b) exit flow angle.

converged at a significantly lower iteration count than was needed to satisfy the convergence criterion ($\hat{\epsilon} = 0.001$); typically about one-third fewer iterations than are shown in Table 4.3 are needed. Thus, even greater efficiency could be achieved in many cases by measuring convergence by the degree to which the parameters of interest have approached "asymptotic" values. This is demonstrated by the results presented in Figure 4.12, which show the behavior of $\bar{\omega}$ and $\Omega_{+\infty}$, respectively, as functions of the iteration count for the EGV cascade operating at $Re = 10^6$ and $\Omega_{-\infty} = 40$ deg. This behavior is typical of that observed for all of the cases studied herein. The solution for the case illustrated in Figure 4.12 converged to within $\hat{\epsilon} = 0.001$ in 24 iterations while the asymptotic value, indicated by the dashed horizontal line, was determined by converging the solution to $\hat{\epsilon} = 0.0001$, for which 41 iterations were needed. For engineering purposes, this solution could be considered to be converged after about 15 iterations, for which $t_C \approx 120$ seconds.

Discussion

Existing nonlinear inviscid and inverse viscous-layer analyses have been extended and coupled to provide a strong inviscid/viscid interaction analysis (SFLOW-IVI) for two-dimensional, steady, subsonic cascade flows. This IVI solution procedure can be used to predict the effects of local strong interactions, including trailing-edge/near-wake interactions and small- to moderate-scale viscous-layer separations, on cascade performance. The present analysis is restricted to subsonic flows, but it can be extended to treat transonic flows in the future.

The SFLOW–IVI analysis has proven to be both efficient and robust. Converged solutions for each of the baseline configurations examined were obtained in less than five CPU minutes on an HP-Apollo 720 Workstation. Even lower CPU times could be obtained by basing convergence on the global quantities of interest to an engine designer. Robustness was demonstrated via application to a wide range of inlet conditions, including cases with large-scale separation, spanning up to 35 percent of blade chord.

A number of issues still need to be addressed in order to improve the accuracy of the SFLOW–IVI analysis and to expand its range of applicability. Among them are the inclusion of quasi-three-dimensional (i.e., streamtube contraction and radius change) effects, the incorporation of better models for transition and turbulence, and the addition of a procedure for updating the location of the wake streamline during the global iteration process. In addition, the overall utility of this SFLOW–IVI analysis for design-system applications needs to be explored through further testing and validation. Finally, as this effort continues, a steady transonic capability should be developed and the focus should turn increasingly towards the development of a strong inviscid/viscid interaction capability for subsonic and transonic unsteady flows.

4.4 Numerical Examples: Effects of Strong Steady Inviscid/Viscid Interaction on Unsteady Response

We have applied the SFLOW–IVI and LINFLO analyses in an effort to estimate the effects of steady viscous displacement on the unsteady aerodynamic response of a cascade undergoing prescribed blade motions. The calculation procedure is as follows. A strong inviscid/viscid interaction solution is first determined by applying the SFLOW–IVI analysis using an H-type mesh for the flow in the outer or inviscid region. The blade and wake displacement-thickness distributions resulting from this calculation are then used in the surface conditions (4.2) and (4.4), and the SFLOW analysis is applied on a composite-mesh to determine an accurate solution for the inviscid component of the high Reynolds number flow. This composite-mesh SFLOW solution is then used to provide the steady background flow information needed to determine a linearized inviscid unsteady solution, also on a composite mesh, using LINFLO.

In this approach, the SFLOW inviscid solution accounts for the effects of steady viscous-displacement via the imposition of the appropriate blade and wake boundary conditions. The linearized inviscid flow is determined as a solution of the field equation (3.9), with $\mathbf{v}_* \equiv 0$, and the blade and wake surface conditions (3.11) and (3.12). Thus, steady viscous displacement effects are incorporated into the linearized inviscid analysis through the steady potential Φ, which is the potential for the outer inviscid flow of a strong inviscid/viscid interaction calculation. Unsteady viscous-displacement effects are not taken into account by this procedure.

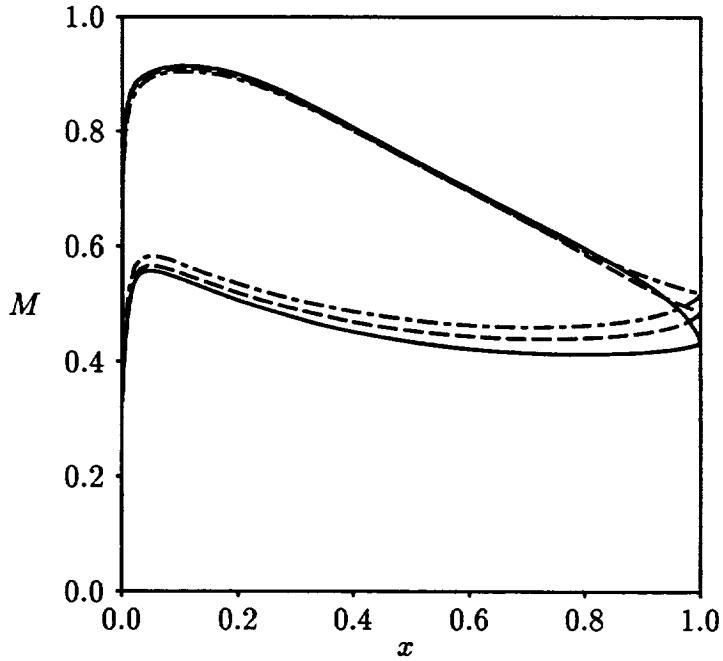

Figure 4.13: Surface Mach-number distributions for inviscid (——) and viscous, at $Re = 10^5$ (- - - - -) and $Re = 10^6$ (- - -), flows through the 10th Standard Cascade operating at $M_{-\infty} = 0.70$, $\Omega_{-\infty} = 55$ deg.

The foregoing approach has been applied to predict steady and unsteady flows through the 10th Standard or HSC cascade operating at an inlet Mach number of 0.7 and inlet flow angle of 55 deg. The blade-surface, Mach number distributions, as determined using SFLOW on a composite mesh, for pure inviscid flow and for viscous flows are $Re = 10^6$ and $Re = 10^5$ are shown in Figure 4.13. The C_p, $\bar{\delta}$ and $\bar{\tau}_w$ distributions for these flows, as determined by an H-mesh IVI solution, are shown in Figure 4.8. The predicted exit Mach number, exit flow angle, and lift force for three steady flows are 0.447, 40.2 deg, and 0.348 for $Re \to \infty$; 0.470, 41.5 deg, and 0.321 for $Re = 10^6$; and 0.488, 42.2 deg, and 0.303 for $Re = 10^5$. The viscous flows at $Re = 10^6$ and $Re = 10^5$ separate from the suction surface at $x_{sep} = 0.927$ and $x_{sep} = 0.808$, respectively. The trailing-edge streamlines for the flow at $Re = 10^5$ are depicted in Figure 4.14.

Unsteady response predictions, i.e., predictions for the global and local works per cycle [Ver89a, Ver93], are shown in Figures 4.15–4.17 for blades undergoing single-degree-of-freedom torsional, with $\alpha = (1, 0)$, and bending, with $h_y = (1, 0)$, vibrations. The torsional vibrations occur about the blade midchords. The global work per cycle, W_C, is the work done by the airstream on a given blade over one cycle of its motion. Therefore, a prescribed blade motion is stable, neutrally stable, or unstable according to whether the (global) work per cycle is less than, equal to, or greater than zero, respectively. The local work per cycle or pressure-displacement function, w_C, describes the distribution of the work per cycle over a blade surface. For subsonic flows in which the blades are undergoing small-amplitude rigid-body motions these quantities are determined from the relations

$$W_C = \oint_B w_C(\tau_B) d\bar{\tau}_B \ , \tag{4.29}$$

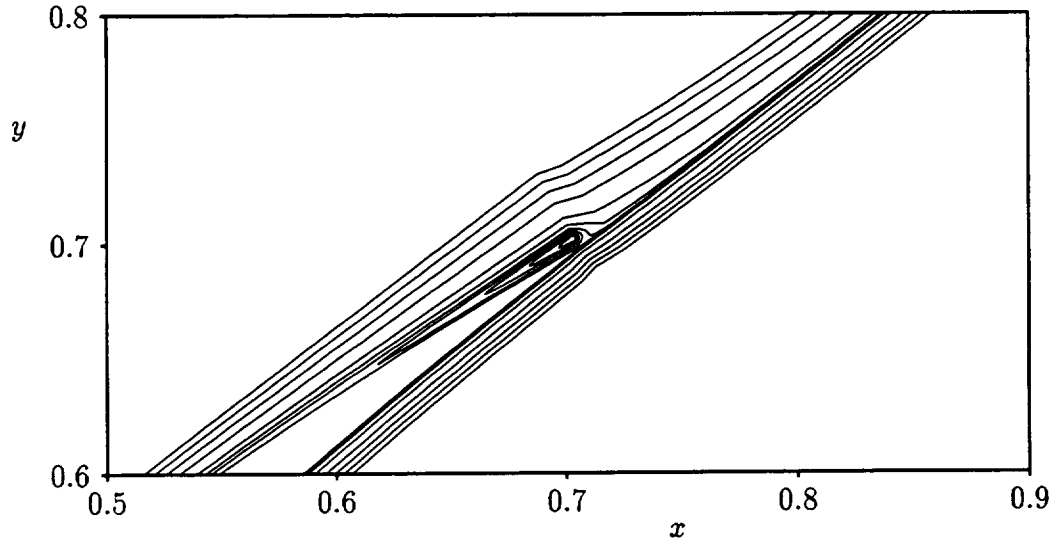

Figure 4.14: Trailing-edge streamlines for 10th Standard Cascade operating at $M_{-\infty} = 0.70$, $\Omega_{-\infty} = 55$ deg, and $Re = 10^5$.

and

$$w_C = -\pi Im\{P_B \alpha \mathbf{R}_B^* \cdot \boldsymbol{\tau}_B + p_B \mathbf{R}_B^* \cdot \mathbf{n}_B\} + \dots \quad (4.30)$$

Here $\mathbf{R}_B = \mathbf{h} + \boldsymbol{\alpha} \times \mathbf{R}_P$, $\mathbf{R}_P$ is the distance from the moving pitching axis to a point on the moving blade surface, P_B is the steady pressure at a point on the mean blade surface, p_B is the complex amplitude of the unsteady pressure at the corresponding point on the moving blade surface, and the superscript $*$ denotes the complex conjugate.

The local work-per-cycle or pressure displacement function distributions for unit frequency ($\omega = 1$) in- ($\sigma = 0$) and out-of-phase ($\sigma = 180$ deg) torsional blade motions about midchord are shown in Figure 4.15. For the in-phase torsional motion there are small differences between the inviscid and the viscous solutions, and no clear trend in the behavior of w_C with increasing Reynolds number. The normalized global works per cycle $|\alpha|^{-2} W_C$ for the three flows at $\sigma = 0$ are -0.897, -0.777 and -0.784 for $Re = 10^5$, $Re = 10^6$ and $Re \to \infty$, respectively. For the out-of-phase torsional motion the local work per cycle decreases with Reynolds number on both the blade pressure and suction surfaces over approximately the first thirty (30) percent of blade chord, indicating that the stability margin for the out-of-phase torsional blade motion increases with decreasing Reynolds number. Here, $|\alpha|^{-2} W_C = -1.732$, -1.578, and -1.252 for the flows at $Re = 10^5$, $Re = 10^6$ and $Re \to \infty$, respectively.

Similar results for unit frequency, in- and out-of-phase, bending vibrations are shown in Figure 4.16. For the in-phase bending motion there are changes in the local work per cycle with Reynolds number on both the blade suction and pressure surfaces in the vicinity of the leading edge, and along the suction surface, where w_C increases with decreasing Reynolds number over an interval extending from 15% to 60% of blade chord. The local work per cycle distributions for the two viscous flows at $Re = 10^5$ and $Re = 10^6$ are almost identical. The normalized global works per cycle, $|h_y|^{-2} W_C$, for these flows are -3.488 for $Re \to \infty$, -3.270 for $Re = 10^6$ and -3.261 for $Re = 10^5$. Thus, for the in-phase bending vibration, the stability margin decreases slightly with decreasing Reynolds number. For the out-of-phase bending

vibration, viscous displacement effects cause a small increase in w_C on the pressure surface over the first twenty (20) percent of blade chord and a large increase over most of the suction surface. As a result of the latter, viscous effects, which increase with decreasing Re, are strongly destabilizing for the out-of-phase bending motion, but this type of blade motion has a substantial stability margin. The global works per cycle, $|h_y|^{-2}W_C$, for the flows analyzed in Figure 4.16b are: $= -10.14$ for $Re \to \infty$, -8.812 for $Re = 10^6$ and -8.667 for $Re = 10^5$.

Global work per cycle, W_C, predictions for flows at $Re = 10^5$, $Re = 10^6$ and $Re \to \infty$ through the 10th Standard Cascade are shown in Figure 4.17. Here the blades are undergoing pure torsional and pure bending vibrations at unit frequency, and the response predictions are given over an entire 360 deg range of interblade phase angle. For the inviscid flows, the interblade phase-angles at which acoustic resonances occur are $\sigma^-_{-\infty} = -26.9$ deg, $\sigma^+_{-\infty} = 117.1$ deg, $\sigma^-_{+\infty} = -31.8$ and $\sigma_{+\infty} = 59.8$ deg, where the subscripts refer to the far upstream ($-\infty$) and far downstream ($+\infty$) regions and the superscripts refer to the direction of wave propagation. The viscous flows have the same upstream resonant conditions, but, since the steady exit flows vary with Reynolds number, slightly different downstream conditions. The results in Figure 4.17a indicate that steady viscous effects have a negligible impact on the torsional stability margins for superresonant blade motions, i.e., the motions ocurring between the lowest and highest resonant interblade phase angles. Also, viscous effects are stabilizing for the subresonant torsional blade motions. Viscous effects are destabilizing for both superresonant and subresonant bending vibrations (Figure 4.17b), but such motions tend to have substantial stability margins.

We must emphasize that the foregoing parametric studies are very limited and much more detailed studies will have to be conducted in order to understand the effects of viscous displacement on blade flutter characteristics. Also, these results account, only partially, for steady viscous displacement effects and neglect unsteady viscous effects. In particular, the contributions from the right-hand-sides of the linearized surface boundary conditions (2.56)–(2.58) have not been taken into account. That said, if the analysis described above is found to provide useful approximations to the effects of viscous displacement on the unsteady pressure responses of blade rows, then convenient and very efficient viscous unsteady aerodynamic models could be applied to predict a wide range of blade-row aeroelastic and aeroacoustic phenomena.

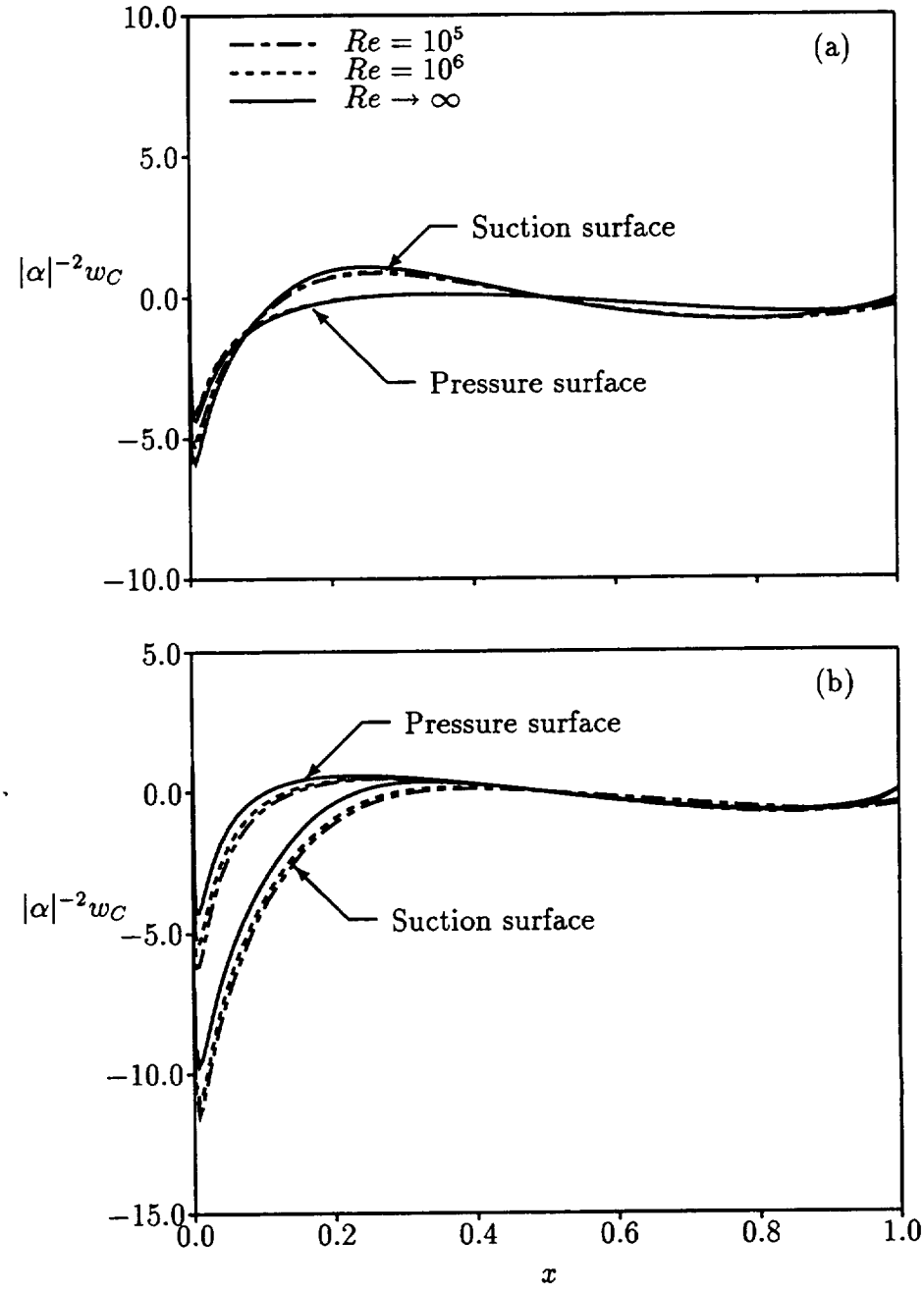

Figure 4.15: Effect of steady viscous displacement on pressure-displacement function response for subsonic flow ($M_{-\infty} = 0.7$, $\Omega_{-\infty} = 55$ deg) through the 10th Standard Cascade undergoing torsional blade vibrations about midchord at $\omega = 1$: (a) in-phase ($\sigma = 0$ deg) blade motion; (b) out-of-phase ($\sigma = 180$ deg) blade motion.

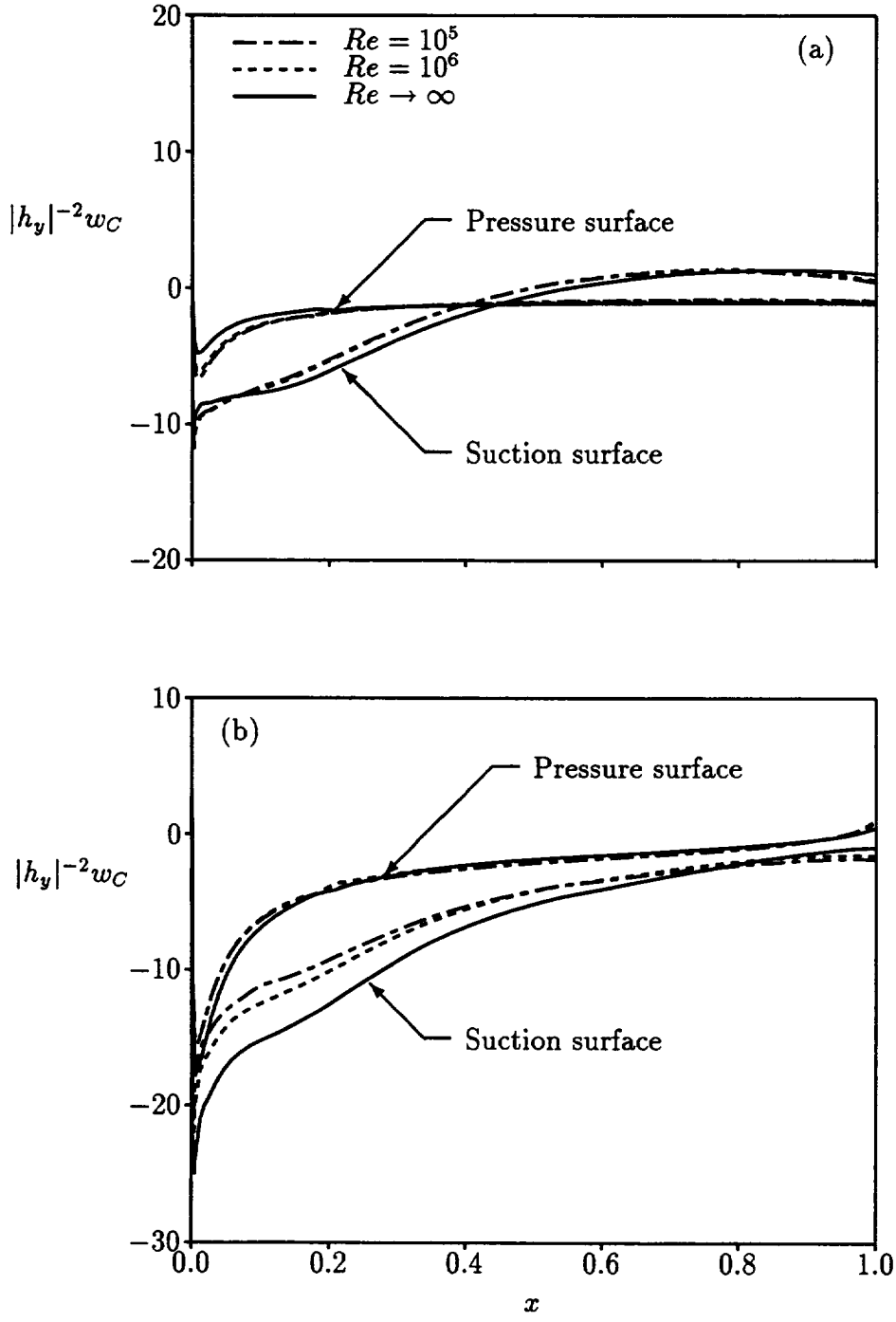

Figure 4.16: Effect of steady viscous displacement on pressure-displacement function response for subsonic flow ($M_{-\infty} = 0.7$, $\Omega_{-\infty} = 55$ deg) through the 10th Standard Cascade undergoing bending blade vibrations at $\omega = 1$: (a) in-phase ($\sigma = 0$ deg) blade motion; (b) out-of-phase ($\sigma = 180$ deg) blade motion.

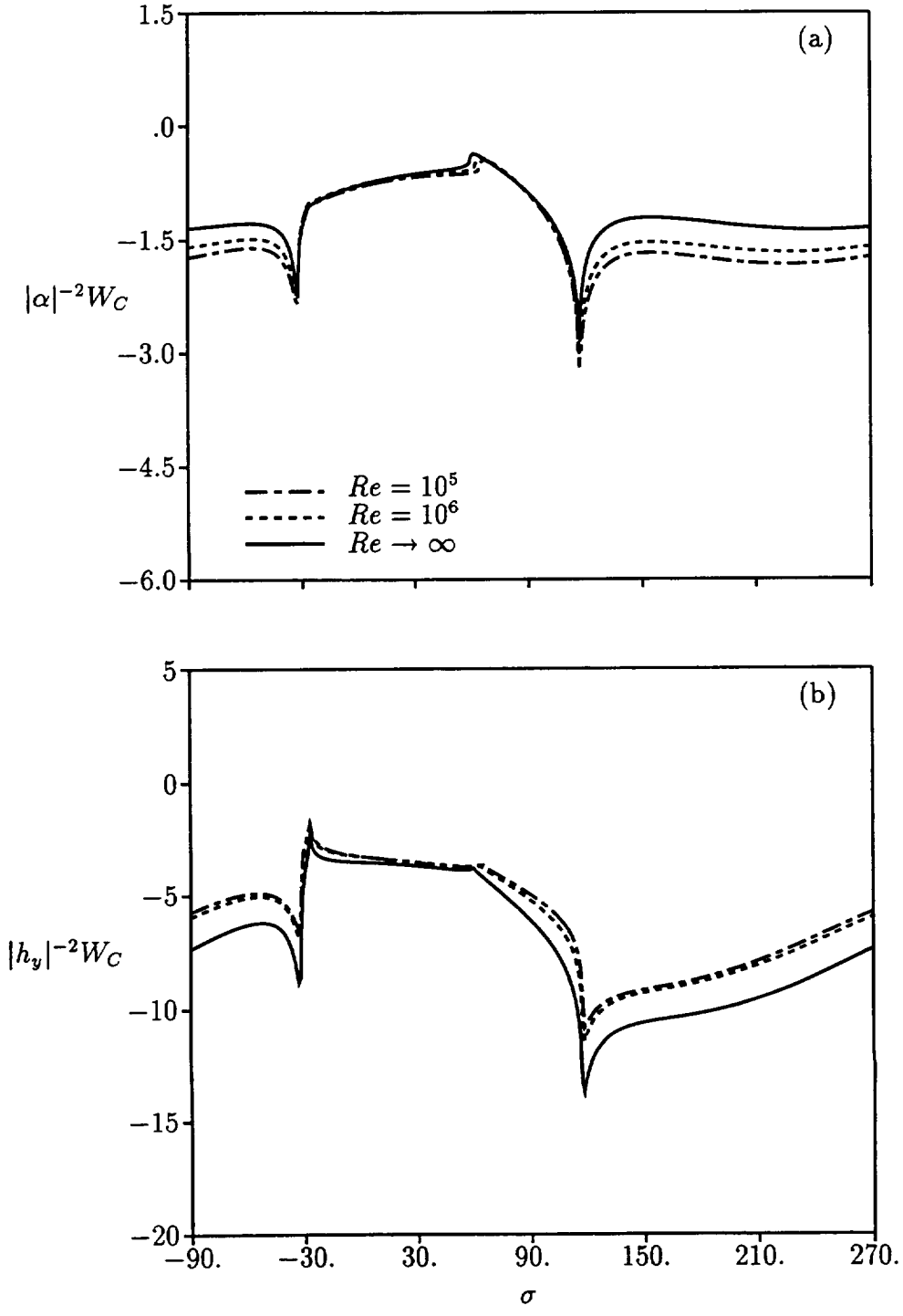

Figure 4.17: Effect of steady viscous displacement on work per cycle responses for subsonic flow ($M_{-\infty} = 0.7$, $\Omega_{-\infty} = 55$ deg) through the 10th Standard Cascade undergoing prescribed blade vibrations at unit frequency ($\omega = 1$): (a) torsional vibrations about midchord (b) bending vibrations.

5. The Unsteady Viscous Layer Analysis: UNSVIS

The viscous layer analysis, UNSVIS, applies to the unsteady compressible flows in blade boundary layers and wakes. It was originally developed [DBJ+89, PVK91] to determine the effects of unsteadiness on turbine blade heat transfer. In this analysis, the equations that govern the flows in viscous layers are transformed using an unsteady turbulent generalization of the Levy-Lees transformation. The transformed equations are then solved using a finite difference technique in which the solution proceeds by marching in time and in the streamwise direction. Both laminar and turbulent flows can be studied, the latter using algebraic turbulence and transition models. Laminar solutions for a flat plate have been shown to approach classical asymptotic results for both high and low-frequency unsteady motions; turbulent flat-plate results, to be in qualitative agreement with earlier predictions and experimental measurements [PVK91]. The numerical technique has also been applied to the stator and rotor of a low-speed turbine stage to determine unsteady effects on surface heating [DBJ+89]. The results compare reasonably well with measured heat transfer data and indicate that nonlinear effects have minimal impact on the mean and unsteady components of the flow.

Under the present contract, the UNSVIS analysis has been extended so that the unsteady viscous effects in the vicinity of leading-edge stagnation points and in blade wakes can be predicted. The stagnation point analysis also provides the "initial" upstream information needed to advance or march a numerical viscous-layer calculation downstream along the blade and wake surfaces. In addition, a wake analysis, used previously in UNSVIS, has been extended so that the changes or jumps in the inviscid velocity that occur across vortex-sheets unsteady wakes could be accommodated.

The UNSVIS analysis is described in detail below and demonstrated via application to two cascade configurations. In particular, this nonlinear unsteady viscous-layer analysis has been applied to study the viscous-layer responses of an unstaggered flat-plate cascade and a turbine cascade to external pressure excitations. The flat-plate results indicate that viscous-layers respond linearly to upstream pressure excitations over a broad range of excitation amplitudes and temporal frequencies, but the responses to downstream pressure excitations at high amplitude and/or high temporal frequency have significant nonlinear content. The coupled LINFLO/UNSVIS analysis has been applied to a turbine cascade subjected to a pressure excitation from upstream to demonstrate the current, weak, inviscid/viscid interaction solution capability for unsteady flows on a realistic cascade configuration.

5.1 Governing Equations

For flows through blade rows, occurring at high Reynolds number, the viscous region consists of thin boundary layers that lie along the upper and lower surfaces of each blade and thin wakes which extend downstream from the blade trailing edges, as indicated in Figure 2.3. The equations that govern such flows have been derived in § 2.3 with respect to moving, reference, shear-layer surfaces $\mathcal{S}_m$, each of which is contained entirely within a viscous layer. These surfaces are taken to coincide with the suction and pressure surfaces of the blades and to lie entirely within the viscous wake. The curvatures of a reference shear layer surface are assumed to be $\mathcal{O}(1)$ and, at this point, we assume that the amplitude, $|\mathcal{R}|$, of the unsteady

blade motion and the local time derivative $\partial/\partial t|_{\mathbf{x}}$ are of $\mathcal{O}(1)$. Subsequently, we will restrict our consideration to blades undergoing small (i.e., $\mathcal{O}(\epsilon)$) amplitude motions. The exact locations of the wake shear-layer surfaces (lines) are unknown *a priori*; however, to within lowest order, wake boundary conditions can be referred to any arbitrary surface emanating from the trailing edge and lying within the actual viscous wake [Vel80]. For steady flow calculations, the reference wake surfaces are taken to be the aft stagnation stream surfaces, as determined from an inviscid solution.

It is convenient to use forms of the viscous-layer equations that contain the relative fluid velocity and relative total enthalpy, i.e.,

$$\tilde{\mathbf{U}} = \tilde{\mathbf{V}} - \dot{\boldsymbol{\mathcal{R}}} \quad \text{and} \quad \tilde{H}_R = \tilde{H} + \tilde{U}^2/2 \;, \tag{5.1}$$

respectively, as dependent flow variables. Here $\boldsymbol{\mathcal{R}}(\bar{\mathbf{x}}, t) = \mathbf{x}(\bar{\mathbf{x}}, t) - \bar{\mathbf{x}}$ is prescribed such that $\boldsymbol{\mathcal{R}}(\bar{\mathbf{x}}, t) = \boldsymbol{\mathcal{R}}_{\mathrm{B}}(\bar{\mathbf{x}}, t)$ for $\bar{\mathbf{x}} \in \mathrm{B}$. Thus, the two-dimensional flows in the thin boundary layers that lie along the upper and lower surfaces of each blade and in the thin wake that extends downstream from the blade trailing edge are governed approximately by the following system of field equations, cf. (2.28)–(2.30):

$$\left.\frac{\partial \tilde{\bar{\rho}}}{\partial t}\right|_{\mathbf{x}} + \frac{\partial}{\partial \tau}(\tilde{\bar{\rho}}\tilde{U}_\tau) + \frac{\partial}{\partial n}(\tilde{\bar{\rho}}\tilde{U}_n) = \tilde{S}_1(\mathbf{x}, t) \;, \tag{5.2}$$

$$\tilde{\bar{\rho}}\left[\left.\frac{\partial \tilde{U}_\tau}{\partial t}\right|_{\mathbf{x}} + (\tilde{\mathbf{U}}\cdot\boldsymbol{\nabla})\tilde{U}_\tau\right] + \frac{\partial \tilde{P}}{\partial \tau} - (\mathrm{Re})^{-1}\frac{\partial}{\partial n}\left(\tilde{\bar{\mu}}\frac{\partial \tilde{U}_\tau}{\partial n} - \tilde{\bar{\rho}}\overline{v'_\tau v'_n}\right) = \tilde{S}_2(\mathbf{x}, t) \;, \tag{5.3}$$

and

$$\tilde{\bar{\rho}}\left[\left.\frac{\partial \tilde{H}_R}{\partial t}\right|_{\mathbf{x}} + (\tilde{\mathbf{U}}\cdot\boldsymbol{\nabla})\tilde{H}_R\right] - \left.\frac{\partial \tilde{P}}{\partial t}\right|_{\mathbf{x}} - (\mathrm{Re})^{-1}\frac{\partial}{\partial n}\left[\left(\tilde{\bar{\mu}} - (Pr)^{-1}\tilde{\bar{k}}\right)\tilde{U}_\tau\frac{\partial \tilde{U}_\tau}{\partial n} + \tilde{\bar{k}}(Pr)^{-1}\frac{\partial \tilde{H}_R}{\partial n} - \tilde{\bar{\rho}}\overline{h'_T v'_n}\right]$$

$$= \tilde{S}_3(\mathbf{x}, t) \;. \tag{5.4}$$

Here, τ and n measure distances along and normal to the moving shear layer surface, and $\tilde{U}_\tau$ and $\tilde{U}_n$ are the fluid velocity components in the positive τ- and n-directions, respectively, relative to the moving shear-layer surface. A distinction should be made between the independent variables that describe the flows in the upper and lower surface boundary layers and in the wakes, e.g., by attaching subscripts to τ and n. However, as a convenience, we are neglecting to make this distinction explicitly.

The source terms on the right-hand-sides of (5.2)–(5.4) are given by

$$\tilde{S}_1 = -\boldsymbol{\nabla}_{\mathbf{x}}\cdot(\tilde{\bar{\rho}}\dot{\boldsymbol{\mathcal{R}}}) \;, \quad \tilde{S}_2 = -\tilde{\bar{\rho}}\left[\frac{D\dot{\boldsymbol{\mathcal{R}}}}{Dt}\cdot\boldsymbol{\tau} + (\dot{\boldsymbol{\mathcal{R}}}\cdot\boldsymbol{\nabla}_{\mathbf{x}})\tilde{U}_\tau\right] \;,$$

and

$$\tilde{S}_3 = -\tilde{\bar{\rho}}\left[\frac{D}{Dt}(\tilde{U}_\tau\dot{\mathcal{R}}_\tau + \dot{\mathcal{R}}_\tau^2/2) + (\dot{\boldsymbol{\mathcal{R}}}\cdot\boldsymbol{\nabla}_{\mathbf{x}})\tilde{H}_R\right] \;, \tag{5.5}$$

where $\dot{\boldsymbol{\mathcal{R}}} = \partial\boldsymbol{\mathcal{R}}/\partial t|_{\bar{\mathbf{x}}}$. If the blade motions are of small-amplitude, i.e., on the order of the displacement thickness, $\tilde{\bar{\delta}}$, then to within the order of the viscous-layer approximation, the right-hand sides of (5.2)–(5.4) can be regarded as negligible.

The symbols $\tilde{\rho}$, $\tilde{U}_\tau$, $\tilde{U}_n$, $\tilde{P}$, $\tilde{H}_R$, $\tilde{\mu}$ and $\tilde{\bar{k}}$ in (5.2)–(5.4) refer to ensemble (or Reynolds) averaged values of the fluid dynamic variables; v'_τ, v'_n and h'_T are the values associated with random turbulent fluctuations; and the overbar indicates a turbulent correlation, which must be determined empirically. As a consequence of the high Re and surface curvature assumptions, the pressure in the thin viscous layers is a function only of τ and t, and $\tilde{H}_R \approx \tilde{T} + \tilde{U}_\tau^2/2$. Also, the pressure and the flow properties at the edge of each viscous layer are equal to the inviscid values of these variables at the reference shear layer surface. If the interactions between the flows in the viscous layer and the external inviscid stream are weak, then the pressure within a viscous layer and the flow properties at its edge are determined by an inviscid solution for these flow variables. The latter is determined subject to surface conditions that account for the effects of viscous displacement.

In addition to the foregoing field equations, the equation of state for a perfect gas, i.e., (2.11), empirical laws relating the molecular viscosity and the thermal conductivity to the temperature, e.g., (2.10), and equations relating the turbulent correlations $\overline{v'_\tau v'_n} = \overline{u'_\tau u'_n}$ and $\overline{h'_T v'_n} = \overline{h'_R u'_n}$ to the ensemble-averaged flow quantities, are also required. The turbulent correlations $\overline{v'_\tau v'_n}$ and $\overline{h'_T v'_n}$ are related to gradients of the mean-flow variables, using Prandtl's mixing-length hypothesis, cf., (2.32).

Initial and Boundary Conditions

The foregoing system of field equations, (5.2)–(5.4) is parabolic in time and in the streamwise or τ-direction. Therefore, the streamwise component of the relative velocity, $\tilde{U}_\tau$, and the relative total enthalpy, $\tilde{H}_R$, must be known for all time at some upstream streamwise location, and these variables, along with the normal velocity, $\tilde{U}_n$, must be known throughout the solution domain at some initial time. Also, conditions on the fluid properties at the edge(s) of the viscous layer, i.e.,

$$\tilde{U}_\tau \to \tilde{U}_{\tau,e}(\tau,t) \quad \text{and} \quad \tilde{H}_R \to \tilde{H}_{R,e}(\tau,t) \quad \text{for} \quad n \to \pm\infty \,, \tag{5.6}$$

where the limits $+\infty$ and $-\infty$ refer to the edges of the upper $(+)$ and lower $(-)$ surface boundary layers and the upper and lower edges of a wake, a no-slip condition and either a prescribed temperature or heat flux condition at a solid blade surface, i.e.,

$$\tilde{\mathbf{U}} = 0 \quad \text{and} \quad \tilde{H}_R = \tilde{H}_{R,w}(\tau,t) \quad \text{or} \quad \frac{\partial \tilde{H}_R}{\partial n} = -\tilde{\bar{\kappa}}^{-1}(Re \cdot Pr)^{-1}\tilde{Q}_w \quad \text{for} \quad n = 0 \,, \quad \tau \le \tau_{\text{TE}} \,; \tag{5.7}$$

and a condition on the fluid velocity normal to a reference wake streamline, i.e.,

$$\tilde{\mathbf{U}} \cdot \mathbf{n} = 0 \quad \text{for} \quad n = 0 \,, \quad \tau > \tau_{\text{TE}} \,, \tag{5.8}$$

must be enforced. Here the subscripts w and e denote the values of the fluid properties at a solid wall and at the edge of the viscous layer, respectively, and the subscript TE refers to the airfoil trailing-edge point. The relative fluid velocity, $\tilde{U}_{\tau,e}$, and relative total enthalpy, $\tilde{H}_{R,e}$, at the edges of the viscous layers are determined by the inviscid solution along the blade surfaces and the reference wake surfaces.

The models used here and in [PVK91] to simulate the effects of turbulence and transition on the flow in the viscous layer are the algebraic eddy-viscosity model proposed by Cebeci and Smith [CS74], the transition length correlation model proposed by Dhawan and Narashima [DN58], and the wake turbulence model proposed by Chang *et al* [CBCW86]. Also, since flows in turbomachines are known to be characterized by high freestream turbulence levels, a simple modification, developed by Yuhas [Yuh81], has been incorporated into the turbulence model to account for the effects of freestream turbulence on the viscous layer. These models are easy to implement, and are known to be reasonably accurate for steady flows with mild pressure gradients; however, they have only been developed for steady flows. We have modified them here for application to unsteady flows simply by replacing steady flow variables by their time-dependent counterparts. Thus, the ability of the models given below to accurately represent turbulence and transition in unsteady flows is not known; therefore, any resulting unsteady flow predictions must be interpreted with some caution.

The Cebeci-Smith algebraic model divides a solid-surface boundary layer into inner and outer regions, where $\tilde{\bar{\epsilon}} = \tilde{\bar{\epsilon}}_i$ and $\tilde{\bar{\epsilon}} = \tilde{\bar{\epsilon}}_o$, respectively. The inner model is applied from the wall out to the point at which $\tilde{\bar{\epsilon}}_i = \tilde{\bar{\epsilon}}_o$; the outer model, from this point to the edge of the boundary layer. For unsteady flows over moving blades, we set the eddy viscosity in the inner region according to

$$\tilde{\bar{\epsilon}}_i = \tilde{\bar{\gamma}}_{Tr}\tilde{\bar{\rho}}(0.41n)^2[1-\exp(-n/\tilde{A}_T)]^2\mathrm{Re}\left|\frac{\partial \tilde{U}_\tau}{\partial n}\right| , \tag{5.9}$$

where

$$\tilde{A}_T = \frac{26\tilde{\bar{\mu}}}{\tilde{\bar{\rho}}\sqrt{\mathrm{Re}}}\left\{\left(\tilde{\bar{\rho}}^{-1}\tilde{\bar{\mu}}\frac{\partial \tilde{U}_\tau}{\partial n}\right)_w\left[1-11.8\tilde{P}^+\left(\frac{\tilde{\bar{\mu}}_w}{\tilde{\bar{\mu}}_e}\right)\left(\frac{\tilde{\bar{\rho}}_e}{\tilde{\bar{\rho}}_w}\right)^2\right]\right\}^{-\frac{1}{2}} ,$$

$$\tilde{P}^+ = \sqrt{\mathrm{Re}}\frac{\tilde{\bar{\mu}}_e}{\tilde{\bar{\rho}}_e}\left(\frac{\partial \tilde{U}_{\tau,e}}{\partial t}+\tilde{U}_{\tau,e}\frac{\partial \tilde{U}_{\tau,e}}{\partial \tau}\right)\left(\tilde{\bar{\rho}}^{-1}\tilde{\bar{\mu}}\frac{\partial \tilde{U}_\tau}{\partial n}\right)_w^{-\frac{3}{2}} , \tag{5.10}$$

and $\tilde{\bar{\gamma}}_{Tr}$ is a longitudinal intermittency factor which models transitional flow.

The eddy viscosity in the outer region is given by

$$\tilde{\bar{\epsilon}}_o = \tilde{\bar{\gamma}}_{Tr}\mathrm{Re}\tilde{\bar{\rho}}\tilde{U}_{\tau,e}\tilde{\bar{\chi}}\int_0^\infty (1-\tilde{U}_\tau/\tilde{U}_{\tau,e})dn , \tag{5.11}$$

where

$$\tilde{\bar{\chi}} = 1.55\chi_0(1+\tilde{\bar{\pi}})^{-1} , \quad \tilde{\bar{\pi}} = 0.55[1-\exp(-.243\tilde{Z}_1^{1/2}-.298\tilde{Z}_1)] ,$$

$$\tilde{Z}_1 = \begin{cases} \tilde{\mathrm{Re}}_\theta/425-1 & \text{for } \tilde{\mathrm{Re}}_\theta > 425 \\ 0 & \text{for } \tilde{\mathrm{Re}}_\theta \le 425 , \end{cases} \tag{5.12}$$

and

$$\tilde{\mathrm{Re}}_\theta = \frac{\tilde{\bar{\rho}}_w\tilde{U}_{\tau,e}\mathrm{Re}}{\tilde{\bar{\mu}}_w}\int_0^\infty \frac{\tilde{U}_\tau}{\tilde{U}_{\tau,e}}\left(1-\frac{\tilde{U}_\tau}{\tilde{U}_{\tau,e}}\right)dn .$$

The parameter $\tilde{\tilde{\pi}}$ has been defined to account for low momentum thickness Reynolds number. The Clauser constant, χ_0, is usually set equal to 0.0168, but following Yuhas [Yuh81] we set

$$\chi_0 = 0.0168[1.0 + 18.4(\overline{\mathbf{v}' \cdot \mathbf{v}'})^{\frac{1}{2}}_{-\infty} + 99.6(\overline{\mathbf{v}' \cdot \mathbf{v}'})_{-\infty}] \ , \tag{5.13}$$

where $(\overline{\mathbf{v}' \cdot \mathbf{v}'})_{-\infty}$ is the mean-square of the inflow freestream turbulence velocity, to account for the effects of freestream turbulence on the development of the turbulent boundary layer.

Blade boundary layers can contain transitional regions of significant extent. Therefore, a transition model is needed to predict such flows. Several models have been proposed for steady transitional flows, based upon correlations with experimental data. One of these is the Dhawan-Narashima forced transition model [DN58] in which the intermittency factor in the transition region is given by

$$\tilde{\tilde{\gamma}}_{T_\tau} = 1 - \exp\left[-4.6513\left(\frac{\tau - \tau_1}{\tau_2 - \tau_1}\right)^2\right] \ , \quad \tau_1 < \tau < \tau_2 \ , \tag{5.14}$$

Here τ_1 and τ_2 are the streamwise locations at the beginning and end of the transition region, respectively. These locations can be specified as functions of time to model unsteady flows. The intermittency factor is set equal to 0 and 1 in laminar and fully turbulent regions, respectively. Therefore if τ_2 is set equal to τ_1 the transition is regarded as instantaneous.

The eddy viscosity in the wake is based on the model developed by Chang *et al* [CBCW86]. At each streamwise station in the wake equation (5.11) is evaluated twice: once for $-\infty < n \leq n_{\min}$, where $n_{\min}$ is the location at which the streamwise velocity reaches a minimum value, and once for $n_{\min} \leq n < \infty$. The maximum of these two values, $\epsilon_{\max}$, is then used to set the eddy viscosity, $\tilde{\tilde{\epsilon}}_{\mathcal{W}}$, i.e., we set,

$$\tilde{\tilde{\epsilon}}_{\mathcal{W}} = \tilde{\tilde{\epsilon}}_{\max} - [\tilde{\tilde{\epsilon}}_{\max} - \tilde{\tilde{\epsilon}}_{\max,\mathrm{TE}}] \exp\left[-\frac{\tau - \tau_{\mathrm{TE}}}{20\tilde{\tilde{\delta}}_{\mathrm{TE}}}\right] \ . \tag{5.15}$$

In this equation $\tau - \tau_{\mathrm{TE}}$ is the distance measured along the reference wake surface from the trailing edge point, and $\tilde{\tilde{\delta}}_{\mathrm{TE}}$ is the sum of the upper and lower surface boundary-layer thicknesses at the trailing edge. The boundary-layer thickness is defined to be the normal distance from a blade surface to the point at which $\tilde{V}_\tau / \tilde{V}_{\tau,e} = 0.995$.

5.2 Transformed Equations

For laminar flows, the Levy-Lees transformation [see Blottner [Blo70]] provides independent variables that effectively capture the growth of the viscous layer with increasing streamwise distance. In addition, the transformed equations reduce to similarity equations at an airfoil leading edge. These features facilitate the determination of a numerical solution. Thus, an extension of the Levy-Lees transformation, in which the laminar edge viscosity is replaced by an effective turbulent viscosity [VWV82], is applied herein to accommodate unsteady turbulent flows. Note that the dependent variables defined below differ from those used in § 4 for steady flows. Also, in the present implementation, we do not restrict our consideration to adiabatic flows at unit Prandtl number.

We define new independent variables ξ and η according to

$$\xi = \int_0^\tau \bar{Q} d\tau \quad \text{and} \quad \eta = \frac{\tilde{U}_{\tau,e}\sqrt{\mathrm{Re}}}{\sqrt{2\xi}} \int_0^n \tilde{\rho} dn \ , \tag{5.16}$$

where $\bar{Q} = \bar{\rho}_e U_{\tau,e} \bar{\mu}_e [1 + (\bar{\epsilon}/\bar{\mu})_e] = \bar{\rho} U_{\tau,e} \mu_{\mathrm{eff},e}$ and $\bar{\epsilon}$ and $\bar{\mu}$ are the turbulent eddy and molecular viscosities in the steady background flow. In [PVK91] the temporal mean values of the fluid properties, $\tilde{\bar{\rho}}_e$, $\tilde{U}_{\tau,e}$, and $\tilde{\bar{\mu}}_e$, at the edge of the viscous layer were used to define $\tilde{Q}$. However, in the present discussion, we regard the unsteady inviscid flow as a small perturbation of a nonlinear mean flow. Therefore, we can replace the temporal mean values of these variables by their values in the steady background flow to avoid introducing additional nomenclature. The coordinate ξ in (5.16) is a function of τ alone; the coordinate η, by contrast, is a function of τ, n, and t.

We also introduce the new dependent variables

$$\mathcal{F} = \frac{\tilde{U}_\tau}{\tilde{U}_{\tau,e}}, \quad \mathcal{V} = \frac{2\xi}{\tilde{Q}} \left(\frac{1}{\tilde{U}_{\tau,e}} \frac{\partial \eta}{\partial t} + \mathcal{F} \frac{\partial \eta}{\partial \tau} + \sqrt{\frac{\mathrm{Re}}{2\xi}} \tilde{\rho} \tilde{U}_n \right) \quad \text{and} \quad \mathcal{G} = \frac{\tilde{H}_R}{\tilde{H}_{R,e}} \ , \tag{5.17}$$

where $\tilde{Q} = \tilde{\bar{\rho}}_e \tilde{U}_{\tau,e} \tilde{\bar{\mu}}_e [1 + (\tilde{\bar{\epsilon}}/\tilde{\bar{\mu}})_e]$. After substituting Eqs. (5.16) and (5.17) into the viscous-layer field equations and performing some algebra, we find that

$$2\xi \frac{\bar{Q}}{\tilde{Q}} \frac{\partial \mathcal{F}}{\partial \xi} + \frac{\bar{Q}}{\tilde{Q}} \mathcal{F} + \frac{\partial \mathcal{V}}{\partial \eta} - \alpha_1 \alpha_3 = \frac{2\xi \tilde{S}_1(\xi, \eta, t)}{\tilde{\rho} \tilde{U}_{\tau,e} \tilde{Q}} \tag{5.18}$$

$$\begin{aligned} &\frac{2\xi}{\tilde{Q} \tilde{U}_{\tau,e}} \frac{\partial \mathcal{F}}{\partial t} + 2\xi \frac{\bar{Q}}{\tilde{Q}} \mathcal{F} \frac{\partial \mathcal{F}}{\partial \xi} + \mathcal{V} \frac{\partial \mathcal{F}}{\partial \eta} + \alpha_3 (\alpha_1 \mathcal{F} + \frac{\alpha_2}{2} \mathcal{F}^2 - \mathcal{G}) \\ &+ \alpha_4 (\mathcal{F}^2 - \mathcal{G}) - \frac{\partial}{\partial \eta} \left(l \frac{\partial \mathcal{F}}{\partial \eta} \right) = \frac{2\xi \tilde{S}_2(\xi, \eta, t)}{\tilde{\rho} \tilde{U}_{\tau,e}^2 \tilde{Q}} \end{aligned} \tag{5.19}$$

and

$$\begin{aligned} &\frac{2\xi}{\tilde{Q} \tilde{U}_{\tau,e}} \frac{\partial \mathcal{G}}{\partial t} + 2\xi \frac{\bar{Q}}{\tilde{Q}} \mathcal{F} \frac{\partial \mathcal{G}}{\partial \xi} + \mathcal{V} \frac{\partial \mathcal{G}}{\partial \eta} + \alpha_5 (\mathcal{F}^2 - \mathcal{G}) + \alpha_6 (\alpha_1 \mathcal{F} \mathcal{G} + \frac{\alpha_2}{2} \mathcal{F}^2 - \mathcal{G}) \\ &+ \alpha_2 \frac{\partial}{\partial \eta} \left[(\hat{l} - l) \mathcal{F} \frac{\partial \mathcal{F}}{\partial \eta} \right] - \frac{\partial}{\partial \eta} \left(\hat{l} \frac{\partial \mathcal{G}}{\partial \eta} \right) = \frac{2\xi \tilde{S}_3(\xi, \eta, t)}{\tilde{\rho} \tilde{U}_{\tau,e} \tilde{H}_{R,e} \tilde{Q}} \ , \end{aligned} \tag{5.20}$$

where the following parameters have been introduced:

$$\alpha_1 = \left(1+\frac{\tilde{U}^2_{\tau,e}}{2\tilde{T}_e}\right)^{-1}, \qquad \alpha_2 = \tilde{U}^2_{\tau,e}\tilde{T}_e^{-1}\alpha_1 ,$$

$$\alpha_3 = 2\xi(\tilde{\mathcal{Q}}\alpha_1\tilde{U}^2_{\tau,e})^{-1}\frac{\partial \tilde{U}_{\tau,e}}{\partial t}, \qquad \alpha_4 = 2\xi\bar{\mathcal{Q}}(\tilde{\mathcal{Q}}\alpha_1\tilde{U}_{\tau,e})^{-1}\frac{\partial \tilde{U}_{\tau,e}}{\partial \xi}, \tag{5.21}$$

$$\alpha_5 = 2\xi(\tilde{\mathcal{Q}}\tilde{U}_{\tau,e}\tilde{H}_{R,e})^{-1}\frac{\partial \tilde{H}_{R,e}}{\partial t}\left(\frac{\tilde{U}^2_{\tau,e}}{2\tilde{T}_e}\right), \qquad \alpha_6 = 2\xi\bar{\mathcal{Q}}(\tilde{\mathcal{Q}}\alpha_1\tilde{H}_{R,e})^{-1}\frac{\partial \tilde{H}_{R,e}}{\partial \xi},$$

$$l = \frac{\tilde{\bar{\rho}}\tilde{\bar{\mu}}(1+\tilde{\bar{\epsilon}}/\tilde{\bar{\mu}})}{\tilde{\bar{\rho}}_e\tilde{\bar{\mu}}_e[1+(\tilde{\bar{\epsilon}}/\bar{\mu})_e]}, \quad \text{and} \quad \hat{l} = \frac{\tilde{\bar{\rho}}\tilde{\bar{\mu}}[1+\tilde{\bar{\epsilon}}Pr/(\tilde{\bar{\mu}}Pr_T)]}{\tilde{\bar{\rho}}_e\tilde{\bar{\mu}}_e[1+(\tilde{\bar{\epsilon}}/\tilde{\bar{\mu}})_e]Pr}.$$

Special attention must be exercised in applying the foregoing transformation to unsteady wakes. In the present analysis all quantities on the upper (i.e., $n > 0$) and lower ($n < 0$) sides of a wake are referenced to their respective edge conditions, i.e., we set $\mathcal{F} = \tilde{U}_\tau/\tilde{U}^+_{\tau,e}$ for $n > 0$ and $\mathcal{F} = \tilde{U}_\tau/\tilde{U}^-_{\tau,e}$ for $n < 0$. In general, the inviscid streamwise relative velocity, $\tilde{U}_{\tau,e}$, and relative total enthalpy, $\tilde{H}_{R,e}$, will be discontinuous across unsteady wakes. As a consequence, the dependent variables $\mathcal{F}$ and $\mathcal{G}$ are discontinuous across reference ($n = 0$) wake streamlines. These discontinuities must be taken into account in developing a numerical solution procedure, to ensure that the physical variables ($\tilde{U}_\tau$, $\tilde{U}_n$ and $\tilde{H}_R$) are continuous across viscous wakes. Also, the upper- and lower-surface values of the independent variable ξ will generally differ at a blade trailing edge. In the present effort, the upper-surface ξ-variable is used to continue the viscous calculation into the wake, i.e., we set

$$\xi_W = \xi^+_{\mathrm{TE}} + \int_{\tau_{\mathrm{TE}}}^{\tau} \bar{\mathcal{Q}}^+ d\tau , \quad \tau > \tau_{te} \tag{5.22}$$

However, two different η-coordinates

$$\eta^{\pm}_W = \frac{\tilde{U}^{\pm}_{\tau,e}\sqrt{\mathrm{Re}}}{\sqrt{2\xi_W}}\int_0^n \tilde{\bar{\rho}} dn , \quad \tau > \tau_{TE} , \quad n \gtrless 0 , \tag{5.23}$$

are used for the wake calculation. Thus, at the trailing edge, the lower-surface boundary-layer solution must be interpolated onto the wake η-mesh before continuing the viscous calculation into the wake.

Boundary and Initial Conditions on $\mathcal{F}$ and $\mathcal{G}$

In addition to satisfying the field equations (5.18)—(5.20), the dependent variables $\mathcal{F}$ and $\mathcal{G}$ must be prescribed functions of ξ and η at some initial time, and prescribed functions of η and t at initial or upstream streamwise locations on the upper and lower surfaces of each blade. Also, in terms of the transformed variables, the following conditions must be imposed at the edge(s) of the viscous layer, on the blade surface, and along the reference wake streamline, cf. (5.6), (5.7) and (5.8):

$$\mathcal{F} \to 1 \quad \text{and} \quad \mathcal{G} \to 1 \quad \text{for} \quad |\eta| \to \infty , \tag{5.24}$$

$$\mathcal{F} = 0,\ \mathcal{V} = 0, \quad \text{and} \quad \mathcal{G} = \mathcal{G}_w(\xi,t) = \tilde{H}_{R,w}/\tilde{H}_{R,e} \quad \text{or}$$

$$(\partial\mathcal{G}/\partial\eta)_w = \frac{-(2\xi Re)^{\frac{1}{2}}\tilde{\bar{k}}Pr\tilde{Q}_w(\xi,t)}{\tilde{\bar{\rho}}_e\tilde{U}_{\tau,e}\tilde{H}_{R,e}} \quad \text{for} \quad \eta = 0,\ \xi \le \xi_{\text{TE}}\ , \tag{5.25}$$

and

$$\mathcal{V} = 0 \quad \text{for} \quad \eta = 0,\ \xi > \xi_{\text{TE}}\ , \tag{5.26}$$

respectively.

For the calculations reported herein, the condition at the initial time is the viscous-layer solution in the absence of unsteady excitation, i.e., the solution for the steady background flow. The calculated transients resulting from this approximation have been found to die out with increasing time. The upstream profiles, required at each time step of the unsteady viscous-layer calculation, are obtained from a similarity analysis of the flow in the stagnation region, as described below.

5.3 Solution Procedure

Stagnation Region

To determine solutions for the flows in the viscous layers, we first seek a local, similarity solution for the flow in a leading-edge stagnation region. This solution can then be used to set the instantaneous upstream profiles, $\mathcal{F}(\xi_I^{\pm},\eta,t)$ and $\mathcal{G}(\xi_I^{\pm},\eta,t)$, that are required to initiate a space-marching, numerical, viscous-layer calculation. The overall strategy is to develop a similarity solution for a simple flow configuration and then, to adapt this result for application to the unsteady cascade problem. The present analysis for unsteady, compressible flow is modeled after the incompressible analyses developed independently by Rott [Rot56] and Glauert [Gla56]. Their analyses provided an exact solution to the Navier-Stokes equations for incompressible flow. An exact result can not be determined for compressible flow, however, because it is necessary to neglect the dissipation term in the energy equation to obtain a similarity solution. Fortunately, frictional heat dissipation in the stagnation region is of limited importance for a wide range of practical flows.

We consider two-dimensional, compressible flow around a flat plate, which is oriented normal to the stream direction and undergoes a harmonic motion at velocity $i\omega R_\tau \exp(i\omega t)$ in its own plane. As a mathematical convenience, we use complex-variable representations for the unsteady flow properties, but it is to be understood that the real parts of the various complex parameters represent the actual physical variables. The flow in the viscous layer will be determined in terms of space-fixed Cartesian coordinates, τ_S and n_S. The resulting stagnation-region solution can then be expressed in terms of plate-fixed coordinates as a prerequisite to its implementation into a complete unsteady viscous-layer calculation. The τ_S and n_S axes are directed along and normal to the plate, respectively, and the coordinate origin lies at the point at which the dividing inviscid streamline impinges on the plate. The fluid velocity components in the τ_S- and n_S-directions are $\tilde{V}_{\tau_S}$ and $\tilde{V}_{n_S}$, respectively.

The inviscid flow is steady in the space-fixed frame, with velocity and pressure gradient at the edge of the viscous layer (i.e., at $n_S = 0$ in the inviscid region) given by

$$\tilde{\mathbf{V}}_e = \tilde{V}_{\tau_S,e}\mathbf{e}_{\tau_S} = c\tau_S\mathbf{e}_{\tau_S}\ , \tag{5.27}$$

and

$$\boldsymbol{\nabla}\tilde{P} = \frac{\partial \tilde{P}}{\partial \tau_S}\mathbf{e}_{\tau_S} = -\tilde{\tilde{\rho}}_e \tilde{V}_{\tau_S,e}\frac{\partial \tilde{V}_{\tau_S,e}}{\partial \tau_S}\mathbf{e}_{\tau_S} = -\tilde{\tilde{\rho}}_e c^2 \tau_S \mathbf{e}_{\tau_S} \ . \tag{5.28}$$

The constant c in these equations is determined from the behavior of the inviscid solution in the vicinity of the mean stagnation-point location ($\tau_S = 0$). The total enthalpy at the edge of the viscous layer is constant, i.e., $\tilde{H}_{T,e} = \tilde{T}_e + \tilde{V}^2_{\tau_S,e}/2 = H_{-\infty}$.

The flow in the viscous layer is described by the field equations (5.2)–(5.4) or, in this case, (2.28)–(2.30), the edge conditions (2.36) and the surface conditions (2.34). The surface velocity components are

$$\tilde{V}_{\tau_S}(\tau_S, n_S, t) = i\omega R_\tau \exp(i\omega t) \quad \text{and} \quad V_{n_S} = 0 \quad \text{for} \quad n_S = 0 \ . \tag{5.29}$$

We assume that the flow in the stagnation region is laminar and that the heat generated by viscous dissipation is negligible, i.e., $\tilde{\tilde{\mu}}\partial^2 \tilde{V}_{\tau_S}/\partial n_S^2 \approx 0$. The streamwise velocity and temperature can be expressed in the forms

$$\tilde{V}_{\tau_S}(\tau_S, \eta, t) = c\tau_S f'(\eta) + i\omega R_\tau g(\eta)\exp(i\omega t) \quad \text{and} \quad \tilde{T}(\tau_S, \eta, t) = \tilde{T}_e(\tau_S, t)\tilde{\tilde{\theta}}(\eta) \ , \tag{5.30}$$

where $c\tau_S f'(\eta)$ and $i\omega R_\tau g(\eta)\exp(i\omega t)$ are the steady and unsteady components of the fluid velocity in the viscous layer and

$$\eta = \left(\frac{c}{\tilde{\tilde{\rho}}_e \tilde{\tilde{\mu}}_e}\right)^{1/2} \int_0^{n_S} \tilde{\tilde{\rho}} dn_S \ . \tag{5.31}$$

Note that $\partial \tilde{P}/\partial n_S \approx 0$ and $\tilde{V}_{n_S} \ll \tilde{V}_{\tau_S}$; therefore, in the viscous layer, $\tilde{\tilde{\rho}}_e/\tilde{\tilde{\rho}} \approx \tilde{T}/\tilde{T}_e \approx \tilde{\tilde{\theta}}$ and $H_T \approx \tilde{T} + \tilde{V}^2_{\tau_S}/2$.

After substituting the foregoing results into the field equations that govern the flow in the viscous layer and performing the necessary algebra, we obtain an expression for the normal component of the fluid velocity, $\tilde{V}_{n_S}$, and the following set of ordinary differential equations for f, g and $\tilde{\tilde{\theta}}$.

$$f'^2 - ff'' - (lf'')' - \tilde{\tilde{\theta}} = 0 \ , \tag{5.32}$$

$$\left(\frac{i\omega}{c} + f'\right)g - fg' - (lg')' = 0 \ , \tag{5.33}$$

and

$$\left(\frac{l}{Pr}\tilde{\tilde{\theta}}'\right)' + f\tilde{\tilde{\theta}}' = 0 \ , \tag{5.34}$$

where $l = \tilde{\tilde{\rho}}\tilde{\tilde{\mu}}/(\tilde{\tilde{\rho}}_e\tilde{\tilde{\mu}}_e)$. The conditions on f, g and $\tilde{\tilde{\theta}}$ at the plate surface ($\eta = 0$) and at the edge of the viscous layer ($\eta \to \infty$) are

$$f(0) = f'(0) = 0 \ , \quad g(0) = 1 \quad \text{and} \quad \tilde{\tilde{\theta}}'(0) = 0 \quad \text{or} \quad \tilde{\tilde{\theta}}(0) = \tilde{T}_w/\tilde{T}_e \ ; \tag{5.35}$$

and

$$f'(\infty) = 1 \ , \quad g(\infty) = 0 \quad \text{and} \quad \tilde{\tilde{\theta}}(\infty) = 1 \ . \tag{5.36}$$

Note that for steady ($g \equiv 0$), incompressible ($\tilde{\tilde{\theta}} \equiv 1$) flow, we recover the classical stagnation-region problem studied by Hiemenz. Also, equation (5.34) is identical in form to the energy

equation that describes steady, compressible, stagnation-point flow [Whi74]. Finally, the present analysis can be readily extended to consider more general unsteady plate motions, e.g.,

$$\tilde{V}_{\tau_S} = c\tau_S f'(\eta) + \sum_{n=1}^{N} i\omega_n r_{\tau,n} g_n(\eta) \exp(i\omega_n t) \ . \tag{5.37}$$

In this case solutions for N uncoupled equations for the g_n, $n = 1, 2, 3, \ldots, N$, are required.

The set of nonlinear ordinary differential equations for f, $\tilde{\bar{\theta}}$ and g can be solved using an implicit finite-difference technique similar to that described in the next sub-section and used herein to obtain solutions to the full unsteady viscous equations. The functions f and $\tilde{\bar{\theta}}$ must be determined simultaneously, but they are independent of g, which can be determined once f is known.

To provide the upstream profiles required for a complete viscous-layer calculation it is convenient to express the stagnation-region solution in terms of body- or plate-fixed coordinates. Thus, we consider plate-fixed Cartesian coordinates (τ, n), where the τ- and n-axes are parallel to the spaced-fixed τ_S- and n_S-axes, respectively, and the mean position of the τ, n coordinate origin coincides with the origin of the spaced-fixed τ_S, n_S-frame. The streamwise positions and velocities of a fluid particle in the two coordinate frames are related by

$$\tau_S = \tau + R_\tau \exp(i\omega t) \tag{5.38}$$

and

$$\tilde{V}_{\tau_S} = \tilde{U}_\tau + i\omega R_\tau \exp(i\omega t) \ . \tag{5.39}$$

After combining (5.38) and (5.39), we find that

$$\tilde{U}_\tau = c\tau f'(\eta) + b\lambda(\eta) \exp(i\omega t) \ , \tag{5.40}$$

where

$$b = cR_\tau(1 - i\omega/c) \quad \text{and} \quad (1 - i\omega/c)\lambda(\eta) = f'(\eta) + (i\omega/c)[g(\eta) - 1] \ . \tag{5.41}$$

At the plate surface $\tilde{U}_\tau = 0$, and at the edge of the viscous layer

$$\tilde{U}_\tau(\eta \to \infty) = \tilde{U}_{\tau,e} = c\tau + b\exp(i\omega t) \ . \tag{5.42}$$

The relative total enthalpy $\tilde{H}_R = \tilde{U}_\tau^2/2 + \tilde{T}$ is given by

$$\tilde{H}_R = (c\tau f')^2/2 + cb\tau f'\lambda \exp(i\omega t) + b^2\lambda^2 \exp(2i\omega t)/2 + \tilde{T}_e\tilde{\bar{\theta}} \ . \tag{5.43}$$

The locations, i.e., $\tau = \pm|\tau_I|$, at which the stagnation-region solution can be applied as an initial condition for an unsteady viscous-layer calculation are determined by two criteria. First, the stagnation-point motion must be contained within the interval $[-|\tau_I|, |\tau_I|]$ and second, to avoid stability problems in the subsequent boundary-layer calculation, those points at which flow reversals, i.e., $(\partial\tilde{U}_\tau/\partial n)_w < 0$, occur must also be contained within this interval. Reverse flow is associated with the lag in the response of the low-momentum fluid near the wall to changes in the velocity at the edge of the viscous layer. The extent of the interval over which the stagnation point moves, i.e., $[-|\tau_M|, |\tau_M|]$, is determined from the inviscid velocity distribution (5.42) and is given by $[-c^{-1}|b|, c|b|]$. The extent of the reverse-flow

interval, i.e., $[-|\tau_R|, |\tau_R|]$, is determined by the maximum and minimum values of τ for which $(\partial \tilde{U}_\tau/\partial\eta)_w = 0$. We find that

$$|\tau_R| \leq c^{-1}|b| \left| \frac{1 + i\omega c^{-1} g'(0)/f''(0)}{1 - i\omega/c} \right| . \tag{5.44}$$

Thus, $|\tau_I| \geq \max(|\tau_M|, |\tau_R|)$. For our application to unsteady cascade flows, we have found that setting $|\tau_I| = 2c^{-1}|b|$ leads to reasonable results in the stagnation region and allows us to continue the viscous-layer calculation along the blades and their wakes.

In applying the foregoing stagnation-region analysis to unsteady cascade flows, we use the inviscid velocity distribution along a moving blade surface, i.e.,

$$\tilde{\mathbf{V}}_e \cdot \boldsymbol{\tau} = [\mathbf{V}_e + \mathbf{v}_e \exp(i\omega t) + \dots] \cdot \boldsymbol{\tau} = [\mathbf{V}_e + (\mathbf{u}_e + \mathbf{R}) \exp(i\omega t) + \dots] \cdot \boldsymbol{\tau}, \tag{5.45}$$

where $\mathbf{V}_e(\tau)$ and $\mathbf{v}_e = \mathbf{u}_e + \mathbf{R}$ are the nonlinear steady velocity and the complex amplitude of the linearized unsteady velocity, respectively, to determine the parameters c and b in (5.40) and (5.43). In particular, these parameters are determined by matching the analytical velocity profile (5.40) to the calculated inviscid velocities at $\pm|\tau_I|$. Thus, with ω specified as an input quantity, the functions f $\tilde{\tilde{\theta}}$ and g determined by an implicit finite-difference procedure and the parameters b and c determined by the inviscid solution in the vicinity of the stagnation point, the streamwise velocity and total enthalpy profiles needed to initiate the unsteady viscous-layer calculation can be specified.

Viscous-Layer Numerical Solution Procedure

The transformed viscous-layer equations (5.18)–(5.20) are solved by applying finite-difference approximations for the various partial derivatives that appear, to convert this system of differential equations into a system of algebraic equations [VBHA91]. Streamwise and temporal derivatives are approximated by first-order accurate backward difference expressions and normal derivatives, by second-order accurate central difference expressions The streamwise momentum and energy equations contain nonlinear terms, which must be li ized to ob n solutions a ach point in space and time. This is accomplished by using a wton itera n procedure ... which the initial guess for the profiles comes from the solutio... at the pre s streamwise (τ) station or time step. The equations are solved by using a local iteration to remove the linearization error, and by repeating this iteration until the values of the flow variables converge to within a specified tolerance level. The finite-difference approxi n results in a block tridiagonal system of linear algebraic equations at each step, which is d using the Thomas block inversion algorithm.

The analyses for surface boundary layers and wakes are identical, except for the implementation of different boundary conditions. In addition to replacing the surface no-slip condition with a zero normal velocity condition at the reference wake position, the possibility of jumps in the relative tangential velocity and the relative total enthalpy across a viscous wake must be taken into account. As discussed previously, the transformed governing equations are written in terms of two different sets of variables, each applying on one side of the wake, and scaled to the edge conditions for that side. For example, on the upper side of the wake, $\mathcal{F}^+ = \tilde{U}_\tau/\tilde{U}^+_{\tau,e}$ and $\mathcal{G}^+ = \tilde{H}_R/\tilde{H}^+_{R,e}$; on the lower side, $\mathcal{F}^- = \tilde{U}_\tau/\tilde{U}^-_{\tau,e}$ and $\mathcal{G}^- = \tilde{H}_R/\tilde{H}^-_{R,e}$. The discretized

equations on either side of the reference wake streamline are written in terms of that side's variables. However, at the reference wake line, ($\eta = 0$), variables from both sides of the wake are used in the momentum and energy equations, due to the use of central-difference approximations for the η-derivatives. For consistency, the equations must be written in terms of a single set of variables. This is accomplished by writing the equations in terms of the upper surface quantities. Thus, whenever a lower surface variable appears in the equations at $\eta = 0$, it is rewritten in terms of the upper surface edge conditions. For example, the variable $\mathcal{F}^-$ is written in terms of upper surface variables as $\mathcal{F}^- \cdot (\tilde{U}^-_{\tau,e}/\tilde{U}^+_{\tau,e}) = \tilde{U}^-_{\tau}/\tilde{U}^+_{\tau,e}$.

The finite-difference approximation is implemented on a grid that is nonuniform in both the ξ- and η- directions, but uniform in time. The grid distribution in the streamwise direction is chosen so as to cluster points near the blade leading and trailing edges, with each mesh interval being set equal to a constant times the previous one, according to the relation

$$\Delta\xi_{l+1} = K_\xi \Delta\xi_l \ , \quad l = 1,\ 2,\ \ldots\ , L \tag{5.46}$$

where l is the streamwise mesh point index ($l = 1$ at the blade leading edge and increases with distance downstream), $K_\xi > 1$ from the leading edge of the blade to midchord, and $K_\xi < 1$ from midchord to the trailing edge. The grid is then stretched (i.e., $K_\xi > 1$) aft of the trailing edge, and generally extends between one and two blade chords downstream of the trailing edge.

A stretched grid is also employed in the normal direction, with clustering near the blade surface to capture the large velocity gradients that occur, and to ensure that, for turbulent flow, there are enough points in the near-wall region to adequately resolve the laminar sublayer. Geometric stretching is again employed, with

$$\Delta\eta_{n+1} = K_\eta \Delta\eta_n \ , \quad n = 1,\ 2,\ \ldots\ , N \tag{5.47}$$

where n is a normal mesh point index ($n = 1$ at the blade surface or reference wake streamline and increases with increasing distance into the flow). Since the resolution requirements are a function of the solution, the normal grid stretching, K_η, and the spacing at the wall, $\Delta\eta_1$, must be determined for each case. For turbulent flow, this is accomplished by monitoring the value of Y^+ at the first mesh point off the wall (i.e., $Y^+_{n=2}$), where Y^+ is a Reynolds number based on the friction velocity, $(\tilde{\bar{\tau}}_w/\tilde{\bar{\rho}}_w)^{1/2}$ and the normal distance from the blade surface. For accuracy, Y_2^+ should be close to one, which can be achieved by adjusting $\Delta\eta_1$. The stretching parameter K_η is then adjusted to place the outer edge of the mesh, $\eta = \eta_N$, far enough from the surface to allow the edge conditions to be approached asymptotically. The number of points used in the normal direction is chosen to allow the flow over the entire viscous layer to be resolved accurately at all streamwise stations — generally, between 50 and 100 points are sufficient.

The constant value of the time-step used for the temporal discretization is chosen based on the frequency of the imposed unsteady excitation and the number of time-steps prescribed for each period of oscillation, generally between 20 and 50. More complete details on the finite-difference analysis, used herein, for viscous-layer flows are given in [VBHA91].

5.4 Numerical Results: Unsteady Flows Driven by Acoustic Disturbances

Response predictions will be given below for two-dimensional blade rows operating at subsonic Mach numbers to demonstrate the present capabilities of the unsteady viscous-layer analysis, UNSVIS. In particular, this analysis will be applied to predict the viscous-layer responses of flat-plate and turbine cascades to acoustic excitations. For these applications, the blades are assumed to be stationary in the cascade frame of reference. Hence, $\mathcal{R} \equiv 0$, $\tilde{\mathbf{U}} = \tilde{\mathbf{V}}$ and $\tilde{H}_R = \tilde{H}_T$.

Unstaggered Flat-Plate Cascade

As a benchmark case to demonstrate the UNSVIS analysis, we consider unsteady flows through an unstaggered flat-plate cascade. Here, the uniform inlet velocity $\mathbf{V}_{-\infty}$ is aligned with the mean positions of the blade chord lines. Hence, the inviscid steady background flow is uniform with velocity, pressure and total enthalpy given by $\mathbf{V} = \mathbf{e}_\xi$, $P = (\gamma M^2)^{-1}$, and $H_T = 1/2 + (\gamma - 1)^{-1} M^{-2}$, respectively. The unsteadiness is excited by incident pressure disturbances, that carry energy toward the blade row from either far upstream ($-\infty$) or far downstream ($+\infty$). The acoustic excitations travel in the axial (or chordwise) direction, i.e., $\kappa_\eta = \kappa_y = \sigma/G = 0$, and are therefore, described by a velocity potential of the form [cf. (3.20) and (3.21)].

$$\tilde{\phi}(\mathbf{x}, t) = -\mathrm{Re}\{[i(\kappa_{\xi,\mp\infty} + \omega)]^{-1} p_{I,\mp\infty} \exp[i(\kappa_{\xi\mp\infty}\xi + \omega t)]\} \ , \tag{5.48}$$

where ω, $\kappa_\xi = \kappa_x$ and $p_{I,\mp\infty}$ are the temporal frequency, axial wave number and complex amplitude of the unsteady pressure excitation, respectively. The axial wave number is related to the temporal frequency by [cf. (3.24)]

$$\kappa_{\xi,\mp\infty} = \frac{\mp\omega M}{1 \pm M} \ . \tag{5.49}$$

Note that for $|\kappa_{\xi,+\infty}| > |\kappa_{\xi,-\infty}|$, because a downstream acoustic excitation travels upstream against the freestream flow direction, whereas an excitation from upstream travels in the direction of the freestream flow.

The flat-plate cascade produces no response to the pressure excitation described by (5.48); therefore, this equation describes the first-harmonic component of the inviscid unsteady flow. The time-dependent velocity, $\tilde{\mathbf{V}}$, pressure, $\tilde{P}$, and total enthalpy, $\tilde{H}_T$, in this flow are given by

$$\begin{aligned}
\tilde{\mathbf{V}} &= \mathbf{V} + \tilde{\mathbf{v}} + \ldots = [1 \pm M\mathrm{Re}\{p_{I,\mp\infty} \exp[i(\kappa_{\xi,\mp\infty}\xi + \omega t)]]\}\mathbf{e}_\xi + \ldots \ , \\
\tilde{P} &= P + \tilde{p} + \ldots = (\gamma M^2)^{-1} + \mathrm{Re}\{p_{I,\mp\infty} \exp[i(\kappa_{\xi,\mp\infty}\xi + \omega t)]\} + \ldots \ , \\
\text{and} \\
\tilde{H}_T &= H_T + \tilde{h}_T + \ldots = H_T + (1 \pm M)\mathrm{Re}\{p_{I,\mp\infty} \exp[i(\kappa_{\xi,\mp\infty}\xi + \omega t)]\} + \ldots \ ,
\end{aligned} \tag{5.50}$$

where $\tilde{\mathbf{v}} = \nabla\tilde{\phi}$, $\tilde{p} = -\bar{D}\tilde{\phi}/Dt$, and $\tilde{h}_T = -\bar{D}\tilde{\phi}/Dt + \nabla\phi \cdot \mathbf{e}_\xi$ are the first-harmonic components of the unsteady velocity, pressure and total enthalpy, respectively. The real and imaginary components of the complex amplitude of the first-harmonic unsteady pressure acting along each blade and wake surface ($0 \le x = \xi \le 2$) for a flat-plate cascade operating at $M = 0.5$

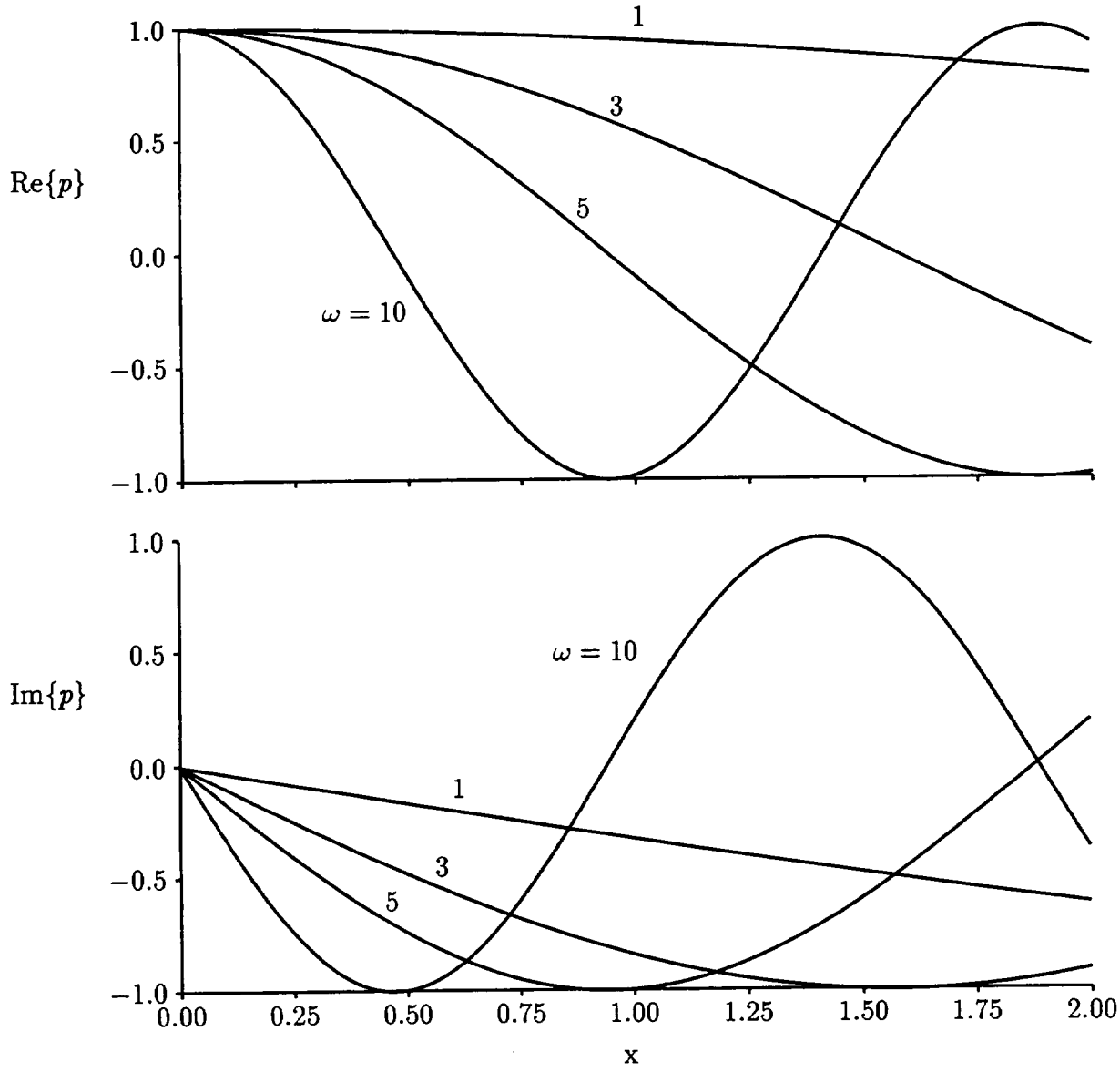

Figure 5.1: Unsteady pressure distributions along a blade and its wake for an unstaggered flat-plate cascade ($\Omega = \Theta = 0\,\text{deg}$, $M_{-\infty} = 0.5$ and $G = 1$) subjected to a unit-amplitude, $|p_{I,-\infty}| = 1$, pressure excitation from upstream with $\kappa_{\eta,-\infty} = \sigma G^{-1} = 0$.

and subjected to upstream acoustic disturbances with $p_{I,-\infty} = (1,0)$ and $\omega = 1$, 2, 5 and 10 are shown in Figure 5.1; similar results for downstream acoustic disturbances, are shown in Figure 5.2.

The inviscid results (5.50) have been used to provide the pressure and edge-condition information for a series of unsteady viscous-layer calculations. The latter will allow us to examine the effects of the amplitude, temporal frequency and axial wave number of a pressure excitation on the behavior of various viscous-layer response quantities; in particular, the displacement thickness, $\tilde{\bar{\delta}}(\mathbf{x}, t)$, surface shear stress $\tilde{\bar{\tau}}_w = (\text{Re})^{-1}(\tilde{\bar{\mu}}\partial\tilde{V}_\tau/\partial n)_w$ and wake centerline

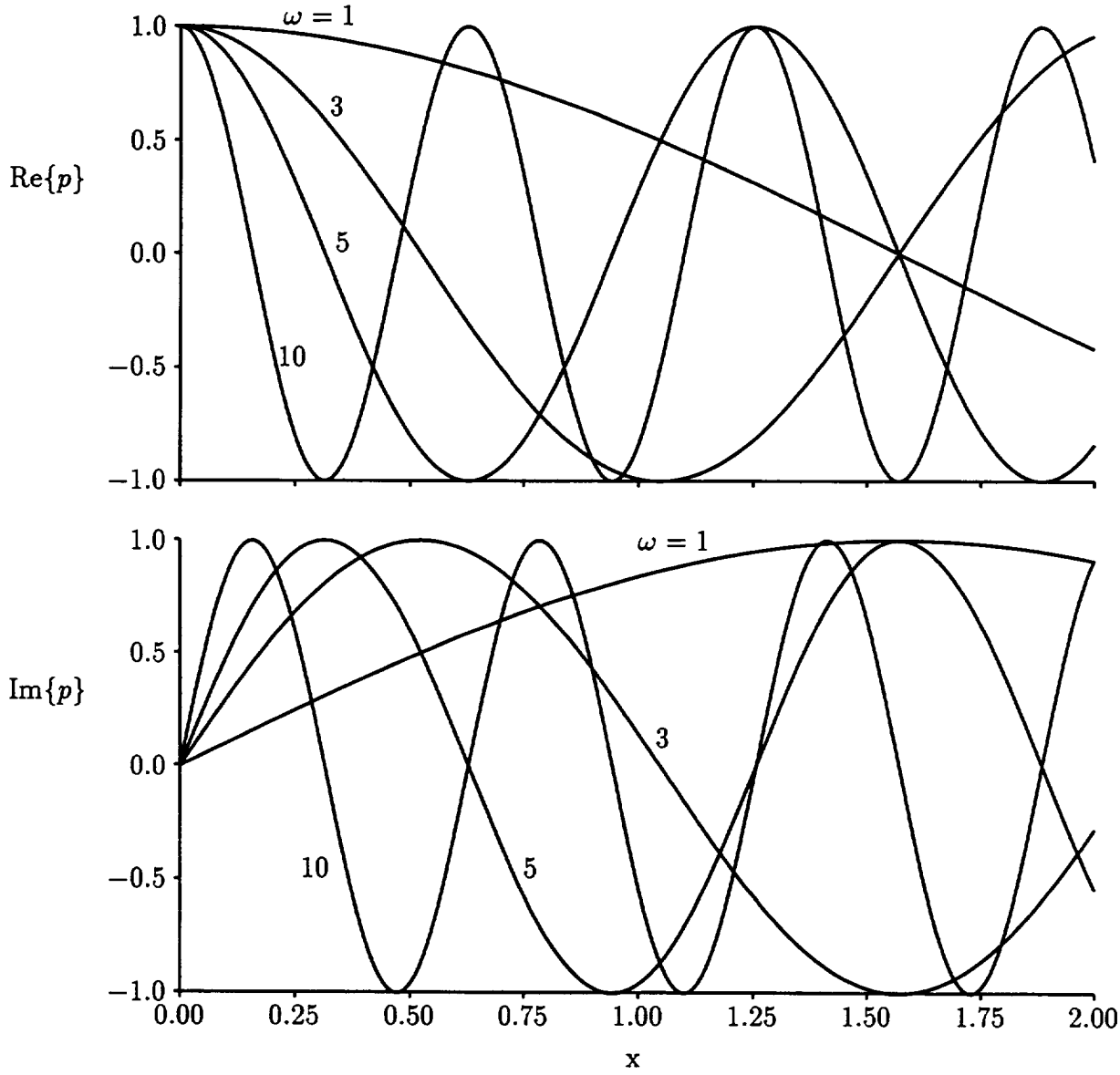

Figure 5.2: Unsteady pressure distributions along a blade and its wake for an unstaggered flat-plate cascade (with $\Omega = \Theta = 0\,\text{deg}$, $M_{-\infty} = 0.5$ and $G = 1$) subjected to a unit-amplitude, $|p_{I,+\infty}| = 1$, pressure excitation from downstream with $\kappa_{\eta,+\infty} = \sigma G^{-1} = 0$.

velocity $\tilde{V}_{\mathcal{L}}$. We can decompose each of these quantities into Fourier series; e.g.,

$$\tilde{\tilde{\delta}}(\mathbf{x},t) = \int_0^\infty [1 - \tilde{\tilde{\rho}}\tilde{V}_\tau/(\tilde{\tilde{\rho}}_e\tilde{V}_{\tau,e})]dn = \sum_{n=-\infty}^{\infty} \delta_n(\mathbf{x})\exp(in\omega t)\ , \tag{5.51}$$

where

$$\delta_n(\mathbf{x}) = \frac{\omega}{2\pi}\int_0^{2\pi/\omega} \tilde{\tilde{\delta}}(\mathbf{x},t)\exp(-in\omega t)dt\ , \quad n = 0, \pm1, \pm2, \ \ldots\ , \tag{5.52}$$

to examine the behavior of their Fourier components. In this way we can gain insight into the relative importance of nonlinear effects on the flow in a viscous layer and, therefore, into

whether or not a linearized viscous analysis could be applied to provide efficient and meaningful unsteady viscous-layer solutions. Note that the lower limit on the integral in (5.51) must be changed to $-\infty$, if the wake displacement thickness is to be determined.

A series of results were determined for acoustic excitations travelling towards the blade row from upstream or downstream. In each case the steady Mach number is 0.5 and the Reynolds number, Re, is 10^6. The excitations occur at the frequencies, ω, listed above, and at complex amplitudes, $p_{I,\pm\infty}$, of (0.1,0), (0.3,0), (0.5,0) and (0.75,0). The pressure, $P = (\gamma M^2)^{-1}$, in the steady background flow is 2.857. The viscous-layer numerical calculations were initiated at $(x,t) = (0.01, 0)$. Laminar similarity solutions were used for $0 \leq x \leq 0.1$ and imposed as the initial conditions in x and t for the numerical calculations. The viscous flows were assumed to undergo an instantaneous transition from laminar to turbulent flow at $x = 0.02$.

The boundary layer calculations were carried out using 51 uniformly stretched (with $K_\eta = 1.10$) points across each boundary layer, with $\Delta\eta = 0.0175$ at the blade surface. In the wake the grid consisted of 101 points across the viscous layer stretched in the same manner as for the surface boundary layers. A total of 25 uniform time steps were used per temporal period of the unsteady excitation. Two different axial or streamwise mesh distributions were used — one for the excitations coming from upstream; the other, for excitations coming from downstream. In each case the streamwise distribution was selected so that there were at least 20 axial mesh lines per wave length, $2\pi/\kappa_{\xi,\mp\infty}$, for the highest frequency considered, i.e., $\omega = 10$.

For disturbances originating upstream, a variably spaced streamwise mesh was used with points clustered near the blade leading and trailing edges. The minimum streamwise spacing on the blade was $\Delta x \approx 0.0177$ at the blade edges, and the maximum was $\Delta x \approx 0.0611$ near midchord. The stretching used in the wake was identical to that used for the forward portion of the blade, with $\Delta x \approx 0.0177$ in the first wake interval and monotonically increasing to $\Delta x \approx 0.11$ at the downstream boundary of the computational domain ($x = 2.0$). The resulting grid had 29 points on the blade surface and 20 points along the wake. For the disturbances originating downstream a nearly uniform grid was employed, with $\Delta x \approx 0.025$ on the blade and $0.025 \leq \Delta x \leq 0.030$ along the wake, where the grid was mildly stretched in the flow direction to distribute the points throughout the interval $x \in (1, 2]$. The resulting grid had 40 points along the blade and 36 points along the wake.

First, we consider the solution for a pressure disturbance from upstream with $p_{I,-\infty} = (0.5, 0)$, $\omega = 5$ and $\sigma = 0$ deg. The temporal means, δ_0, $\tau_{w,0}$ and $V_{\mathcal{L},0}$, and the magnitudes, $|\delta_n|$, $|\tau_{w,n}|$ and $|V_{\mathcal{L},n}|$, of the first two harmonics ($n = 1, 2$) of the displacement thickness, $\tilde{\bar{\delta}}$, surface shear stress, $\tilde{\bar{\tau}}_w$, and wake centerline velocity, $\tilde{V}_{\mathcal{L}}$, as determined by the unsteady viscous-layer solution, are presented in Figure 5.3 along with the corresponding steady ($|p_{I,-\infty}| \equiv 0$) results, which were also determined using the UNSVIS code. The steady displacement thickness and surface shear stress are given by

$$\bar{\delta}(\mathbf{x}) = \int_0^\infty [1 - \bar{\rho} V_\tau / (\bar{\rho}_e V_{\tau,e})] dn \tag{5.53}$$

and $\bar{\tau}_w = (\mathrm{Re})^{-1}(\bar{\mu}\partial V_\tau/\partial n)_w$, where $\bar{\rho}$ and V_τ are the density and streamwise velocity, respectively, in the steady background flow. The differences between the steady and the temporal mean values of the unsteady viscous quantities, and the amplitudes of the higher ($n \geq 2$) harmonic unsteady quantities provide a measure of the relative importance of nonlinear effects on the unsteady flow in the viscous layer.

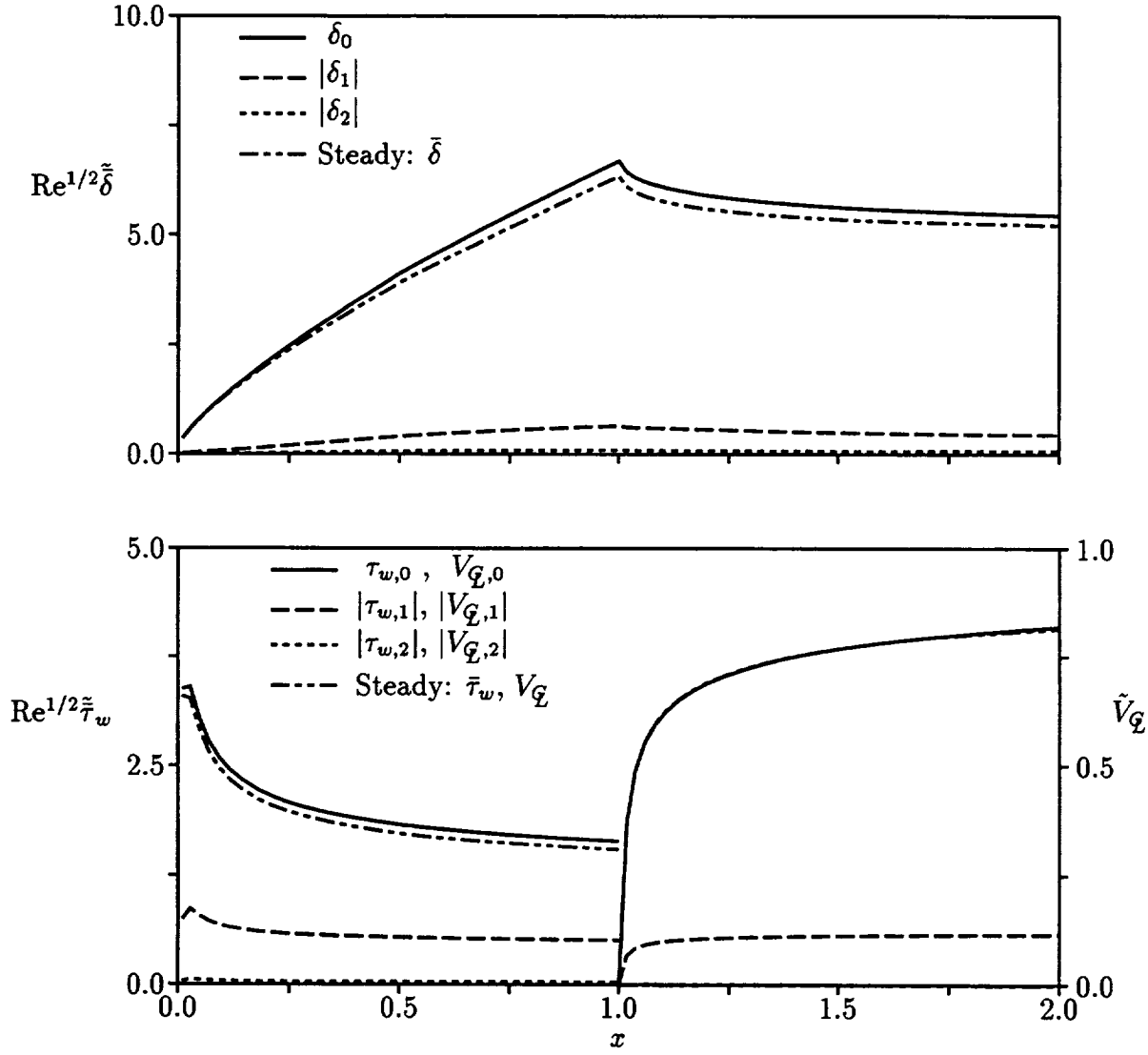

Figure 5.3: Temporal mean and Fourier magnitudes of the displacement thickness, $\tilde{\bar{\delta}}$, wall shear stress, $\tilde{\bar{\tau}}_w$, and wake centerline velocity, $\tilde{V}_{\mathcal{L}}$, for turbulent flow through an unstaggered flat-plate cascade ($\Omega = \Theta = 0\,\mathrm{deg}$, $G = 1$, $M = 0.5$ and $\mathrm{Re} = 10^6$) subjected to an incident pressure disturbance from upstream with $p_{I,-\infty} = (0.5, 0)$, $\omega = 5$ and $\sigma = 0\,\mathrm{deg}$.

The results in Figure 5.3 indicate that nonlinear effects are relatively small for the unsteady flow driven by the prescribed upstream pressure excitation. However, similar results in Figure 5.4 for an acoustic excitation from downstream, with $p_{I,+\infty} = (0.5, 0)$, $\omega = 5$ and $\sigma = 0$, indicate the nonlinear content in the viscous-layer displacement-thickness response to be quite significant. An unexpected result of the latter calculation is the increase in the predicted time-mean of the unsteady displacement thickness with increasing distance along the wake (i.e., as $x \to 2.0$). In an attempt to determine whether this effect is physical or numerical in origin, an unsteady viscous solution was calculated using a grid with twice as many uniformly distributed streamwise points. It was found that, although slightly less pronounced,

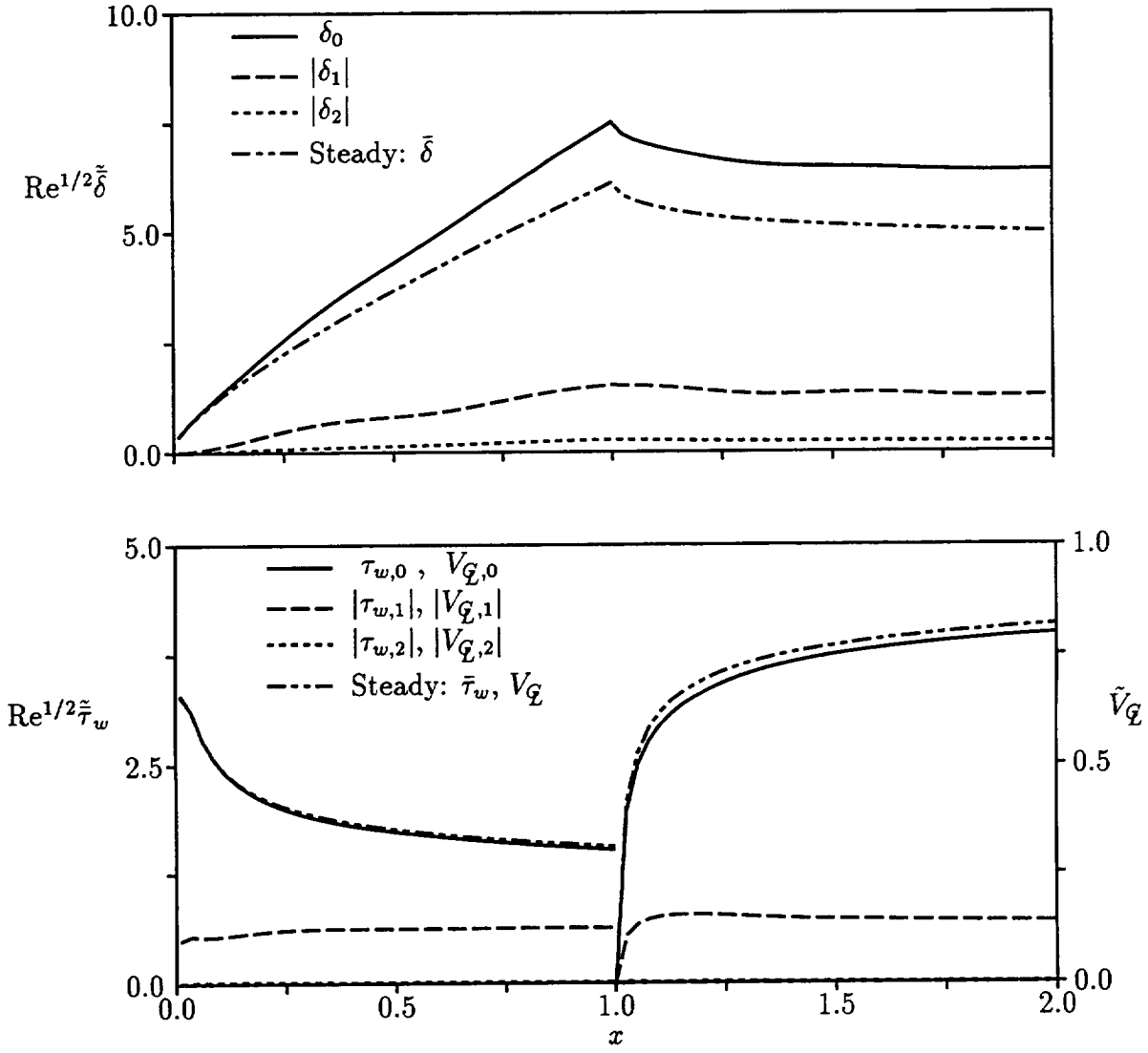

Figure 5.4: Temporal mean and Fourier magnitudes of the displacement thickness, $\tilde{\bar{\delta}}$, wall shear stress, $\tilde{\bar{\tau}}_w$, and wake centerline velocity, $\tilde{V}_{\mathcal{L}}$, for turbulent flow through an unstaggered flat-plate cascade ($\Omega = \Theta = 0\,\mathrm{deg}$, $G = 1$, $M = 0.5$ and $\mathrm{Re} = 10^6$) subjected to an incident pressure disturbance from downstream with $p_{I,+\infty} = (0.5, 0)$, $\omega = 5$ and $\sigma = 0\,\mathrm{deg}$.

a similar behavior was also present in the fine grid calculation. This unexpected behavior of the viscous layer solution for an upstream traveling acoustic disturbance will require some further study to resolve.

The behaviors of the zeroth- and first-harmonic components of the viscous parameters are illustrated in Figures 5.5 and 5.6 for upstream acoustic excitations with $p_{I,-\infty} = (0.5, 0)$, $\sigma = 0$, and $\omega = 1, 2, 5$ and 10. Corresponding results for downstream acoustic excitations are given in Figures 5.7 and 5.8. For the upstream excitations, the time-mean values and the magnitudes of the first-harmonic viscous-layer response quantities (Figure 5.5) are not affected significantly by changes in excitation frequency. In addition, the first-harmonic displacement

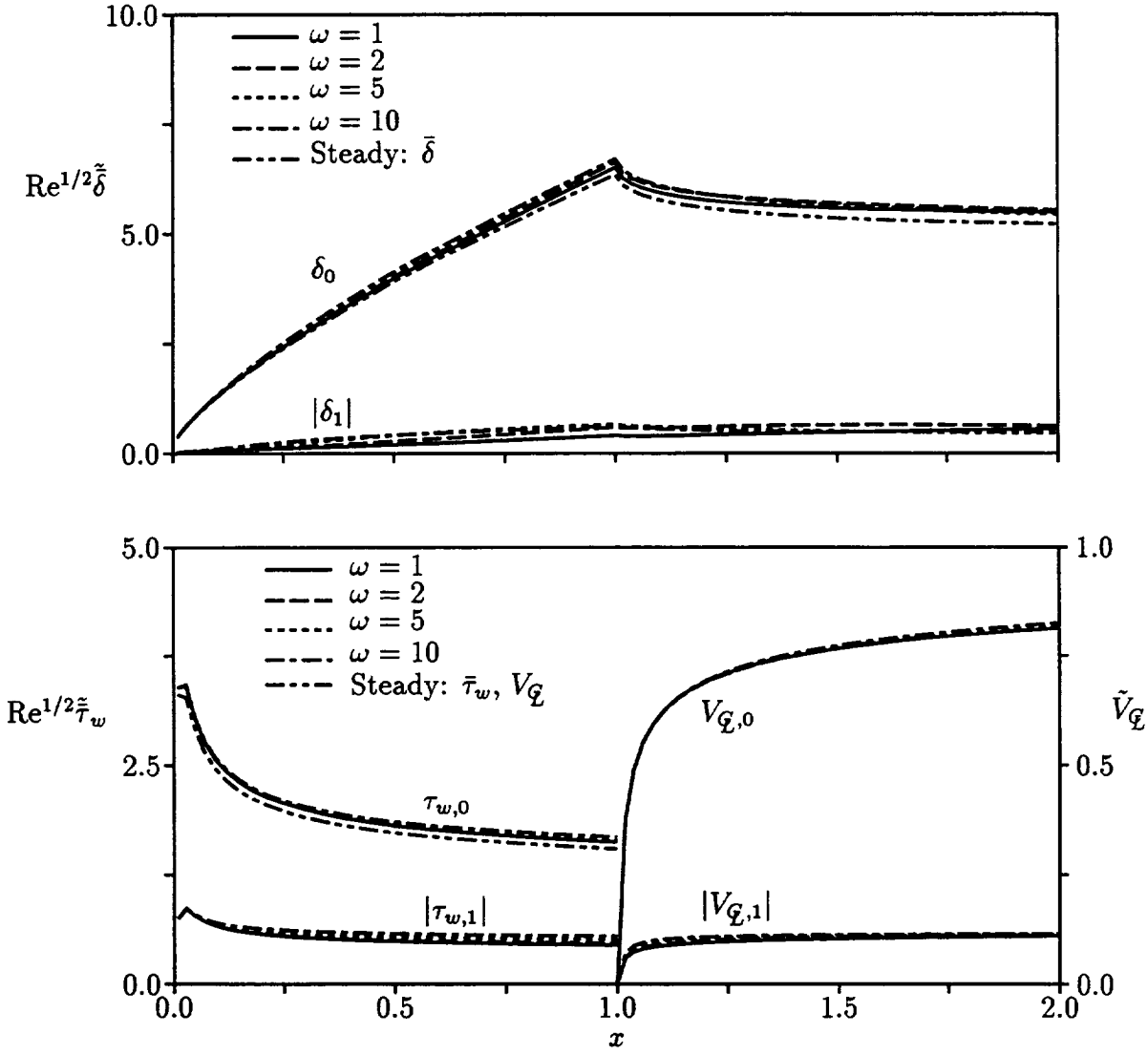

Figure 5.5: Fourier amplitudes of $\tilde{\bar{\delta}}$, $\tilde{\bar{\tau}}_w$ and $\tilde{V}_{\mathcal{L}}$ for an unstaggered flat-plate cascade ($\Omega = \Theta = 0\,\mathrm{deg}$, $G = 1$, $M = 0.5$ and $\mathrm{Re} = 10^6$) subjected to pressure excitations from upstream with $p_{I,-\infty} = (0.5, 0)$ and $\sigma = 0\,\mathrm{deg}$.

thickness is essentially out-of-phase with the first-order streamwise velocity fluctuation, $\tilde{v}_{\tau,e}$, at the edge of the viscous layer (Figure 5.6), and the first-harmonic wall shear stress and wake centerline velocity are essentially in phase with this edge-velocity fluctuation.

The corresponding results in Figures 5.7 and 5.8 for acoustic excitations from downstream show that frequency has a much greater impact on the temporal mean and the first-harmonic amplitudes of the viscous-layer response quantities. In particular, the time-mean displacement thicknesses vary significantly with ω, indicating that nonlinear effects become increasingly important with increasing frequency. As shown in Figure 5.8, the first-harmonic displacement thickness lags the fluctuating component of the streamwise velocity at the edge of the viscous-layer by a phase angle ranging from approximately -140 to -180 deg; the first-harmonic

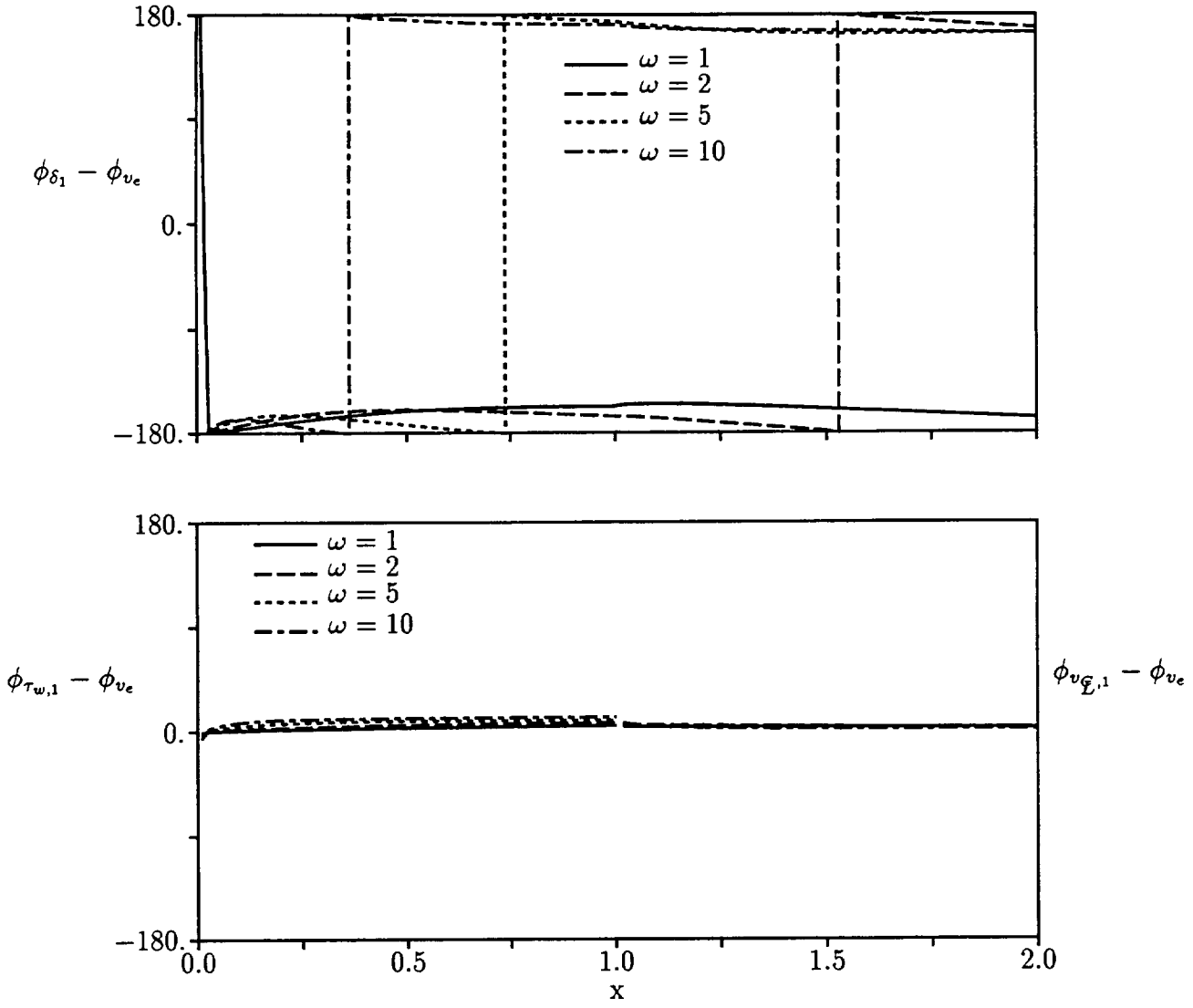

Figure 5.6: Relative phase angles of first-harmonic displacement thickness, wall shear stress, and wake centerline velocity for an unstaggered flat-plate cascade ($\Omega = \Theta = 0\,\text{deg}$, $G = 1$, $M = 0.5$ and $\text{Re} = 10^6$) subjected to pressure excitations from upstream with $p_{I,-\infty} = (0.5, 0)$ and $\sigma = 0\,\text{deg}$.

wall shear stress leads this fluctuating velocity by an angle ranging from 0 to 40 deg; and the minimum wake-streamwise velocity is approximately in-phase with the wake-edge velocity fluctuation.

As a final illustration, we consider the response of the viscous layer to acoustic excitations at different amplitudes. Numerical results are presented in Figures 5.9 and 5.10 for excitations at $\omega = 5$, $\sigma = 0$ and $p_{I,\mp\infty} = (0.1,0)$, (0.3,0), (0.5,0) and (0.75,0). For disturbances from upstream (Figure 5.9) the effects of unsteadiness on the time-mean values of $\tilde{\bar{\delta}}$ and $\tilde{\bar{\tau}}_w$ are small, except, perhaps, for the highest disturbance amplitude, $|p_{I,-\infty}| = 0.75$, considered. The effects of disturbance amplitude on the time-mean wake centerline velocity are negligible. The

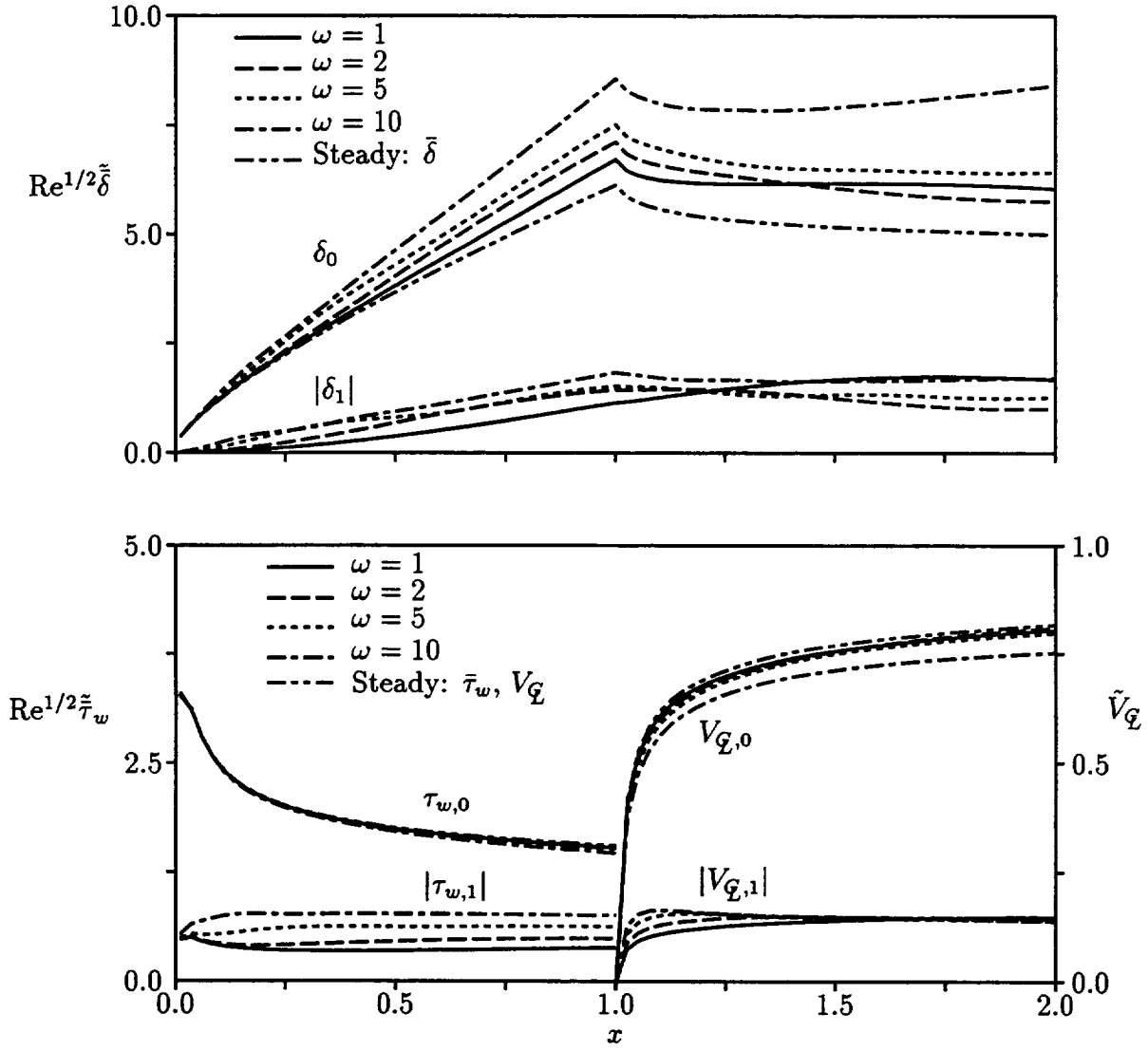

Figure 5.7: Fourier amplitudes of $\tilde{\bar{\delta}}$, $\tilde{\bar{\tau}}_w$ and $\tilde{V}_{\mathcal{L}}$ for an unstaggered flat-plate cascade ($\Omega = \Theta = 0\,\mathrm{deg}$, $G = 1$, $M = 0.5$ and $\mathrm{Re} = 10^6$) subjected to pressure excitations from downstream with $p_{I,+\infty} = (0.5, 0)$ and $\sigma = 0\,\mathrm{deg}$.

results for the acoustic excitations from downstream in Figure 5.10 once again indicate that such disturbances produce much stronger nonlinear viscous-layer responses, particularly in the displacement thickness. For both the upstream and downstream acoustic excitations, the phase angles (not shown) of the first-harmonic viscous quantities relative to the edge velocity fluctuation are almost independent of the excitation amplitude.

The foregoing results indicate that the viscous-layer response parameters $\tilde{\bar{\delta}}$, $\tilde{\bar{\tau}}_w$ and $\tilde{V}_{\mathcal{L}}$ behave essentially in a linear manner for acoustic excitations originating upstream of the blade row. For excitations coming from downstream, nonlinear effects can be significant for high temporal frequencies (say $\omega \geq 5$) and/or high excitation amplitudes ($|p_{I,+\infty}| > 0.5$). For $M = 0.5$, the magnitude of the axial wave number for a pressure excitation from downstream

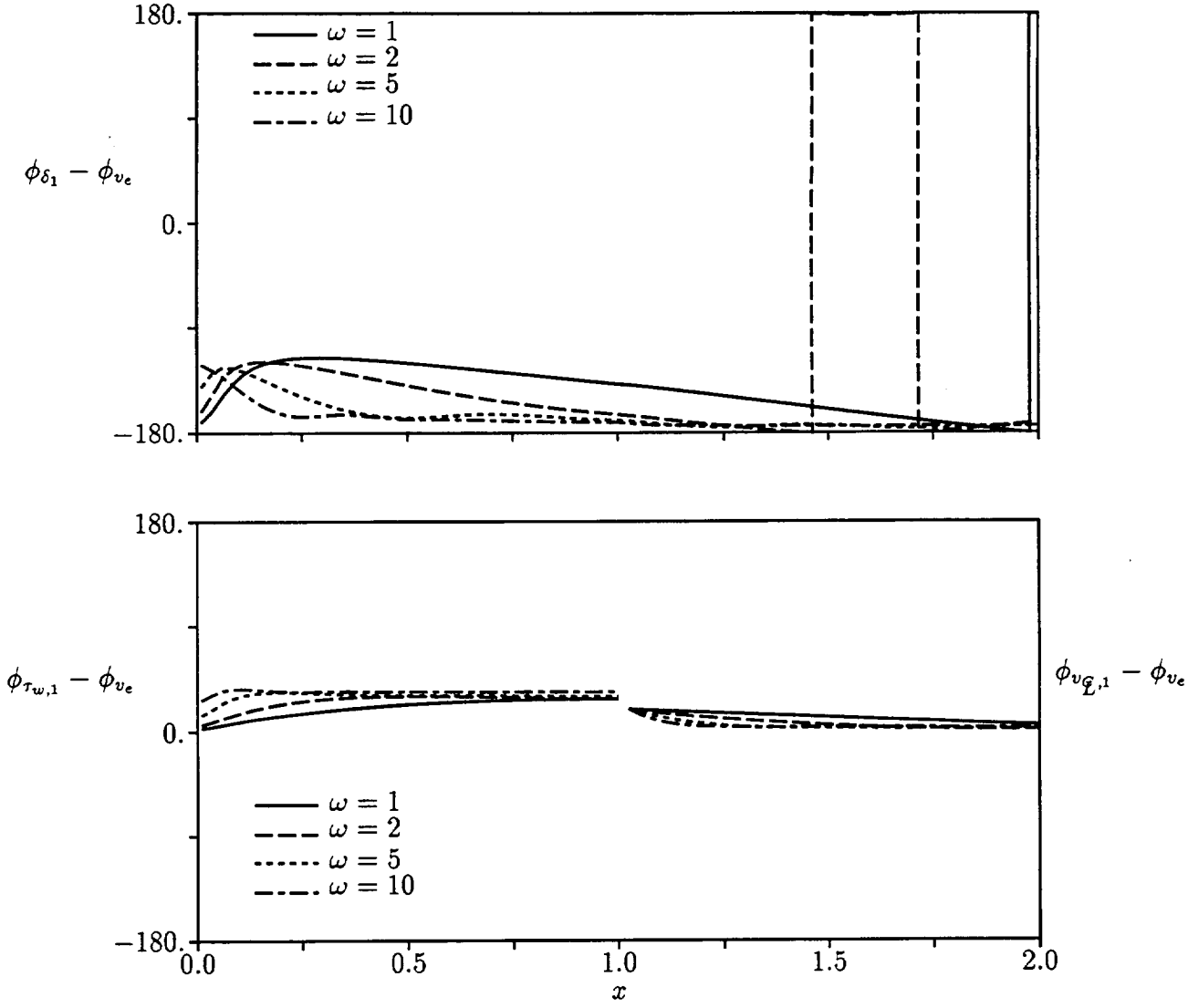

Figure 5.8: Relative phase angles of first-harmonic displacement thickness, wall shear stress, and wake centerline velocity for an unstaggered flat-plate cascade ($\Omega = \Theta = 0\,\text{deg}$, $G = 1$, $M = 0.5$ and $\text{Re} = 10^6$) subjected to pressure excitations from downstream with $p_{I,+\infty} = (0.5, 0)$ and $\sigma = 0\,\text{deg}$.

is three times that for an excitation from upstream. This produces a corresponding ratio in the magnitudes of the pressure gradients that drive the viscous-layer solution, and is perhaps responsible for the relatively strong nonlinear content in the responses of the viscous layer to downstream disturbances. Another factor is the direction of propagation of the acoustic excitation. We have performed a series of calculations to isolate these effects and have found that the latter, i.e., direction of propagation, to be the dominant factor in promoting a nonlinear response of the viscous layer. It should also be noted that Navier-Stokes calculations have been performed recently for compressor cascades excited by acoustic disturbances [DV94]. The Navier-Stokes results indicate that the unsteady surface pressure responses to acoustic

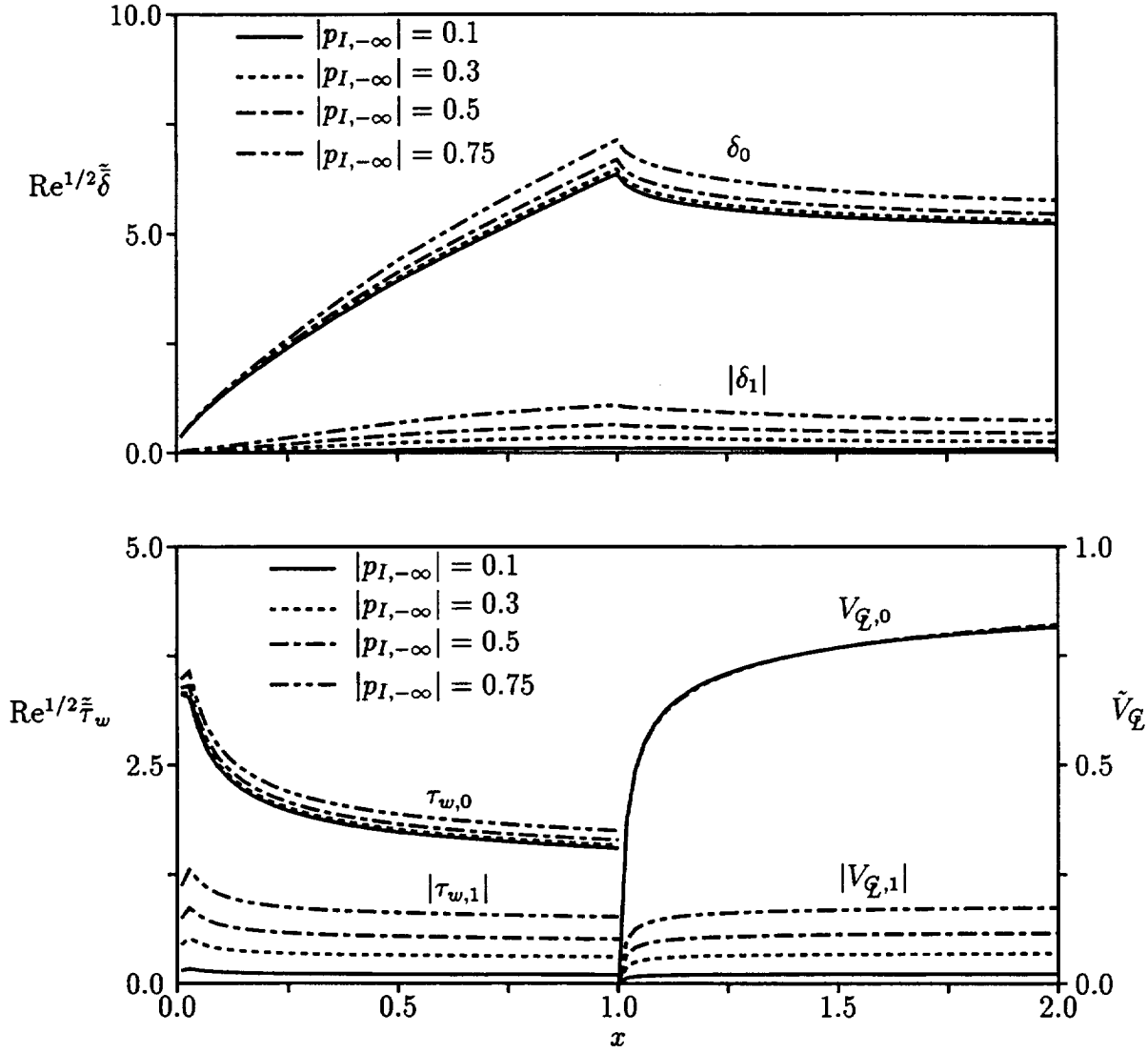

Figure 5.9: Fourier amplitudes of $\tilde{\bar{\delta}}$, $\tilde{\bar{\tau}}_w$ and $\tilde{V}_{\mathcal{L}}$ vs amplitude, $|p_{I,-\infty}|$, for an acoustic excitation from upstream, with $\omega = 5$ and $\sigma = 0$ deg, interacting with an unstaggered flat-plate cascade ($\Omega = \Theta = 0$ deg, $G = 1$, $M = 0.5$ and $\mathrm{Re} = 10^6$).

excitations from upstream are linear over a wide range of excitation amplitudes, but acoustic excitations from downstream produce responses with significant nonlinear content.

The spurious predictions for the behavior of the displacement thickness in the far wake, i.e., increasing with increasing x, for high frequency or high amplitude disturbances from downstream is a somewhat disturbing aspect of the present unsteady viscous-layer solutions. A series of laminar calculations were performed, and the results showed a similar behavior. Thus, the increase in displacement thickness in the far wake ($x \to 2$) cannot be attributed to the turbulence model used in the present study.

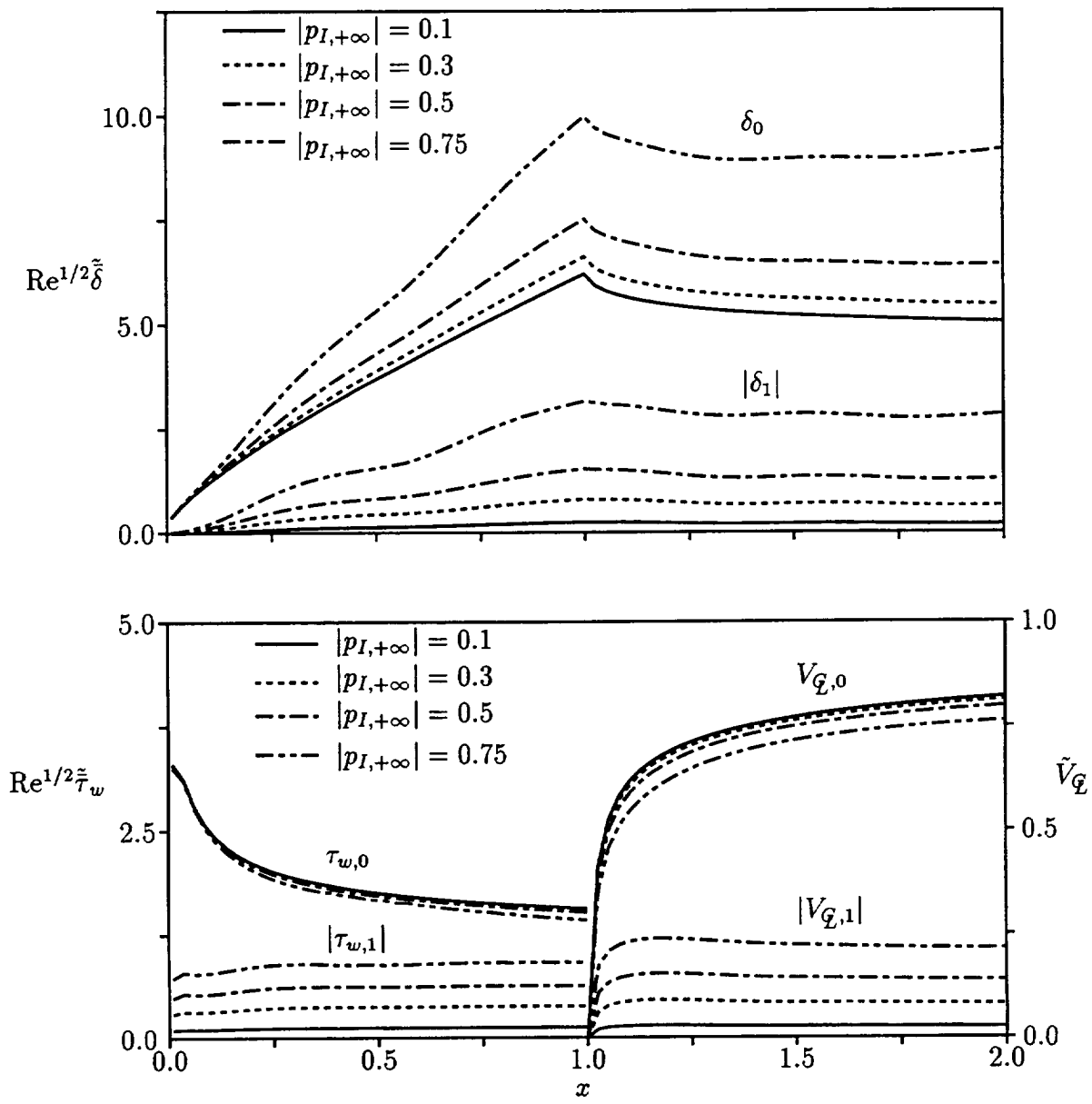

Figure 5.10: Fourier amplitudes of $\tilde{\tilde{\delta}}$, $\tilde{\tilde{\tau}}_w$ and $\tilde{V}_{\mathcal{L}}$ vs amplitude, $|p_{I,+\infty}|$, for an acoustic excitation from downstream with, $\omega = 5$ and $\sigma = 0$ deg, interacting with an unstaggered flat-plate cascade ($\Omega = \Theta = 0$ deg, $G = 1$, $M = 0.5$ and $\mathrm{Re} = 10^6$).

Turbine Cascade

We proceed to consider an unsteady flow through a "real" blade cascade to demonstrate the coupled LINFLO/UNSVIS weak, inviscid/viscid interaction, solution capability. In particular, we consider a flow at a Reynolds number, Re, of 5.0×10^5, an inlet Mach number, $M_{-\infty}$, of 0.19 and an inlet flow angle, $\Omega_{-\infty}$, of 45 deg, through the turbine cascade known as the 4th Standard Configuration. The unsteadiness is excited by an acoustic or pressure disturbance from upstream, characterized by $p_{I,-\infty} = (0.35, 0)$, $\kappa_{\eta,-\infty} = \sigma/G = 0$ and $\omega = 1.0$. The

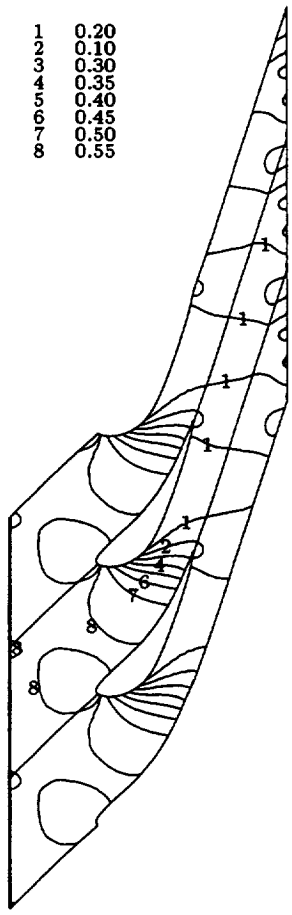

Figure 5.11: Contours of the in-phase component (real part) of the unsteady pressure for the turbine cascade subjected to an acoustic excitation from upstream with $p_{I,-\infty} = (0.35, 0)$, $\omega = 1$ and $\sigma = 0$.

inviscid steady Mach number field and steady Mach number distribution along a blade surface are shown in Figure 3.2. For the unsteady flow being considered, the unsteady pressure at a given point in the field is essentially in phase with the acoustic excitation. The in-phase component (real part) of the unsteady pressure field, as determined using LINFLO, is depicted in Figure 5.11. The acoustic excitation at $\omega = 1$, $\sigma = 0$ produces a superresonant (1,1) acoustic response. Therefore, the pressure contours in Figure 5.11 indicate much different pressure amplitudes at the far upstream and downstream boundaries than that associated with the acoustic excitation alone.

The temporal mean value and the upper and lower bounds (envelope) for the inviscid surface velocity are shown in Figure 5.12. The amplitude of the first-harmonic component of the surface velocity, which is proportional to $|p_{I,-\infty}|$, is relatively small for this case. But, for pressure excitations of higher amplitude, the viscous-layer separates from the suction surface of a blade, just upstream of the trailing edge, thereby precluding the continuation of the direct unsteady viscous-layer calculation into the wake.

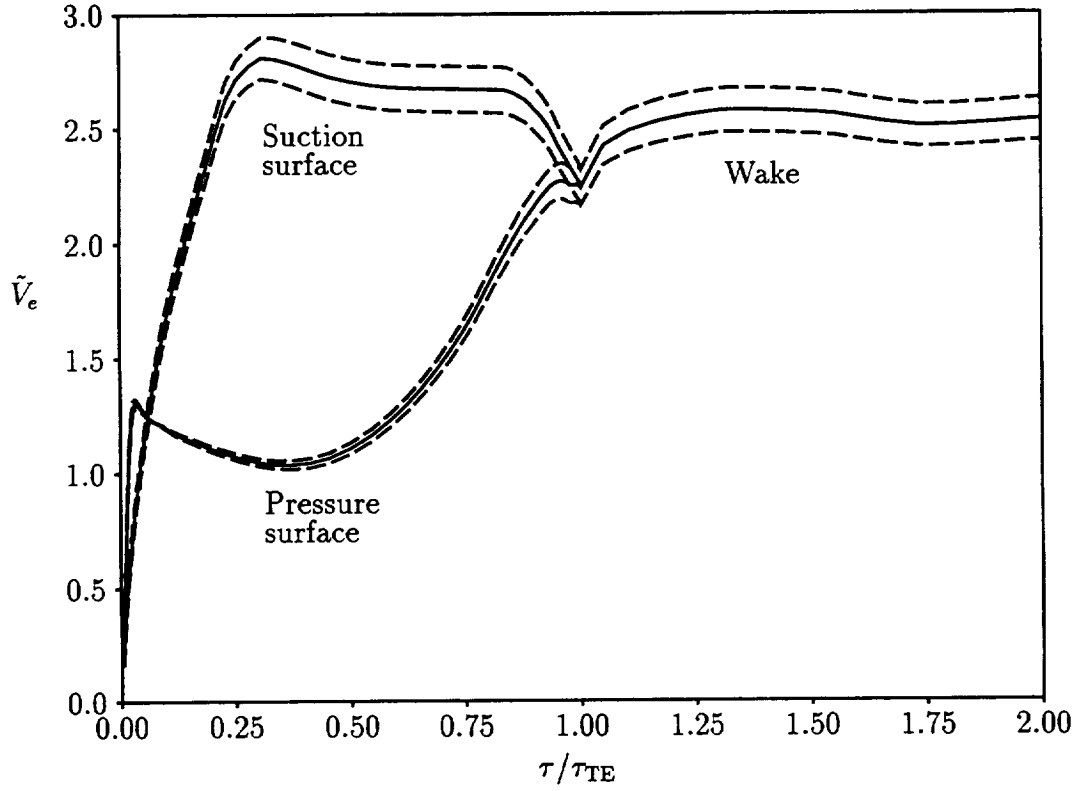

Figure 5.12: Temporal mean values and upper and lower bounds of the inviscid surface (viscous-layer edge) velocity for the turbine cascade subjected to an upstream pressure excitation with $p_{I,-\infty} = (0.35, 0)$, $\omega = 1$ and $\sigma = 0$.

Since the turbine blade has a blunt leading edge, the unsteady stagnation-point analysis, described in § 5.3, was applied at each time step to provide the upstream velocity profiles needed to advance the viscous-layer solutions along the blade suction and pressure surfaces. For this case, the motion of the stagnation point is confined to a small interval of length $2|\tau_I| \approx 0.0037$. A series of velocity profiles associated with the periodic flow within the stagnation region at four different times, i.e., $t = \pi/2, \pi, 3\pi/2$ and 2π, are shown in Figures 5.13 and 5.14. Here the instantaneous streamwise-velocity profiles are presented in the blade fixed frame of reference, and the abscissa on each plot refers to the location on the blade surface at which the velocity profile is determined. The interval shown in Figure 5.13 is centered about the mean location of the stagnation point; that in Figure 5.14, about the instantaneous location, i.e., the location at which $\tilde{U}_{\tau,e} = 0$ in the blade-fixed frame of reference. Note that the velocity profiles are shown over a much narrower interval, $[-0.02|\tau_I|, 0.02|\tau_I|]$, in Figure 5.14, where the profiles indicate that reverse flow occurs in the immediate vicinity of the instantaneous stagnation point location.

The viscous-layer calculation for the reference turbine blade and its wake was performed assuming that instantaneous transition from laminar to turbulent flow occurs at $\tau/\tau_{TE} = 0.05$ on both the pressure and suction surfaces of each blade. Here, τ is the distance along the blade surface measured from the mean, leading-edge, stagnation point location, and the subscript

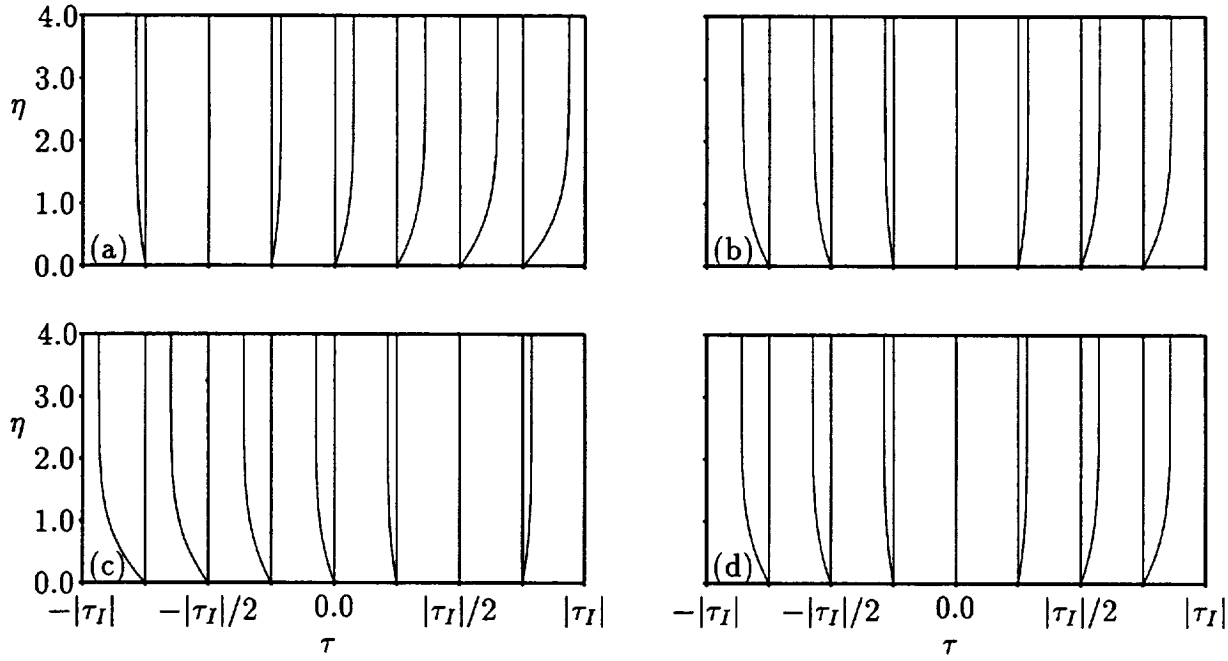

Figure 5.13: Velocity profiles in the neighborhood of a mean stagnation point location for the turbine cascade subjected to an upstream acoustic excitation with $p_{I,-\infty} = (0.35, 0)$, $\omega = 1$ and $\sigma = 0$: (a) $t = \pi/2$; (b) $t = \pi$; (c) $t = 3\pi/2$; (d) $t = 2\pi$.

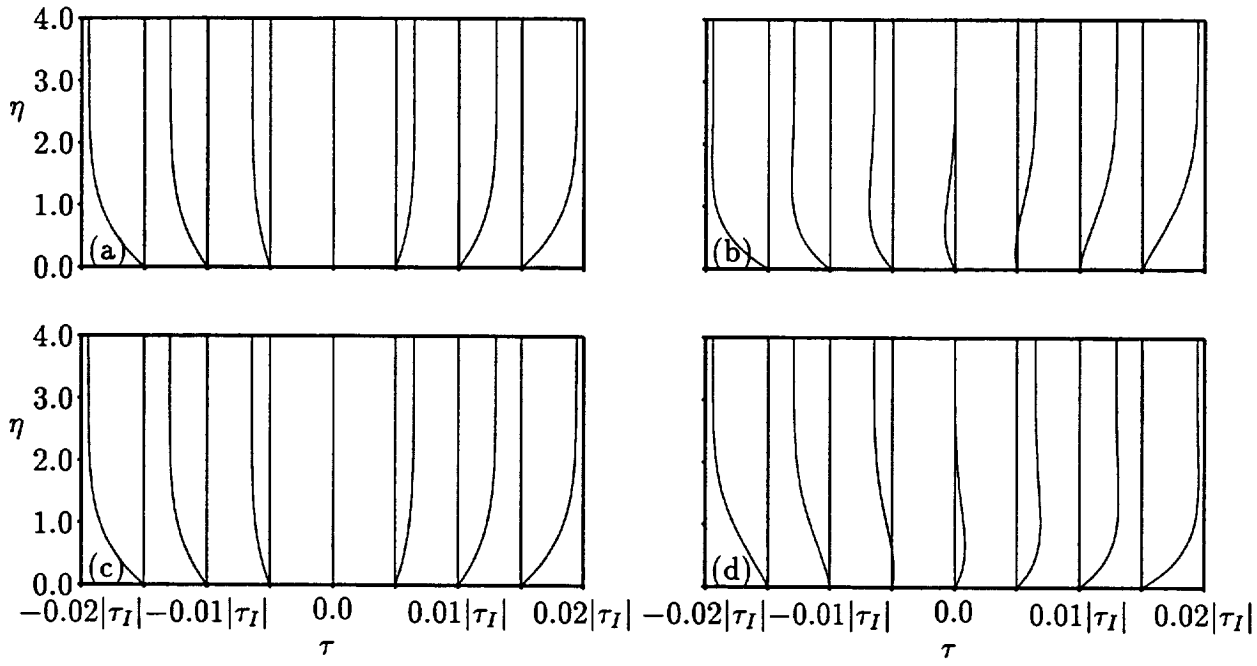

Figure 5.14: Velocity profiles in the neighborhood of an instantaneous stagnation point location for the turbine cascade subjected to an upstream acoustic excitation with $p_{I,-\infty} = (0.35, 0)$, $\omega = 1$ and $\sigma = 0$: (a) through (d) as in Fig. 5.13.

TE refers to the values of τ at the blade trailing edge. The grid used in this calculation had 77 points along the blade surface and 54 points along the reference wake line. It was stretched with $\Delta\tau \approx 0.002$ at the furthest upstream point and $\Delta\tau \approx 0.0001$ at the trailing edge. The largest value of $\Delta\tau$ on the blade, i.e., 0.052, occurs near midchord. The streamwise intervals grow aft of the trailing edge from $\Delta\tau \approx 0.0001$ to approximately 0.083 one chord length downstream of the blade row. The viscous-layer calculation was carried out using 71 uniformly stretched points across each boundary layer, with $K_\eta = 1.045$ and $\Delta\eta = 0.04$ at the blade surface. The wake grid consisted of 141 points across the viscous layer stretched in the same manner as on the blade surface. A total of 40 uniform time steps were used per temporal period of the unsteady excitation.

Results of the unsteady viscous-layer calculation are shown in Figures 5.15 through 5.17. Temporal mean values and upper and lower bounds for the displacement thickness and wall shear stress along the upper and lower surfaces of the reference ($m = 0$) turbine blade are shown in Figure 5.15; corresponding results for the wake displacement thickness, $\tilde{\bar{\delta}}_W$, and minimum streamwise velocity, $\tilde{V}_{\tau,\min}$ in Figure 5.16. Here, the upper and lower bounds of a viscous-layer response quantity, say the displacement thickness, are defined by

$$\tilde{\bar{\delta}}^{\pm} = \delta_0 \pm 2 \sum_{n=1}^{\infty} |\delta_n| \,. \tag{5.54}$$

Wake velocity profiles at four different instants of time are depicted in Figure 5.17. The unsteady response of the viscous layer is essentially linear for this example, i.e., the temporal mean and the steady viscous solutions are almost identical, and the Fourier amplitudes of the higher ($n > 2$) harmonic components of $\tilde{\bar{\delta}}$, $\tilde{\bar{\tau}}_w$ and $\tilde{V}_{\tau_{\min}}$ are negligible.

The foregoing results demonstrate the new capabilities that have been added to the UNSVIS code under Contract NAS3–25425, i.e., an unsteady stagnation region analysis and an unsteady wake analysis. These results also demonstrate the present weak, inviscid/viscid interaction, prediction capability that results from a sequential coupling of a linearized, inviscid, unsteady solution, determined using LINFLO, and a nonlinear unsteady viscous-layer solution. Unfortunately, since boundary-layer separation usually occurs in realistic configurations and a weak interaction analysis breaks down in such cases, the present analysis has only a limited range of application. This is particularly true for compressor cascades where, because of adverse mean pressure gradients, local separations almost always occur. There is, therefore, an important need to develop a simultaneous coupling (or strong interaction) solution procedure for unsteady cascade flows.

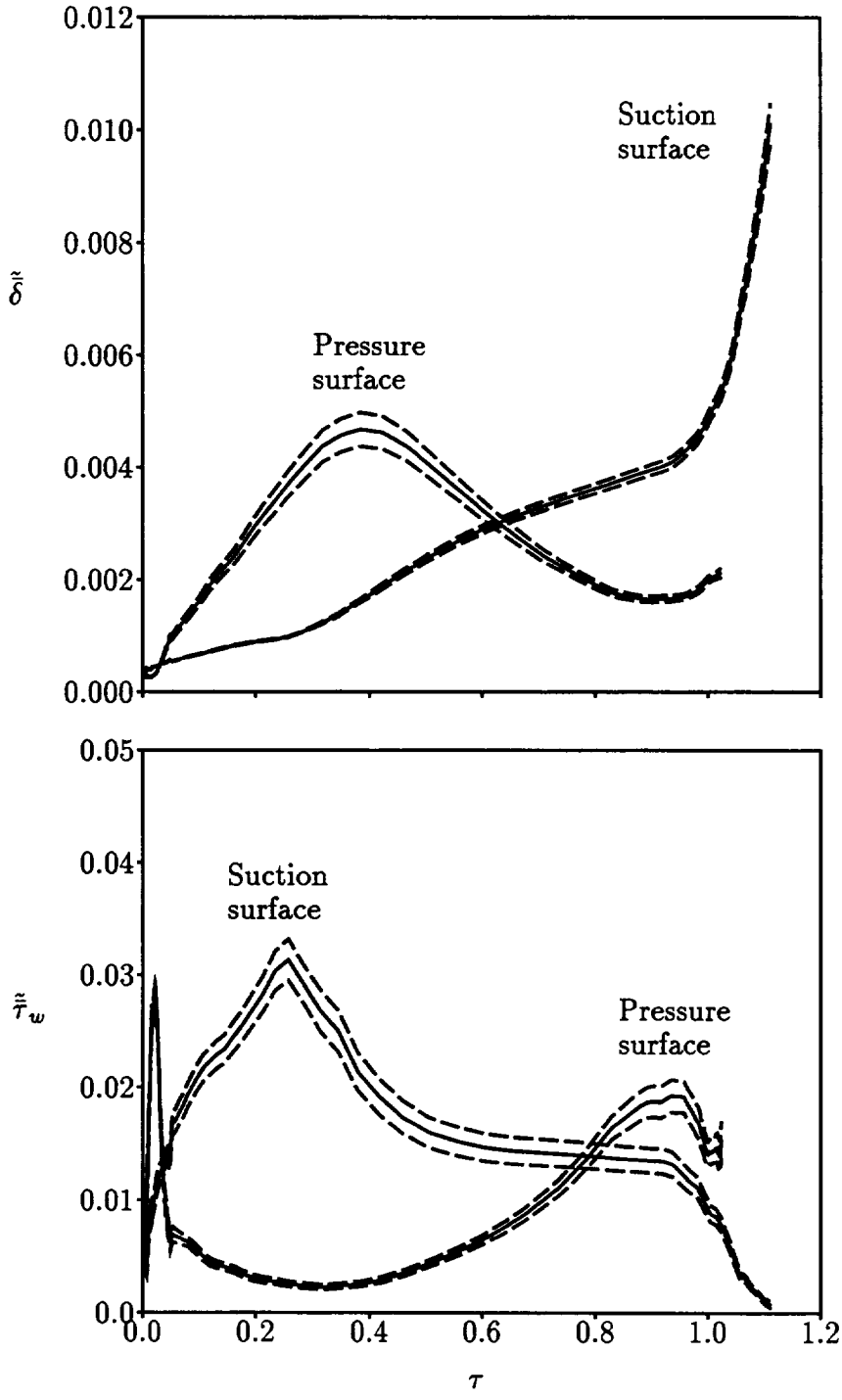

Figure 5.15: Temporal mean values and upper and lower bounds for the displacement thickness and surface shear stress along a turbine blade surface for an unsteady flow excited by an upstream pressure excitation with $p_{I,-\infty} = (0.35, 0)$, $\omega = 1$ and $\sigma = 0$.

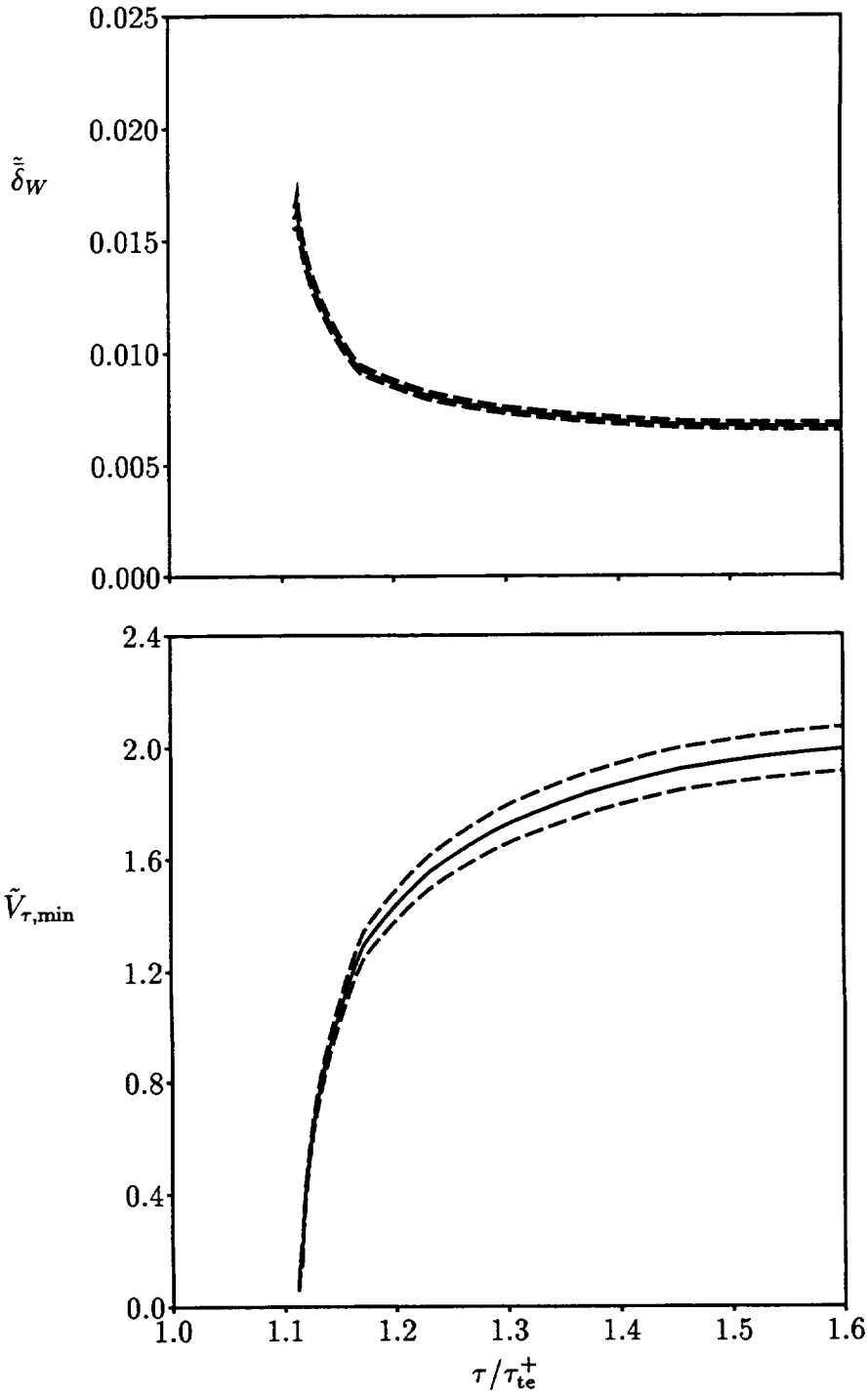

Figure 5.16: Temporal mean values and upper and lower bounds for the displacement thickness and minimum wake streamwise velocity along a turbine wake for an unsteady flow excited by an upstream pressure excitation with $p_{I,-\infty} = (0.35, 0)$, $\omega = 1$ and $\sigma = 0$.

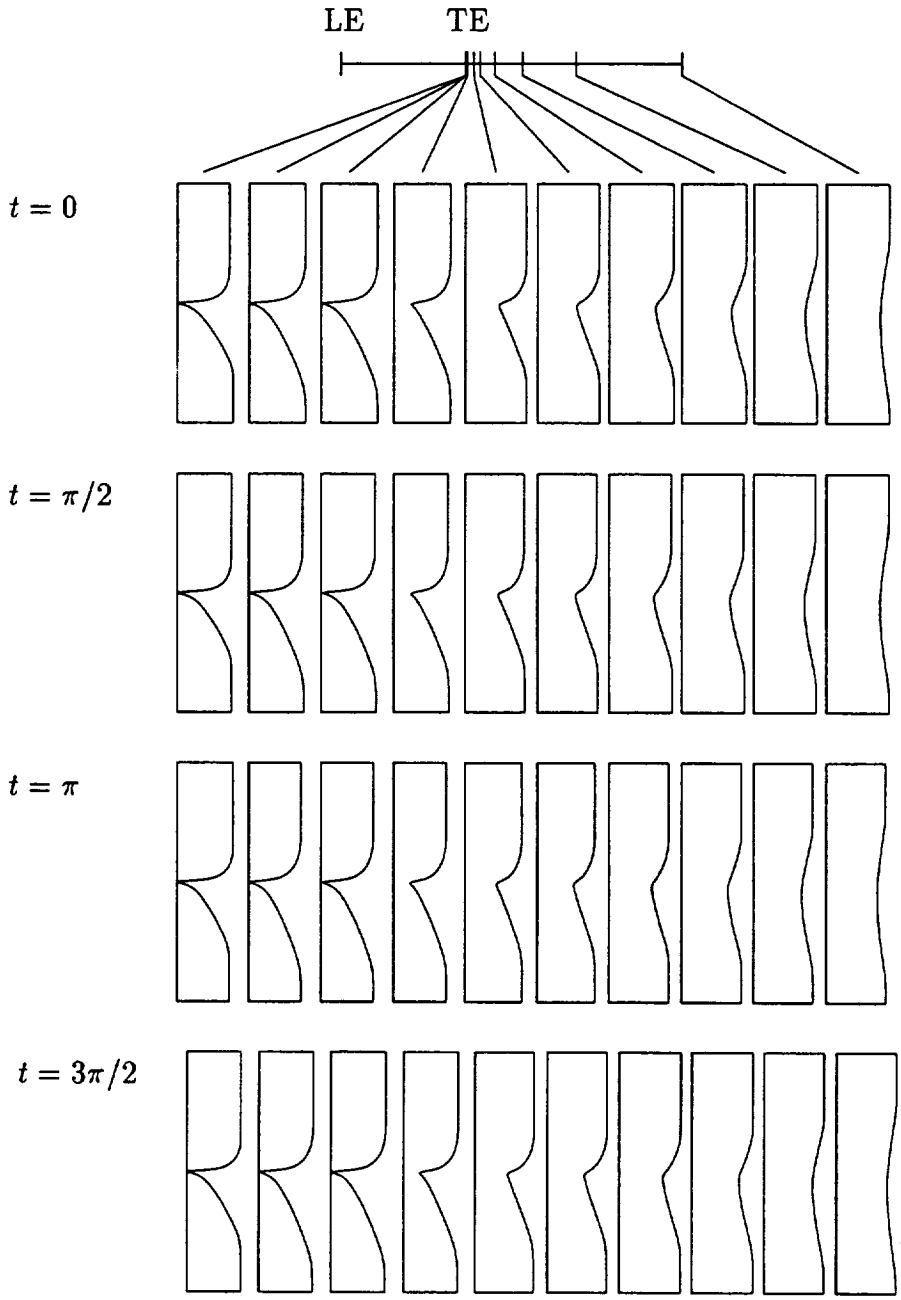

Figure 5.17: Streamwise velocity profiles in the wake of a turbine for an unsteady flow excited by an acoustic excitation from upstream with $p_{I,-\infty} = (0.35, 0)$, $\omega = 1$ and $\sigma = 0$.

6. Concluding Remarks

Under the present effort, we have contributed to the development of efficient, and reasonably comprehensive, unsteady fluid dynamic analyses that can be used in turbomachinery aeroelastic and aeroacoustic design studies. In particular, we have invoked the assumptions of high-Reynolds-number, "attached" flow and small-amplitude unsteady excitation to develop asymptotic unsteady aerodynamic models that apply to realistic cascade configurations and mean operating conditions. Based on the high Reynolds number assumption, an inviscid/viscid interaction model has been formulated for unsteady flows through two-dimensional cascades. In addition, based on the small-disturbance assumption, a linearized analysis has been formulated for the unsteady flow in the inviscid region, but at this point, the unsteady flows in viscous layers, i.e., boundary layers and wakes, are still regarded as nonlinear. To further expedite the unsteady flow predictions, we have assumed that the nonlinear steady background flow in the inviscid region is isentropic and irrotational — an assumption that leads to considerable simplifications in the equations that describe the behavior of inviscid unsteady perturbations. The foregoing assumptions can lead to very efficient predictions of the unsteady pressure responses of realistic cascades to prescribed structural (blade) motions and external unsteady aerodynamic (entropic, vortical, and acoustic) disturbances.

To provide a strong inviscid/viscid interaction analysis for unsteady cascade flows, several component analyses must be constructed, along with methods for coupling these components into an overall solution procedure. Here, the component analyses include a full potential analysis to predict the isentropic and irrotational steady background flow, a linearized inviscid analysis to predict the behaviors of unsteady entropic, vortical and acoustic perturbations, and a nonlinear unsteady viscous layer analyses, which, in the future, might be replaced by nonlinear steady and linearized unsteady analyses, to predict the flows in boundary layers and wakes. In the present report, we have described and demonstrated the linearized inviscid analysis LINFLO, the steady, strong, inviscid/viscid interaction analysis SFLOW–IVI and the nonlinear unsteady viscous-layer analysis UNSVIS. The steady full-potential analysis, SFLOW, developed at NASA Lewis under a related research program [HV93, HV94], serves as the inviscid component of the steady inviscid/viscid interaction analysis, and is also used to provide the steady background flow information needed for a LINFLO linearized inviscid analysis. The SFLOW–IVI analysis entails the iterative coupling of SFLOW to a steady, inverse, viscous-layer analysis.

The LINFLO analysis describes unsteady perturbations of a potential steady background flow. It applies to unsteady flows excited by prescribed blade vibrations and external entropic, vortical and acoustic disturbances. Applications of LINFLO to blade flutter and blade-row aeroacoustic response predictions are described in [Ver89a, UV91, Ver93] and [KV93b, KV94], respectively. Under the present contract, LINFLO was extended to predict the unsteady flows excited by entropic and vortical gusts. Because the steady background flow is assumed to be potential, closed form solutions can be determined for the entropy and vorticity or rotational velocity fluctuations. Consequently, numerical field methods are only required to determine the unsteady potential, and hence, the unsteady pressure. The former is governed by an inhomogeneous wave equation in which the source term depends upon the rotational velocity field. Since only a single partial differential equation must be solved numerically, the LINFLO

analysis provides very efficient unsteady aerodynamic response predictions. Moreover, such predictions have been shown to be in good agreement with those based upon time-accurate, nonlinear, Euler and Navier-Stokes solutions for subsonic unsteady flows excited by vortical and acoustic excitations [DV94] and for subsonic and transonic unsteady flows excited by blade vibrations [AV94].

In future work, the LINFLO vortical gust response prediction capability should be extended to transonic flows. Also, the convected potential developed in [AG89] and used herein, cf. (3.33), should be modified to remove the indeterminacy in the unsteady velocity, associated with entropic gusts, at blade and wake surfaces. This would lead to improved resolutions of unsteady flows excited by entropic disturbances. Finally, since we have experienced some difficulties in providing accurate unsteady pressure responses for thick, highly-cambered, turbine blades, particularly the pressure responses to high frequency vortical gusts, work should be directed towards improving LINFLO for application to vortical gust/turbine blade-row interactions.

The SFLOW–IVI analysis describes high Reynolds number, steady flows, containing regions of strong inviscid interaction, including local separations, through turbomachine cascades. Here, the flow in the outer or inviscid region is governed by the full potential equation; that in the inner or viscous layer regions, by Prandtl's viscous layer equations. Inviscid and viscid solutions are iteratively matched using a semi-inverse global iteration procedure until a converged result for the complete flow field is determined. The SFLOW analysis [HV93, HV94], with modified surface conditions to account for the effects of viscous displacement, is used to determine the inviscid component of the flow, and an inverse viscous layer analysis, to determine the flows in viscous-layer regions.

As part of the present effort, the SFLOW-IVI analysis has been applied to predict steady viscous flows through compressor and turbine cascades, including flows with extensive trailing-edge separations. Results, for selected cases, particularly those for surface shear stress, have been shown to be in good agreement with corresponding Navier-Stokes predictions. The inviscid components of SFLOW–IVI solutions have also been used to provide the steady background flow information for a linearized inviscid analysis, in an effort to determine the effects of steady viscous displacement on blade flutter margins. For the limited applications considered here, steady viscous displacement effects tend to be stabilizing for torsional blade motions, but destabilizing for bending vibrations.

As it stands, the SFLOW–IVI analysis is efficient and robust, but it is restricted to subsonic, adiabatic flows at unit Prandtl number. In future work the viscous-component of the SFLOW–IVI analysis could be easily extended so that heat conducting flows at arbitrary Prandtl numbers can be considered. More importantly, the SFLOW–IVI analysis should be extended for application to transonic flows. A steady, transonic, inviscid/viscid interaction analysis would be of value for steady-state design applications, and could be used in conjunction with LINFLO to determine the impact of steady viscous displacements on unsteady shock loads. Recent Navier-Stokes studies [AV94] have indicated that, for cascades operating near design, the effects of viscous-displacement on unsteady aerodynamic response are significant only in the vicinity of a shock, where such effects tend to weaken the shock and shift its mean position. In this case, a steady analysis that accounted for such effects could be coupled to LINFLO to provide useful unsteady aerodynamic response information for transonic flows. This type of approach has been applied successfully in external aerodynamics [Edw93]. Its

use for internal flows could lead to very efficient unsteady aerodynamic response predictions for viscous transonic unsteady flows.

The nonlinear unsteady viscous-layer analysis and code, UNSVIS, has been developed to predict the unsteady flows in blade boundary layers and wakes. This analysis can be applied to predict the viscous-layer responses that arise from imposed inviscid conditions at the blade and wake surfaces. At present only a direct viscous-layer calculation and a weak or sequential coupling of inviscid and viscous-layer solutions has been considered. The development of a strong inviscid/viscid interaction analysis involving a simultaneous coupling of the inviscid and viscous solutions should be considered in future work. Under the present effort, the existing unsteady viscous layer analysis has been extended, by incorporating a similarity analysis for the flow in the vicinity of a moving stagnation point and by accounting for the jumps in the inviscid flow variables across vortex-sheet unsteady wakes, and applied to predict unsteady cascade flows excited by prescribed acoustic excitations.

The coupled linearized inviscid LINFLO and nonlinear viscous-layer UNSVIS analyses have been demonstrated via applications to an unstaggered flat-plate cascade subjected to acoustic excitations from upstream and downstream, and to a turbine cascade interacting with an upstream acoustic excitation. The flat-plate example is, perhaps, the simplest unsteady cascade problem that can be analyzed, both because of its geometric simplicity and because the unsteady pressure is nonsingular at the flat-plate leading edges. The numerical results indicate that the viscous layer responds linearly, for the most part, to acoustic excitations from upstream, but significant nonlinear response components occur for downstream excitations at high temporal frequency and/or high amplitude, which travel against the mainstream flow velocity. A similar conclusion, based on Navier-Stokes solutions for acoustic excitations interacting with a low-speed compressor cascade has also been reported in [DV94]. The numerical results for the turbine demonstrate the present weak inviscid/viscid interaction solution capability for a realistic cascade configuration.

Because of boundary-layer separation, the range of application of a weak unsteady inviscid/viscid interaction analysis is severely limited. For example, the mean pressure rise produced by a compressor blade row typically causes boundary-layer separations near blade leading edges, thereby precluding a continuation of a direct viscous-layer calculation along the blades and into their wakes. Thus, the development of a strong inviscid/viscid interaction analysis for unsteady flows will be needed so that the effects of steady and unsteady viscous displacements on the unsteady aerodynamic responses of blade rows can be predicted. The responses of viscous layers to prescribed blade vibrations and entropic and vortical excitations are other issues that require further study. In particular, as an important next step, the UNSVIS analysis should be applied to unsteady cascade flows excited by prescribed blade motions. The viscous layer responses in such flows should be studied to understand the relative importance of nonlinearities and the potential impact of unsteady viscous displacement on unsteady pressure response.

References

[AG89] H. M. Atassi and J. Grzedzinski. Unsteady Disturbances of Streaming Motions around Bodies. *Journal of Fluid Mechanics*, 209:385–403, December 1989.

[AV94] T. C. Ayer and J. M. Verdon. Numerical Unsteady Aerodynamic Simulator for Vibrating Blade Rows, 1994. Final Report prepared for the GUIde Consortium under Air Force Contract F33615–92–C–2212, to be published as an Air Force Contractor Report, 1995.

[BHE91] M. Barnett, D. E. Hobbs, and D. E. Edwards. Inviscid-Viscous Interaction Analysis of Compressor Cascade Performance. *Transactions of the ASME: Journal of Turbomachinery*, 113(4):538–553, October 1991.

[BL78] B. S. Baldwin and H. Lomax. Thin-Layer Approximation and Algebraic Model for Separated Turbulent Flow. AIAA Paper 78–257, 16th Aerospace Sciences Meeting, Huntsville, Alabama, January 16–18 1978.

[Blo70] F. G. Blottner. Finite Difference Method of Solution of the Boundary-Layer Equations. *AIAA Journal*, 18:193–205, February 1970.

[BV87] M. Barnett and J. M. Verdon. Viscid/Inviscid Interaction Analysis of Subsonic Turbulent Trailing-Edge Flows. *AIAA Journal*, 25(9):1184–1193, September 1987.

[BV89] M. Barnett and J. M. Verdon. Theoretical Prediction of High Reynolds Number Viscid/Inviscid Interaction Phenomena in Cascades. In *Proceedings of the Fourth Symposium on Numerical and Physical Aspects of Aerodynamic Flows*, Long Beach, California, January 1989.

[BV93] M. Barnett and J. M. Verdon. Analysis of Blade Unsteady Boundary Layers and Wakes. *Unsteady Aerodynamics, Aeroacoustic, and Aeroelasticity of Turbomachines and Propellers*, pages 377–395, 1993. Springer-Verlag, New York, edited by H. M. Atassi.

[BVA93a] M. Barnett, J. M. Verdon, and T. C. Ayer. An Analysis for High Reynolds Number Inviscid/Viscid Interaction in Cascades. CR 4519, NASA, May 1993.

[BVA93b] M. Barnett, J. M. Verdon, and T. C. Ayer. Analysis for High Reynolds Number Inviscid/Viscid Interaction in Cascades. *AIAA Journal*, 31(11):1969–1976, 1993.

[Car79] J. E. Carter. A New Boundary Layer Inviscid Iteration Technique for Separated Flow. Paper 78–1459, AIAA Fourth Computational Fluid Dynamics Meeting, Williamsburg, Virginia, July 23–24 1979.

[Cas83] J. R. Caspar. Unconditionally Stable Calculation of Transonic Potential Flow through Cascades using an Adaptive Mesh for Shock Capture. *Transactions of the ASME: Journal of Engineering for Power*, 105(3):504–513, July 1983.

[CBCW86] K. C. Chang, M. N. Bui, T. Cebeci, and J. H. Whitelaw. The Calculation of Turbulent Wakes. *AIAA Journal*, 24:200–201, February 1986.

[CH80] W. J. Calvert and M. V. Hebert. An Inviscid-Viscous Interaction Method to Predict the Blade-to-Blade Performance of Axial Compressors. *Aeronautical Quarterly*, XXXI:173–196, 1980. Part 3.

[CS74] T. Cebeci and A. M. O. Smith. *Analysis of Turbulent Boundary Layers*, pages 211–239. Academic Press, New York, 1974.

[CV81] J. R. Caspar and J. M. Verdon. Numerical Treatment of Unsteady Subsonic Flow Past an Oscillating Cascade. *AIAA Journal*, 19(12):1531–1539, December 1981.

[DBJ+89] R. P. Dring, M. F. Blair, H. D. Joslyn, G. D. Power, and J. M. Verdon. The Effects of Inlet Turbulence and Rotor/Stator Interactions in the Aerodynamics and Heat Transfer of a Large-Scale Rotating Model. Vol. I — Final Report CR 4079, NASA, June 30 1989.

[DDE92] D. J. Dorney, R. L. Davis, and D. E. Edwards. Investigation of Hot Streak Migration and Film Cooling Effects on Heat Transfer in Rotor/Stator Interacting Flows. Report 91-29, UTRC, East Hartford, CT, April 1992. Prepared under Contract N00014–88–C–0677 (Report 1).

[DN58] S. Dhawan and R. Narashima. Some Properties of Boundary-Layer Flow During the Transition from Laminar to Turbulent Motion. *Journal of Fluid Mechanics*, 3, 1958.

[DV94] D. J. Dorney and J. M. Verdon. Numerical Simulations of Unsteady Cascade Flows. *Trans. of the ASME: Journal of Turbomachinery*, 116(4):665–675, October 1994.

[Edw93] J. W. Edwards. Transonic Shock Oscillations Calculated with a New Interactive Boundary Layer Coupling Method. Paper 93–0777, AIAA 31st Aerospace Sciences Meeting and Exhibit, Reno, Nevada, January 11-14 1993.

[FS83] T. H. Fransson and P. Suter. Two-Dimensional and Quasi Three-Dimensional Experimental Standard Configurations for Aeroelastic Investigations in Turbomachine-Cascades. Report LTA–TM–83–2, Ecole Polytechnique Federale de Lausanne, Lausanne, Switzerland, September 1983.

[FV93] T. H. Fransson and J. M. Verdon. Standard Configurations for Unsteady Flow through Vibrating Axial-Flow Turbomachine Cascades. *Unsteady Aerodynamics, Aeroacoustics and Aeroelasticity of Turbomachines and Propellers*, pages 859–889, 1993. Springer-Verlag, New York, edited by H. M. Atassi.

[Gil90] M. B. Giles. Nonreflecting Boundary Conditions for Euler Equation Calculations. *AIAA Journal*, 28(12):2050–2058, December 1990.

[Gla56] M. B. Glauert. The Laminar Boundary Layer on Oscillating Plates and Cylinders. *Journal of Fluid Mechanics*, 1:97–110, 1956.

[Gol78] M. E. Goldstein. Unsteady Vortical and Entropic Distortions of Potential Flows Round Arbitrary Obstacles. *Journal of Fluid Mechanics*, 89(Part 3):433–468, December 1978.

[Gol79] M. E. Goldstein. Turbulence Generated by the Interaction of Entropy Fluctuations with Non-uniform Mean Flows. *Journal of Fluid Mechanics*, 93(Part 2):209–224, July 1979.

[HC93a] K. C. Hall and W. S. Clark. Linearized Euler Predictions of Unsteady Aerodynamic Loads in Cascades. *AIAA Journal*, 31(3):540–550, March 1993.

[HC93b] D. G. Holmes and H. A. Chuang. 2D Linearized Harmonic Euler Flow Analysis for Flutter and Forced Response. *Unsteady Aerodynamics, Aeroacoustics, and Aeroelasticity of Turbomachines and Propellers*, pages 213–230, 1993. Springer-Verlag, New York, edited by H. M. Atassi.

[HSS79] E. C. Hansen, G. K. Serovy, and P. M. Sockol. Axial-Flow Compressor Turning Angle and Loss by Inviscid-Viscous Interaction Blade-to-Blade Computation. Paper 79–GT–5, ASME, 1979.

[HV91] K. C. Hall and J. M. Verdon. Gust Response Analysis for Cascades Operating in Nonuniform Mean Flows. *AIAA Journal*, 29(9):1463–1471, September 1991.

[HV93] D. Hoyniak and J. M. Verdon. Development of a Steady Potential Solver for Use with Linearized Unsteady Aerodynamic Analyses. *Unsteady Aerodynamics, Aeroacoustic, and Aeroelasticity of Turbomachines and Propellers*, pages 177–194, 1993. Springer-Verlag, New York, edited by H. M. Atassi.

[HV94] D. Hoyniak and J. M. Verdon. Steady and Linearized Unsteady Transonic Analyses of Turbomachinery Blade Rows. Paper, presented at the Seventh International Symposium on Unsteady Aerodynamics and Aeroelasticity of Turbomachines, Fukuoka, Japan, September 25–29 1994. Conference Proceedings to be published by Elsevier Press, 1995.

[JH83] P. Janssens and Ch. Hirsch. A Viscid Interaction Procedure for Two-Dimensional Cascades. Technical Report CP–351, AGARD, 1983. pp. 3-1– 3-18.

[KK93] G. Kahl and A. Klose. Computation of Time Linearized Transonic Flow in Oscillating Cascades. ASME Paper 93–GT–269, 38th International Gas Turbine and Aeroengine Congress and Exposition, Cincinnati, Ohio, May 24–27 1993.

[KV93a] K. A. Kousen and J. M. Verdon. Active Control of Wake/Blade-Row Interaction Noise. CR 4556, prepared under Contract NAS3–25425, for NASA Lewis Research Center, Cleveland, Ohio, December 1993.

[KV93b] K. A. Kousen and J. M. Verdon. Aeroacoustics of Real Blade Cascades. *Unsteady Aerodynamics, Aeroacoustic, and Aeroelasticity of Turbomachines and Propellers*, pages 725–742, 1993. Springer-Verlag, New York, edited by H. M. Atassi.

[KV94] K. A. Kousen and J. M. Verdon. Active Control of Wake/Blade-Row Interaction Noise. *AIAA Journal*, 32(10):1953–1960, October 1994.

[Mel80] R. E. Melnik. Turbulent Interactions on Airfoils at Transonic Speeds — Recent Developments. In *AGARD–CP–291*, February 1980. Paper No. 10.

[MM94] M. M. Morel and D. V Murthy. Turbomachinery Forced Response Prediction System: Users manual. CR 194465, NASA, March 1994. Prepared for NASA Lewis Research Center under Contract NAS3–25266 and Grant NAG3–1669.

[MV94] M. D. Montgomery and J. M. Verdon. A Linearized Unsteady Euler Analysis for Turbomachinery Blade Rows Using an Implicit Wave-Split Scheme. Paper, presented at Seventh International Symposium on Unsteady Aerodynamics and Aeroelasticity of Turbomachines, Fukuoka, Japan, September 25–29 1994. Conference Proceedings to be published by Elsevier Press, 1995.

[MVF94] M. D. Montgomery, J. M. Verdon, and S. Fleeter. A Linearized Aerodynamic Analysis for Supersonic Cascades. Paper, presented at Seventh International Symposium on Unsteady Aerodynamics and Aeroelasticity of Turbomachines, Fukuoka, Japan, September 25–29 1994. Conference Proceedings to be published by Elsevier Press, 1995.

[Nam87] M. Namba. Three Dimensional Flows. In M. F. Platzer and F. O. Carta, editors, *AGARD Manual on Aeroelasticity in Axial-Flow Turbomachines*, chapter IV. AGARD, March 1987. Vol. 1, *Unsteady Turbomachinery Aerodynamics*, AGARD–AG–298.

[PVK91] G. D. Power, J. M. Verdon, and K. A. Kousen. Analysis of Unsteady Compressible Viscous Layers. *Transactions of the ASME: Journal of Turbomachinery*, 113(4):644–653, October 1991.

[Rot56] N. Rott. Unsteady Viscous Flow in the Vicinity of a Stagnation Point. *Quarterly Journal of Applied Mathematics*, 13:444–451, 1956.

[Sch60] H. Schlichting. *Boundary Layer Theory*, page 339. McGraw Hill Book Company, Inc., New York, 1960.

[Smi72] S. N. Smith. Discrete Frequency Sound Generation in Axial Flow Turbomachines. R&M 3709, British Aeronautical Research Council, London, England, UK, March 1972.

[Smi90] T. E. Smith. Aerodynamic Stability of a High-Energy Turbine Blade. Paper 90–2351, AIAA/SAE/ASME/ASEE 26th Joint Propulsion Conference, Orlando, Florida, July 16–18 1990.

[SS90] A. Suddhoo and P. Stow. Simulation of Inviscid Blade-Row Interaction Using a Linearized Potential Code. Paper 90–1916, AIAA/SAE/ASME/ASEE 26th Joint Propulsion Conference, Orlando, Florida, July 16–18 1990.

[Ste55] W. L. Stewart. Analysis of two-dimensional compressible flow loss characteristics downstream of turbomachine blade rows in terms of basic boundary-layer characteristics, 1955. NACA TN 3515.

[UV91] W. J. Usab, Jr. and J. M. Verdon. Advances in the Numerical Analysis of Linearized Unsteady Cascade Flows. *Transactions of the ASME: Journal of Turbomachinery*, 113(4):633–643, October 1991.

[VBHA91] J. M. Verdon, M. Barnett, K. C. Hall, and T. C. Ayer. Development of Unsteady Aerodynamic Analyses for Turbomachinery Aeroelastic and Aeroacoustic Applications. CR 4405, NASA Lewis Research Center, Cleveland, Ohio, October 1991.

[VC82] J. M. Verdon and J. R. Caspar. Development of a Linear Unsteady Aerodynamic Analysis for Finite-Deflection Subsonic Cascades. *AIAA Journal*, 20(9):1259–1267, September 1982.

[VC84] J. M. Verdon and J. R. Caspar. A Linearized Unsteady Aerodynamic Analysis for Transonic Cascades. *Journal of Fluid Mechanics*, 149:403–429, December 1984.

[Vel80] A. E. P. Veldman. The Calculation of Incompressible Boundary Layers with Strong Viscous-Inviscid Interaction. In *AGARD–CP–291*, February 1980. Paper No. 12.

[Ver87] J. M. Verdon. Linearized Unsteady Aerodynamic Theory. In M. F. Platzer and F. O. Carta, editors, *AGARD Manual on Aeroelasticity in Axial-Flow Turbomachines*, chapter II. AGARD, March 1987. Vol. 1, *Unsteady Turbomachinery Aerodynamics*, AGARD–AG–298.

[Ver89a] J. M. Verdon. The Unsteady Aerodynamic Response to Arbitrary Modes of Blade Motion. *Journal of Fluids and Structures*, 3(3):255–274, May 1989.

[Ver89b] J. M. Verdon. The Unsteady Flow in the Far Field of an Isolated Blade Row. *Journal of Fluids and Structures*, 3(2):123–149, March 1989.

[Ver92] J. M. Verdon. Linearized Unsteady Aerodynamics for Turbomachinery Aeroelastic Applications. *Journal de Physique III*, 2(4):481–506, April 1992. Also presented as Paper 90–2355, AIAA/SAE/ASME/ASEE 26th Joint Propulsion Conference, Orlando, Florida, July 16–18, 1990.

[Ver93] J. M. Verdon. Unsteady Aerodynamic Methods for Turbomachinery Aeroelastic and Aeroacoustic Applications. *AIAA Journal*, 31(2):235–250, February 1993.

[VH90] J. M. Verdon and K. C. Hall. Development of a Linearized Unsteady Aerodynamic Analysis for Cascade Gust Response Predictions. CR 4308, prepared under Contract NAS3–25425 for NASA Lewis Research Center, Cleveland, Ohio, July 1990.

[VV85] V. N. Vatsa and J. M. Verdon. Viscous/Inviscid Interaction Analysis of Separated Trailing-Edge Flows. *AIAA Journal*, 23(4):481–489, 1985.

[VWV82] V. N. Vatsa, M. J. Werle, and J. M. Verdon. Viscid/Inviscid Interaction at Laminar and Turbulent Symmetric Trailing Edges. Paper 82–0165, AIAA 20th Aerospace Sciences Meeting, Orlando, Florida, January 11–14 1982.

[Whi74] F. M. White. *Viscous Fluid Flow*, page 596. McGraw Hill Book Company, Inc., New York, 1974.

[Whi87] D. S. Whitehead. Classical Two-Dimensional Methods. In M. F. Platzer and F. O. Carta, editors, *AGARD Manual on Aeroelasticity in Axial-Flow Turbomachines*, chapter III. AGARD, March 1987. Vol. 1, *Unsteady Turbomachinery Aerodynamics*, AGARD–AG–298.

[Wig81] L. B. Wigton. Viscous-inviscid interaction in transonic flow, 1981. AIAA Paper 81–1003.

[Wil79] M. H. Williams. Linearization of Unsteady Transonic Flows Containing Shocks. *AIAA Journal*, 17(4):394–397, April 1979.

[WN85] D. S. Whitehead and S. G. Newton. A Finite Element Method for the Solution of Two-Dimensional Transonic Flows in Cascades. *International Journal for Numerical Methods in Fluids*, 5(2):115–132, February 1985.

[Yuh81] L. J. Yuhas. An optimization technique for the development of a two-dimensional turbulent boundary layer model. Master's thesis, Lehigh University, 1981.

REPORT DOCUMENTATION PAGE

Form Approved
OMB No. 0704-0188

1. AGENCY USE ONLY (*Leave blank*)	2. REPORT DATE	3. REPORT TYPE AND DATES COVERED
	November 1995	Final Contractor Report

4. TITLE AND SUBTITLE
Unsteady Aerodynamic Models for Turbomachinery Aeroelastic and Aeroacoustic Applications

5. FUNDING NUMBERS
WU-505-63-5B
C-NAS3-25425

6. AUTHOR(S)
Joseph M. Verdon, Mark Barnett, and Timothy C. Ayer

7. PERFORMING ORGANIZATION NAME(S) AND ADDRESS(ES)
United Technologies Research Center
411 Silver Lane, MS 129-20
East Hartford, Connecticut 06108-1049

8. PERFORMING ORGANIZATION REPORT NUMBER
E-10011

9. SPONSORING/MONITORING AGENCY NAME(S) AND ADDRESS(ES)
National Aeronautics and Space Administration
Lewis Research Center
Cleveland, Ohio 44135-3191

10. SPONSORING/MONITORING AGENCY REPORT NUMBER
NASA CR-4698
R95-957907

11. SUPPLEMENTARY NOTES
Project manager, George L. Stefko, Structures Division, NASA Lewis Research Center, organization code 5230, (216) 433-3920.

12a. DISTRIBUTION/AVAILABILITY STATEMENT
Unclassified - Unlimited
Subject Categories 02 and 07

This publication is available from the NASA Center for Aerospace Information, (301) 621-0390.

12b. DISTRIBUTION CODE

13. ABSTRACT ***(Maximum 200 words)***

Theoretical analyses and computer codes are being developed for predicting compressible unsteady inviscid and viscous flows through blade rows of axial-flow turbomachines. Such analyses are needed to determine the impact of unsteady flow phenomena on the structural durability and noise generation characteristics of the blading. The emphasis has been placed on developing analyses based on asymptotic representations of unsteady flow phenomena. Thus, high Reynolds number flows driven by small amplitude unsteady excitations have been considered. The resulting analyses should apply in many practical situations and lead to a better understanding of the relevant flow physics. In addition, they will be efficient computationally, and therefore, appropriate for use in aeroelastic and aeroacoustic design studies. Under the present effort, inviscid/viscid interaction and linearized inviscid unsteady flow models have been formulated, and inviscid and viscid prediction capabilities for subsonic steady and unsteady cascade flows have been developed. In this report, we describe the linearized inviscid unsteady analysis, LINFLO, the steady inviscid/viscid interaction analysis, SFLOW-IVI, and the unsteady viscous layer analysis, UNSVIS. These analyses are demonstrated via application to unsteady flows through compressor and turbine cascades that are excited by prescribed vortical and acoustic excitations and by prescribed blade vibrations. Recommendations are also given for the future research needed for extending and improving the foregoing asymptotic analyses, and to meet the goal of providing efficient inviscid/viscid interaction capabilities for subsonic and transonic unsteady cascade flows.

14. SUBJECT TERMS	15. NUMBER OF PAGES
Unsteady aerodynamics; Turbomachinery cascades; High Reynolds number flow; Inviscid/viscid interactions; Small unsteady disturbances; Linearized inviscid analysis; Unsteady viscous layers; Aeroelastic and Aeroacoustic responses	139
	16. PRICE CODE: A07

17. SECURITY CLASSIFICATION OF REPORT	18. SECURITY CLASSIFICATION OF THIS PAGE	19. SECURITY CLASSIFICATION OF ABSTRACT	20. LIMITATION OF ABSTRACT
Unclassified	Unclassified	Unclassified	